PH.D. THESIS OF THE UNIVERSITY PARIS VI

Discipline : THEORETICAL PHYSICS

Thermoelectric conversion in disordered nanowires

presented by :

Riccardo Bosisio

in partial fulfillment of the requirements for the degree of

Doctor of University PARIS VI

Supervisor : Jean - Louis PICHARD

Jury members :

Mr. Dominique DELANDE .....

Mr. Colin LAMBERT .....

Mr. Jean-Louis PICHARD .....

Mr. Marc SANQUER .....

Mr. Sebastian VOLZ .....

fulfilled at Service de Physique de l'Etat Condensé of CEA Saclay

Wir müssen wissen. Wir werden wissen. - D. Hilbert

Without deviation from the norm, progress is not possible. - F. Zappa

Acknowledgements

My first personal acknowledgment goes to my supervisor, Prof. Jean-Louis Pichard, for having constantly guided me throughout these three years, for his continuous support, and for having shared his experience and passion for the fields of thermoelectricity and, more generally, mesoscopic physics.

I am also grateful to Dominique Delande, Colin Lambert, Marc Sanquer and Sebastian Volz, for having accepted to be part of my jury.
I sincerely thank Dr. Geneviéve Fleury for all the discussions about physics, for her essential advices in drawing up papers and for having carefully reviewed this manuscript.

I also wish to extend my gratitude to other members of the group and to the people with whom I have collaborated during my Ph. D.: Prof. Giuliano Benenti, Prof. Michel Roger, Dr. Andrii Kleshchonok, Dr. Guido Intronati, the members of Prof. Rosario Fazio's group in Pisa, and especially Dr. Cosimo Gorini, who boosted me a lot in the final stages of my Ph. D.

Finally, I personally think that many people would deserve gratitude, simply for having shared with me few or more moments during these exciting three years. If it has been a great and rewarding experience, it is thanks to them.
Family, (longtime and new) friends and Debby, I thank you all.

Contents

1 Generalities on thermoelectricity **11**

Summary of chapter 1 . . . 12

1.1 Thermoelectric effects . . . 13

1.1.1 Seebeck effect . . . 13

1.1.2 Peltier effect . . . 15

1.1.3 Thomson effect . . . 15

1.1.4 Joule effect . . . 16

1.1.5 Thomson/Kelvin relations . . . 16

1.2 Linear response: Onsager formalism . . . 17

1.2.1 Transport coefficients . . . 18

1.2.2 Thermoelectric figure of merit . . . 18

1.3 Applications of thermoelectricity . . . 20

1.3.1 Overview . . . 20

1.3.2 Thermoelectric modules . . . 22

2 Thermoelectric conversion in nanowires:state of the art and motivations **25**

Summary of chapter 2 . . . 26

2.1 Low dimensional systems: toward efficient thermoelectrics . . . 27

2.2 Advantages of semiconductor nanowires . . . 29

2.3 Nanowires fabrication techniques . . . 32

2.4 Strategy adopted in this thesis . . . 36

2.4.1 Experimental overview . . . 36

2.4.2 Theoretical overview . . . 39

2.4.3 Our theoretical approach . . . 39

3 Coherent Regime **43**

Summary of chapter 3 . . . 44

3.1 Landauer-Büttiker formalism . . . 45

3.2 Model and method . . . 46

3.2.1 Calculation of the transport coefficients . . . 48

3.2.2 Scanning the impurity band of the Anderson model . . . 49

3.2.3 Localization length of the Anderson model . . . 49
3.3 Thermopower . . . 51
3.3.1 Typical thermopower . . . 51
3.3.2 Thermopower distributions . . . 55
3.4 Figure of merit . . . 61
3.5 Temperature range of validity of the Sommerfeld expansion . . . 64
3.6 Appendix . . . 66
3.6.1 Recursive Green Function algorithm . . . 66
3.6.2 Self-energy of the 2D leads . . . 70
3.6.3 Thermopower of a clean tunnel barrier . . . 70

4 Activated Regime **73**
Summary of chapter 4 . . . 74
4.1 Model and method . . . 75
4.1.1 Transport mechanisms and temperature scales . . . 75
4.1.2 Formulation in terms of a random resistor network . . . 80
4.1.3 Anderson model for the localized states . . . 82
4.2 Electrical Conductance . . . 83
4.2.1 Background . . . 83
4.2.2 Numerical results . . . 85
4.3 Thermopower . . . 86
4.3.1 Background . . . 86
4.3.2 Numerical results . . . 88
4.3.3 Limitations of the present approach . . . 92
4.4 Appendix . . . 93
4.4.1 Thermodynamics of the three-terminal setup . . . 93
4.4.2 Solution of the random resistor network . . . 95
4.4.3 Calculation of the hopping probability . . . 96

5 Arrays of Parallel Nanowires **99**
Summary of chapter 5 . . . 100
5.1 Model and method . . . 101
5.2 Fluctuations . . . 103
5.3 Power factor and figure of merit . . . 103
5.3.1 On the dependency on the couplings γ_e and γ_{ep} . . . 107
5.3.2 Size effects . . . 108
5.4 Hot spots cooling . . . 109

6 Three-terminal Quantum Machines **115**
Summary of chapter 6 . . . 116
6.1 Linear response for 3-terminal systems . . . 117
6.1.1 Transport coefficients . . . 117
6.2 Efficiency for 3-terminal systems . . . 120
6.2.1 Carnot efficiency . . . 121
6.2.2 Efficiency at Maximum Power . . . 122
6.3 Examples . . . 125
6.3.1 Single dot . . . 126
6.3.2 Double Dot . . . 131
6.4 Appendix . . . 134
6.4.1 Calculation of the transport coefficients and thermopowers . . . 134
6.4.2 Cholesky Decomposition of the three-terminal Onsager matrix . . . 136
6.4.3 Scattering approach in linear response: the Onsager coefficients . . . 137
6.4.4 Transmission function of a single-level dot . . . 138

7 Epilogue **141**

Chapter 1

Generalities on thermoelectricity

Contents

Summary of chapter 1 . . . . . **12**

1.1 Thermoelectric effects **13**

1.1.1 Seebeck effect 13

1.1.2 Peltier effect 15

1.1.3 Thomson effect 15

1.1.4 Joule effect 16

1.1.5 Thomson/Kelvin relations 16

1.2 Linear response: Onsager formalism **17**

1.2.1 Transport coefficients 18

1.2.2 Thermoelectric figure of merit 18

1.3 Applications of thermoelectricity **20**

1.3.1 Overview 20

1.3.2 Thermoelectric modules 22

Summary of chapter 1

In this chapter, we review some basic but fundamental aspects about thermoelectricity.
The first section is a general introduction on the various thermoelectric effects, namely the Seebeck, Peltier, Thomson and Joule effects. Also, the Thomson/Kelvin relations are presented.

In section 1.2, we introduce the Onsager formalism within linear response approximation, which is used throughout all this thesis. Following Callen [32], we discuss the concepts of *affinities* (or thermodynamic generalized forces) and *fluxes* (the currents flowing through a system), the Onsager matrix $\mathbf{L}$, and the properties of its elements L_{ij}. We show that in this regime the expressions for the charge and heat currents J^e and J^Q can be linearized, resulting in coupled equations involving the coefficients L_{ij}'s. After, we derive expressions for all the transport coefficients (electric conductance G, thermal conductance K, Seebeck coefficient S, Peltier coefficient Π) in terms of the Onsager matrix elements L_{ij}'s. We then go through the problem of optimizing the efficiency η and the output power $\dot{W}$ of a generic thermoelectric system, leading to the key concepts of *maximum efficiency* η_{max} and *efficiency at maximum power* $\eta(\dot{W}_{\max})$, both expressed in terms of a dimensionless *figure of merit* ZT.

Finally, in section 1.3 we briefly overview some applications of themoelectricity and we conclude by illustrating the working operation of the *thermoelectric module*, which can operate as a cooler (in the Peltier configuration) as well as a power generator (in the Seebeck configuration), and which constitutes the building-block of many thermoelectric devices.

1.1 Thermoelectric effects

Thermoelectric effects are phenomena associated with the simultaneous flow of electric current and energy (or heat) current in a system. Although the pioneering experiments by Volta and Seebeck date back to about two centuries ago, a really strong interest of the scientific community for thermoelectricity arose only in 1950's, when Abram Ioffe discovered that doped semiconductors exhibit large thermoelectric effect [82]. Curiously, at that time he became famous for having stated that thanks to this phenomenon everyone in Siberia could have supplied a radio by using a common kerosene lamp (see Fig. 1.1). Before that, the most remarkable contribution of thermoelectricity had been rather in supporting the theoretical development of thermodynamics: indeed, it played an important role in the works by Thomson [170] and later by Onsager [128]. From a more practical/technological point of view, the requirements needed to design an efficient thermoelectric generator (a large electrical conductivity σ and Seebeck coefficient (thermopower) S, and a poor thermal conductivity κ) were first pointed out by Altenkirch in 1909 [2] and then formalized by Ioffe [82]. The latter introduced a unique dimensionless parameter called the *figure of merit* which is a combination of the three aforementioned transport coefficient, $ZT = (S^2\sigma/\kappa)\,T$, and that has been used since then to estimate the thermoelectric performance. Nowadays, many studies are still focused on the quest of materials with the highest ZT, which would allow to design highly efficient thermoelectric generators [163]. In parallel to Ioffe's works, Goldsmid showed that the same principles could be exploited to achieve thermoelectric refrigeration [60].

Motivated by the improvements of performances on the one hand, and by the intriguing idea that home refrigerators could be built with semiconductors on the other [47, 107, 109], thermoelectric materials such as Bismuth Telluride (Bi_2Te_3) were developed for commercial purposes, envisaging large scale applications. However, this activity lasted only few years until the mid 1960's since, in spite of all efforts and consideration of all type of semiconductors, it turned out that thermoelectric refrigerators had still poor efficiency as compared to compressor based ones. This rapidly confined thermoelectricity to niche markets, such as aerospace and submarine technology.

1.1.1 Seebeck effect

The first acknowledged experiment on thermoelectricity dates back to 1794, when A. Volta discovered thermoelectromotive forces arising under the influence of a temperature difference [5, 180]. Some years after Volta's work, in 1821, T. J. Seebeck performed an experiment which would have been worth the reputation of pioneer of the thermoelectric effect for the Estonian-German scientist. He observed that a compass needle, put inside a closed loop formed by two different metals, was deflected in presence of a temperature difference between the junctions [157] (see Fig. 1.2(a)). This was because the metals responded differently to the temperature difference, creating a current loop and hence a magnetic field. Curiously,

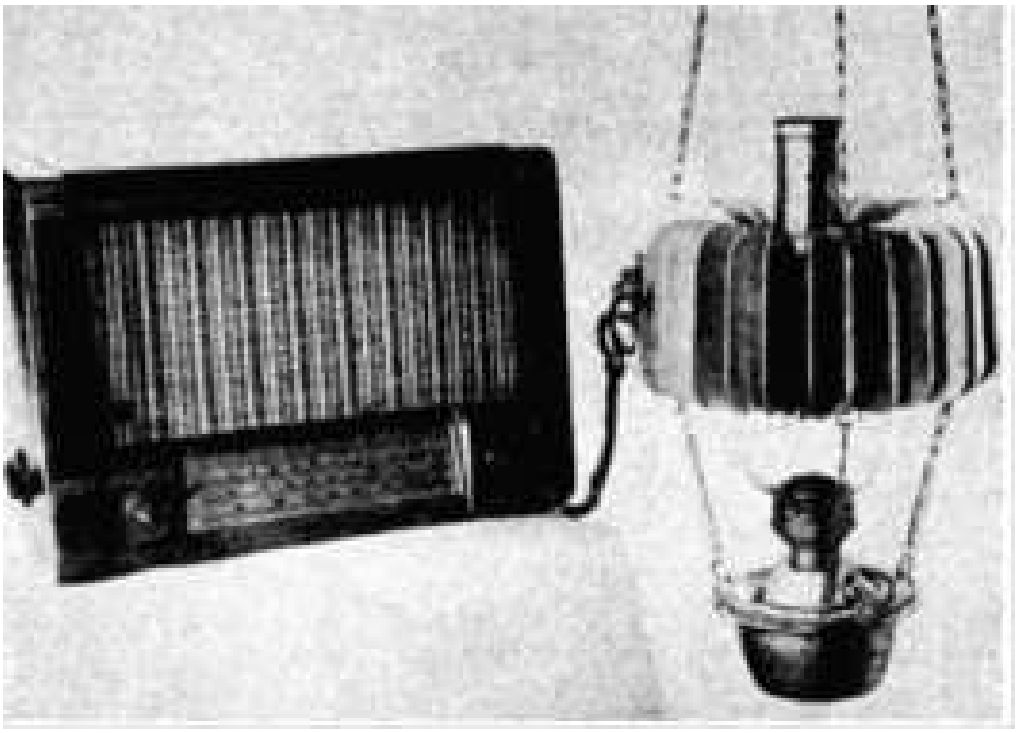


Figure 1.1: Model TGK-3 thermoelectric generator: a series of thermocouples is arranged around the upper portion of the lamp. As each set of elements is heated at one end by the lamp, a small amount of electricity flows through the pair. Metallic fins remove the excess heat. (URSS, 1948)

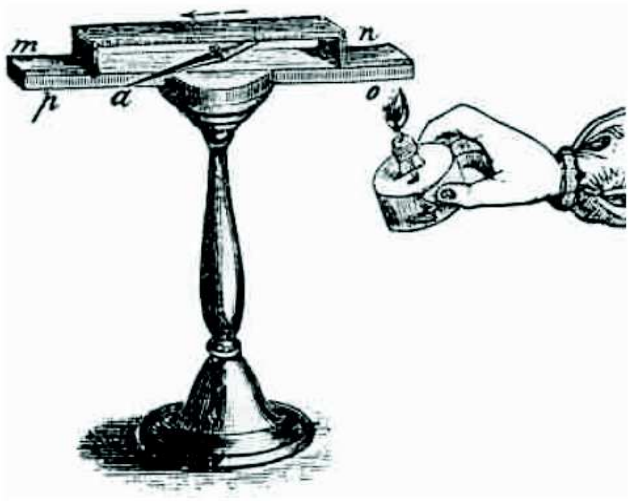
at the beginning, Seebeck interpreted the phenomenon as a thermomagnetic, rather than a thermoelectric effect. It was H. C. Ørsted who rectified the mistake and coined the term *thermoelectricity*.

If the temperature difference ΔT is small, the electromotive force is proportional to it, the proportionality coefficient being called *Seebeck coefficient*, or *thermoelectric power* (or simply *thermopower*):

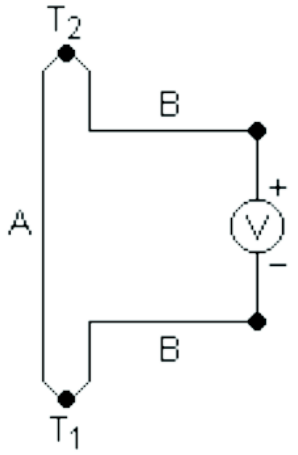
$$S_{AB} = S_B - S_A = \frac{V_2 - V_1}{T_2 - T_1}, \tag{1.1}$$

where V denotes the electric potential and T the temperature, following the convention of Fig. 1.2(b). S_{AB} is associated to the thermocouple: in particular, its sign is chosen as positive if the voltage increment is such as to drive the current from A to B at the hot junction. It is not possible to measure the Seebeck coefficient of a single material (A or B) directly, as the measure of the electric potentials has to be carried out at a unique temperature, otherwise the voltmeter's Seebeck coefficient shall be taken into account. However, if the thermopower of one of the two materials, say B, is much smaller than the S_A, we can approximate

$$S_A \simeq -\frac{V_2 - V_1}{T_2 - T_1}. \tag{1.2}$$



(a)



(b)

Figure 1.2: (a) Sketch of the experiment performed by Seebeck: a junction (o,n) between two metals is heated, causing an electromotive force to appear in the circuit which deflects the compass needle a. (b) Sketch of the experiment by Seebeck: a thermocouple made of two distinct materials A and B joined at tempeatures T_1 and T_2. A voltmeter is inserted in one arm of the circuit, allowing no passage of electric current but offering no resistance to the flow of heat.

1.1.2 Peltier effect

In 1834, J. C. A. Peltier observed that a flow of an electric current across an isothermal junction of two materials is accompanied by an evolution of heat through it [131]. With reference to the same experimental sketch of Fig. 1.2(b) with now $T_1 = T_2$, if the electric current is small, the heat flux absorbed (or released) at the junctions 1 and 2 is proportional to it, the proportionality coefficient being called *Peltier coefficient*:

$$\Pi_{AB} = \Pi_B - \Pi_A = \frac{J^Q_B - J^Q_A}{J^e}, \tag{1.3}$$

where $J^Q_{A(B)}$ is the heat absorbed or released at junction 1(2), while J^e is the electric current. In other words, the Peltier coefficient represents how much heat is carried per unit charge. Since charge current must be continuous across a junction, the associated heat flow will develop a discontinuity if Π_A and Π_B are different. For a positive charge current flowing from conductor A to B, a positive $\Pi_{AB} > 0$ will be associated to absorption of heat at the junction, while there will be a release of heat for $\Pi_{AB} < 0$.

1.1.3 Thomson effect

In 1851, presenting a dissertation about the two previously discovered thermoelectric effects [169], W. Thomson introduced a novel effect, associated to the evolution of heat as

an electric current traverses a temperature gradient in a material. This, in contrast to the Seebeck and Peltier effects, could be observed even in a *single* material.

More in detail, we consider a conductor in which a gradient of temperature ∇T has been set up. In response to a current J^e, heat is exchanged among the material and the environment, consisting of two parts: the Joule heat (to be discussed in the next subsection) and the Thomson heat. The latter, under condition of small electric current and temperature gradient, can be written as:

$$J_\tau^Q = \tau \nabla T J^e, \tag{1.4}$$

the proportionality coefficient τ being called *Thomson coefficient*. By convention, a negative τ is associated to a dissipation of heat from the conductor to the environment, and vice-versa for a positive τ. Qualitatively, this effect can be interpreted as a "continuum" version of the Peltier effect: if we separate the material into slices, in each of which the temperature may be considered constant, we can define a sequence of *local* Peltier coefficients, one for each slice. The flow of electric current through each of these (nearly) isothermal slices is accompanied by a Peltier heating or cooling: summing up along the entire material gives J_τ^Q, the Thomson heat.

1.1.4 Joule effect

Analogously to the Thomson effect, the Joule effect is related to the evolution of heat associated to the flow of an electric current through a conductor; however, it does not require any temperature gradient, but rather it depends on the electric resistance R of the material. For a small electric current J^e, the dissipated Joule heat exhibits a quadratic dependence on R:

$$J_J^Q = R^2 J^e. \tag{1.5}$$

Evidenced by J. P. Joule in 1843 [86], this effect is a direct consequence of the proportionality between the voltage drop ΔV across the material and the current flowing through it, i.e. the Ohm's law [127].

1.1.5 Thomson/Kelvin relations

Thomson, besides explaining the effect which is named after him, gave a significant contribution to the unification of the thermoelectric effects, by understanding that the Seebeck, Peltier and Thomson effects are different manifestation of a unique phenomenon: the electric current can transport heat by a convective process [171]. Also, he found two relationships among the various thermoelectric coefficients, which are called *Kelvin relations* after him (he got the appellation of "Lord Kelvin" in 1892).

The first Kelvin relation links the Thomson coefficient to the thermopower:

$$\tau = T \frac{dS}{dT}, \tag{1.6}$$

where T is the local temperature. The second Kelvin relation links the Peltier coefficient to the thermopower:

$$\Pi = TS, \tag{1.7}$$

and it was not satisfactorily proven until the advent of the Onsager relations [128]. It is worth to note that this relation is only guaranteed in presence of time-reversal symmetry (see also next section).

1.2 Linear response: Onsager formalism

In the framework of non-equilibrium thermodynamics [32], processes are described on the basis of two kinds of parameters: *generalized forces* X_i (also called *affinities*), and the *fluxes* J_i characterizing the response of a system to these forces.

The Onsager formalism lies on the hypothesis of local equilibrium, both in a *temporal* as well as in a *spatial* sense. The former implies that the time variations of the macroscopic thermodynamic quantities shall be slow enough for the microscopic quantities to relax on a much shorter time scale. In other words, it τ_{macro} and τ_{micro} are the macroscopic and the microscopic relaxation times respectively, the relation $\tau_{macro} \gg \tau_{micro}$ must hold [130]. The latter means that it must be possible to consider the system as made of cells, the size of which should be small enough for any thermodynamic variations inside them to be weak, but at the same time large enough to allow them to be considered as thermodynamic systems in contact with their environment [32].

When these conditions are fulfilled, if the generalized forces are small, the relationship between fluxes and forces is approximately linear:

$$J_i = \sum_j L_{ij} X_j \tag{1.8}$$

These relations are referred to as phenomenological coupled transport equations or *linear response* equations, where the term "coupled" refers to the fact that each flux J_i depends not only on its *associated* affinity X_i, but also on the other $X_{j \neq i}$.

The coefficients L_{ij} are known as *Onsager (kinetic) coefficients*, and they satisfy the Onsager theorem [33, 128], that is, the value of the kinetic coefficient L_{ij} $(j \neq i)$ measured in an external magnetic field $\mathbf{B}_e$ is identical to the value of L_{ji} measured in the reversed magnetic field $-\mathbf{B}_e$:

$$L_{ij}(\mathbf{B}_e) = L_{ji}(-\mathbf{B}_e). \tag{1.9}$$

This theorem establishes a symmetry between the linear effect of the jth affinity on the ith flux and vice-versa when these effects are measured in opposite magnetic fields. In particular, if the system is symmetric with respect to time inversion (e.g., in absence of any magnetic field), $L_{ij} = L_{ji}$ is always satisfied.

Furthermore, the rate of entropy production, $\dot{\mathcal{S}}$, must be non negative:

$$\dot{\mathcal{S}} = \sum_i J_i X_i \geq 0. \tag{1.10}$$

As a consequence, the symmetric matrix $\mathbf{L}^{\mathrm{S}} = (\mathbf{L}+\mathbf{L}^{\mathrm{T}})/2$, constructed starting by the matrix $\mathbf{L}$ made of the Onsager coefficients L_{ij}'s, shall be semi-positive definite; this entails, among other properties, that all the diagonal terms L_{ii} have to be non-negative.

1.2.1 Transport coefficients

Let's consider a prototypical model consisting of a generic system in contact to two electronic reservoirs at temperatures T_1, T_2 and electrochemical potentials μ_1, μ_2, which can exchange particles and heat with it. In linear response, we assume the temperature difference $\Delta T = T_1 - T_2$ to be small compared to $T_1 \approx T_2 \equiv T$ and the difference among electrochemical potentials $\Delta\mu = \mu_1 - \mu_2$ to be small compared to $\mu_1 \approx \mu_2 \equiv \mu$ and $k_B T$. Since the total electric and energy currents through the system are conserved, only two fluxes are independent:

$$\begin{cases} J_1 = L_{11} X_1 + L_{12} X_2, \\ J_2 = L_{21} X_1 + L_{22} X_2. \end{cases} \tag{1.11}$$

There is a certain arbitrariness in the choice of J_1 and J_2. For instance, if $J_1 = J^e$ is the electric current and $J_2 = J^Q$ is the heat current, the associated affinities will be $X_1 = \Delta\mu/T$ and $X_2 = \Delta T/T^2$. We can then easily relate the Onsager coefficient to the *transport coefficient*, i.e., electrical and thermal conductances, thermoelectric power and Peltier coefficient:

$$G = \left(\frac{J^e}{\Delta V}\right)_{\Delta T=0} = \frac{e^2}{T} L_{11}, \tag{1.12a}$$

$$K = \left(\frac{J^Q}{\Delta T}\right)_{J^e=0} = \frac{1}{T^2} \frac{\det \mathbf{L}}{L_{11}}, \tag{1.12b}$$

$$S = -\left(\frac{\Delta V}{\Delta T}\right)_{J^e=0} = \frac{1}{eT} \frac{L_{12}}{L_{11}}, \tag{1.12c}$$

$$\Pi = \left(\frac{J^Q}{J^e}\right)_{\Delta T=0} = \frac{1}{e} \frac{L_{21}}{L_{11}}, \tag{1.12d}$$

where $\Delta V = \Delta\mu/e$, e being the electron charge.

1.2.2 Thermoelectric figure of merit

Following the previous section, let us consider a generic system connected to electronic reservoirs at temperatures T_1, T_2 and electrochemical potentials μ_1, μ_2, in linear response regime. Furthermore, let us assume $T_1 > T_2$ and $\mu_1 < \mu_2$, such that $X_1 = \Delta\mu/T < 0$ and $X_2 = \Delta T/T^2 > 0$: under these condition, the setup works as a *thermoelectric engine*, exploiting a (positive) thermal bias in order to drive particles toward regions of higher potential. In

any thermodynamic cycle between two reservoirs at temperatures T_1 and T_2, the *efficiency* is defined as the ratio of the performed work W over the heat Q_1 extracted from the high temperature reservoir:

$$\eta \equiv \frac{W}{Q_1}. \tag{1.13}$$

In stationary and steady state situations, all the forces and responsive currents are independent of time, on average, apart from fluctuations. Under these conditions, W and Q_1 in Eq. (1.13) can be replaced by their time derivatives, giving:

$$\eta = \frac{\dot{W}}{\dot{Q}_1} = \frac{-TX_1J^e}{J^Q}, \tag{1.14}$$

where $J^Q = \dot{Q}_1 > 0$ and the power $\dot{W} > 0$. Maximizing η over X_1 for fixed X_2 yields:

$$X_1 = \frac{L_{22}}{L_{21}}\left(-1 + \sqrt{\frac{\det \mathbf{L}}{L_{11}L_{22}}}\right) X_2. \tag{1.15}$$

If the system is time-reversal symmetric $L_{12} = L_{21}$ and the *maximum efficiency* is given by

$$\eta_{max} = \eta_C \frac{\sqrt{ZT+1}-1}{\sqrt{ZT+1}+1}, \tag{1.16}$$

where $\eta_C = 1 - T_2/T_1$ is the Carnot efficiency and the *figure of merit*

$$ZT = \frac{L_{12}^2}{\det \mathbf{L}} \tag{1.17}$$

is a dimensionless parameter. Note that the only restriction imposed on ZT by thermodynamics is $ZT \geq 0$, and that η_{max} is a monotonous growing function of ZT, with $\eta_{max} = 0$ when $ZT = 0$ and $\eta_{max} \to \eta_C$ when $ZT \to \infty$.

Furthermore, ZT may be re-expressed in terms of the transport coefficients given in Eqs. (1.12a)-(1.12d) as:

$$ZT = \frac{GS^2}{K}T. \tag{1.18}$$

If we set instead $X_1 = \Delta\mu/T > 0$ and $X_2 = \Delta T/T^2 < 0$ the device can operate as a *refrigerator*. In this case the most important benchmark is the *coefficient of performance* (COP)

$$\eta^{(r)} = \frac{J^Q}{\dot{W}}, \tag{1.19}$$

given by the ratio of the heat current *extracted* ($J^Q < 0$) from the cold system over the absorbed power ($\dot{W} < 0$). By optimizing this quantity within linear response, we obtain

$$\eta_{max}^{(r)} = \eta_C^{(r)} \frac{\sqrt{ZT+1}-1}{\sqrt{ZT+1}+1}, \tag{1.20}$$

where $\eta_C^{(r)} \equiv T_2/(T_1 - T_2) \approx 1/(TX_2)$ is the efficiency of an ideal, dissipasionless refrigerator [13]. From Eqs. (1.16) and (1.20) we note that the ratio $\eta_{max}^{(r)}/\eta_C^{(r)}$ for refrigeration is equal

to the ratio η_{max}/η_C for power generation, meaning that ZT is the figure of merit for both regimes.

When thinking about practical applications, maximizing the efficiency is not the (only) ultimate goal. Indeed Carnot efficiency is only achieved in reversible systems, which have vanishing output power. Another possible approach is to maximize the output power, and than to look at the corresponding efficiency. The output power $\dot{W} = -TX_1J^e$ is maximal when

$$X_1 = -\frac{L_{12}}{2L_{11}}X_2 \tag{1.21}$$

and is given by

$$\dot{W}_{\max} = -\frac{\eta_C}{4}\frac{L_{12}^2}{L_{11}}X_2 = \frac{1}{4}S^2G\,(\Delta T)^2. \tag{1.22}$$

From the rightmost member, we observe that the maximum is directly set by the combination $\mathcal{Q} = S^2G$, known for this reason as *power factor*. The efficiency at maximum power reads [175]

$$\eta(\dot{W}_{\max}) = \eta_{CA}\,\frac{ZT}{ZT+2}, \tag{1.23}$$

where $\eta_{CA} = 1-\sqrt{T_2/T_1}$ is the Curzon-Ahlborn upper bound [34, 41, 126] to $\eta(\dot{W}_{\max})$, which in linear response reduces to $\eta_{CA} \simeq \eta_C/2$.

In Fig. 1.3 the maximum efficiency η_{max} and the efficiency at maximum power $\eta(\dot{W}_{\max})$, corresponding to Eqs. (1.16) and (1.23), are plotted as function of the figure of merit ZT. Note that in linear response, the difference between these two quantities is appreciable only for $ZT \gtrsim 1$.

1.3 Applications of thermoelectricity

1.3.1 Overview

To conclude this introductive chapter, in this section we briefly give an overview of the most relevant fields in which thermoelectrics devices are nowadays used, and then we present the operational principle of the basic building block of any thermoelectric device, the *thermoelectric module*.

Despite being still limited to relatively low performances, thermoelectric devices are used in a variety of applications, especially in situations in which factors such as reliability, geometrical constraints, low noise and environmental concerns are more important than efficiency. Among their great advantages we may include, for instance, the absence of moving parts (thus making them virtually maintenance free), the possibility of being designed at very small sizes and with different shapes, and the ability to heat and cool with the same module (depending on current polarization).

In a period in which the need of providing a sustainable energy to the world population is becoming increasingly important, it is natural to attempt reducing energy waste, when

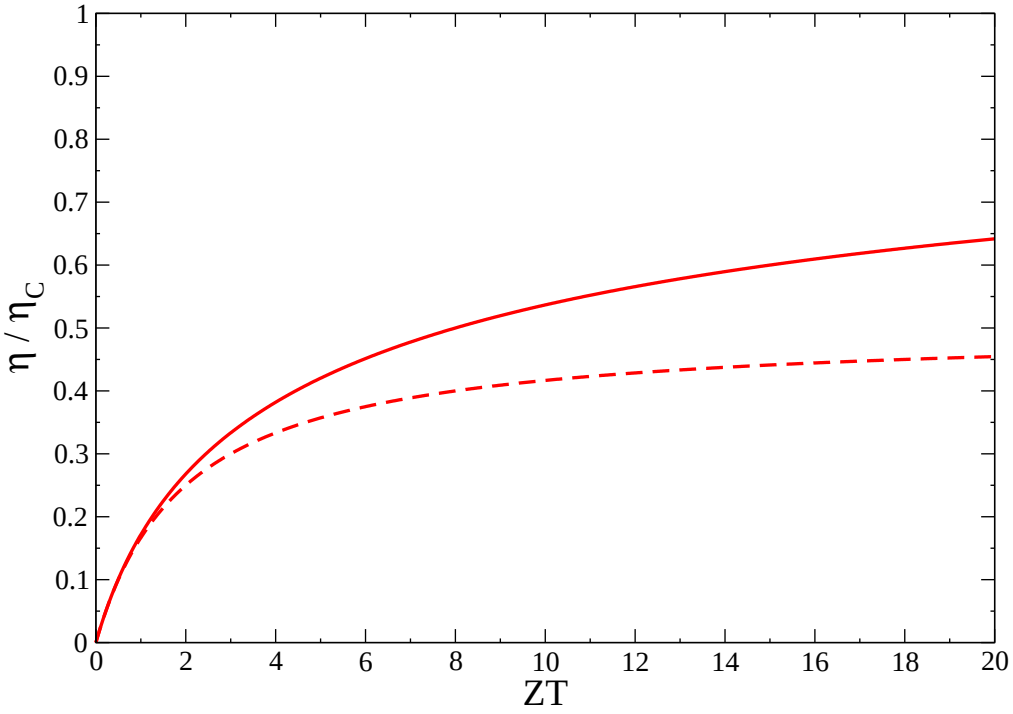


Figure 1.3: Linear response maximum efficiency η_{max} (upper full line) and efficiency at maximum power $\eta(\dot{W}_{\max})$ (bottom dashed line) in unit of the Carnot efficiency η_C, as a function of the figure of merit ZT.

possible. For instance, thinking about automobiles energy consumption, it could be really astonishing to realize that only 25% of the total power supplied to a car is effectively used, while around 40% of it is lost through exhaust pipes. Thermoelectric energy scavengers could hence help exploiting energy which would be otherwise lost.

Another significant example concerns nanotechnologies. The recent progresses in the miniaturization of electronic microprocessors have the counterindication that the power density in such devices may become extraordinary large, of the order of 10^2 W/cm^2 [140]: as a consequence, the overheating of nanocircuits can be a limiting factor for the progress of nanoelectronics. Embedding thermoelectric devices may provide a solution to evacuate heat at such scales via active micro-cooling of hot spots, thus preserving circuitry components and simplifying packaging operations.

Other fields in which thermoelectric devices are used include spacecrafts, medical and military equipments, photovoltaics, and all the processes which involve wasted heat that could be recovered and converted into useful energy (ship industry, wood stoves, oil and gas fields).

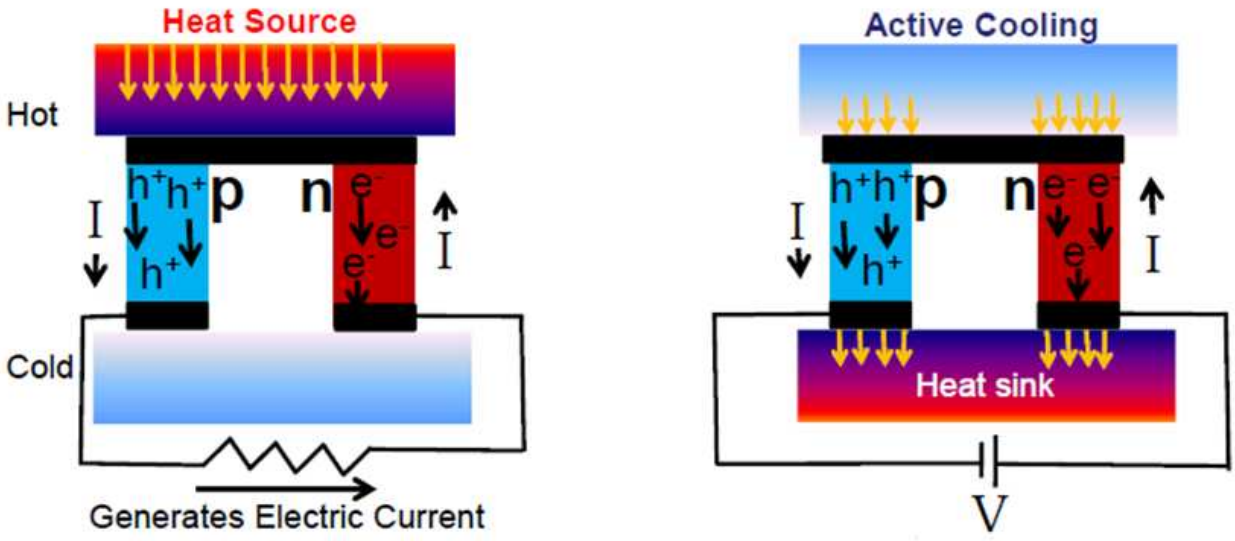


Figure 1.4: (Left) Sketch of a thermoelectric (Seebeck) power generator. Two p-doped and n-doped semiconductors are electrically biased in series with a load resistance to form an electric circuit. When a thermal bias is applied between the upper and the bottom ends of the device, it causes holes in the p-doped semiconductor and electrons in the n-doped semiconductor to move away from the hot side, thus resulting in a net current flowing throughout the circuit. (Right) Sketch of a thermoelectric (Peltier) cooler. Two p-doped and n-doped semiconductors are electrically biased in series with a battery to form an electric circuit. When a DC current flows through the device, it causes holes in the p-doped semiconductor and electrons in the n-doped semiconductor to move downward, thus cooling the upper end of the device.

1.3.2 Thermoelectric modules

Thermoelectric generators and coolers are solid state devices that can be used to convert heat (temperature differences) directly into electrical energy or vice versa, by exploiting the Seebeck and Peltier effects respectively.

In practice, they usually consist of two or more elements of semiconductor material, connected electrically in series and thermally in parallel, and mounted between two ceramic substrates. The substrates serve to hold the overall structure together mechanically and to electrically insulate all the individual elements from one another and from external mounting surfaces. Typical sizes of thermoelectric modules range from approximately $2.5 - 50\,mm^2$ of surface and $2.5 - 5mm$ of height. The most common materials used to produce them are Bismuth Telluride (Bi_2Te_3) and Lead Telluride (PbTe), but also other alloys like Silicon Germanium (SiGe), and Bismuth-Antimony (Bi-Sb) may be used depending on the circumnstances [61].

Thermoelectric cooler

A *thermoelectric cooler* is a solid-state active heat pump which uses the Peltier effect to transfer heat from one side of the device to the other. Such an instrument is also called a Peltier (or solid state) refrigerator.

A sketch of this device is shown in Fig. 1.4, on the left: it consists of a thermoelectric circuit composed of materials with different Peltier coefficients (p-doped and n-doped semiconductors), connected to a battery which makes a DC current flow through the device. The operational principle of this setup is rather intuitive: when the circuit is closed, the exceeding holes inside the p-doped semiconductor move along the direction of the current, while the exceeding electrons inside the n-doped semiconductor move against it in opposite direction. Globally, *both* charge carriers leave the upper end to reach the bottom end, and these two processes cooperate to lower the entropy of the upper end, which thus becomes colder.

Thermoelectric power generator

A *thermoelectric power generator* is a solid-state device which uses the Seebeck effect to exploit a temperature difference to perform useful electrical work.

Its structure (showed on the right side of Fig. 1.4), as well as its operational principle, are analogous to the thermoelectric cooler's ones. The main difference comes from the fact that the force which drives the carriers does not come from a battery, but rather from a thermal bias, which is applied between the upper and the bottom ends of the device. This causes electrons in the n-doped semiconductor, and holes in the p-doped semiconductor to diffuse away from the hot side, thus resulting in a net current flowing throughout the circuit which can supply a passive element (such as a load resistance).

Chapter 2

Thermoelectric conversion in nanowires: state of the art and motivations

Contents

Summary of chapter 2 . . . . . **26**

2.1 Low dimensional systems: toward efficient thermoelectrics **27**

2.2 Advantages of semiconductor nanowires **29**

2.3 Nanowires fabrication techniques **32**

2.4 Strategy adopted in this thesis **36**

2.4.1 Experimental overview 36

2.4.2 Theoretical overview 39

2.4.3 Our theoretical approach 39

Summary of chapter 2

In this chapter we present a general discussion on the thermoelectric performance of low dimensional systems, with particular emphasis on semiconductor nanowires. The aim is to illustrate the experimental and theoretical state of the art of thermoelectric conversion in such devices, and to motivate our interest in studying this field.

In section 2.1 we briefly overview the historical progresses made in the quest for a large ZT. We stress that the significant turning point coincides with the prediction by Hicks and Dresselhaus that low dimensional systems should exhibit much better thermoelectric performances, compared to bulk ones. This feature is discussed by analyzing some of the peculiarities of these systems.

In section 2.2 we show how semiconductor nanowire-based devices allow to match the requirements needed in order to design a performant thermoelectric converter: a poor thermal conductance, large (scalable) electrical conductance and output power, and a large thermopower. Specific examples are mentioned for each one of these points.

Section 2.3 is aimed to review the most common experimental techniques nowadays used to fabricate semiconductor nanowires. In a first part we present some examples of top-down and bottom-up approaches, detailing with examples, and finally we discuss some post-assembly techniques, by which nanowires can be integrated into technology platforms.

Finally, section 2.4 we summarize the state of the art of thermoelectric conversion in semiconductor nanowires: motivated by the intense experimental activity on the one hand, and on a substantial lack of theoretical work on the other, we outline the plan of this work and its goals.

2.1 Low dimensional systems: toward efficient thermoelectrics

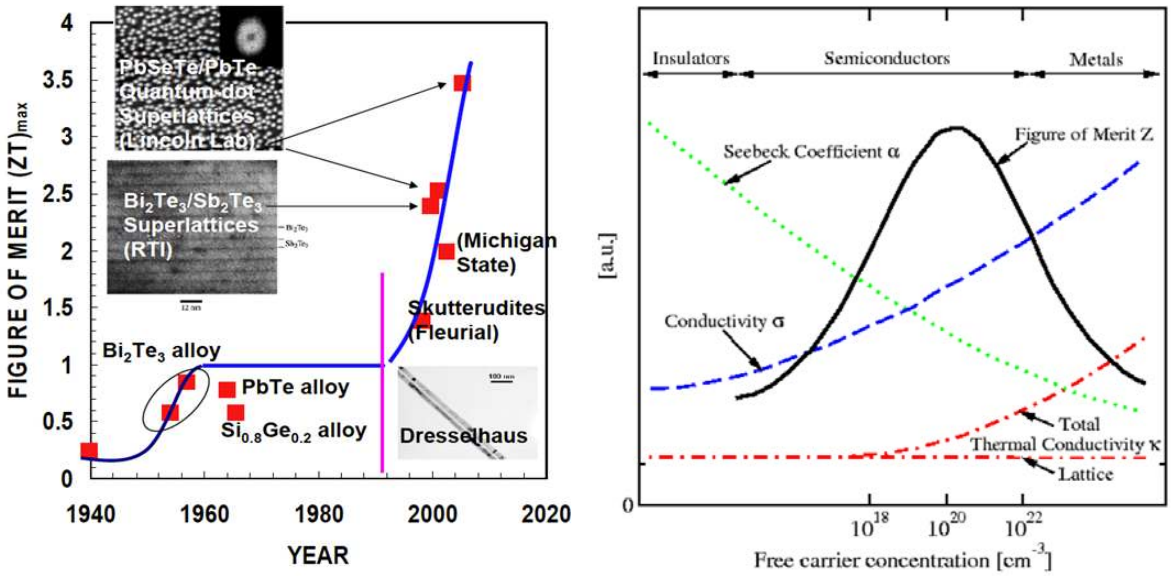
Fig. 2.1(a) shows the progress made over the last seventy years in the quest for the best figure of merit ZT. It is remarkable to observe that after the discovery of Bi_2Te_3 in the late 1950's, that allowed for a $ZT \approx 1$, no further improvements have been made for more than half a century, except for recent progresses made in skutterudite materials [58, 118, 179]. This is why the technology developed at that time still essentially dominates today [125]. The main challenge lies in engineering materials for which the values of the electric and thermal conductivities, and of the thermopower, can be controlled separately in order to optimize ZT, and hence the thermoelectric efficiency. The problem is that these transport coefficients are interdependent, thus making optimization a very delicate task. For instance, increasing the carrier density n would lead to a larger electrical conductivity σ, but would also have the unwanted effect of decreasing the thermopower S: this is what happens in metals. The situation is opposite in insulators, in which S could be large, at the expense of σ. Generally, a compromise has to be found and *semiconductors* turn out to be a good solution [49], exhibiting at the same time a good thermopower and a finite electrical conductivity thanks to doping (see Fig. 2.1(b)).

According to the definition of $ZT = (S^2\sigma/\kappa)T$, the best thermoelectric materials are believed to be "phonon-glass electron-crystals", meaning that they should strongly suppress phonon transport while maintaining high electron mobility [161]. In semiconductors, the thermal conductivity κ involves the contributions from both phonons (κ_{ph}) and electrons (κ_e), the former being usually dominating over the latter. The problem is that in general the mechanisms that may degrade κ_{ph} in bulk systems, such as alloying [167], do decrease the electron (or hole) mobility as well [69], thus affecting σ.

A very important turning point toward the modern trend of research was constituted by the works of Hicks and Dresselhaus [71, 72], who in the early 1990's observed that low-dimensional systems should result in materials with much better thermoelectric efficiencies than bulk ones, thanks to low-dimensional effects on both charge carriers and lattice waves [69]. These theoretical predictions have been later experimentally demonstrated on Bi_2Te_3 superlattices [178] and PbTe/PbSnSeTe quantum dot superlattices [64] (inset of Fig. 2.1(a)), allowing for $ZT \gtrsim 3$.

Generally speaking, the hallmark of low dimensional thermoelectric materials is the introduction of a design parameter d [69], which lessens the limitations arising from the interrelation among the various transport coefficients. Depending on the geometry of a system, this characteristic length scale could be for instance the thickness of the quantum well in a two-dimensional system (2D), the diameter of a quantum wire in a 1D system, or the size of a quantum dot in a 0D system.

Let us see in more detail how this can happen. Quantum confinement in semiconductor



(a) (b)

Figure 2.1: (a) Time evolution of the best figure of merit ZT (blue line). After an initial improvement on Bi_2Te_3 alloys, no progresses were made until the works by Hicks and Dresselhaus (pink line) on low-dimensional systems. In the last decade, a ZT larger than 1 has been observed in skutterudites [58, 118, 179], Bi_2Te_3 superlattices [178] and PbTe/PbSnSeTe quantum dot superlattices [64]. (b) Diagram showing the Seebeck coefficient S, electrical conductivity σ, thermal conductivity κ and figure of merit ZT with respect to free carrier concentration (after [49]). Seeking for a compromise between S and κ candidates semiconductors, over insulators or metals, as the most promising materials in terms of thermoelectric performance.

nanostructures increases the local carrier density of states per unit volume near the Fermi energy thus increasing the Seebeck coefficient [71], while the lattice thermal conductivity can be decreased due to phonon confinement [10, 11] and phonon scattering at the material interfaces [71, 73, 186].

To better understand how the thermopower S is enhanced, let us consider as an example the case of coherent transport, in which only electrons at energies very close to the Fermi energy matter. As it will be explained in much detail in Chapter 3, in this regime S only depends essentially on how the electrical conductivity σ varies with energy: the stronger its energy dependence is, the larger S will be. Since σ is proportional to the electron Density Of States (DOS) ρ, enhancing $d\rho/dE$ will result in a better thermopower. Fig. 2.2 shows how size-quantization effects may help in this direction, inducing a sharper structure for the DOS in low-dimensional systems.

The lattice thermal conductivity depends on the phonon mean free path l_{ph}, which is usually (much) larger than its electronic counterpart l_e [21, 48]. This makes possible to design

low dimensional semiconductor systems characterized by a reduced thermal conductivity, provided that the condition $d \approx l_{ph} > l_e$ holds, without significantly affecting the electrical conductivity [29].

The combined benefits of reduced thermal conductivity and improved Seebeck coefficient imply a theoretically higher ZT compared to the bulk structures. However, nowadays, a full and satisfactory comprehension of the physics underlying thermoelectric conversion in low-dimensional nanoscale devices is still missing, both theoretically and experimentally: on the one hand, for instance, a number of recent experiments on semiconductor nanowires [16, 28, 40, 89, 146, 166] make them appear as a very promising central building block of flexible, efficient and environmentally friendly thermoelectric converters. Nevertheless, so far, much less theoretical work has been done to clarify transport mechanism in such systems [19, 20, 85]. On the other hand, experimental observations have not been able yet to achieve the presumed benefits of superlattice thermoelectric devices despite theoretically predicted improvements in ZT and experimentally observed reduction in the thermal conductivity of superlattices compared to their bulk counterparts [93, 122].

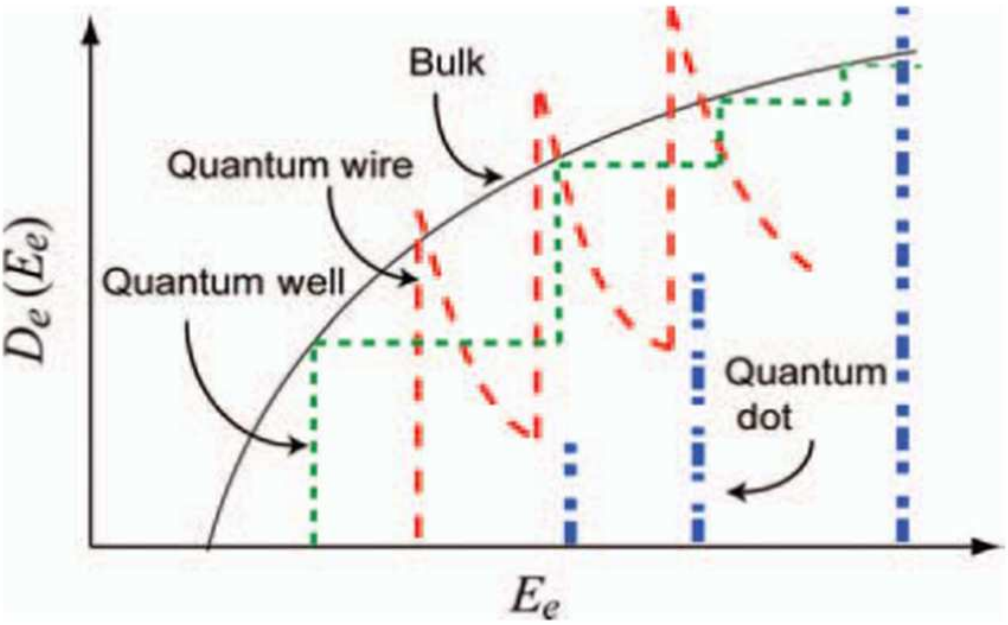


Figure 2.2: Energy dependence of the electronic density of states in 3-, 2-, 1- and 0- dimensional crystals (after [194]).

2.2 Advantages of semiconductor nanowires

Referring to the previous section, let us recall the main ingredients to design a performant thermoelectric device, characterized at the same time by a good figure of merit ZT while

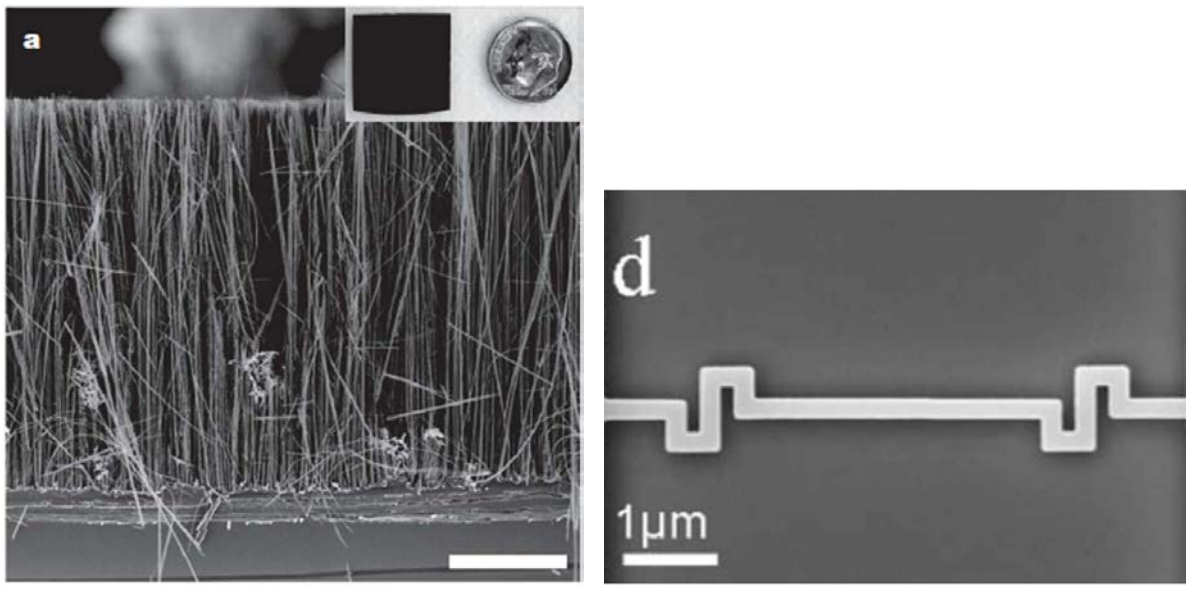
allowing for a finite output power:

- a poor thermal conductance,
- a large electrical conductance,
- a large thermoelectric power.

In the following, we will show through suitable experimental examples that semiconductor nanowires-based systems allow to match each one of these requirements.

Reducing the thermal conductance

Hochbaum *et al.* [74] compared the thermoelectric performance of bulk silicon with respect to an array of Si nanowires (see Fig. 2.3(a)): whereas the electrical resistivity and thermopower are substantially unchanged, they observed a reduced thermal conductivity of about 100 times. Heron *et al.* [70] show how the phononic contribution to the thermal conductance in a 5μm Si nanowire can be suppressed by a suitable geometrical design. In more detail, they compared the thermal conductance of a straight nanowire to that of a nanowire of the same size, but in which two "serpentines" were introduced (see Fig. 2.3(b)): they found that the latter's thermal conductance is reduced up to 40% at T$\approx$5K.



(a) (b)

Figure 2.3: (a) Cross-sectional Scanning Electron Microscope image of a Si nanowire array, realized via electroless etching method [134, 133]. In the inset, typical size of a Si nanowire array wafer chip (after [74]). (b) Top view of a 5μm "serpentine" Si nanowire composed of two serpentine connections to a heat bath (after [70]).

Enhancing the thermoelectric power

In Fig. 2.4 we show the results of simultaneous electric conductance and thermopower measurements of a Ge/Si nanowire at room temperature performed by Brovman *et al.* [28]. The setup they studied was in a Field Effect Transistor (FET) configuration, in which the carriers density in the wire could be varied by means of a back gate voltage: from the figure it can be seen that the thermopower is largely enhanced up to values of few hundreds of mV/K in a region of low electronic density in which electrical conductance drops.

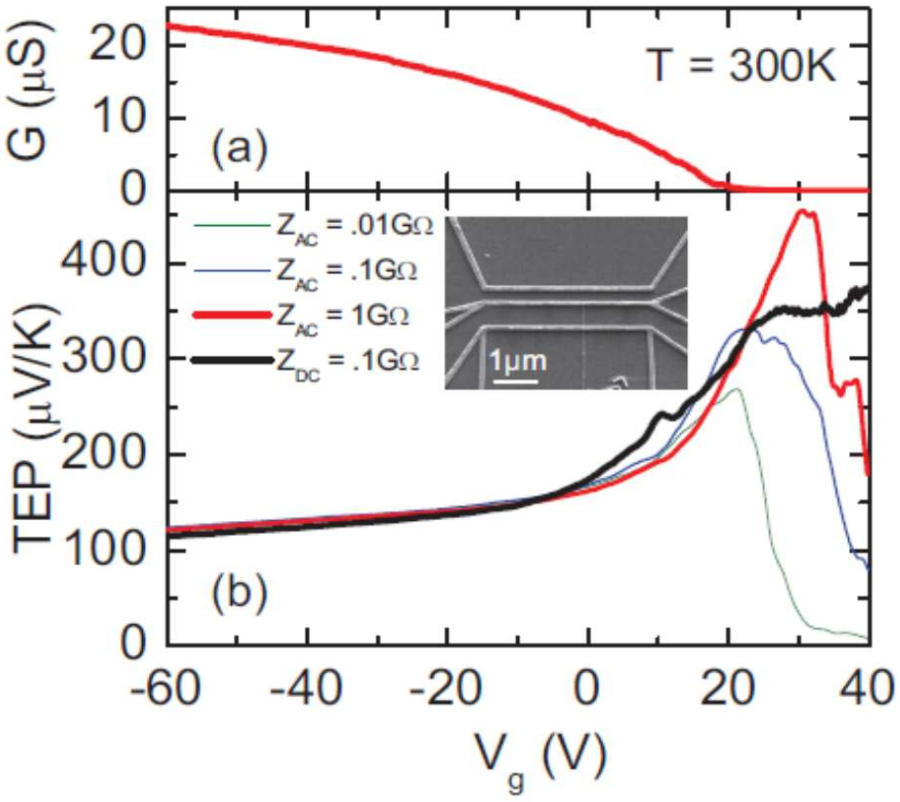


Figure 2.4: Conductance (a) and thermopower (b) of a Ge/Si nanowire as a function of gate voltage measured at T = 300 K (after Brovman *et al.*[28]). The inset in (b) shows a typical SEM image of a 12 nm-wide Ge/Si device. Large input impedance becomes important when measuring TEP near the band edge of a semiconductor, as the FET device turns off.

Scaling the electrical conductance to deliver high output powers

Parallel nanowires-based devices are characterized by an electrical conductance which scales as the number of wires, possibly allowing to deliver large currents, and hence, output powers. As an example, Pregl *et al.* [141] have recently studied Schottky barrier field effect transistors consisting of a parallel array of bottom-up grown silicon nanowires that are able

to deliver high current outputs (Fig. 2.5(a)). These device leverage the transport properties of nanoscale junctions to boost device performance for macroscopic applications, their transconductance being thus increased significantly while maintaining the transfer characteristics of single nanowire devices. Furthermore, they show that by incorporating several hundred nanowires into a parallel array, the yield of functioning transistors is dramatically increased. Allowing for on-currents of over 500 μA at a source-drain voltage of 0.5 V (Fig. 2.5(b)), this nanowires-based platform provides sufficient current output to be employed as a transducer for biosensors or a driving stage for organic light-emitting diodes (LEDs).

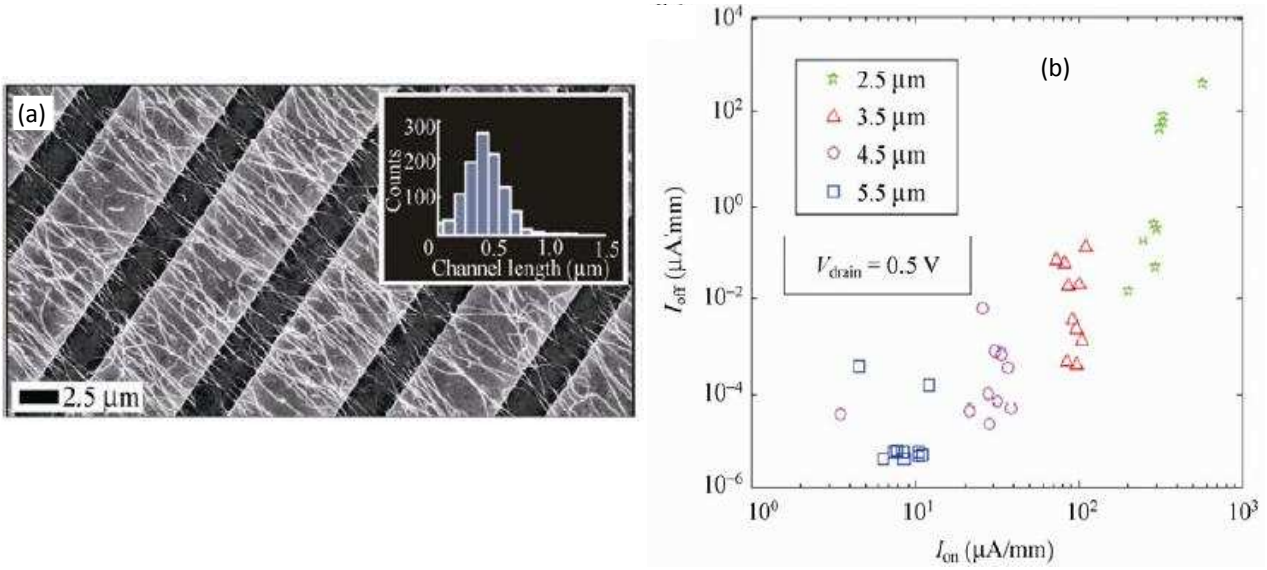


Figure 2.5: (a) High density nanowires contacted by nickel electrodes. The inset displays the histogram of channel lengths of individual nanowires after silicidation for a device with 2.5 μm interelectrode spacing. (b) On-off current ratio per mm electrode width of field effect transistors with 0.5 V source-drain voltage. Data are shown for devices with four different inter-electrode spacings: note that large on-current of $\sim 500\mu A$ have been measured (after [141]).

2.3 Nanowires fabrication techniques

A number of methods to synthesize semiconductor nanowires (SNWs) have been reported in the past decade, such as laser ablation [117], vapor transport [190], solvothermal [68], molecular beam epitaxy (MBE) [65], template-assisted electrochemical synthesis [156], and chemical vapor deposition (CVD) methods [1, 92]. These synthetic methods have made a significant progress, enabling nowadays a precise control on the NWs size, morphology, chemical composition, and single crystalline quality [54, 191].

Generally, there are two different strategies to synthesize 1D SNWs, the so-called "top-down" and "bottom-up" approaches. The top-down approach has been exceedingly successful

in the area of microelectronic fabrication, its basic idea being to make use of a predesigned patterned substrate to obtain the complex high density nanostructures in well-defined positions. A prototypical example of such technique is nanolithography [142, 195]. Using top-down approaches allows to produce 1D SNWs with very uniform size, shape, and electronic properties. However, this technique suffers the current trend of microelectronic industry, which constantly asks for smaller devices, and it is believed that it will soon reach both its resolution and economic limits in physical size and in manufacturing facility cost [112].

On the other hand, in bottom-up approach, "functional structures are assembled from well-defined chemically and/or physically synthesized nanoscale building blocks, much like the way nature uses proteins and other macromolecules to construct complex biological systems" [67]. It is likely that the bottom-up approach can break the limits of resolution and expand the functionality of top-down technology by designing key nanometer-scale building blocks and controlling the parameters in synthesis and subsequent assembly. Furthermore, the bottom-up method shall readily facilitate the new device concepts and functions that cannot be realized in top-down fabrication. For instance, it is possible to integrate chemically different nanoscale building blocks together to achieve novel and multiple functionality 1D nanosystems that cannot be combined in top-down methods.

Nowadays, one of the most common class of bottom-up methods for NWs fabrication consists in making use of a catalyst to achieve anisotropic 1D growth. On the basis of the phases involved in the reaction, this method can be defined in different ways.

- Vapor-solid (VS) growth [15, 28, 42, 154, 184] is a form of chemical vapor deposition which consists of a chemical process in which the *wafer* (substrate) is exposed to one or more volatile molecular *precursors*, that react and/or decompose on the substrate surface to produce the desired *deposit*. Precursor transport takes place via gas flow (commonly oxygen, argon, hydrogen or nitrogen), which also aids removing undesired volatile deposition sub-products. An easy examples of such a process is the oxidation of Silane to produce Silicon dioxide and Hydrogen: $SiH_4 + O_2 \rightarrow SiO_2 + 2H_2$.

- Another example is vapor-liquid-solid (VLS) growth [28, 36, 37, 181, 189, 196, 198], still based on vapor deposition, but which makes use of a catalytic liquid alloy phase that can rapidly adsorb a vapor to supersaturation levels, and from which crystal growth can subsequently occur from nucleated seeds at the liquid-solid interface. The main advantages of this technique are that the adsorption process becomes much faster with respect to the standard CVD, and that the physical characteristics of nanowires grown in this manner depend in a controllable way upon the size and properties of the liquid alloy.

- A third important growth mechanism, similar to VLS, is solution-liquid-solid (SLS) growth [174]. In this case, a nanometer-scale metallic droplet catalyzes the precursor decomposition and crystalline growth in solution.

Quite often, these techniques are combined with *Selective Area Epitaxy* (SAE) [15, 89], allowing local growth of epitaxial layers through (nanolithography) patterned dielectric masks deposited on a semiconductor substrate. In particular, nanowires can also be grown by deposition within a (sacrificial) nanotube template [42], which defines the shape of the targeted nanowire, thereby enabling the sequential deposition of material without the formation of parasitic core-shell structures.

In addition to the methods discussed above, let us finally mention (without further analysis) several other potentially useful approaches that have also been demonstrated as alternative routes to the synthesis of 1D SNWs: self-assembly of nanoparticles [76], DNA-based template [25], carbon-nanotube- and carbon-nanofiber-based template [197], and virus-based template [110]. However most of these techniques are still at a developmental stage so far, and many issues remain to be addressed before they can be used for large-scale growth of 1D SNWs.

In Fig. 2.6 two examples of the aforementioned techniques used to grow InAs nanowires are illustrated, while Fig. 2.7 shows typical patterns of parallel arrays of semiconductor NWs vertically grown by chemical vapor deposition. Finally, in Fig. 2.8 a typical setup used to investigate thermoelectric properties of a single (suspended) semiconductor nanowire is reported.

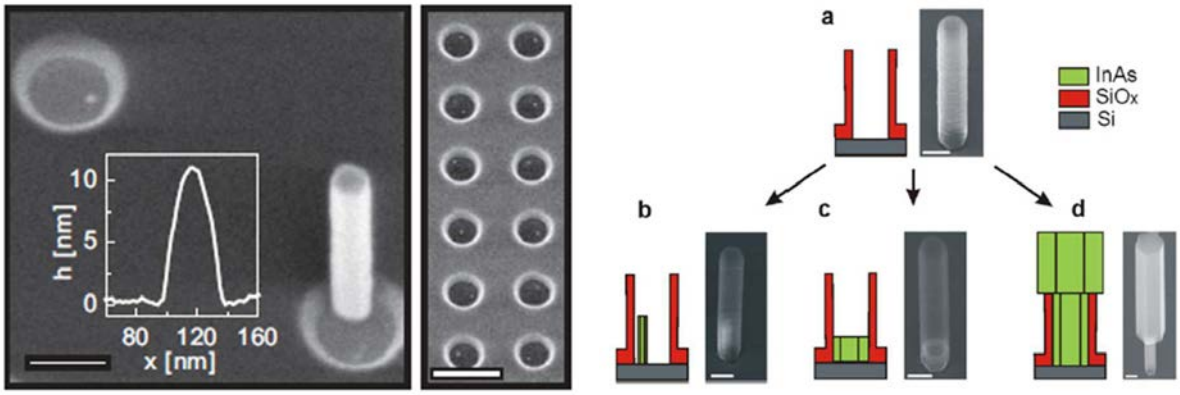


Figure 2.6: (Left) Growth of InAs nanowires on <111> Si substrate (after [15]). Scanning Electron Microscope (SEM) image of two mask openings showing a successfully grown nanowire and an InAs cluster. Scale bar is 200nm. Inset shows an atomic force microsope line scan across the cluster. (Right) Schematics and corresponding SEM images of heteroepitaxial growth of InAs on Si in a hollow SiO_x nanotube template (after [42]). The steps *a* to *d* describe the various stages of the nanowire growth. The scale bar in the SEM images corresponds to 100 nm.

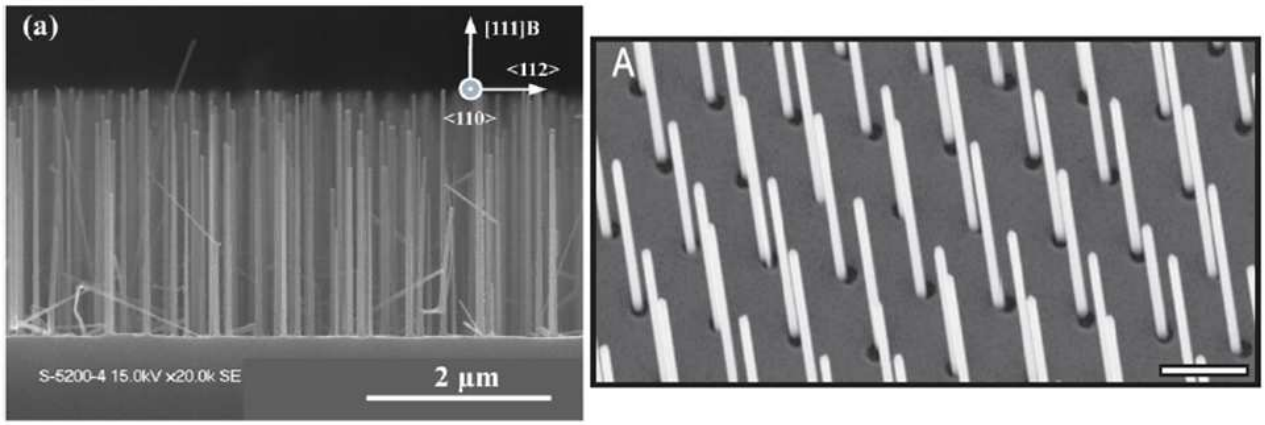


Figure 2.7: Two examples showing growth of nanowire arrays by chemical vapor deposition (CVD) method. (Left) SEM image showing structural analysis of InAs nanowires grown on Si substrate. Scale bar depicts 1 μm. (Right) SEM images of GaAs NWs grown on GaAs substrate. (after [15] and [196]).

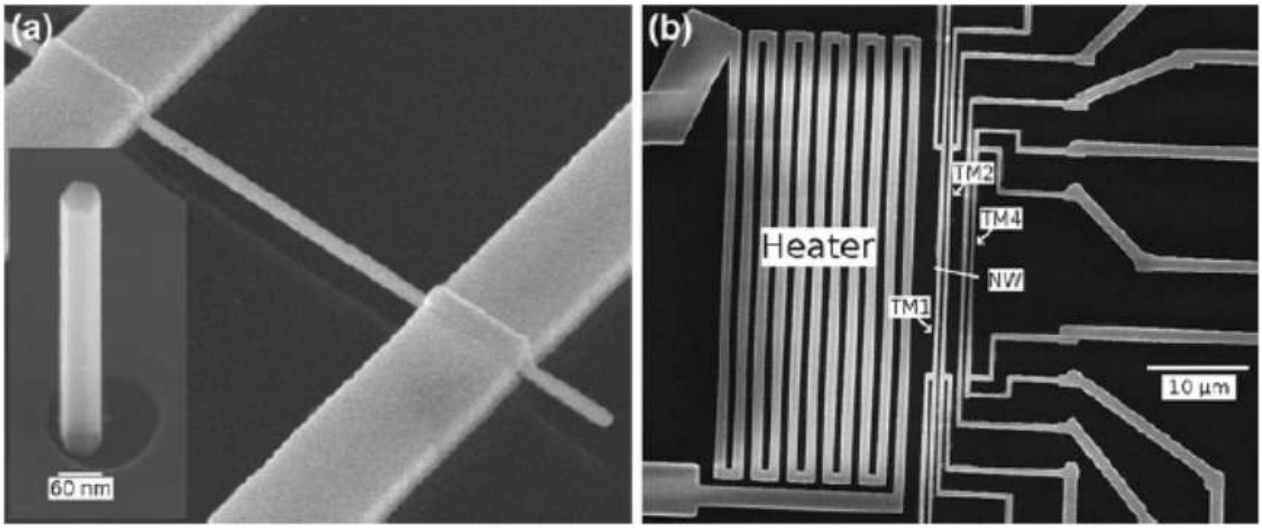


Figure 2.8: (a) Scanning electron microscope image of a suspended InAs NW (diameter: 80 nm) contacted by 500-nm-wide, 150-nm-thick nickel electrodes. Insert shows an InAs NW (diameter: 60 nm) vertically grown on a Si wafer masked by an opening in the SiO_2 coating. (b) InAs NW contacted with four platinum leads of width 300 nm, three of them consisting of four-probe resistive thermometers. A resistive heater is placed a few microns aside the NW. (after [89]).

Post-production assembly

Several post-production techniques can be used in order to assemble or rearrange arrays of nanowires as controllable building blocks to be integrated into technology platforms [183]. The basic method consists in processing the NWs as a solution, which makes them easy to

handle and which allows also a control on their concentration through dilution. Droplets containing NWs are then cast onto a substrate, and finally the solvent is evaporated. Before this last stage, a number of manipulation can be done, resulting in different assembly ways:

- Assembly by molecular forces, in which as the solvent is removed, interactions between the NWs and the substrate determine both the adhesion between the two, as well as the nanowire orientation. In case the NWs have an inherent charge, the procedure could be assisted by electrostatic interactions. This simple method has the disadvantage that the nanowires usually result randomly oriented.

- Assembly driven by shear forces, which consists in making a fluid move against the solution containing the nanowires. This could be obtained, for instance, by the wetting/dewetting of surfaces as well as by mechanical movements of two surfaces in opposite directions. The effect is to generate a force parallel to the direction of fluid motion, that tends to align the NWs. This method is applicable both for nanowires suspended in a solution and fixed to a substrate.

- Assembly within magnetic fields, which can direct the alignment of nanowires composed by ferromagnetic and superparamagnetic materials. Magnetic fields could be external, or due to magnets embedded in the substrate. In the latter case, NWs often form chain like structures extending from the magnet along its field lines.

- Assembly by dielectrophoresis, in which a spatial modulated electric fields allows to modify the NWs polarization, and hence their orientation.

Fig. 2.9 shows two different post-production arrangements of parallel semiconductor nanowires, which are deposited onto a substrate (left) or suspended (right).

2.4 Strategy adopted in this thesis

In this thesis we focus on *electronic* transport in nanowire-based devices and we mainly consider two transport coefficients: the electrical conductance and the thermoelectric power. We conclude this chapter by summarizing the experimental and theoretical states of the art of these issues, motivating our interests.

2.4.1 Experimental overview

As mentioned before, in the last decades the experimental activity in designing nanowire-based thermoelectric devices (see, e.g., Refs. [22, 28, 36, 37, 38, 39, 89, 98, 116, 138, 146, 154, 166, 172]) has been very intense. In this subsection our purpose is to give a brief overview of some relevant recent experimental results.

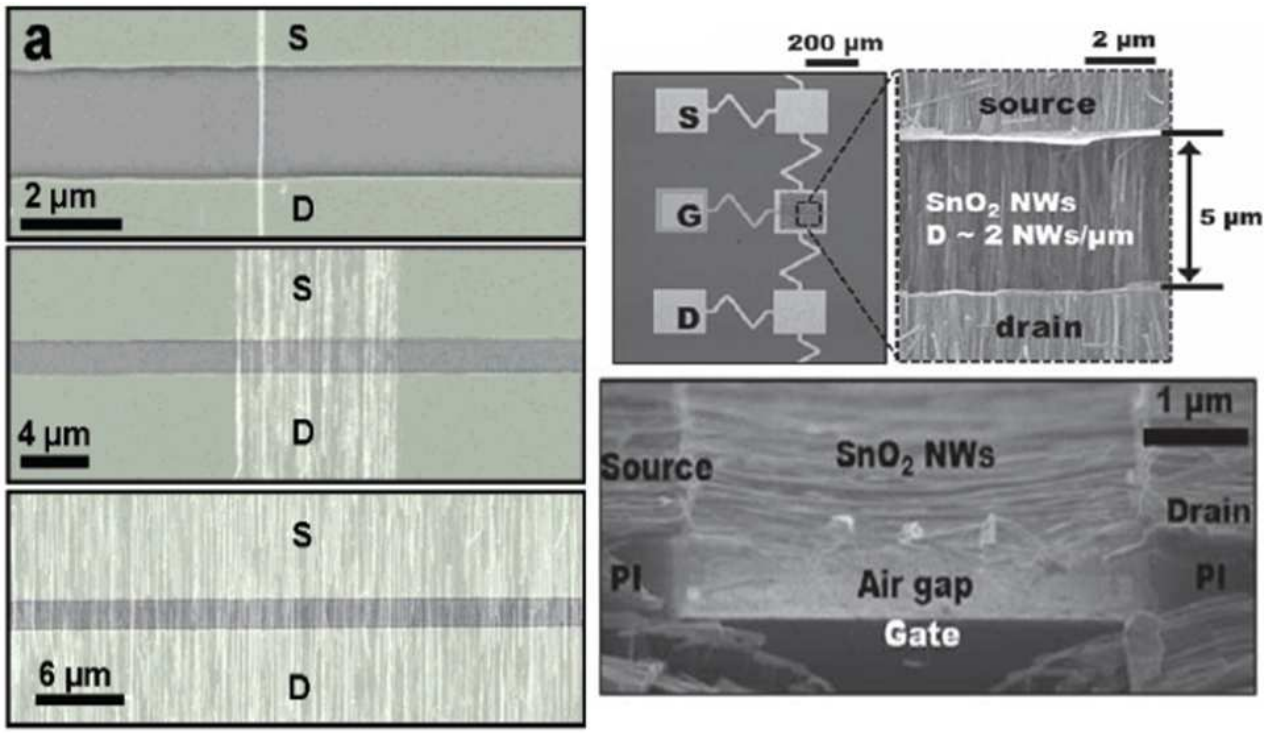


Figure 2.9: Devices based on nanowire arrays. (Left) Ge/Si Nanowires are deposited onto a substrate, contacted to Ni/Pd source (S) and drain (D) contacts and put into a Field Effect Transistor (FET) configuration, with a metallic back gate (below the substrate) acting on them. From top to bottom, SEM images of single NW FET, 10 μm and 250 μm wide parallel arrayed NW FETs. (Right) Suspended SnO_2 NWs. Above: optical microscope and SEM images taken from the fabricated devices and aligned NWs in the channel, respectively. Below: Tilted cross-sectional SEM images of the SnO_2 NW channel (after [55] and [159]).

In a certain number of papers, simultaneous measurements of the electrical conductance and of the thermopower of individual semiconductor nanowires in the field effect transistor configuration are performed. It is the case, for instance, of Refs. [89, 146] in which the techniques and the results obtained using Si and InAs nanowires are similar to those by Brovman *et al.* [28], already discussed in the first section of this chapter and shown in Fig. 2.4. All these kinds of devices exhibit a thermopower of the order of few hundreds of μV/K at room temperature in the regime of band edge transport. The same procedure is adopted also by Schmidt *et al.* [154], but here the Seebeck measurement is performed with the ulterior motive of determining charge carrier concentration, mobility, and relaxation time in InAs nanowires.

As an alternative to the usually studied doped nanowires, Curtin [39] and Moon [116] consider multigated crystalline Si and Ge/Si NWs, in which transport is due to electric-field-induced charge carriers and occurs at the nanowires surface only. Since these carriers exhibit greater mobility over those contributed by chemical dopants [105], field-effect doping

candidates as a promising strategy for optimizing thermopower and power factor in smaller diameter Si NWs, where high average carrier densities can be obtained with induced surface charge (see Fig. 2.10(a)).

Tian *et al.* [172] observe that InAs nanowires at low temperatures (T $<$ 100 K) exhibit oscillations in the thermopower and power factor concomitant with the stepwise conductance increases, as the gate voltage shifts the chemical potential of electrons through quasi-one-dimensional subbands (see Fig. 2.10(b)). This is interpreted as a quantum confinement effect, allowing to modulate the NW thermoelectric properties by controlling 1D subband formation in the regime of diffusive transport for electrons.

In conclusion to this short list, we point out that measurements of thermopower of arrays of stacked parallel Si nanowires can be found, for instance, in [166]: in Fig. 2.10(c) we report their results, in which the Seebeck coefficient of a n-type silicon NW array is compared to that of bulk silicon and bismuth telluride.

All these examples are nothing but a glimpse over the wide panorama of experimental results which support the idea that semiconductor-nanowires-based devices are promising high-performance thermoelectrics.

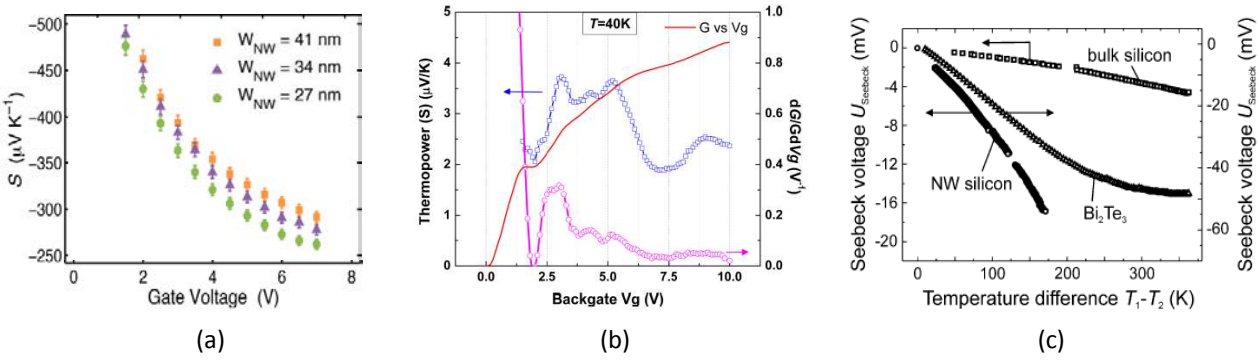


Figure 2.10: (a) Measured thermoelectric power of electrically gated square Si NWs with a height of 35 nm, widths of 27, 34, and 41 nm, and gate biases between 0 and 7 V (after [39]). (b) Gate dependence of thermopower S (blue), conductance G (red), and $G^{-1}\,dG/dV_g$ (magenta) at 40 K, showing the correspondence between thermopower oscillations and the conductance steps as electrons populate 1D subbands in a InAs nanowire of 23 nm diameter and 9.5 μm length (after [172]). (c) Seebeck voltage of an n-type silicon NW array (220 to 270 nm diameter, 7 μm length and 2 mm $\times$ 2 mm device surface) with respect to n-type bulk silicon (0.5 mm length and 2 mm $\times$ 2 mm surface) and Bi_2Te_3 (2 mm length and 1.4 mm $\times$ 1.4 mm surface) measured in the temperature range from 293 K to 743 K (after [166]).

2.4.2 Theoretical overview

From the theory side, less efforts have been done so far; nevertheless, a number of works deserve to be mentioned. In some cases, the question of determining the dopant density maximizing the thermopower has been addressed via ab-initio calculations [38, 104, 114, 124] based on the nanowires band structures, in regimes in which the semi-classical Boltzmann theory can be used. In others [103], the study has been carried out in the ballistic regime, where the presence of the disorder is completely neglected. The main goal in these examples was to describe thermoelectric properties of nanowires at room temperature where the quantum effects become negligible, and in particular to probe the role of their geometry (diameter, aspect ratio, orientation, etc.).

Recently, Jiang *et al.* [84, 85] raised the interest for the thermoelectricity in the regime of thermally activated transport, where electrons can make hops between localized states thanks to the interaction with phonons. These works motivated us in pursuing the study of such systems in the field effect transistor configuration (see chapters 4 and 5).

Finally, we mention a work by Bejenari [12], who makes use of a DFT calculation to determine the full electronic structure of Si-nanowires, taking into account electron-phonon interaction. His approach allows him to evaluate the thermoelectric properties of nanowires in a wide range of temperatures, accounting for both elastic and inelastic scattering.

2.4.3 Our theoretical approach

In the two previous subsections we tried to draw attention on the imbalance between the experimental and theoretical state of the art of thermoelectric conversion in semiconductor nanowires. The approach adopted in this thesis consists in studying thermoelectric conversion in doped semiconductor nanowires in the field effect transistor configuration, in which electron transport takes place in the impurity band. Our theoretical study has been carried out at low temperatures in the regime of elastic coherent transport, and at higher temperatures in case of inelastic thermally activated transport. Our results are supported by numerical simulations based on a 1D single-band disordered Anderson model (see Fig. 2.11(a)).

In Fig. 2.11(b) we anticipate a discussion detailed in chapter 4: different regimes of electronic transport are shown in a temperature-gate voltage diagram. Depending on the values of T and V_g, electrons may tunnel through the nanowires elastically (regions "1"), or via thermally activated transport in the Variable Range Hopping regime (regions "2") and Nearest Neighbor Hopping regime (regions "3").

In chapter 3 we mainly focus on the thermopower of disordered 1D nanowires in the low temperature regime (regions "1" of Fig. 2.11(b)), in which electronic transport through the wires is elastic and coherent [19]. We introduce the Landauer-Büttiker formalism to calculate the transport coefficients. Using weak-disorder expansions of the Lyapunov exponents in 1D

systems [46], we are able to calculate analytical expressions for the typical thermoelectric power S, for both situations in which transport takes place in the bulk or around the edges of the nanowires impurity band. Numerical simulations carried out using a 1D Anderson model in presence of an external gate voltage (field effect transistor configuration), based on a recursive Green function calculation of the thermopower, confirm the validity of our results: we observe a strong enhancement of S as the band edges are approached. Also, we study its mesoscopic fluctuations [176], and we show that the thermopower distribution is basically always Lorentzian, as long as the nanowire is not completely depleted by the applied gate voltage. When this happens, at large, the thermopower distribution becomes Gaussian with tiny fluctuations: this transition is characterized numerically.

In chapter 4, we consider a higher temperature regime, in which electronic transport is inelastic and takes place via thermally activation among localized states by phonons (Mott Variable Range Hopping regime, regions "2" of Fig. 2.11(b)) [20, 85]. The latter are supposed to come from an insulating substrate, onto which the nanowire is deposited. We calculate the charge and heat currents flowing through the system by solving the Miller-Abrahams random resistor network in the VRH regime, and then we discuss both the electrical conductance and the thermopower, showing that huge values of the latter (up to the order of $1\text{mV}K^{-1}$) can be attained when the nanowire band edges are probed. Extending an approach that was first introduced by Zvyagin [200], we provide a qualitative explanation of the thermopower behavior around the band edge, by emphasizing a nontrivial dependence on temperature and on gate voltage. We underline that the distinctive feature of VRH regime is the concept of Mott hopping energy, i.e. a finite range of energy levels which matter for describing transport.

We extend this analysis to a set of parallel nanowires in chapter 5. In particular, we point out two features which makes this system, and more generally any semiconductor nanowires-based device operating in the activated transport regime, a promising thermoelectric converter. First, we demonstrate that such system allows to scale the output power up to finite values, in a regime where the thermoelectric effect is large. We show that it is possible to properly tune the temperature and the gate voltage in order to maximize the power factor, and this can be achieved without compromising too much the figure of merit. A second intriguing feature is the possibility of generating and controlling hot and cold spots near the boundaries of the substrate, an effect which could be very interesting for cooling issues in electronic circuits.

We observe that what really makes the systems considered in the two previous chapters very promising is the role of the phonon bath, which at an abstract level is nothing but a third (bosonic) terminal added to the standard two-terminal configuration. This leads naturally to wonder whether a third terminal treated on a more general footing is beneficial

for thermoelectric conversion: in chapter 6 we tackle this problem within a rather general and technical approach [111]. We discuss local and non-local transport coefficients, the latters being naturally requested in a multi-terminal setup, since they connect temperature or voltage biases introduced between two terminals to heat and charge transport among the remaining terminals. Then, we show that the third terminal could be exploited to improve thermoelectric performances with respect to the two-terminal case, by focusing our investigations on the efficiency at maximum power of two simple quantum systems.

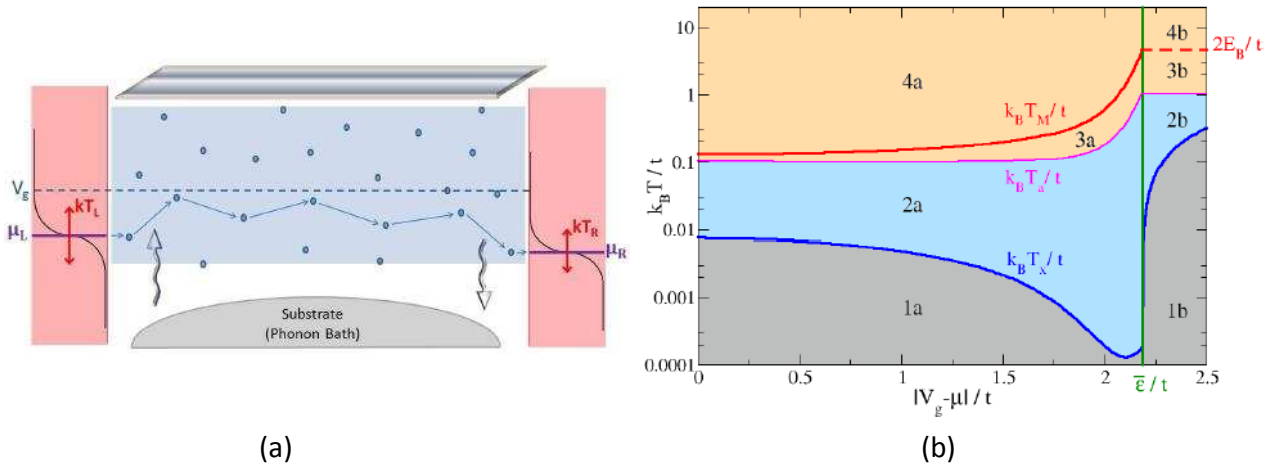


Figure 2.11: (a) Sketch of the 1D model used for numerical simulations: two ohmic contacts thermalized at temperatures $T_{L(R)}$ and with electrochemical potentials $\mu_{L(R)}$ are connected by a 1D disordered chain of length L where the electron states are localized in the position-energy space. Possibly, a phonon bath at temperature T_{ph} is coupled to the nanowire, allowing energy exchanges between electrons and phonons. Electrons are first injected from the left electrode, and then proceed through the NW with or without changing their energy (depending on the transport regime) until they reach the opposite side. (b) Gate dependence of the temperature scales separating the different regimes of electronic transport in a disordered nanowire: Elastic regime (gray), inelastic VRH regime (blue) and simply activated NNH regime (red). More details about these two figures are discussed in chapter 4.

Chapter 3

Coherent Regime

Contents

Summary of chapter 3 . . . . . **44**

3.1 Landauer-Büttiker formalism **45**

3.2 Model and method **46**

3.2.1 Calculation of the transport coefficients 48

3.2.2 Scanning the impurity band of the Anderson model 49

3.2.3 Localization length of the Anderson model 49

3.3 Thermopower **51**

3.3.1 Typical thermopower 51

3.3.2 Thermopower distributions 55

3.4 Figure of merit **61**

3.5 Temperature range of validity of the Sommerfeld expansion . . . **64**

3.6 Appendix **66**

3.6.1 Recursive Green Function algorithm 66

3.6.2 Self-energy of the 2D leads 70

3.6.3 Thermopower of a clean tunnel barrier 70

Summary of chapter 3

In this chapter, we investigate the thermopower of a single disordered nanowire in the low temperature elastic regime. More precisely, we focus on a subregion of temperatures $T < T_s$ in which the thermopower can be evaluated using the Landauer-Büttiker scattering formalism and Sommerfeld expansion. An experimental study of the gate dependence of the electrical conductance of Si-doped GaAs nanowires in this elastic coherent regime can be found in Ref.[138].

We mainly consider nanowires of size N much larger than their localization length ξ, characterized by exponentially small values of the electrical conductance. If on one hand, this drastically reduces the output power associated with the thermoelectric conversion, on the other it has the advantage that the typical transmission at an energy E is simply given by $\exp[-2N/\xi]$. Moreover, in the limit of weak disorder, expansions can be made and $\xi(E)$ is analytically known both inside the impurity band of the nanowire and around its band edges. This makes possible to derive analytical expressions describing the typical behavior of the thermopower.

In section 3.1 we remind some basics of the Landauer-Büttiker formalism which allow to calculate thermoelectric coefficients in the coherent regime. In section 3.2, we introduce the model and outline the numerical method used in this work, which is based on a standard recursive Green function algorithm.

Section 3.3 is devoted to the study of the thermopower as the carrier density in the nanowire is modified with a gate voltage V_g. We show that the typical thermopower is drastically enhanced when the nanowire is being depleted and we provide an analytical description of this behavior in the localized limit. Also, we study its mesoscopic fluctuations, and we show that the thermopower distribution is basically always Lorentzian, as long as the nanowire is not completely depleted by the applied gate voltage, and provided it is long enough with respect to the localization length. When this happens, at large V_g, the thermopower distribution becomes Gaussian with tiny fluctuations: this transition is characterized numerically.

In section 3.4 we extend these considerations to the figure of merit ZT, analyzing its typical behavior, fluctuations and the implications concerning the performance of the system.

Finally, in section 3.5 we evaluate the "crossover temperature" T_s, the upper bound for the validity of the Sommerfeld expansion used to calculate the thermoelectric coefficients.

3.1 Landauer-Büttiker formalism

We consider a conductor connected via reflectionless leads to two reservoirs L (left) and R (right) in equilibrium at temperatures T_L and T_R, and chemical potentials μ_L and μ_R. To describe the thermoelectric transport across the conductor, we use the Landauer-Büttiker formalism [43]. The heat and charge transport are supposed to be mediated only by electrons and the phase coherence of electrons during their propagation through the conductor is supposed to be preserved. In this approach, the dissipation of energy takes place exclusively in the reservoirs while the electronic transport across the conductor remains fully elastic. The method is valid as long as the phase-breaking length (mainly associated to electron-electron and electron-phonon interactions) exceeds the sample size. From a theoretical point of view, it can be applied to (effective) non-interacting models.

In this framework, the electric (J^e) and heat (J^Q) currents flowing through the system are given by [30]

$$J^e = \frac{e}{h}\int dE\,\mathcal{T}(E)[f_L(E) - f_R(E)] \tag{3.1}$$

$$J^Q = \frac{1}{h}\int dE\,(E-\mu_L)\mathcal{T}(E)[f_L(E) - f_R(E)] \tag{3.2}$$

where $f_\alpha(E) = (1+\exp[(E-\mu_\alpha)/(k_B T_\alpha)])^{-1}$ is the Fermi distribution of the lead α and $\mathcal{T}(E)$ is the transmission probability for an electron to tunnel from the left to the right terminal. k_B is the Boltzmann constant, $e<0$ the electron charge and h the Planck constant. The above expressions are given for spinless electrons and shall be doubled in case of spin degeneracy.

We now assume that the differences $\Delta\mu = \mu_L - \mu_R$ and $\Delta T = T_L - T_R$ to the equilibrium values $\mu \approx \mu_L \approx \mu_R$ and $T \approx T_L \approx T_R$ are small. Expanding the currents in Eqs. (3.1, 3.2) to first order in $\Delta\mu$ and ΔT around μ and T, one obtains [30]

$$\begin{pmatrix} J^e \\ J^Q \end{pmatrix} = \begin{pmatrix} L_0 & L_1 \\ L_1 & L_2 \end{pmatrix} \begin{pmatrix} \Delta\mu/eT \\ \Delta T/T^2 \end{pmatrix}, \tag{3.3}$$

where the linear response coefficients L_i are the Onsager coefficients introduced in section 1.2, given by

$$L_i = \frac{e^2}{h} T \int dE\,\mathcal{T}(E) \left(\frac{E-\mu}{e}\right)^i \left(-\frac{\partial f}{\partial E}\right). \tag{3.4}$$

Recalling section 1.2.1, the electrical conductance G, the (electronic contribution to the) thermal conductance K^e, the Seebeck coefficient (thermopower) S and the Peltier coefficient

Π can all be expressed in terms of the L_is as

$$G \equiv \left.\frac{eJ^e}{\Delta\mu}\right|_{\Delta T=0} = \frac{L_0}{T}, \tag{3.5}$$

$$K^e \equiv \left.\frac{J^Q}{\Delta T}\right|_{J^e=0} = \frac{L_0L_2 - L_1^2}{T^2L_0}, \tag{3.6}$$

$$S \equiv -\left.\frac{\Delta\mu}{e\Delta T}\right|_{J^e=0} = \frac{L_1}{TL_0}, \tag{3.7}$$

$$\Pi \equiv \left.\frac{J^Q}{J^e}\right|_{\Delta T=0} = \frac{L_1}{L_0} \quad . \tag{3.8}$$

Note that, since the system is time-reversal symmetric, the Kelvin-Onsager relation [33, 128] implies that $\Pi = ST$. By virtue of Eq. (3.4), in presence of particle-hole symmetry we have $S = \Pi = 0$. Further, the link between the electrical and thermal conductances is quantified by the Lorenz number $\mathcal{L} = K^e/GT$.

In the zero temperature limit $T \to 0$, the Sommerfeld expansion [6] can be used to estimate the integrals (3.4). To the lowest order in (k_BT/μ), the electrical conductance reduces to $G \approx \frac{e^2}{h}\mathcal{T}(\mu)$ while the thermopower simplifies to

$$S \approx \frac{\pi^2}{3}\frac{k_B}{e}\,k_BT\,\left.\frac{\mathrm{d}\ln\mathcal{T}}{\mathrm{d}E}\right|_{\mu} . \tag{3.9}$$

The Lorenz number $\mathcal{L}$ takes in this limit a constant value,

$$\mathcal{L} \approx \mathcal{L}_0 \equiv \frac{\pi^2}{3}\left(\frac{k_B}{e}\right)^2, \tag{3.10}$$

as long as $|S| \ll \sqrt{\mathcal{L}_0} \simeq 156\,\mu\mathrm{V.K}^{-1}$. This reflects the fact that the electrical and thermal conductances are proportional and hence cannot be manipulated independently, an important although constraining property known as the Wiedemann-Franz (WF) law. This law is known to be valid for non-interacting systems if the low temperature Sommerfeld expansion is valid [9, 177], when Fermi liquid (FL) theory holds [6, 35] and for metals at room temperatures [6], while it could be largely violated in interacting systems due to non FL behaviors [87, 182].

3.2 Model and method

The system under consideration is sketched in Fig. 3.1(a). It is made of a 1D disordered nanowire coupled via perfect leads to two reservoirs L (left) and R (right) of non-interacting electrons, in equilibrium at temperature $T_L = T + \Delta T$ $[T_R = T]$ and chemical potential $\mu_L = \mu + \Delta\mu$ $[\mu_R = \mu]$. The nanowire is modeled as a 1D Anderson chain of N sites, with lattice spacing $a = 1$. Its Hamiltonian reads,

$$\mathcal{H} = -t\sum_{i=1}^{N-1}\left(c_i^\dagger c_{i+1} + \mathrm{h.c.}\right) + \sum_{i=1}^{N}\epsilon_i c_i^\dagger c_i\,, \tag{3.11}$$

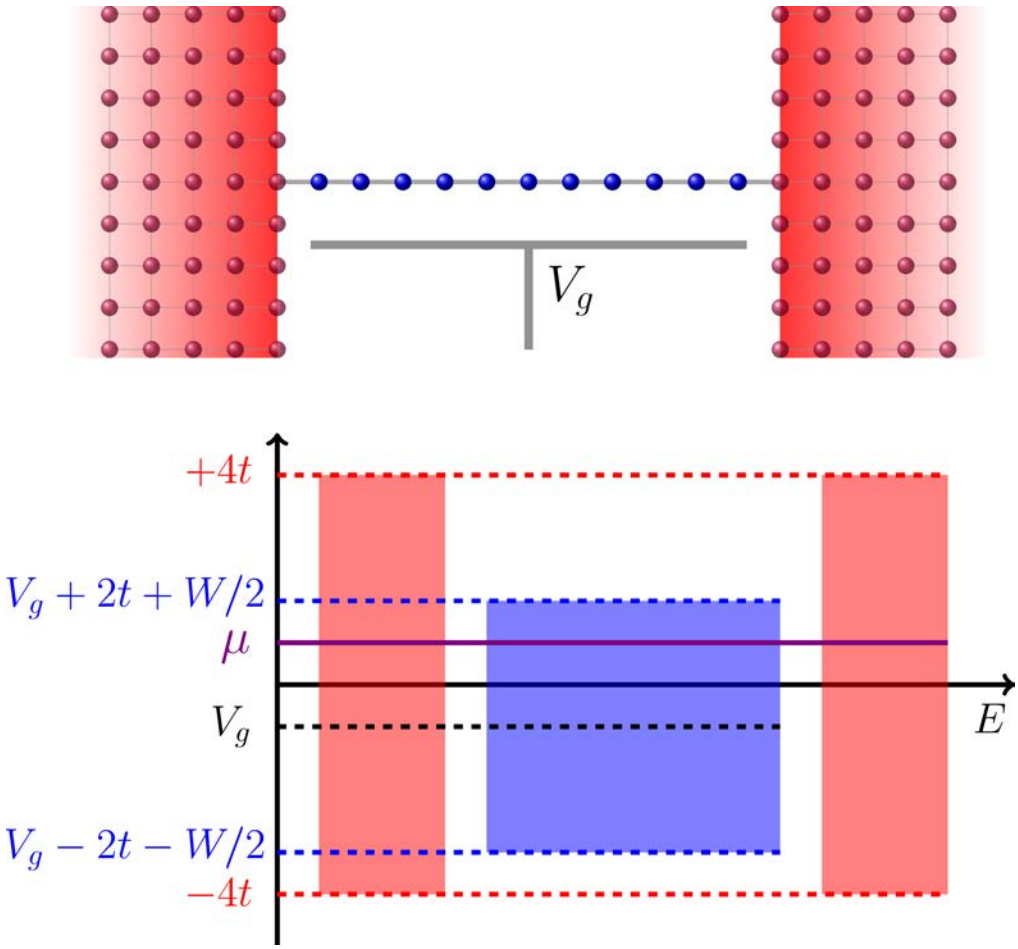


Figure 3.1: (a) Sketch of the system: a 1D nanowire made of N sites is connected to two leads at its extremities. An external gate voltage V_g is applied. (b) Band diagram. The impurity band of the nanowire (in blue) can be shifted by the application of V_g in order to probe either the bulk, the edges or the outside of the impurity band at Fermi energy μ. Here, the leads are bidimensional (conduction band of the leads in red) and hence, $\mu \in [-4t, 4t]$.

where $c_i^\dagger$ and c_i are the creation and annihilation operators of one electron on site i and t is the hopping energy. The disorder potentials ϵ_i are (uncorrelated) random numbers uniformly distributed in the interval $[-W/2, W/2]$. The two sites at the ends of the nanowire are connected with hopping term t to the leads which can be 1D semi-infinite chains or 2D semi-infinite square lattices, with zero on-site potentials and the same hopping term t. The simpler case of the Wide Band Limit (WBL) approximation, where the energy dependence of the self-energies of the leads is neglected, is also considered. Finally, an extra term

$$\mathcal{H}_{gate} = \sum_i V_g c_i^\dagger c_i \tag{3.12}$$

is added in the Hamiltonian (3.11) to mimic the presence of an external metallic gate. It allows to shift the whole impurity band of the nanowire.

3.2.1 Calculation of the transport coefficients

In the Green function formalism, the transmission $\mathcal{T}(E)$ of the system at an energy E is given by the Fisher-Lee formula [43]

$$\mathcal{T}(E) = \mathrm{Tr}[\Gamma_L(E)\mathcal{G}(E)\Gamma_R(E)\mathcal{G}^\dagger(E)] \tag{3.13}$$

in terms of the retarded single particle Green function $\mathcal{G}(E) = [E - \mathcal{H} - \Sigma_L - \Sigma_R]^{-1}$ and of the retarded self-energies Σ_L and Σ_R of the left and right leads. The operators $\Gamma_\alpha = i(\Sigma_\alpha - \Sigma_\alpha^\dagger)$ describe the coupling between the conductor and the lead $\alpha = L$ or R. A standard recursive Green function algorithm allows us to compute the transmission $\mathcal{T}(E)$ (see section 3.6.1 for details). The logarithmic derivative $(\mathrm{d}\ln\mathcal{T}/\mathrm{d}E)$ can be calculated as well with the recursive procedure, without need for a discrete evaluation of the derivative. It yields the thermopower S in the Mott-Sommerfeld approximation (3.9). Let us precise, to settle the notations, that in the following we will refer to a dimensionless thermopower

$$\mathcal{S} = -t \left.\frac{\mathrm{d}\ln\mathcal{T}}{\mathrm{d}E}\right|_\mu \tag{3.14}$$

which is related, in the Mott-Sommerfeld approximation, to the thermopower S in physical units as

$$S = \frac{\pi^2}{3}\left(\frac{k_B}{|e|}\right)\left(\frac{k_B T}{t}\right)\mathcal{S}\,. \tag{3.15}$$

We now discuss the expressions of the self-energies $\Sigma_L(E)$ and $\Sigma_R(E)$ of the left and right leads which are to be given as input parameters in the recursive Green function algorithm. The nanowire of length N sites is supposed to be connected on one site at its extremities to two identical leads, which are taken 1D, 2D or in the WBL approximation. Hence, the self-energies Σ_α (as well as the operator Γ_α) are $N \times N$ matrices with only one non-zero component (identical for both leads) that we denote with Σ (or Γ). When the wide-band limit is assumed for the leads, Σ is taken equal to a small constant imaginary number independent of the energy E.

When the leads are two 1D semi-infinite chains or two 2D semi-infinite square lattices, Σ is given by the retarded Green function $\mathcal{G}_{\mathrm{lead}}$ of the lead under consideration evaluated at the site X (in the lead) coupled to the nanowire, $\Sigma = t^2\langle X|\mathcal{G}_{\mathrm{lead}}|X\rangle$. Knowing the expressions of the retarded Green functions of the infinite 1D chain and the infinite 2D square lattice [50], it is easy to deduce $\mathcal{G}_{\mathrm{lead}}$ for the semi-infinite counterparts by using the method of mirror images. For 1D leads, one finds $\Sigma(E) = -te^{ik(E)}$ where $E = -2t\cos k$ and k is the electron wavevector [43]. For 2D leads, the expression of $\Sigma(E)$ is more complicated (see section 3.6.2).

As far as the Fermi energy μ is not taken near the edges of the conduction band of the leads, the thermopower behaviors using 1D and 2D leads coincide with those obtained using the WBL approximation (see section 3.3.1). This shows us that the dimensionality D becomes irrelevant in that limit, and we expect that taking 3D leads will not change the results.

3.2.2 Scanning the impurity band of the Anderson model

The density of states per site $\nu(E)$ of the Anderson model, obtained by numerical diagonalization of the Hamiltonian (3.11), is plotted in Fig. 3.2(a) in the limit $N \to \infty$. It is non-zero in the interval $[E_c^-, E_c^+]$ where $E_c^\pm = \pm(2t + W/2)$ are the edges of the impurity band. In the bulk of the impurity band (*i.e.* for energies $|E| \lesssim 1.5t$), the density of states is given with a good precision by the formula derived for a clean 1D chain (red dashed line in Fig. 3.2(a)),

$$\nu_b(E) = \frac{1}{2\pi t\sqrt{1-(E/2t)^2}} \,. \tag{3.16}$$

As one approaches the edges $E_c^\pm$, the disorder effect cannot be neglected anymore. The density of states is then well described by the analytical formula obtained by Derrida and Gardner around $E_c^\pm$, in the limit of weak disorder and large N (see Ref. [46]),

$$\nu_e(E) = \sqrt{\frac{2}{\pi}} \left(\frac{12}{tW^2}\right)^{1/3} \frac{\mathcal{I}_1(X)}{[\mathcal{I}_{-1}(X)]^2} \tag{3.17}$$

where

$$X = (|E| - 2t)t^{1/3} \left(\frac{12}{W^2}\right)^{2/3} \tag{3.18}$$

and

$$\mathcal{I}_n(X) = \int_0^\infty y^{n/2}\, e^{-\frac{1}{6}y^3 + 2Xy}\, dy \,. \tag{3.19}$$

In this paper, we study the behavior of the thermoelectric coefficients as one probes at the Fermi energy μ electron transport either inside or outside the nanowire impurity band, and more particularly in the vicinity of its band edges. Such a scan of the impurity band can be done in two ways. One possibility is to vary the position of the Fermi energy μ in the leads. Doing so, we modify the distance between μ and the band edges $E_c^\pm$ but also the one between μ and the band edges of the leads. This can complicate the analysis of the data, the dimensionality of the leads becoming relevant when $|E_c^\pm - \mu| \to 0$. To avoid this complication, we can keep μ fixed far from $E_c^\pm$ and vary the gate voltage V_g (see Fig. 3.1(b)).

3.2.3 Localization length of the Anderson model

In the disordered 1D model (3.11) we consider, all eigenstates are exponentially localized, with a localization length ξ. As a consequence, the typical transmission of the nanowire drops off exponentially with its length N. More precisely, when $N \gg \xi$ (localized limit), the distribution of $\ln \mathcal{T}$ is a Gaussian [135, 165] centered around the value

$$[\ln \mathcal{T}]_0(E) = -\frac{2N}{\xi(E)} \,, \tag{3.20}$$

as long as the energy E of the incoming electron is inside the impurity band of the nanowire. The inverse localization length $1/\xi$ can be analytically obtained as a series of integer powers

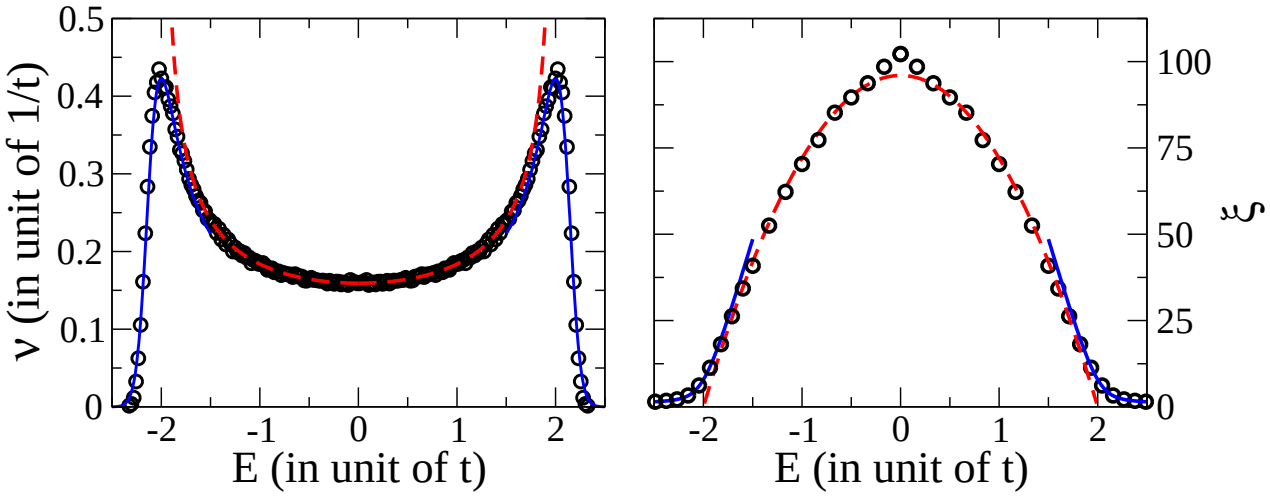


Figure 3.2: (a) Density of states per site ν as a function of energy E for the 1D Anderson model (3.11) with disorder amplitude $W/t = 1$. The circles correspond to numerical data (obtained with $N = 1600$). The red dashed line and the blue line are the theoretical predictions (3.16) and (3.17), expected in the bulk and at the edges of the nanowire conduction band for $N \to \infty$. (b) Localization length ξ of the 1D Anderson model (3.11) (with $W/t = 1$) as a function of energy E. The circles correspond to numerical data (obtained with Eq. (3.20)). The red dashed line and the blue line are the theoretical predictions (3.21) and (3.22) obtained in the limit $N \to \infty$.

of W when $W \to 0$. To the leading order (see e.g. [94]), this gives

$$\xi_b(E) = \frac{24}{W^2}\left(4t^2 - E^2\right) . \tag{3.21}$$

The formula is known to be valid in the weak disorder limit inside the bulk of the impurity band (hence the index b). Strictly speaking, it fails in the vicinity of the band center $E = 0$ where the perturbation theory does not converge [88] but it gives nevertheless a good approximation. As one approaches one edge of the impurity band, the coefficients characterizing the expansion of $1/\xi$ in integer powers of W diverge and the series has to be reordered. As shown by Derrida and Gardner [46], this gives (to leading order in W) the non analytical behavior $1/\xi \propto W^{2/3}$ as one edge is approached instead the analytical behavior $1/\xi \propto W^2$ valid in the bulk of the impurity band. More precisely, one find in the limit $W \to 0$ that

$$\xi_e(E) = 2\left(\frac{12t^2}{W^2}\right)^{1/3} \frac{\mathcal{I}_{-1}(X)}{\mathcal{I}_1(X)} \tag{3.22}$$

as E approaches the band edges $\pm 2t$. The integrals $\mathcal{I}_i$ and the parameter X have been defined in Eq. (3.19) and Eq. (3.18). As shown in Fig. 3.2(b), both formula (3.21) and (3.22) are found to be in very good agreement with our numerical evaluation of $\xi(E)$, in the respective range of energy that they describe, even outside a strictly weak disorder limit ($W = t$ in Fig. 3.2(b)).

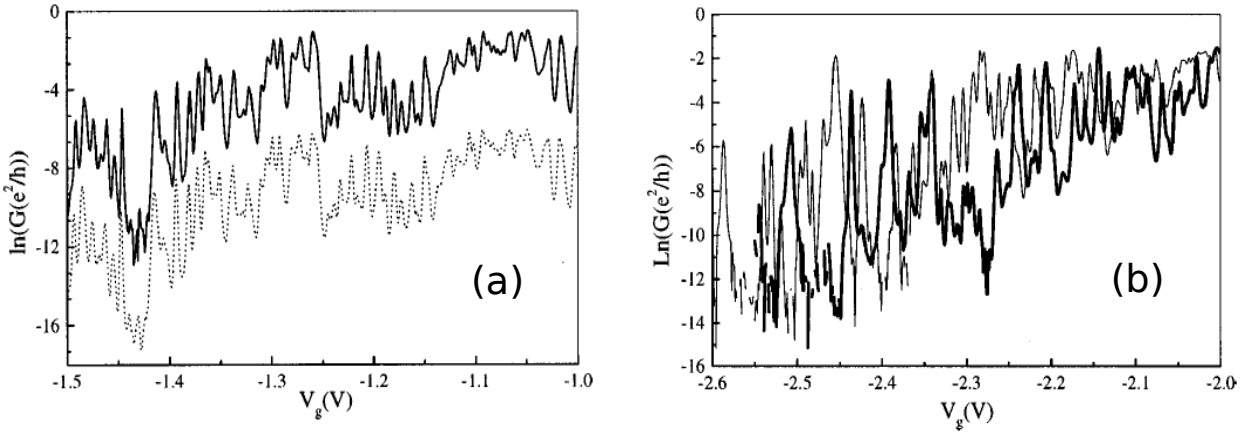


Figure 3.3: Logarithm of the electrical conductance as function of the gate voltage of a 0.5 mm-long sample at T=100 mK (after [138]). The conductance fluctuations amplitude in the case of bulk transport (a) is smaller compared to the case of edge transport (b).

3.3 Thermopower

As explained in section 3.1, the thermopower at low temperatures in the regime of coherent transport depends only on the logarithmic derivative of the electrical conductance with respect to the energy (see Eq.(3.9)). Poirier *et al.* [138] studied experimentally the conductance mesoscopic fluctuations of small one-dimensional metal-semiconductor field-effect transistors. They observed that when the system is strongly depleted by means of a gate voltage (i.e., at band edge), the amplitude of such fluctuations is larger with respect to the bulk case (see Fig. 3.3). Hence, by extending this idea to our model, larger values of the thermopower are predicted to be achievable when transport takes place around the nanowires impurity band edges. This statement is confirmed both by calculations and numerical simulations presented in the following.

3.3.1 Typical thermopower

In order to investigate the behavior of the *typical* thermopower $\mathcal{S}_0$, we compute numerically $\mathcal{S}$ for many realizations of the disorder potentials ϵ_i in Eq. (3.11), and we define the typical value $\mathcal{S}_0$ as the median of the resulting distribution $P(\mathcal{S})$. As it will be shown in section 3.3.2, $P(\mathcal{S})$ is typically a smooth symmetric function (Lorentzian or Gaussian), and thus its median coincides with its most probable value. We study the behavior of $\mathcal{S}_0$ as one scans the energy spectrum of the nanowire by varying the position of the Fermi energy μ in the leads or the gate voltage V_g.

In Fig. 3.4(a), the typical thermopower $\mathcal{S}_0$ of a long nanowire in the localized regime ($N \gg \xi$) is plotted as a function of μ without gate voltage ($V_g = 0$). Since $\mathcal{S}_0 \to -\mathcal{S}_0$ when

$\mu \to -\mu$, data are shown for positive values of μ only. In the figure, three different kinds of leads are considered: 1D leads, 2D leads or leads in the WBL approximation. In all cases, as expected, we find that $\mathcal{S}_0 = 0$ at the center of the conduction band of the leads ($\mu = 0$). Indeed, the random potentials being symmetrically distributed around a zero value, one has a statistical particle-hole symmetry at the band center and the thermopower can only be a statistical fluctuation around a zero typical value. As μ is increased, the statistical particle-hole symmetry breaks down and $\mathcal{S}_0$ gets finite. Here $\mathcal{S}_0 > 0$ because charge transport is dominated by holes for $\mu > 0$.

When the wide band limit is assumed for both leads (triangles in Fig. 3.4(a)), we find that the typical thermopower $\mathcal{S}_0$ increases with μ and reaches a maximum just before $E_c^+ = 2t + W/2$, the asymptotic $N \to \infty$ value for the edge ($E_c^+ = 2.5\,t$ in Fig. 3.4(a) where $W = t$) before decreasing. The same curve is obtained with 1D [2D] leads as long as the Fermi energy μ remains far enough below the upper band edge of the D-dimensional leads. When μ approaches $2t$ [$4t$], the typical thermopower $\mathcal{S}_0$ of the nanowire is found to increase drastically, contrary to the WBL case (of course, no data are available for $|\mu| \geq 2t\,[4t]$, charge transfer being impossible outside the conduction band of the leads). This singularity at the band edge of the leads can be easily understood using Eqs. (3.13) and (3.14) and noticing that for 1D [2D] leads, $\mathrm{d}\ln\Gamma/\mathrm{d}E \to -\infty$ as $E \to 2t$ [$4t$]. This is obvious in the case of 1D leads where $\Gamma(E) = 2t\sqrt{1-(E/2t)^2}$ and it can also be shown for 2D leads. We will see in section 3.5 that this apparent divergence of the thermopower is actually only valid in an infinitesimally small range of temperatures above 0 K.

With the gate voltage V_g, we can explore the impurity band of the nanowire while keeping μ fixed. The behavior of $\mathcal{S}_0$ as a function of V_g is shown in Fig. 3.4(b) for $\mu = 0$ and 1D leads. It is found to be identical to the behavior of $\mathcal{S}_0$ as a function of μ obtained at $V_g = 0$ in the WBL approximation. This remains true if 2D leads are used in Fig. 3.4(b) and we have no doubt that it also remains true with 3D leads. Moreover, the results are unchanged if μ is fixed to any other value, as long as it does not approach too closely one edge of the conduction band of the leads (but it can be chosen close enough to one band edge to recover the continuum limit of the leads).

Our main observation is that the typical thermopower $\mathcal{S}_0$ increases importantly when the Fermi energy probes the region around the edges of the impurity band of the nanowire. Qualitatively, this is due to the fact that the typical transmission of the nanowire drops down when the edges are approached: this huge decrease results in a enhancement of the typical thermopower, the thermopower being somehow a measure of the energy dependence of the transmission. A quantitative description of this behavior can also be obtained. Indeed, since the distribution of the transmission $\mathcal{T}$ is log-normal in the localized regime [135, 165] and the thermopower S is calculated for each disorder configuration with the Mott approxima-

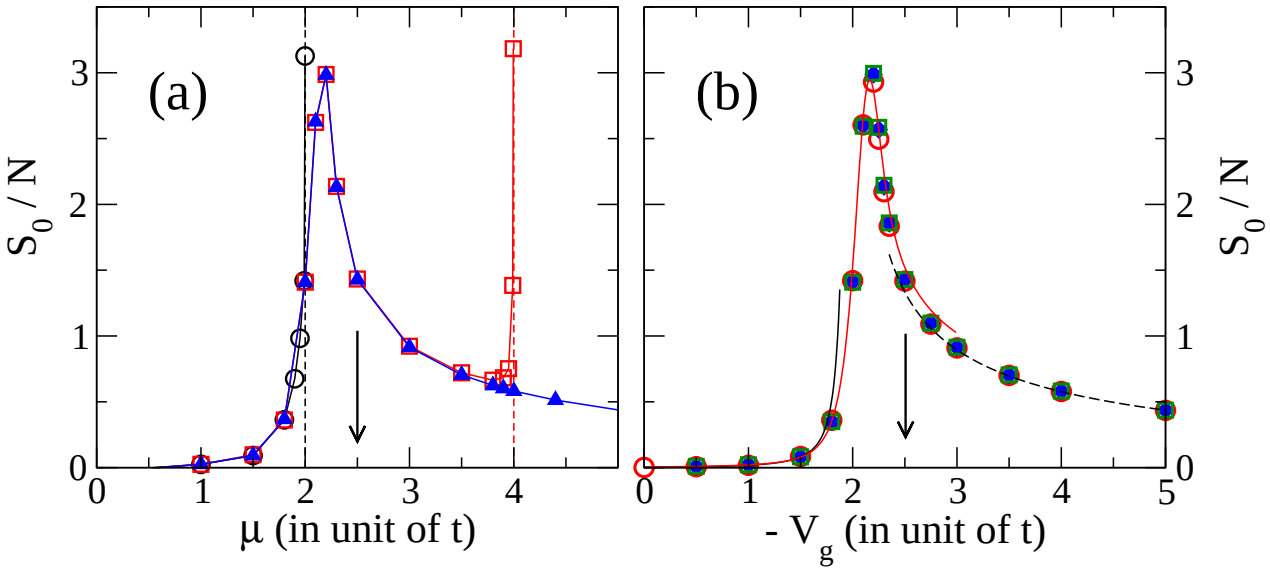


Figure 3.4: Typical value of the dimensionless thermopower per unit length, $\mathcal{S}_0/N$, as a function of the Fermi energy μ at $V_g = 0$ (a) and as a function of the gate voltage V_g at $\mu = 0$ (b). In panel (a), the data were obtained at fixed $N = 500$, by using either 1D leads (○), 2D leads (□) or the wide-band limit approximation (▲). With 1D [2D] leads, the typical thermopower shows a divergent behavior at the band edge of the leads (black [red] vertical dashed line). In panel (b), 1D leads are used. The symbols stand for different lengths of the nanowire ($N = 200$ (○), 800 (□) and 1600 (♦)). The full black line, the full red line and the dashed black line correspond respectively to the theoretical fits (3.24), (3.25) and (3.27) expected when μ probes the bulk, the edge and the outside of the impurity band. In both panels, $W/t = 1$. The arrows indicate the position of the edge of the impurity band of the nanowire.

tion (3.14), one expects to have

$$\mathcal{S}_0 = -t \left. \frac{\mathrm{d}[\ln \mathcal{T}]_0}{\mathrm{d}E} \right|_\mu \tag{3.23}$$

where $[\ln \mathcal{T}]_0$ is the median of the $\ln \mathcal{T}$ Gaussian distribution (which in this case coincides with the most probable value). Moreover, according to Eq. (3.20), the energy dependence of $[\ln \mathcal{T}]_0$ is given by the energy dependence of the localization length, *i.e.* by Eqs. (3.21) and (3.22). This allows us to derive the following expressions for the typical thermopower in the bulk and at the edges:

$$\mathcal{S}_0^b = N \frac{(\mu - V_g)\, W^2}{96 t^3 [1 - ((\mu - V_g)/2t)^2]^2}, \tag{3.24}$$

$$\mathcal{S}_0^e = 2N \left(\frac{12 t^2}{W^2} \right)^{1/3} \left\{ \frac{\mathcal{I}_3(X)}{\mathcal{I}_{-1}(X)} - \left[\frac{\mathcal{I}_1(X)}{\mathcal{I}_{-1}(X)} \right]^2 \right\}, \tag{3.25}$$

where now X is modified to

$$X = (|\mu - V_g| - 2t) t^{1/3} (12/W^2)^{2/3} \tag{3.26}$$

in order to take into account the effect of the gate voltage V_g. When the outside of the impurity band, rather than the inside, is probed at μ (i.e. when the wire is completely depleted), no more states are available in the nanowire to tunnel through. Electrons coming from one lead have to tunnel directly to the other lead through the disordered barrier of length N. We have also calculated the typical thermopower of the nanowire in that case, assuming that the disorder effect is negligible (see Appendix 3.6.3). We find

$$\frac{\mathcal{S}_0^{TB}}{N} \underset{N \to \infty}{\approx} -\frac{1}{N} \frac{2t}{\Gamma(\mu)} \left. \frac{\mathrm{d}\Gamma}{\mathrm{d}E} \right|_\mu \mp \frac{1}{\sqrt{\left(\frac{\mu - V_g}{2t} \right)^2 - 1}} \tag{3.27}$$

with a $+$ sign when $\mu \leq V_g - 2t$ and a $-$ sign when $\mu \geq V_g + 2t$. Fig. 3.4(b) shows a very good agreement between the numerical results (symbols) and the expected behaviors (Eqs. (3.24), (3.25) and (3.27)). One consequence of these analytical predictions is that the peak in the thermopower curves gets higher and narrower as the disorder amplitude is decreased (and vice-versa).

In conclusion of this section, we remark that the thermopower enhancement which we predict around the edges looks in qualitative agreement with the recent experimental observation reported in Ref [28], using silicon and germanium/silicon nanowires in the field effect transistor device configuration. We stress out however that those measurements were carried out at room temperatures, and not in the low temperature coherent regime which we consider. To describe them, inelastic effects shall be included. The next chapter goes toward this direction, being focused to the activated Variable Range Hopping regime [20]. The low temperature coherent regime considered in this paper has been studied in Ref. [138], where

the conductances G of half a micron long Si-doped GaAs nanowires have been measured at $T = 100mK$ in the field effect transistor device configuration. Assuming Eq. (3.9) for evaluating the thermopower S from $\ln G(V_g)$, the typical behavior and the fluctuations of $\ln G(V_g)$ given in Ref. [138] are consistent with the large enhancement of S near the band edges which we predict.

3.3.2 Thermopower distributions

In the coherent elastic regime we consider, the sample-to-sample fluctuations of the thermopower around its typical value are expected to be large. The most striking illustration occurs at the center of the impurity band of the nanowire ($\mu = V_g$), when the typical thermopower is zero due to statistical particle-hole symmetry but the mesoscopic fluctuations allow for large thermopower anyway. Van Langen *et al* showed in Ref. [176] that in the localized regime $N \gg \xi$ without gate ($V_g = 0$) and around the band center ($\mu \approx 0$), the distribution of the low-temperature thermopower is a Lorentzian,

$$P(\mathcal{S}) = \frac{1}{\pi} \frac{\Lambda}{\Lambda^2 + (\mathcal{S} - \mathcal{S}_0)^2}, \tag{3.28}$$

with a center $\mathcal{S}_0 = 0$ and a width

$$\Lambda = \frac{2\pi t}{\Delta_F} \tag{3.29}$$

given by $\Delta_F = 1/(N\nu_F)$, the average mean level spacing at μ. This was derived under certain assumptions leading to $\mathcal{S}_0 = 0$. As we have shown, $\mathcal{S}_0 = 0$ is exact only at the impurity band center ($\mu = 0$ when $V_g = 0$) and remains a good approximation as far as one stays in the bulk of the impurity band. But the distribution $P(\mathcal{S})$ is no more centered around zero as one approaches the band edge.

We propose here to investigate how the thermopower distribution $P(\mathcal{S})$ is modified when this is not only the bulk, but the edges (or even the outside) of the impurity band which are probed at the Fermi energy μ. To fix the ideas, we set the Fermi energy to $\mu = 0$ and the disorder amplitude to $W = t$ (so that the band edges are $V_g + E_c^{\pm} = V_g \pm 2.5t$). First, we check in Fig. 3.5(a) that at $V_g = 0$ and in the localized regime, the thermopower distribution is indeed a Lorentzian with a width $\Lambda \propto N$. We note that very long chains of length $N \approx 50\xi$ ($\xi \approx 100$ here) are necessary to converge to the Lorentzian (3.28). Moreover, we have checked that this is also in this limit that the delay time distribution converges towards the universal form predicted in Ref [168].

Then we increase the gate potential up to $V_g = 2t$ to approach the edge E_c^- of the impurity band and find that the thermopower distribution remains a Lorentzian in the localized regime ($N \gtrsim 50\xi$) with a width $\Lambda \propto N$, as shown in Fig. 3.5(b). It turns out actually that the fit of the thermopower distribution with a lorentzian (in the large N limit) is satisfactory in a broad range of gate potentials $|V_g| \lesssim 2.25t$, as long as the Fermi energy $\mu = 0$ probes the impurity band without approaching too closely its edges $V_g + E_c^{\pm}$. In Fig. 3.5(c), we

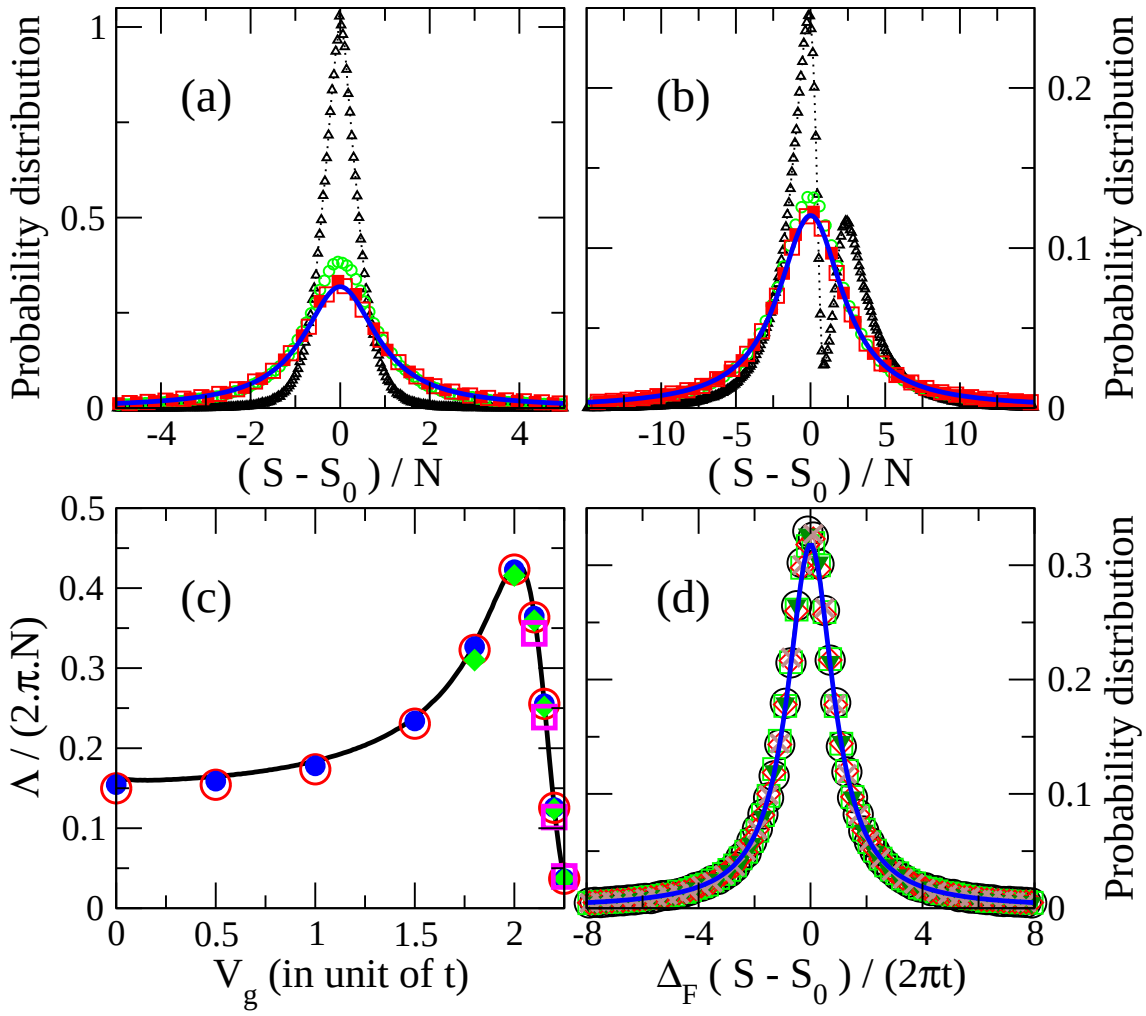


Figure 3.5: Top panels: probability distributions of the rescaled thermopower $(\mathcal{S}-\mathcal{S}_0)/N$ at $V_g = 0$ (a) and $V_g = 2t$ (b), with $W = t$, $\mu = 0$ and 1D leads. In each panel, the different symbols correspond to various lengths of the chain ($N \approx \xi$ (△), $N \approx 10\,\xi$ (○), $N \approx 50\,\xi$ (□) and $N \approx 100\,\xi$ (■), respectively $N = 100$, 1000, 5000 and 10000 in (a) and $N = 10$, 100, 500 and 1000 in (b). The distributions obtained for $N \geq 50\,\xi$ collapse on a single curve which is well fitted by a Lorentzian distribution function (thick blue lines). The widths Λ/N of the Lorentzian fits are plotted as a function of V_g in panel (c), for $N = 200$ (□), 1000 (⧫), 5000 (○) and 10000 (●), together with the density of states per site at μ, $t\nu_F$, of the closed chain (red line). The probability distributions of the rescaled thermopower $(\Delta_F/2\pi t)(S-S_0)$, obtained in the large N limit ($N \approx 100\,\xi$) and for various sets of parameters ($W = 0.5t$ and $V_g = 2t$ (◇), $W = t$ and $V_g = 0$ (○), $W = t$ and $V_g = 2t$ (□), $W = 2t$ and $V_g = 0$ (×), and $W = 2t$ and $V_g = 2.3t$ (▾), with $\mu = 0$ in all cases), are shown in panel (d). They all collapse on the blue line which is the Lorentzian function $y = 1/[\pi(1+x^2)]$.

show in addition that in this regime, the widths Λ of the Lorentzian fits to the thermopower distributions $P(\mathcal{S})$ obey $\Lambda/(2\pi Nt) = \nu_F$, *i.e.* Eq. (3.29). Therefore (Fig. 3.5(d)), we can use this parameter to rescale all the distributions obtained in a broad range of parameters, on the same Lorentzian function $y = 1/[\pi(1+x^2)]$. A direct consequence of Eq. (3.29) is that the mesoscopic fluctuations of the thermopower are maximal for $|\mu - V_g| \approx 2t$.

When the gate voltage $|V_g|$ is increased further, the number of states available at μ in the nanowire decreases exponentially and eventually vanishes: one approaches eventually a regime where the nanowire becomes a long tunnel barrier and where the thermopower fluctuations are expected to be smaller and smaller. In this limit, we find that the thermopower distribution is no more a Lorentzian but becomes a Gaussian,

$$P(\mathcal{S}) = \frac{1}{\sqrt{2\pi}\lambda} \exp\left[-\frac{(\mathcal{S}-\mathcal{S}_0)^2}{2\lambda^2}\right], \tag{3.30}$$

provided the chain is long enough. This result is illustrated in Figs. 3.6(a) and 3.6(b) for two values of V_g. The Gaussian thermopower distribution is centered around a typical value $\mathcal{S}_0$ given by Eq. (3.27) and its width λ is found with great precision to increase linearly with $\sqrt{N}$ and W. To be more precise, we find that the dependency of λ on the various parameters is mainly captured by the following formula

$$\lambda \approx 0.6 \frac{Wt\sqrt{N}}{(\mu - V_g)^2 - (2t + W/4)^2}, \tag{3.31}$$

at least for $0.5t \lesssim W \lesssim 4t$, $2.35t \lesssim |\mu - V_g| \lesssim 6t$ and $N \gtrsim 100$ (see Fig. 3.6(c)). We stress out that Eq. (3.31) is merely a compact way of describing our numerical data. In particular, the apparent divergence of λ when $|\mu - V_g| \to 2t + W/4$ is meaningless and in fact it occurs outside the range of validity of the fit. To double-check the validity of Eq. (3.31), we have rescaled with the parameter λ given by Eq. (3.31), a set of thermopower distributions obtained in the disordered tunnel barrier regime, for various W and V_g. All the resulting curves (plotted in Fig. 3.6(d)) are superimposed on the unit gaussian distribution, except the one for the smallest disorder value $W = 0.5t$ for which the fit (3.31) to λ is satisfactory but not perfect.

To identify precisely the position of the crossover between the Lorentzian regime and the Gaussian regime, we introduce now the parameter η,

$$\eta = \frac{\int d\mathcal{S} |P(\mathcal{S}) - P_G(\mathcal{S})|}{\int d\mathcal{S} |P_L(\mathcal{S}) - P_G(\mathcal{S})|}, \tag{3.32}$$

which measures, for a given thermopower distribution $P(\mathcal{S})$ obtained numerically, how closed it is from its best Gaussian fit $P_G(\mathcal{S})$ and from its best Lorentzian fit $P_L(\mathcal{S})$[1]. If $P(\mathcal{S})$ is a

[1] One could be tempted to compare an arbitrary thermopower distribution $P(\mathcal{S})$ to the Lorentzian and Gaussian distributions given in Eqs. (3.28 - 3.29) and (3.30 - 3.31) respectively. However, to define η for any set of parameters, one should extend to the outside of the spectrum the formula (3.29) for the width Λ of the Lorentzian, and to the inside of the spectrum the formula (3.31) for the width λ of the Gaussian. We avoid this problem by taking instead the best Lorentzian and Gaussian fits to $P(\mathcal{S})$ in the definition of η. It allows us to distinguish whether $P(\mathcal{S})$ is a Lorentzian or a Gaussian (or none of both) but of course, the precise form of $P(\mathcal{S})$ is not probed by η as defined.

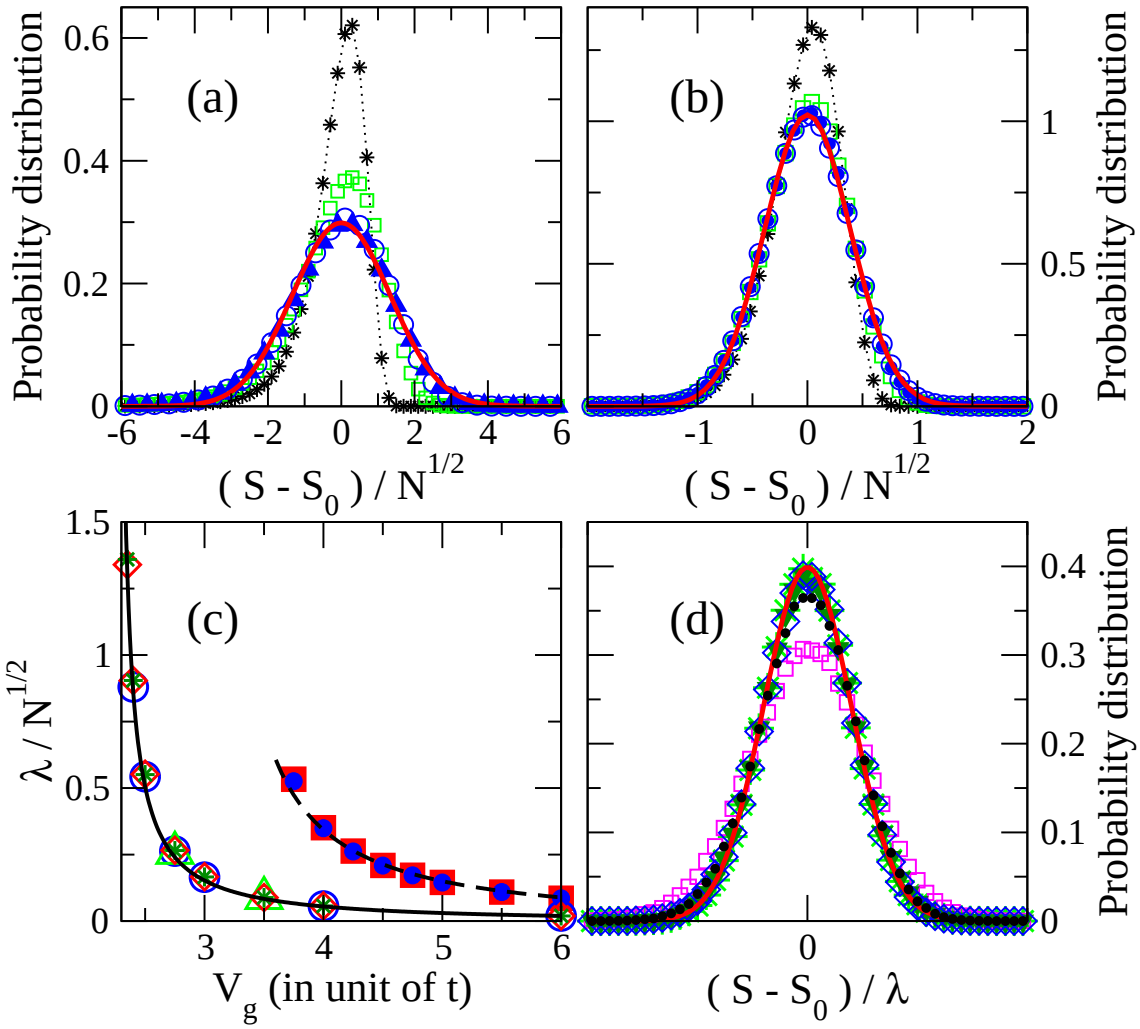


Figure 3.6: Top panels: probability distributions of the rescaled thermopower $(\mathcal{S}-\mathcal{S}_0)/\sqrt{N}$ at $V_g = 2.35t$ (a) and $V_g = 2.6t$ (b), with $W = t$, $\mu = 0$ and 1D leads. In each panel, the distributions are plotted for various lengths of the chain ($N = 10$ (∗), 50 (▫), 200 (•), 500 (◦) and 1000 (▲)) and collapse at large N on one single curve, well fitted by a Gaussian distribution (red line). The widths $\lambda/\sqrt{N}$ of the Gaussian fits are plotted as a function of V_g in panel (c), for various lengths ($N = 50$ (triangle), 200 (circle), 400 (square), 800 (diamond) and 1600 (star)) and two disorder amplitudes ($W = t$ (empty symbols) and $W = 4t$ (full symbols)). The solid and dashed lines are the fits given by Eq. (3.31), respectively for $W = t$ and $W = 4t$. Panel (d): collapse of the thermopower distributions, obtained with $N = 500$ and various parameters ($W = 0.5t$ and $V_g = 2.25t$ (▫), $W = 0.5t$ and $V_g = 5t$ (▼), $W = t$ and $V_g = 2.5t$ (•), $W = t$ and $V_g = 5t$ (∗), and $W = 4t$ and $V_g = 4t$ (◊)), after a rescaling by λ as given in Eq. (3.31). The red line is the Gaussian distribution $y = (1/\sqrt{2\pi})\exp(-x^2/2)$.

Lorentzian, $\eta = 1$ while $\eta = 0$ if it is a Gaussian. Considering first the case where $\mu = 0$ and $W = t$, we show in the left panel of Fig. 3.7 that η converges at large N for any V_g (inset). The asymptotic values of η (given with a precision of the order of 0.05 in the main panel) undergo a transition from $\eta \approx 1$ to $\eta \approx 0$ when V_g is increased from 0 to $4t$. This reflects the crossover from the Lorentzian to the Gaussian thermopower distribution already observed in the top panels of Figs. 3.5 and 3.6. We see in addition that the crossover is very sharp around the value $V_g \approx 2.3t$, indicating a crossover which remains inside the impurity band of the infinite nanowire, since the band is not shifted enough when $V_g \approx 2.3t$ to make the Fermi energy coincide with the band edge $V_g + E_c^- = V_g - 2.5t$.

We have obtained the same results for other values of the disorder amplitude. After checking the convergence of η at large N, we observe the same behavior of the asymptotic values of η as a function of V_g, for any W. Only the position of the crossover is disorder-dependent. Those results are summarized in the right panel of Fig. 3.7 where one clearly sees the crossover (in white) between the Lorentzian regime (in blue) and the Gaussian regime (in red). It occurs around $V_g \approx 1.92t + 0.34W$, not exactly when $\mu = V_g + E_c^-$, but in a region where the number of states available at μ in the nanowire becomes extremely small. To be precise, we point out that the values of η in the 2D colorplot are given with a precision of the order of 0.1. Hence, one cannot exclude that the white region corresponding to the crossover actually reduces into a single line $V_g^c(W)$. One could also conjecture the existence of a third kind of thermopower distribution (neither Lorentzian, nor Gaussian) associated to this critical value V_g^c. Our present numerical results do not allow to favor one scenario (sharp crossover) over the other (existence of a critical edge distribution).

Thermopower and Delay Times

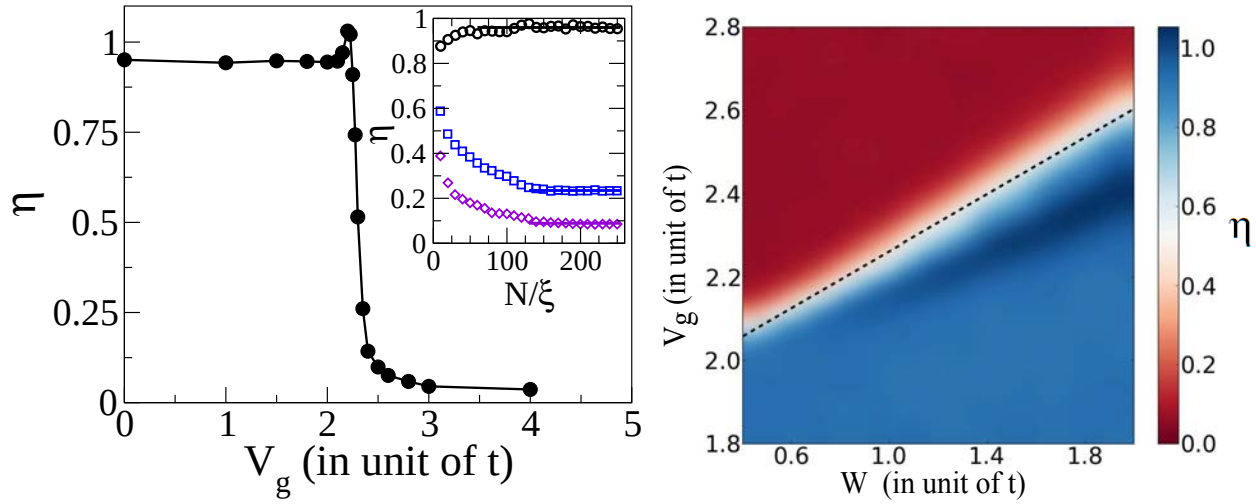
In quantum mechanical scattering problems, an important quantity is the *delay time* [51, 162, 188]. It measures the time spent by a particle inside an interaction region, and it is related to the energy derivative of the scattering matrix $\mathbf{S}(E)$. For a system described by a finite number N of channels, the N delay times are the eigenvalues $\tau_1, ..., \tau_N$ of the Wigner-Smith matrix [162]:

$$\mathcal{Q} = -i\hbar\, \mathbf{S}^\dagger \frac{d\mathbf{S}}{dE}. \tag{3.33}$$

The derivative d/dE is taken with respect to the energy of the incident particle (a conserved quantity).
In the regime of coherent transport considered in this chapter, the thermopower is also related to the energy derivative of $\mathbf{S}$ via the transmission amplitude $\mathcal{T}$. Within a statistical approach, often adopted when dealing with disordered systems, it seems possible to relate the distributions of the time delays and of the thermopower. This has already been done, for instance, for chaotic quantum dots [26, 27, 176]. In the case of one-dimensional random potentials, an analytical form of the Wigner time delay distribution has been derived by Texier [168]:

$$P(\tau) = \frac{\xi}{v\,\tau^2} \exp\left\{-\frac{\xi}{v\,\tau}\right\}, \tag{3.34}$$

where ξ is the localization length and v is the group velocity. In particular, v is equal to twice the wavevector ($v = 2k$) in their calculation based on a continuum model (a waveguide), but their result (Eq. (3.34)) has been generalized by Ossipov [129] to the discrete Anderson model, for which $v \sim \sin k$. The evolution of $P(\tau)$ as function of the incident electron energy E has also been studied by Texier [168] and Ramakrishna



(a) (b)

Figure 3.7: Left panel: in the inset, η parameter as a function of N/ξ for various gate voltages ($V_g = 1.9\,t$ (○), $2.35\,t$ (□) and $2.5\,t$ (◇)), at $\mu = 0$ and $W/t = 1$. The horizontal lines show the convergence of η at large N. The asymptotic values are plotted in the main panel as a function of V_g. Right panel: η parameter in the limit of large N as a function of V_g and W, at $\mu = 0$. Upon shifting the spectrum of the nanowire with V_g, the thermopower distribution moves from a Lorentzian distribution for $V_g \lesssim V_g^c$ ($\eta \approx 1$, blue) to a Gaussian distribution for $V_g \gtrsim V_g^c$ ($\eta \approx 0$, red), where $V_g^c = 1.92t + 0.34W$ (dashed line).

[144], showing deviations from Eq. (3.34) in the limit of low energy (at the band edge). All these works were based on one-dimensional disordered systems with *only one* open channel.
Motivated by these results, and with the purpose of understanding the link between the delay times and the thermopower in the case of 1D disordered nanowires, we investigated the delay time distributions $P(\tau_i)$ of our Anderson model. We checked numerically that the distributions $P(\tau_1)$ and $P(\tau_2)$ associated to the two open channels coincide in the strongly localized limit $L \gg \xi$, both being perfectly described by Eq. (3.34). This remains true as long as the energy is taken in the bulk of the NW impurity band. Furthermore, we observed that the shape of $P(\tau_i)$ was altered at the impurity band edge, but in a conflicting way with respect to Ramakrishna's predictions [144]: our approach is different since we assume a field effect transistor configuration with a gate voltage acting on the impurity energy levels inside the NW only, leaving the electrochemical potential in the electrodes unchanged, while he considers the electron energy E to be the same in the 1D lead *and* in the system. This led us to the conclusion that the occurrence of negative delay times observed in [144] is an artifact of having explored the band edges of the leads, in the regime of vanishing velocity. Albeit our preliminary results seemed promising in order to understand the relationship between the delay times and the thermopower distribution (especially at the band edges), we did not succeed in achieving a satisfactory comprehension of this issue. Hence, this part has not been finalized.

3.4 Figure of merit

Within linear response, the efficiency of steady state heat to work conversion (see section1.2.2) reads

$$\eta = \frac{\dot{W}}{\dot{Q}} = \frac{J^e \Delta\mu}{J^Q}, \tag{3.35}$$

where $J^Q > 0$ is the heat injected, while the numerator is the output power. One could maximize this expression with respect to $\Delta\mu$ to calculate the *maximum efficiency* [32] η_{max}, or rather maximize the output power $\dot{W} = J^e\Delta\mu$ and look then at the *efficiency at maximum power* [175] $\eta(\dot{W}_{max})$. As explained in chapter 1, both these two efficiencies can be expressed in terms of just one dimensionless parameter, the *figure of merit*[2] $Z_eT = (G\mathcal{S}^2/K^e)\,T$, as

$$\begin{aligned} \eta_{max} &= \eta_C \frac{\sqrt{Z_eT+1}-1}{\sqrt{Z_eT+1}+1} \\ \eta(P_{max}) &= \frac{\eta_C}{2}\frac{Z_eT}{Z_eT+2} \end{aligned} \tag{3.36}$$

η_C being the Carnot efficiency. In the low-temperature regime we investigate, the Wiedemann-Franz law is valid and thus the figure of merit can be written as

$$Z_eT = S^2\frac{GT}{K^e} = \frac{S^2}{\mathcal{L}_0}, \tag{3.37}$$

meaning that Z_eT is simply the square of the thermopower, up to a constant (the Lorenz number). In Fig. 3.8 we show the typical behavior of the figure of merit as a function of the gate voltage V_g and the size of the system N. Note that it is related to the dimensionless thermopower $\mathcal{S}$ studied in this work by $Z_eT = \mathcal{S}^2(\pi^2/3)(k_BT/t)^2$. The typical value Z_eT_0 has been defined by exponentiating the median of the distribution of the logarithm of Z_eT. We have chosen to do so because the distribution $P(Z_eT)$ exhibits a singularity[3] for $Z_eT \to 0$, while $P(\ln(Z_eT))$ turns out to be a more symmetric and smooth function. Not surprisingly, Fig. 3.8 shows that the enhancement of the typical thermopower around the edges reflects in a larger figure of merit. Moreover, being $\mathcal{S}_0 \propto \mathrm{d}[\ln\mathcal{T}]_0/\mathrm{d}E \propto N$, we expect $Z_eT_0 \propto N^2$, i.e. the longer the wire is, the better should be in terms of the figure of merit. Despite this, our theory which is only valid in a low-temperature limit cannot predict high performances: even supposing to be at the highest temperature ($\sim T_s$, see section 3.5) where Sommerfeld expansions can be made for describing the thermopower with Eq.(3.9), the region of largest Z_eT_0 in Fig. 3.8 corresponds to values of order $Z_eT_0 \lesssim 0.024$ at $k_BT/t = 5\times10^{-5}$. We emphasize that this low figure of merit characterizes the very low temperatures where Sommerfeld expansion

[2] In principle, the thermal conductance appearing in the definition of ZT should be the sum of an electronic and a phononic contribution, $K = K^e + K^{ph}$. Since here we deal with purely electronic transport, we shall refer to the *electronic contribution* to ZT.

[3] This can be seen by calculating $P(Z_eT)$ analytically from Eqs. (3.28) and (3.30): see the paragraph at the end of the section.

holds, but by no means this sets a physical limit to the efficiency.

On the other hand, if we were to look to the delivered (electric) output power, we would find that a large size would make it vanish, as the electrical conductance in this regime would be exponentially small. Indeed, looking at the power factor $\mathcal{Q} = S^2 G$, which is a measure of the maximum output power [175], we realize that the enhancement of S at the edge of the impurity band would not be enough to face the exponentially small values of G. Obviously, the optimization of the power factor $\mathcal{Q}$ for a single nanowire requires to take shorter sizes ($N \approx \xi$), while the optimization of the figure of merit $Z_e T$ requires to take long sizes ($N \gg \xi$). Moreover, because of the strong variation of the localization length as the energy varies inside the impurity band, the optimization of the power factor for a given size N requires to not be too close from the edges of the impurity band, contrary to the optimization of the efficiency. This illustrates the fact that a compromise has always to be found between efficiency and output power when thinking of practical thermoelectric applications.

Further comments on the thermal conductance

As mentioned in the text, to properly evaluate the efficiency of the thermoelectric conversion [32] in a nanowire, when defining $Z_e T$ one should add to the electronic contribution to the thermal conductance K^e the phononic one K^{ph}, in order to obtain the *full* figure of merit $ZT = GS^2T/(K^e + K^{ph})$. Below the temperature T_s, the electron contribution K^e to K is related to the electrical conductance G by the WF law. This gives $(\pi^2 k_B^2 T)/(3h)[2\exp\{-2N/\xi\}]$ for the typical value of K^e. The evaluation of the phonon contribution K^{ph} to the thermal conductance of a nanowire is beyond the scope of the used Anderson model, since *static* random site potentials are assumed. In one dimension, one can expect that K^{ph} should be also smaller than the thermal conductance quantum $(\pi^2 k_B^2 T)/(3h)$ which characterizes the ballistic phonon regime [132, 145]. However, it remains unlikely that K could be as small as G for giving a large figure of merit ZT in a single insulating nanowire at low temperature.

Analytical form of $\mathbf{P(Z_eT)}$

We sketch here a derivation of the analytical expression of the probability distribution of the figure of merit $P(Z_eT)$, valid in the coherent regime. We recall that the figure of merit $Z_eT = (GS^2/K^e)T$, when the W-F law is satisfied, can be written as

$$Z_eT = \frac{S^2}{\mathcal{L}_0},$$

where $K^e/GT = \mathcal{L}_0$ is the Lorenz number. Knowing the explicit form of the probability distribution of the thermopower $P(S)$ allows to infer $P(Z_eT)$.

Since $Z_eT \sim S^2$, with S being either positive or negative, the change of variable we would need to calculate $P(Z_eT)$ to do is not a bijection [17], and hence we should proceed in a careful way, separating the two situations corresponding to $S > 0$ and $S < 0$. First, let us

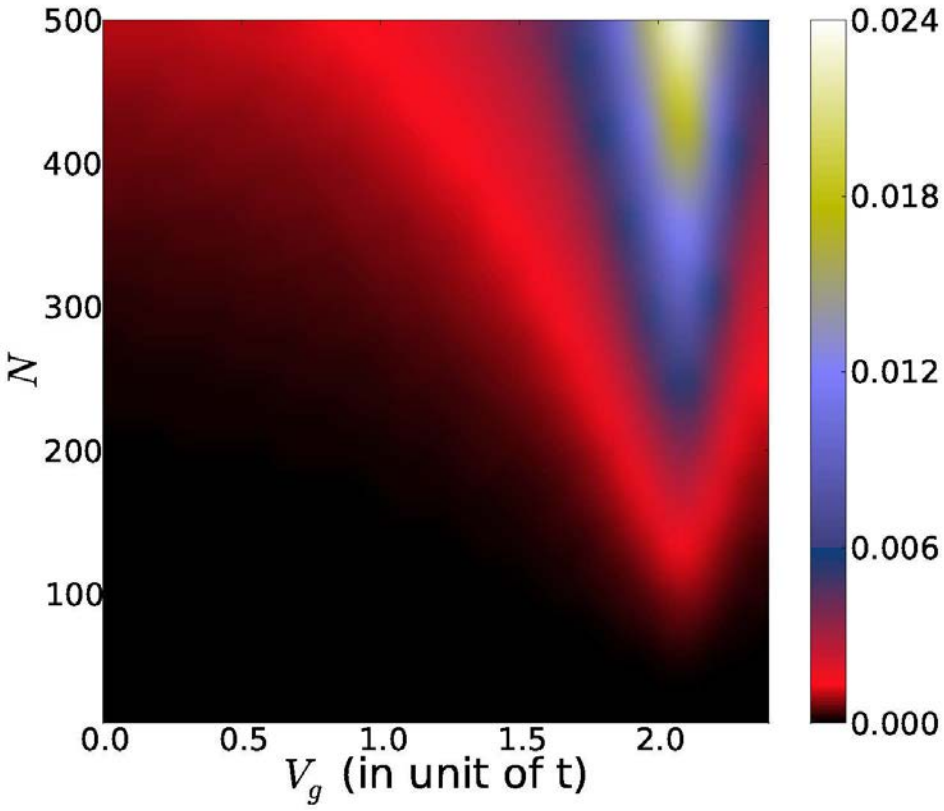


Figure 3.8: Typical value of the figure of merit $Z_eT = S^2/\mathcal{L}_0 = \pi^2/3(k_BT/t)^2S^2$ as a function of V_g and N, at $E_F = 0$, $W = t$, and for a very low temperature $k_BT/t = 5 \times 10^{-5}$ (which is nevertheless the highest temperature below which the Sommerfeld expansion is valid, for all $N \leq 500$ and $V_g \leq 2.5t$, within a tolerance of $\sim 2\%$, see section 3.5). Being proportional to S^2 in the regime of validity of the Wiedemann-Franz law, the largest typical figures of merit are obtained around the edge of the impurity band and for long wires.

define

$$P(Z_eT) = \int_{-\infty}^{+\infty} P(S)\delta(Z_eT - f(S))dS \tag{3.38}$$

where $f(S) = S^2/\mathcal{L}_0$. We now exploit a property of the Dirac delta function:

$$\delta[f(x)] = \frac{\delta(x)}{|f'(x)|},$$

which allows us to write

$$P(Z_eT) = \int_{-\infty}^{0} \frac{P(S)}{|2S/\mathcal{L}_0|}\delta[S - (-\sqrt{Z_eT\mathcal{L}_0})]dS + \int_{0}^{+\infty} \frac{P(S)}{|2S/\mathcal{L}_0|}\delta[S - (\sqrt{Z_eT\mathcal{L}_0})]dS. \tag{3.39}$$

Now, by substituting the explicit expression of $P(S)$, replacing $S = \pm\sqrt{Z_eT\mathcal{L}_0}$ (the sign depending on that of S) we end up with the desired result. In section 3.3.2 we showed that the probability distribution of the dimensionless thermopower $\mathcal{S}$ can be either Lorentzian (Eq. (3.28)) or Gaussian (Eq. (3.30)), depending on which region of the nanowire energy band is probed. We thus expect the two following forms for $P(Z_eT)$:

$$\begin{aligned} P_L(Z_eT) =& \frac{\tilde{\Gamma}}{2\pi}\frac{1}{\sqrt{Z_eT}}\left\{\frac{1}{\Gamma^2 + (\sqrt{Z_eT} + \aleph)^2} + \frac{1}{\tilde{\Gamma}^2 + (\sqrt{Z_eT} - \aleph)^2}\right\}, \\ P_G(Z_eT) =& \frac{1}{2\sqrt{2\pi}\tilde{\gamma}}\frac{1}{\sqrt{Z_eT}}\left\{e^{-\frac{(\sqrt{Z_eT}-\aleph)^2}{2\tilde{\gamma}^2}} + e^{-\frac{(\sqrt{Z_eT}+\aleph)^2}{2\tilde{\gamma}^2}}\right\}, \end{aligned} \tag{3.40}$$

where $\tilde{\Gamma} = \Gamma/\sqrt{\mathcal{L}_0}$, $\tilde{\gamma} = \gamma/\sqrt{\mathcal{L}_0}$ (Γ and γ being the same parameters appearing in Eqs. (3.28) and (3.30)) and $\aleph = S_0/\sqrt{\mathcal{L}_0}$.

We see from the above expressions that $P(Z_eT)$ exhibits a singularity for $Z_eT \to 0$, because of the $(\sqrt{Z_eT})^{-1}$ coming from the Jacobian of the change of variables $S \mapsto Z_eT$. This divergence is "cured" if the distribution of the logarithm of Z_eT, $P(\ln Z_eT)$, is considered. For this reason, we choose to define the typical value of the figure of merit Z_eT_0 studied in this chapter as the median of $P(\ln Z_eT)$.

3.5 Temperature range of validity of the Sommerfeld expansion

All the results discussed in this paper have been obtained in the low temperature limit, after expanding the thermoelectric coefficients to the lowest order in (k_BT/μ). To evaluate the temperature range of validity of this study, we have calculated the Lorenz number $\mathcal{L} = K^e/GT$ beyond the Sommerfeld expansion, and looked at its deviations from the WF law $\mathcal{L} = \mathcal{L}_0$ (see Eq. (3.10)): We have computed numerically the integrals (3.4) enterings Eqs. (3.5) and (3.6), deduced $\mathcal{L}(T)$ for increasing values of temperature, and then recorded the temperature T_s above which $\mathcal{L}(T)$ differs from $\mathcal{L}_0$ by a percentage ϵ, $\mathcal{L}(T_s) = \mathcal{L}_0(1 \pm \epsilon)$. We did it sample by sample and deduced the temperature T_s averaged over disorder configurations. Our results

are summarized in Fig. 3.9.

In panel (a), we analyze how sensitive T_s is to the precision ϵ on the Lorenz number $\mathcal{L}$. We find that T_s increases linearly with $\sqrt{\epsilon}$, $T_s(\epsilon) = T_s^* \sqrt{\epsilon}$, at least for $\epsilon \leq 2\%$. This is not surprising since the Sommerfeld expansion leads to $\mathcal{L} - \mathcal{L}_0 \propto (k_B T)^2$, when one does not stop the expansion to the leading order in temperature ($\mathcal{L} = \mathcal{L}_0$) but to the next order.

The main result of this section is shown in Fig. 3.9(b) where we have plotted the temperature T_s as a function of the gate voltage V_g, for chains of different lengths, at fixed $\mu = 0$ and $W = t$. As long as the Fermi energy probes the inside of the spectrum without approaching too much its edges ($|V_g| \leq 2t$), T_s is found to decrease as V_g is increased. More precisely, we find in the large N limit ($N \gtrsim 10\xi$) that $N k_B T_s \propto \nu_F^{-1}$ with a proportionality factor depending on ϵ (solid line in Fig. 3.9(b)). The temperature T_s is hence given by (a fraction) of the mean level spacing at μ in this region of the spectrum ($k_B T_s \propto \Delta_F$). When V_g is increased further, T_s reaches a minimum around $|V_g| \approx 2.1t$ and then increases sharply. Outside the spectrum, this increase of T_s with V_g is well understood as follows: Since in the tunnel barrier regime, the transmission behaves (upon neglecting the disorder effect) as $\mathcal{T} \propto \exp(-N\zeta)$, with $\zeta = \cosh^{-1}[|E - V_g|/(2t)]$, the temperature scale below which the Sommerfeld expansion of integrals (3.4) holds is given by $k_B T_s \propto [N \frac{\mathrm{d}\zeta}{\mathrm{d}E}\big|_\mu]^{-1}$, which yields $N k_B T_s \propto t\sqrt{[(\mu - V_g)/(2t)]^2 - 1}$. Our numerical results are in perfect agreement with this prediction (dashed line in Fig. 3.9(b)).

In Fig. 3.9(c), we investigate the behavior of T_s when the spectrum of the nanowire is either scanned by varying V_g at $\mu = 0$ or by varying μ at $V_g = 0$. We find that T_s only depends on the part of the impurity band which is probed at μ (*i.e.* the curves $T_s(V_g)$ and $T_s(\mu)$ are superimposed), except when μ approaches closely one edge of the conduction band of the leads. In that case, T_s turns out to drop fast to zero as it can be seen in Fig. 3.9(c) for the case of 1D leads ($T_s \to 0$ when $\mu \to 2t$). This means that the divergence of the *dimensionless* thermopower S observed in Fig. 3.4(a) is only valid in an infinitely small range of temperature above 0 K. It would be worth figuring out wether or not a singular behavior of the thermopower at the band edges of the conduction band persists at larger temperature.

Let us give finally an order of magnitude in Kelvin of the temperature scale T_s. In Fig. 3.9(b), the lowest T_s reached around $V_g \approx 2.1t$ is about $N k_B T_s^{min}/t \sim 0.001$ for $\epsilon = 0.004\%$. Asking for a precision of $\epsilon = 1\%$ on $\mathcal{L}$, we get $N k_B T_s^{min}/t \sim 0.016$. For a bismuth nanowire of length $1\,\mu$m with effective mass $m^* = 0.2 m_e$ (m_e electron mass) and lattice constant $a = 4.7\,$Å, the hopping term evaluates at $t = \hbar^2/(2m^* a^2) \sim 0.84\,$eV and hence, $T_s^{min} \sim 72\,$mK. The same calculation for a silicon nanowire of length $1\,\mu$m with $m^* = 0.2 m_e$ and $a =$5.4 Å yields $T_s^{min} \sim 64\,$mK. Those temperatures being commonly accessible in the

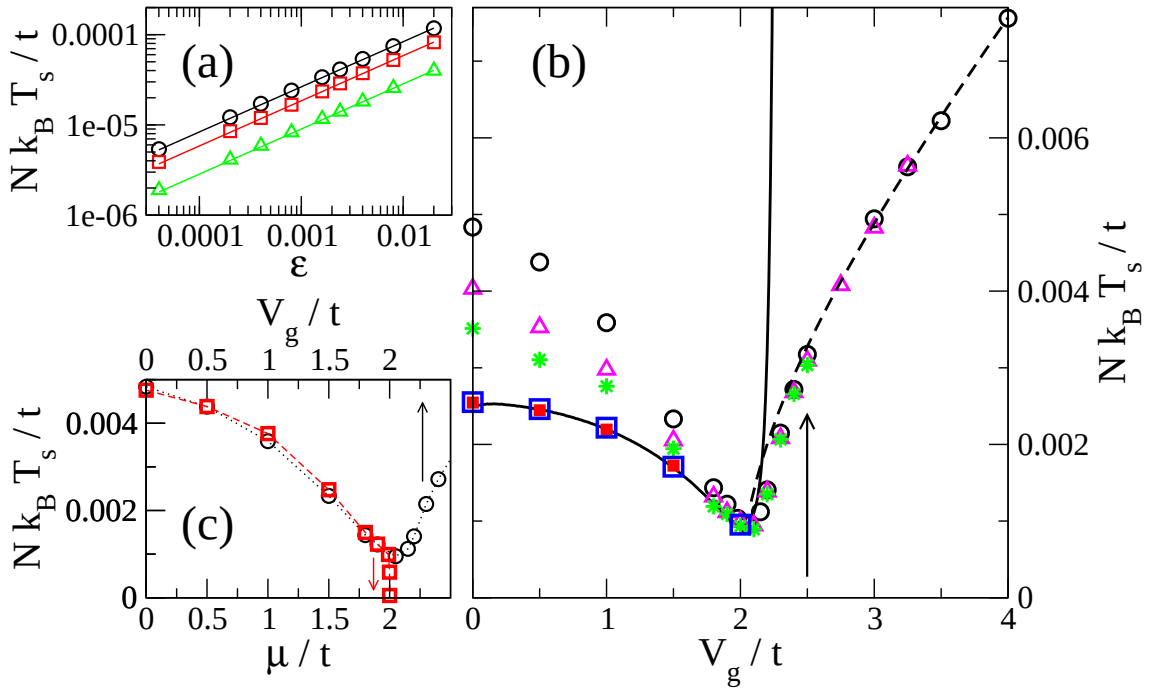


Figure 3.9: Temperature scale T_s above which the WF law breaks down. (a) Nk_BT_s/t as a function of the desired precision ϵ on $\mathcal{L}$. The critical temperatures were extracted for different values of V_g ($V_g = t$ (○), $1.5t$ (□), $2.02t$ (△)), with $\mu = 0$, $W/t = 1$, $N = 500$ and 1D leads. The solid lines are fits $T_s = T_s^*\sqrt{\epsilon}$. (b) Nk_BT_s/t (extracted for $\epsilon = 4 \times 10^{-5}$) as a function of V_g/t, for chains of different length ($N = 150$ (○), 300 (△), 500 (∗), 1500 (□) and 3000 (■)), with $\mu = 0$, $W/t = 1$ and 1D leads. The solid line is $4.04 \times 10^{-4}/(\nu_F t)$, the dashed line is $4.37 \times 10^{-3}\sqrt{(V_g/2t)^2 - 1}$ and the arrow indicates the position of the edge of the impurity band. (c) Nk_BT_s/t (extracted for $\epsilon = 4 \times 10^{-5}$) as a function of μ/t at $V_g = 0$ (□) and as a function V_g/t at $\mu = 0$ (○), with $N = 150$, $W/t = 1$ and 1D leads. Dashed lines are guides to the eye.

laboratories, the results discussed in this paper should be amenable to experimental checks.

3.6 Appendix

3.6.1 Recursive Green Function algorithm

The Recursive Green Function (RGF) algorithm [57, 100] is a technique which is used to compute numerically some or all elements of the Green function of big systems. The basic idea is to build up the full Green function *slice by slice*, instead of evaluating it in one step, thus allowing to greatly reduce the dimensions of the matrices that have to be inverted.

This algorithm is based on the Dyson equations:

$$\begin{aligned} \mathcal{G} &= \mathcal{G}^0 + \mathcal{G}^0 V \mathcal{G}, \\ \mathcal{G} &= \mathcal{G}^0 + \mathcal{G} V \mathcal{G}^0, \end{aligned} \tag{3.41}$$

where V is any perturbation which relates the Green function[4] $\mathcal{G}$ of a system with Hamiltonian $\mathcal{H} = \mathcal{H}^0 + V$ to the Green function $\mathcal{G}^0$ of the unperturbed system described by $\mathcal{H}^0$. For our purposes, referring to a discretized tight-binding model, V will be the hopping matrix between two adjacent slices, $\mathcal{G}^0$ the Green function of a semi-infinite region and an adjacent *isolated* slice, while $\mathcal{G}$ will be the Green function of the *coupled* system. The Green function of a semi-infinite lead can be calculated analytically [50, 57] (see also section 3.6.2); so, it is possible to start with an isolated lead and then add slice by slice until the opposite lead is reached. The resulting Green function contains al the information needed to calculate many physical quantities of interest, and in our particular case, it will be used to compute the transmission probability $\mathcal{T}$ through a disordered nanowire.

As explained in the text (section 3.2), $\mathcal{T}$ is given by the Fisher-Lee formula [43] Eq. (3.13):

$$\mathcal{T}(E) = \mathrm{Tr}[\Gamma_L(E)\mathcal{G}(E)\Gamma_R(E)\mathcal{G}^\dagger(E)], \tag{3.42}$$

where $\Gamma_\alpha = i(\Sigma_\alpha - \Sigma_\alpha^\dagger)$ $(\alpha = L, R)$ is the broadening matrix quantifying the strength of the coupling of the system to the reservoir α, expressed in terms of the corresponding self-energies Σ_α. As we suppose the system to be connected to the reservoirs via semi-infinite perfect leads, the self-energies are

$$\Sigma_\alpha = \tau_\alpha^\dagger \, g_\alpha^R \, \tau_\alpha, \tag{3.43}$$

g_α^R being the Green function of the isolated lead α and τ_α the coupling matrix between the system and the leads [43]. Recalling that our system is a 1D lattice of size N described by the tight-binding Hamiltonian (3.11), this coupling concerns only the first and the last sites of the chain. Hence, the self-energies Σ_α will be matrices in which all but the $(1,1)$ element (for $\alpha = L$) or the (N,N) element (for $\alpha = R$) are zero. As a consequence, in Eq. (3.13) the only element of the Green function that matters when computing the trace is $\mathcal{G}_{1N}$ (and its conjugate transpose, $\mathcal{G}_{1N}^\dagger$). This is the quantity that we need, and the recursive procedure to calculate it is outlined here.

We follow the notation of Lassl *et al.* [100], and we call $\mathcal{G}^{S(n)}$ the Green function of an isolated slice n, and $\mathcal{G}^{L(n)}$ that of the left semi-infinite region starting at slice n. Finally, we denote $\mathcal{G}$ the full Green function of the complete (infinite) system.

In order to couple the Green function $\mathcal{G}^{S(n)}$ of the isolated slice n to the Green function $\mathcal{G}^{L(n-1)}$ that covers all lattice sites to the left of $(n-1)$, we use the first of the Dyson equations Eqs. (3.41):

$$\langle n|\mathcal{G}^{L(n)}|n\rangle = \langle n|\left(\mathcal{G}^{S(n)} + \mathcal{G}^{L(n-1)}\right)|n\rangle + \langle n|\left(\mathcal{G}^{S(n)} + \mathcal{G}^{L(n-1)}\right) V \mathcal{G}^{L(n)}|n\rangle. \tag{3.44}$$

[4] Since we are dealing with retarded Green functions only, we omit the usual label "r" in writing $\mathcal{G}$

By exploiting the fact that $\mathcal{G}^{L(n-1)}$ is decoupled from the n-th slice, we obtain

$$\langle n|\mathcal{G}^{L(n)}|n\rangle = \langle n|\left(\mathcal{G}^{S(n)}\right)|n\rangle + \sum_{a,b}\langle n|\mathcal{G}^{S(n)}|a\rangle\langle a|V|b\rangle\langle b|\mathcal{G}^{L(n)}|n\rangle. \tag{3.45}$$

Since $\mathcal{G}^{S(n)}$ has only nonzero matrix elements with slice n, we get the constraint $a = n$. By the same token, as V couples only adjacent slices, b is restricted to the values $n \pm 1$ only. This leads to:

$$\mathcal{G}^{L(n)}_{n,n} = \mathcal{G}^{S(n)}_{n,n} + \mathcal{G}^{S(n)}_{n,n} V_{n,n-1}\mathcal{G}^{L(n)}_{n-1,n}, \tag{3.46}$$

where $\mathcal{G}_{n,m} = \langle n|\mathcal{G}|m\rangle$ is the submatrix of $\mathcal{G}$ related to the slices n and m. The Green function $\mathcal{G}^{L(n)}_{n-1,n}$ appearing in Eq. (3.46) can be calculated using Dyson equation in a completely analogous way, giving

$$\mathcal{G}^{L(n)}_{n-1,n} = \mathcal{G}^{L(n-1)}_{n-1,n-1} V_{n-1,n}\mathcal{G}^{L(n)}_{n,n}. \tag{3.47}$$

This result, once substituted back in Eq. (3.46), allows to solve for $\mathcal{G}^{L(n)}_{n,n}$:

$$\mathcal{G}^{L(n)}_{n,n} = \left[(E - \mathcal{H}_{n,n}) - V_{n,n-1}\mathcal{G}^{L(n-1)}_{n-1,n-1}V_{n-1,n}\right]^{-1}, \tag{3.48}$$

where we used $\mathcal{G}^{S(n)}_{n,n} = (E - \mathcal{H}_{n,n})^{-1}$. This relation allows to calculate the Green function covering all lattice sites to the right of slice n from the Green function to the left of $(n-1)$.

Using the second of the Dyson equations, we can also calculate the submatrix $\langle 1|\mathcal{G}^{L(n)}|n\rangle$ in an analogous way, and the result is:

$$\mathcal{G}^{L(n)}_{1,n} = \mathcal{G}^{L(n-1)}_{1,n-1} V_{n-1,n}\mathcal{G}^{L(n)}_{n,n}. \tag{3.49}$$

Eqs. (3.48) and (3.49) define the recursion procedure. Once the elements $\mathcal{H}_{nn}$ are given (they are the disorder potentials ϵ_i of Eq. (3.11)), the initial condition is the Green function at the first slice[5]:

$$\mathcal{G}^{L(1)}_{1,1} = \frac{1}{E - \mathcal{H}_{1,1} - \sigma_L(E)}, \tag{3.50}$$

where $\sigma_L(E)$ is the only nonzero element of the self-energy of the left lead Σ_L. Then, Eqs. (3.48) and (3.49) are iterated until the rightmost end of the system is reached. At the N-th step, the self-energy of the right lead is also taken into account, in such a way that the surface Green function computed at this stage becomes the *complete* surface Green function $\mathcal{G}_{NN}$:

$$\mathcal{G}_{NN} = \frac{1}{E - \mathcal{H}_{N,N} - V_{N,N-1}\mathcal{G}^{L(N-1)}_{N-1,N-1}V_{N-1,N} - \sigma_R(E)}. \tag{3.51}$$

Assuming $V_{n,n+1} \equiv t$ for the hopping energies ($n = 1 \ldots N-1$), and using Eq.3.49, we can finally write explicitly the (1,N) element $\mathcal{G}_{1N}$ that we need to compute the transmission:

$$\mathcal{G}_{1N} = \prod_{n=1}^{N} t\,\mathcal{G}^{L(n)}_{1,n} \tag{3.52}$$

The recursion procedure is sketched in Fig. 3.10.

[5]note that, being the system purely 1D, there is the additional simplification that "slices" reduce to simple "sites". All the submatrices $\mathcal{G}^{L(n)}_{n,m}$ are thus just complex numbers.

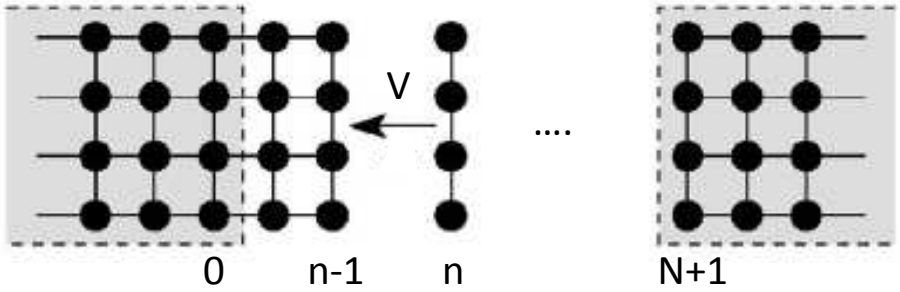


Figure 3.10: Recursive Green Function (RGF) algorithm: the full Green function is constructed by coupling single isolated slices starting from one of the leads (grey regions).

Extension of the RGF method to calculate the thermopower

We have implemented the recursive method reviewed in this section in order to calculate the thermopower of a 1D disordered nanowire. This allows us to compute at the same time the transmission coefficient *and* the thermopower for a given NW realization, without need to perform the derivative of the former numerically. Our calculation is *exact* in the sense that at each recursive step it only requires the evaluation of the derivative of the Green function $\mathcal{G}_{n,n}^{L(n)}$, which can be done analytically.

We recall that dealing with a purely 1D system allows to rewrite the transmission amplitude from Eq. (3.13) in a simple way, in terms of complex numbers, rather than matrices:

$$\mathcal{T}(E) = \Gamma^2(E)\,\mathcal{G}_{1N}\,\mathcal{G}_{1N}^{\dagger}, \tag{3.53}$$

where $\Gamma(E)$ is the only non-zero element of the broadening matrices Γ_L and Γ_R, and $\mathcal{G}_{1N}^{\dagger}$ is nothing but the complex conjugate of $\mathcal{G}_{1N}$. Using Eq. (3.52), the logarithm of $\mathcal{T}$ can be written as

$$\ln\mathcal{T} = 2\ln\Gamma + \ln\prod_{n=1}^{N}\mathcal{G}_{nn} + \ln\prod_{n=1}^{N}\mathcal{G}_{nn}^{\dagger} = 2\ln\Gamma + \sum_{n=1}^{N}\ln\mathcal{G}_{nn} + \sum_{n=1}^{N}\ln\mathcal{G}_{nn}^{\dagger}, \tag{3.54}$$

where we have all the energy dependences and the superscript "$L(n)$" of the Green functions have been dropped for the sake of brevity. We can compute the energy derivative of $\ln\mathcal{T}$:

$$\frac{d\ln\mathcal{T}(E)}{dE} = 2\frac{\dot{\Gamma}}{\Gamma} + \sum_{n=1}^{N}\frac{\dot{\mathcal{G}}_{nn}}{\mathcal{G}_{nn}} + \sum_{n=1}^{N}\frac{\dot{\mathcal{G}}_{nn}^{\dagger}}{\mathcal{G}_{nn}^{\dagger}}, \tag{3.55}$$

where the dot $\dot{}$ denotes the derivative. In conclusion, once we have all the $\mathcal{G}_{nn}$'s and their energy derivatives, we can compute $d\ln\mathcal{T}/dE$, and hence the thermopowers. Recalling Eqs. (3.48), (3.50) and (3.51), these are given by the following sets of equations:

$$\begin{cases} \mathcal{G}_{1,1} = [E - \mathcal{H}_{1,1} - \sigma_L]^{-1} \\ \mathcal{G}_{n,n} = [E - \mathcal{H}_{n,n} - t^2\mathcal{G}_{n-1,n-1}]^{-1} \\ \mathcal{G}_{NN} = [E - \mathcal{H}_{N,N} - t^2\mathcal{G}_{N-1,N-1} - \sigma_R]^{-1} \end{cases} \rightarrow \begin{cases} \dot{\mathcal{G}}_{1,1} = (-1 + \dot{\sigma}_L)\,\mathcal{G}_{1,1}^2 \\ \dot{\mathcal{G}}_{n,n} = (-1 + t^2\dot{\mathcal{G}}_{n-1,n-1})\,\mathcal{G}_{n,n}^2 \\ \dot{\mathcal{G}}_{NN} = (-1 + t^2\dot{\mathcal{G}}_{n-1,n-1} + \dot{\sigma}_R)\,\mathcal{G}_{N,N}^2 \end{cases}.$$

3.6.2 Self-energy of the 2D leads

We give here the expression of the retarded self-energy of a 2D lead (made of a semi-infinite square lattice with hopping term t) connected at one site (with coupling t) to a nanowire of N sites length. It is a $N \times N$ matrix Σ with only one non-zero component denoted σ. To calculate σ, we calculate first the retarded Green function of an infinite square lattice [50] and then deduce with the method of mirror images the retarded Green function of the semi-infinite 2D lead [115], that we evaluate at the site in the lead coupled to the nanowire to get σ. Analytic continuations of special functions are also required, they can be found for example in Ref. [119]. Introducing the notation $z = E/(4t)$, we find for $\sigma = \mathrm{Re}(\sigma) + i\,\mathrm{Im}(\sigma)$

$$\mathrm{Re}(\sigma) = tz \pm \frac{2t}{\pi}\left[\mathcal{E}(z^2) - (1-z^2)\mathcal{K}(z^2)\right] \tag{3.56}$$

$$\mathrm{Im}(\sigma) = \frac{2t}{\pi}\left[-\mathcal{E}(1-z^2) + z^2\mathcal{K}(1-z^2)\right] \tag{3.57}$$

with a + sign in Eq. (3.56) when $-4t \leq E \leq 0$ and a − sign when $0 \leq E \leq 4t$. If the energy E is outside the conduction band of the lead ($|E| > 4t$), we get

$$\sigma = tz\left[1 - \frac{2}{\pi}\mathcal{E}\left(\frac{1}{z^2}\right)\right]. \tag{3.58}$$

In the three above equations, $\mathcal{K}$ and $\mathcal{E}$ stand for the complete elliptic integrals of the first and second kind respectively. They are defined as

$$\mathcal{K}(z) = \int_0^{\pi/2} d\phi\,[1 - z\sin^2\phi]^{-1/2} \tag{3.59}$$

$$\mathcal{E}(z) = \int_0^{\pi/2} d\phi\,[1 - z\sin^2\phi]^{1/2}. \tag{3.60}$$

3.6.3 Thermopower of a clean tunnel barrier

In this appendix, we derive Eq. (3.27). We consider a clean nanowire with on-site potentials V_g, connected via its extreme sites 1 and N to two identical semi-infinite leads. In order to investigate the tunnel barrier regime, we assume that the energy E of the incoming electrons lies outside the spectrum $[-2t, 2t]$ of the nanowire. Let us say that $E \geq V_g + 2t$ to fix the ideas. In the basis $\{1, N, 2, ..., N-2\}$, the retarded Green function $G = [E - \mathcal{H} - \Sigma_L - \Sigma_R]^{-1}$ of the system reads

$$G = \begin{pmatrix} A & B \\ \tilde{B} & C \end{pmatrix}^{-1} \tag{3.61}$$

where *(i)* $A = (E - V_g - \sigma)\mathbf{1_2}$ ($\mathbf{1_2}$ being the 2×2 identity matrix and σ the non-vanishing element of Σ_L and Σ_R), *(ii)* B [$\tilde{B}$] is a $2\times(N-2)$ [$(N-2)\times 2$] matrix with all zero components except two equal to t coupling the sites 1 and N to their neighbors 2 and $N-1$, and *(iii)* C is a $(N-2)\times(N-2)$ symmetric tridiagonal matrix with all diagonal elements equal to $E - V_g$

and all elements on the first diagonals below and above the main one equal to t. Using the Fisher-Lee formula (3.13), we write the transmission function $\mathcal{T}(E)$ as

$$\mathcal{T}(E) = \mathrm{Tr}\left[\begin{pmatrix}\gamma & 0\\ 0 & 0\end{pmatrix} G_A \begin{pmatrix}0 & 0\\ 0 & \gamma\end{pmatrix} G_A^{\dagger}\right] = \gamma^2 |G_A^{(1N)}|^2 \tag{3.62}$$

where G_A is the 2×2 submatrix in the top left-hand corner of G, $G_A^{(1N)}$ its top right element and $\gamma = -2\mathrm{Im}(\sigma)$. To calculate G_A, we first notice that

$$G_A = (A - BC^{-1}\tilde{B})^{-1} = (A - t^2 C_{\square}^{-1})^{-1} \tag{3.63}$$

where $C_{\square}^{-1}$ is a 2×2 submatrix of C^{-1} made up of the four elements located at its four corners. Second, we make use of Ref. [78] for computing the inverse of the symmetric tridiagonal matrix C. We get

$$C_{\square}^{-1} = \begin{pmatrix}\alpha & \beta\\ \beta & \alpha\end{pmatrix} \tag{3.64}$$

with

$$\alpha = -\frac{\cosh(\zeta)\cosh((N-2)\zeta)}{t\sinh(\zeta)\sinh((N-1)\zeta)} \tag{3.65}$$

$$\beta = -\frac{\cosh(2\zeta) + (-1)^{N-1}}{2t\sinh(\zeta)\sinh((N-1)\zeta)} \tag{3.66}$$

and $\zeta = \cosh^{-1}[(E - V_g)/(2t)]$. Plugging Eqs. (3.63-3.66) into Eq. (3.62), we deduce the exact transmission function $\mathcal{T}(E)$, and hence the thermopower S defined by Eq. (3.14). An expansion at large N yields $\mathcal{T} \propto \exp(-2N\zeta)$ (as expected for a tunnel barrier) and the expression (3.27) for the thermopower. The same demonstration can be made for the energy range $E \leq V_g - 2t$.

Chapter 4

Activated Regime

Contents

Summary of chapter 4 . . . . . **74**

4.1 Model and method **75**

4.1.1 Transport mechanisms and temperature scales 75

4.1.2 Formulation in terms of a random resistor network 80

4.1.3 Anderson model for the localized states 82

4.2 Electrical Conductance **83**

4.2.1 Background 83

4.2.2 Numerical results 85

4.3 Thermopower **86**

4.3.1 Background 86

4.3.2 Numerical results 88

4.3.3 Limitations of the present approach 92

4.4 Appendix **93**

4.4.1 Thermodynamics of the three-terminal setup 93

4.4.2 Solution of the random resistor network 95

4.4.3 Calculation of the hopping probability 96

Summary of chapter 4

We study the thermopower of a disordered nanowire in the field effect transistor device configuration, in the inelastic activated regime. We consider the case where charge transport is thermally assisted by phonons (Mott Variable Range Hopping (VRH) regime). For this purpose, we use the Miller-Abrahams random resistor network model as recently adapted by Jiang *et al.* for thermoelectric transport. This approach previously used to study the bulk of the nanowire impurity band is extended for studying its edges.

First, we introduce the model and methods employed in section 4.1. A certain care is devoted to provide a qualitative explanation of the different transport mechanisms taking place at various temperatures as a function of the applied gate voltage V_g. The model we consider is essentially the same introduced in the previous chapter, except that here a source of phonons which can exchange energy with electrons is needed for the VRH regime to take place.

In section 4.2 we discuss the nanowire electrical conductance. We check that the higher temperature allows for a largely enhanced conductance of electrons (Mott law), despite the fact of being in the localized regime. Even if the nanowire we consider operates in linear response with respect to the applied bias, a *finite* width of energies (the Mott *hopping energy* Δ) turns out to be relevant for electronic transport.

This has profound implications also on the thermopower, as it allows to exploit asymmetries of the density of states, a fact of leading importance for thermoelectric conversion. As a consequence, we show that huge values of the typical thermopower (of the order of $1\,\mathrm{mV\,K^{-1}}$) can be attained when the nanowire band edges are probed. Extending an approach that was first introduced by Zvyagin [200], we provide a qualitative explanation of its behavior around the band edge, by emphasizing a non-trivial dependence on temperature and on gate voltage. All this is the content of section 4.3.

Finally, in the appendix we gather various technical details concerning some thermodynamic considerations, the numerical scheme adopted to solve the random resistor network, and an extension of the Miller-Abrahams approach to deal with states localized over different spatial extents, which is the case when band edge transport is considered.

4.1 Model and method

The general setup we have in mind is sketched in Fig. 4.1: A disordered semiconductor nanowire (green) connected to two metallic contacts (yellow) and deposited on an insulating substrate (blue). A heater (gray) and an applied bias voltage can induce a temperature and an electrochemical potential difference between the two contacts. A back gate (dark gray), placed below the substrate, allows to shift the impurity band of the nanowire by means of a gate voltage. This way, the transport of charges and heat can be studied when the Fermi potential of the setup probes either the bulk of the band or its edges. Fig. 4.1 depicts the more commonly used field effect transistor (FET) configuration [28]. Another possibility would be to cover only the nanowire with a top gate (see e.g. Ref. [138]). Putting a back gate is easier, but large gate voltages (a few hundreds volts) are necessary for shifting the impurity band, while few volts are sufficient if one uses a top gate. The nanowire itself could be (i) lightly doped, with electrons localized around distant impurity states, or (ii) highly doped but strongly depleted, or (iii) made of an amorphous semiconductor. A crucial feature of such wires is that their length L should be much longer than the localization length ξ of their electron states, such that their electrical resistance becomes exponentially large when the temperature is lowered below a few Kelvin degrees. A crude modelling of such setup is sketched in Fig. 4.2: A purely 1D disordered chain with $L \gg \xi$, connected to two electron reservoirs and to a phonon bath (represented by the substrate), and coupled to a gate used to modulate its carrier density.

We assume each state i is either empty, or occupied by a single electron, but cannot be doubly occupied owing to a strong on-site Coulomb repulsion [3]. The energy levels E_i of the localized states are distributed within a band of width $2E_B$ and $\nu(E)$ denotes their density of states (DOS) per unit length at energy E. They can be shifted as a whole by an external gate voltage V_g. The nanowire is attached at its ends to two metallic contacts held at electrochemical potentials μ_L and μ_R and temperatures T_L and T_R. It is also coupled to a phonon bath at temperature T_{ph} which provides the energy for electrons to hop between localized states. We focus on the situation in which the temperature T is the same in all reservoirs ($T_L = T_R = T_{ph} \equiv T$) and consider linear response, assuming the difference in electrochemical potentials between left and right leads to be small ($\mu_L = \mu + \delta\mu \gtrsim \mu_R \equiv \mu$).

4.1.1 Transport mechanisms and temperature scales

Transport through the nanowire happens as follows. Since there is a continuum of available states in the leads, we assume that charge carriers, let us say electrons, enter or leave the nanowire by elastic tunneling processes, without absorbing or emitting phonons[1]. Inside the

[1] Phonon absorption and emission in the electrodes could be straightforwardly taken into account. However, it should not add any new physics and we neglect it.

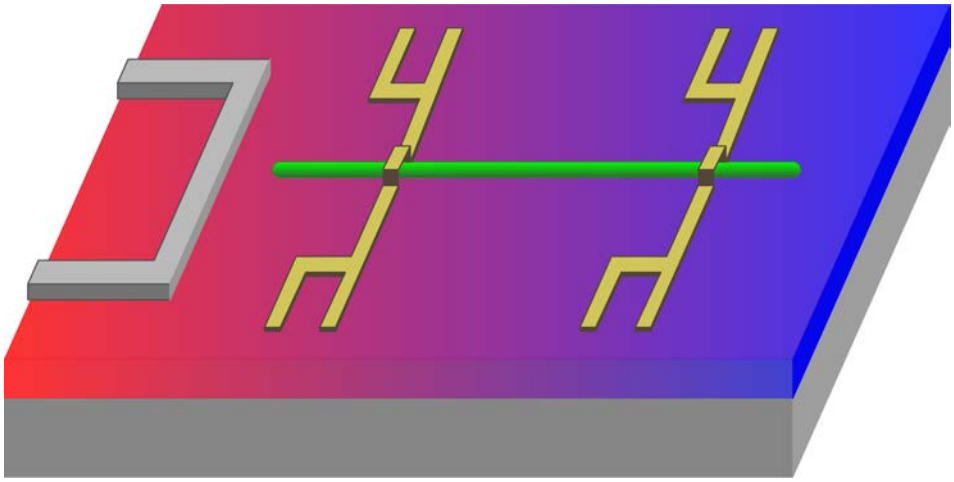


Figure 4.1: Nanowire in the field effect transistor (FET) device configuration: The nanowire (green) with two metal contacts (yellow) is deposited on an insulating substrate (blue). A heater (gray) makes the left side of the setup hotter (red) than its right side. A back gate (dark gray) is put below the substrate.

nanowire they have the possibility to hop either to localized states at higher energies by absorbing phonons, or to localized states at lower energies by emitting them. Determining precisely the favoured electronic paths is a complicated task. The proper way to tackle this issue is to map the hopping model to an equivalent random resistor network [113] and then to reduce it to a percolation problem [3]. Such microscopic approaches are needed for giving precise quantitative predictions, but Mott's original argument [120, 121] gives the main ideas: Assuming the localization lengths and the density of states to be constant within a certain window of energies Δ to be explored ($\xi_i \approx \xi$, $\nu(E) \approx \nu$), the electron transfer from one localized state to another separated by a distance x and an energy $\delta E \propto 1/(\nu x^D)$ ($D = 1$ for us) results from a competition between the elastic tunneling probability $\propto \exp -(2x/\xi)$ to do a hop of length x in space and the Boltzmann probability ($\propto \exp -(\delta E/k_B T)$) to do a hop of δE in energy. Short hops are favoured by the former but are too energy-greedy for the latter, since localized states close in space are far in energy. This competition gives rise to an optimal electron hopping length, the Mott hopping length, which reads

$$L_M = \sqrt{\frac{\xi}{2\nu k_B T}} \tag{4.1}$$

in one dimension. L_M is a decreasing function of the temperature, which allows us to define two characteristic temperature scales: the *activation temperature*

$$k_B T_x = \frac{\xi}{2\nu L^2} \tag{4.2}$$

at which $L_M \simeq L$ and the *Mott temperature*

$$k_B T_M = \frac{2}{\nu \xi}, \tag{4.3}$$

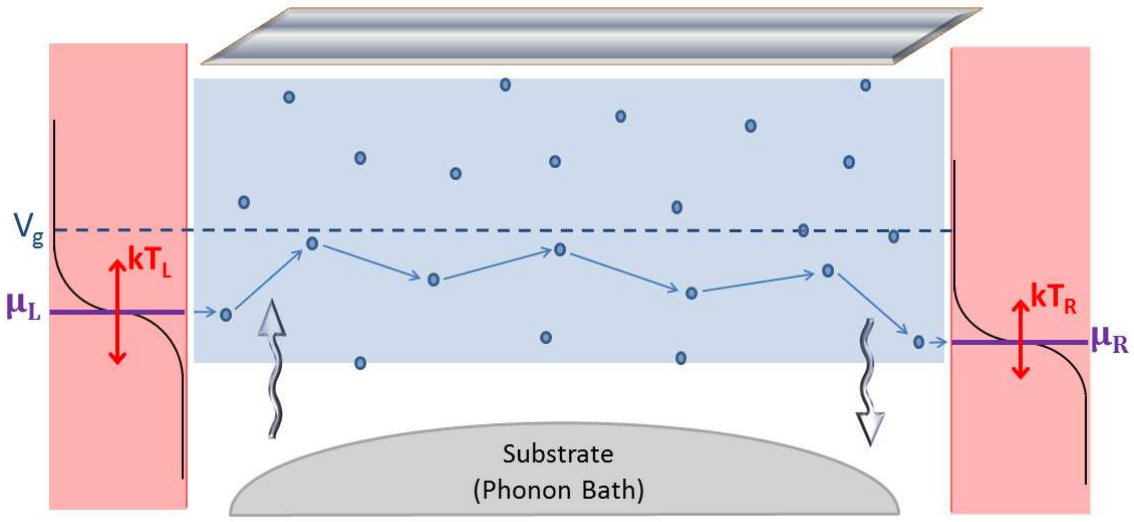


Figure 4.2: Variable Range Hopping (VRH) transport for a disordered nanowire in a FET configuration: Two ohmic contacts are connected by a 1D disordered chain of length L where the electron states are localized. The contacts are thermalized at temperatures $T_L(T_R)$ with electrochemical potentials $\mu_L(\mu_R)$ respectively. The electronic states (blue dots of coordinates (x_i, E_i)) are localized in regions of size $\xi_i \ll L$. Their centres x_i are taken at random along the chain, with energies E_i distributed inside an impurity band of width $2E_B$ (shaded light blue region). A top gate (in gray at the top of the figure) allows to shift the impurity band. The gate potential V_g sets the center of the band (dashed line). In linear response, the carriers are injected from the left (right) contacts inside the electronic states localized near the edges of the chain, in a window of energies of order $k_B T_L(k_B T_R)$ around $\mu_L(\mu_R)$. Inside the chain, the carrier propagation is thermally assisted by phonons (wavy arrows), which allow a carrier to do hops of variable range between localized states at different energies. The phonon bath at temperature T_{ph} is represented by the substrate upon which the chain is deposited.

at which $L_M \simeq \xi$. At low temperatures $T < T_x$, L_M exceeds the system size and transport through the nanowire occurs via elastic coherent tunneling (see Ref. [19]). Above T_x, transport becomes inelastic, and remains coherent at scales smaller than L_M only. The regime of intermediate temperature $T_x < T < T_M$ is known as the variable-range hopping (VRH) regime. As sketched in Fig. 4.2, electronic transport in this regime is achieved via several jumps of length $\approx L_M$ (with $\xi < L_M < L$). As it can be proven using a microscopic approach based on random resistor networks and percolation theory [3, 200, 201], the VRH conductance can be simply expressed in terms either of L_M, T_M or the hopping energy Δ,

$$G \propto \exp\left\{-\frac{2L_M}{\xi}\right\} = \exp\left\{-\sqrt{\frac{T_M}{T}}\right\} = \exp\left\{-\frac{\Delta}{k_B T}\right\}, \tag{4.4}$$

where (it will be of prime importance later on)

$$\Delta = k_B\sqrt{T_M T} \tag{4.5}$$

defines the width of the energy interval around μ inside which are located all states contributing to transport. Let us underline that if $T_x < T \ll T_M$, Δ becomes much larger than $k_B T$, the relevant energy interval for transport in the coherent regime ($T < T_x$). At large temperatures $T > T_M$, L_M becomes of the order of or even smaller than the localization length ξ, and one enters the nearest-neighbour hopping (NNH) regime where transport is simply activated between nearest neighbour localized states. Actually, in 1D, the crossover from VRH to simply activated transport is expected to take place at temperatures lower than T_M. The reason is the presence of highly resistive regions in energy-position space, where electrons cannot find empty states at distances $\sim \Delta, L_M$. These regions can be circumvented in 2D or 3D but not in 1D, where they behave as "breaks" in the percolating path: electrons are topologically constraint to cross them by thermal activation, making the temperature dependence of the overall resistance simply activated [95, 143]. The critical temperature T_a that marks the onset of this simply activated behaviour is given implicitly by the relation [158]

$$L = \frac{\xi}{2}\sqrt{\frac{T_M}{2T_a}}\exp\left\{\frac{T_M}{2T_a}\right\}. \tag{4.6}$$

Below T_a, the probability of having such breaks in the nanowire can be neglected.

In Fig. 4.3 the temperatures T_x, T_M and T_a are given as a function of the gate voltage V_g, taking for the disordered nanowire an Anderson model where the L random site potentials are shifted[2] by V_g, the electrochemical potential μ being fixed in the reservoirs.

Still following Mott's approach, we consider $\xi_i \approx \xi$ and $\nu(E) \approx \nu$ (both evaluated at μ), thus neglecting their variations within Δ. The shape of the curves is a consequence of the

[2]We assume the gate acting only along the nanowire, which corresponds to using a top gate. A FET configuration with a back gate should behave similarly, the field effect in the metallic contacts being negligible.

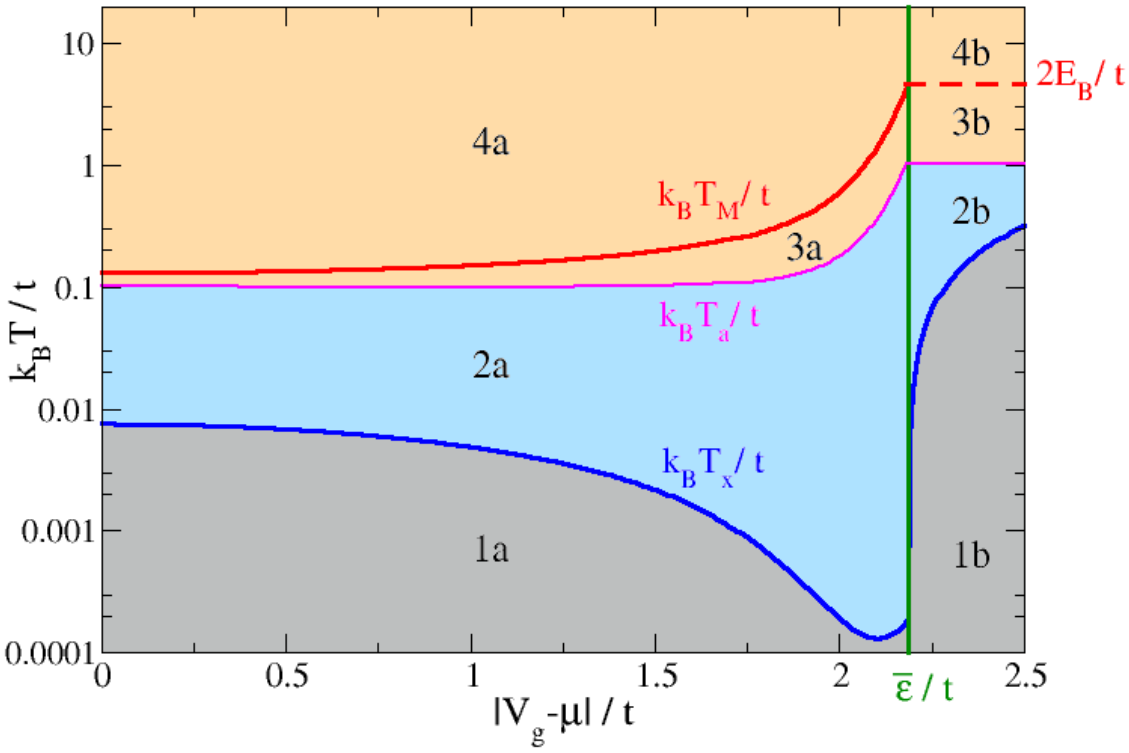


Figure 4.3: Gate dependence of the temperature scales separating the different regimes of electronic transport in a disordered nanowire: Elastic regime (gray), inelastic VRH regime (blue) and simply activated regime (red)). By varying the gate voltage V_g, one scans the impurity band, starting from its center (when $V_g - \mu = 0$) towards its edges (approximately for $|V_g - \mu| = \bar{\epsilon}$) and ending up eventually outside the band (when $|V_g - \mu| \gtrsim \bar{\epsilon}$). The scales T_x, T_a and T_M defined in Sec. 4.1.1 have been plotted for the Anderson model introduced in Sec. 4.1.3, with $W = t$ and $L = 200$.

explicite energy dependence of the localization length ξ and of the DOS ν, which is detailed in Sec. 4.1.3. Approaching an impurity band edge ($\pm E_B$), both ξ and ν decrease rapidly, inducing a large increase of T_M and T_a that must be eventually cut-off when T_M exceeds the bandwidth $2E_B$. Indeed, when $T \to T_M = 2E_B$, $\Delta \to 2E_B$ and the range of states available for hopping transport reaches its limit. More explicitly, we estimate this to happen at an energy scale $|\mu - V_g| \approx \bar{\epsilon}$ (see Fig. 4.3).

When Eqs. (4.2), (4.3), and (4.6) cease to be valid, we will use a simplified model introduced by Zvyagin for estimating the temperatures T_x, T_M and T_a. In this model, the DOS drops abruptly at $\bar{\epsilon}$ ($\nu(E) \approx \theta(|E| - \bar{\epsilon})$). This yields that, when $|\mu - V_g| \gtrsim \bar{\epsilon}$, T_M and T_a do not vary anymore and keep their values at $\bar{\epsilon}$, while the activation temperature T_x gives the energy that electrons need in order to jump inside the band: $k_B T_x \approx |\mu - V_g| - \bar{\epsilon}$. We will show later that the edge behaviours numerically obtained using the Anderson model are well described by this simplified model.

As a summary, let us now discuss the regimes of electronic transport corresponding to each region of the temperature diagram established in Fig. 4.3. Standard VRH regime takes place in region (2a), at intermediate temperatures, when μ lies inside the impurity band. According to Mott law in 1D, the average logarithm of the resistance behaves there as $(T_M/T)^{1/2}$. In Sec. 4.2, we will see how this statement has to be revisited in the vicinity of the band edges, and how to take into account the energy dependency of ξ. At higher temperatures, transport is simply activated (the temperature dependence of the logarithm of the resistance $\propto T^{-1}$). This is due either to the presence of a very resistive link in the best conducting path that dominates the resistance (region (3a)), or simply to the fact that the thermal energy k_BT is so high that transport occurs via hops between nearest neighbour states, no matter how far in energy they are (region (4a)). On the contrary at lower temperatures, in region (1a), $L \leq L_M$ and transport ceases to be thermally activated to become elastic and coherent through the whole nanowire. The thermopower in this regime has been studied in Ref. [19]. If now μ lies outside the impurity band, electrons need to absorb energy in order to enter the band. In region (1b), k_BT is too small for that (the only way for electrons to cross the nanowire is then to tunnel directly from one reservoir to the other, which results in a exponentially vanishing conductance). At higher temperatures, in regions (2b), (3b) and (4b), electrons can be thermally activated. Once they have entered the nanowire, they hop from site to site according to the mechanism prevailing in regions (2a), (3a) and (4a) respectively.

4.1.2 Formulation in terms of a random resistor network

We follow the approach used in Refs. [84, 85] for studying thermoelectric transport in the hopping regime. It consists in solving the Miller-Abrahams resistor network [113] which was first introduced for describing charge transport in weakly doped crystalline semiconductors and later on extended to non crystalline Anderson insulators. The nodes are given by the localized states. Each pair of nodes i, j is connected by an effective resistor, which depends on the transition rates Γ_{ij}, Γ_{ji} induced by local electron-phonon interactions. In addition, one needs to connect this network to the leads, if one wants to calculate the charge and heat currents flowing through it. Usually (and actually, we did not find a reference where this is not the case) one assumes for calculating these transition rates that $\xi_i = \xi(E_i) \equiv \xi$ (evaluated at μ) for the localization lengths of the different states, which can be done if the variations of the ξ_i are negligible within Δ. Here we need to go beyond such an approximation, since we are interested in band edge transport, where those variations cannot be neglected. The procedure is summarized below.

Let us consider a pair of localized states i and j of energies E_i and E_j. Assuming no correlations between their occupation numbers, the (time-averaged) transition rate from state

i to state j is given by the Fermi golden rule as [85]

$$\Gamma_{ij} = \gamma_{ij}\, f_i\,(1-f_j)\,\left[N_{ij} + \theta(E_i - E_j)\right]\,, \tag{4.7}$$

where f_i is the average occupation number of state i and $N_{ij} = [\exp\{|E_j - E_i|/k_BT\} - 1]^{-1}$ is the phonon Bose distribution at energy $|E_j - E_i|$. The presence of the Heaviside function accounts for the difference between phonon absorption and emission [3]. γ_{ij} is the hopping probability $i \to j$ due to the absorption/emission of one phonon when i is occupied and j is empty. Assuming that the energy dependence of ξ can be neglected, in the limit $x_{ij} \gg \xi$ one obtains

$$\gamma_{ij} \simeq \gamma_{ep} \exp(-2x_{ij}/\xi)\,. \tag{4.8}$$

Here $x_{ij} = |x_i - x_j|$ is the distance between the states, whereas γ_{ep}, containing the electron-phonon matrix element, depends on the electron-phonon coupling strength and the phonon density of states. Since it is weakly dependent on E_i, E_j and x_{ij} compared to the exponential factors, it is assumed to be constant. Under the widely used approximation [3, 139, 160, 200] $|E_{ij}| \gg k_BT$, Eq. (4.7) reduces to:

$$\Gamma_{ij} \simeq \gamma_{ep}\, e^{-2x_{ij}/\xi}\, e^{-(|E_i-\mu|+|E_j-\mu|+|E_i-E_j|)/2k_BT}\,. \tag{4.9}$$

Hereafter, we will go beyond these standard approximations by considering the exact expression (4.7) for Γ_{ij}, and by taking

$$\gamma_{ij} = \gamma_{ep} \left(\frac{1}{\xi_i} - \frac{1}{\xi_j}\right)^{-2} \left(\frac{\exp\{-2r_{ij}/\xi_j\}}{\xi_i^2} + \frac{\exp\{-2r_{ij}/\xi_i\}}{\xi_j^2} - \frac{2\exp\{-r_{ij}(1/\xi_i + 1/\xi_j)\}}{\xi_i \xi_j}\right), \tag{4.10}$$

for γ_{ij}. Eq. (4.10) takes into account the energy dependence of $\xi(E)$ and is derived in 4.4.2.

The tunneling transition rates between each state i and the leads α ($\alpha = L$ or R) are written in a similar way as

$$\Gamma_{i\alpha} = \gamma_{i\alpha}\, f_i\,\left[1 - f_\alpha(E_i)\right] \tag{4.11}$$

where

$$\gamma_{i\alpha} \simeq \gamma_e \exp(-2x_{i\alpha}/\xi_i)\,. \tag{4.12}$$

In the above equations $f_\alpha(E) = [\exp\{(E-\mu_\alpha)/k_BT\}+1]^{-1}$ is lead α's Fermi-Dirac distribution, $x_{i\alpha}$ denotes the distance of state i from lead α and γ_e is a rate quantifying the coupling between the localized states and the leads (taken constant for the same reason as γ_{ep}).

Then, the net electric currents flowing between each pair of localized states and between states and leads are obtained by

$$I_{ij} = e\,(\Gamma_{ij} - \Gamma_{ji}) \tag{4.13a}$$

$$I_{i\alpha} = e\,(\Gamma_{i\alpha} - \Gamma_{\alpha i}) \qquad \alpha = L, R \tag{4.13b}$$

$e < 0$ being the electron charge. The linear response solution of this random resistor network problem is reviewed in Ref. [85]. Details of the calculation of the charge currents and heat

currents are summarized in 4.4.2 for the Peltier configuration we consider where the temperature is T everywhere and the reference (equilibrium) electrochemical potential is that of the right reservoir ($\mu \equiv \mu_R$). In this case the electrical conductance G, Peltier coefficient Π and thermopower S are determined within the Onsager formalism by the charge (J_L^e) and heat (J_L^Q) currents exchanged with the left reservoir:

$$G = \frac{J_L^e}{\delta\mu/e}, \tag{4.14a}$$

$$\Pi = \frac{J_L^Q}{J_L^e}, \tag{4.14b}$$

$$S = \frac{\Pi}{T} = \frac{1}{T}\,\frac{J_L^Q}{J_L^e}. \tag{4.14c}$$

In the last equation, the Kelvin-Onsager symmetry relation [32] $\Pi = ST$ has been used for deducing the thermopower.

4.1.3 Anderson model for the localized states

The set of energies E_i and localization lengths ξ_i are required as input parameters of the random resistor network problem. To generate them we use the Anderson model. The disordered nanowire is modeled as a 1D lattice of length L with a lattice spacing a set equal to one, described by a $L \times L$ tight-binding Hamiltonian:

$$\mathcal{H} = -t\sum_{i=1}^{L-1}\left(c_i^\dagger c_{i+1} + \text{h.c.}\right) + \sum_{i=1}^{L}(\epsilon_i + V_g)c_i^\dagger c_i\,, \tag{4.15}$$

where $c_i^\dagger$ and c_i are the electron creation and annihilation operators on site i and t is the hopping energy. In the following all energies will be expressed in unit of t. The disorder potentials ϵ_i are (uncorrelated) random numbers uniformly distributed in the interval $[-W/2, W/2]$. The constant potential V_g is added to take into account the presence of an external top gate, allowing to shift the whole nanowire impurity band.

By diagonalizing the Hamiltonian (4.15), we find the energies E_i of the localized states. They are distributed with the DOS $\nu(E)$ in the interval $[V_g - E_B, V_g + E_B]$, $\pm E_B$ being the band edges of the model at $V_g = 0$. In the limit $L \to \infty$, $E_B = 2t + W/2$. To generate the localization lengths ξ_i, we neglect sample-to-sample fluctuations and assume that ξ_i is given by the typical localization length $\xi(E_i)$ at energy E_i, characterizing the exponential decay of the average logarithm of the elastic conductance ($\ln G \sim -2L/\xi$). The DOS $\nu(E)$ and localization length $\xi(E)$ are shown in Fig. 4.4; their energy dependence is analytically known in the large size and small disorder limits, both in the bulk of the band and close to the edges (see Refs. [46, 19]). Obviously, if μ lies close to the band edges and/or if the available energy window Δ around μ is not small compared to t, the energy dependency of $\nu(E)$ and $\xi(E)$ cannot be neglected. This explains why we need to go beyond the approximation of constant

DOS and localization length when scanning the impurity band with the gate voltage.

Solving the Anderson model gives us the full set of localized states: their energy levels E_i, their localization lengths $\xi_i = \xi(E_i)$ and their positions along the disordered chain. However, to speed up the procedure of building a basis of localized states, we simply assign the levels E_i to random positions x_i between 0 and L along the chain (with a uniform distribution). This approximation is conventional in numerical simulations of VRH transport (see [85, 101, 158] among others) [3].

Hereafter, we will study disordered chains with a disorder strength $W = t$, which is sufficiently small for using weak disorder expansions [19] and sufficiently large for ensuring $L \gg \xi_i$ at relatively small sizes. For $V_g = 0$ and $L \approx 1000$, the spectrum edges of the disordered nanowire are found at $E_B \approx 2.35\,t$, which is smaller than $2.5\,t$, the value characterizing the limit $L \to \infty$. Such finite size effects are a consequence of the infinitely small tails of the asymptotic DOS $\nu(E)$ shown in Fig. 4.4: States of energy close to $2.5\,t$ can only exist in infinitely long chains.

4.2 Electrical Conductance

4.2.1 Background

The electrical conductance of one-dimensional conductors in the VRH regime has been much studied in the literature, both experimentally [63, 66, 96, 98, 185] and theoretically [95, 97, 101, 143, 149, 158]. In particular, the validity of Mott law for the typical conductance in 1D

$$\ln G(T) \sim -\alpha \sqrt{\frac{T_M}{T}}, \tag{4.16}$$

with $\alpha \approx 1$, was a subject of controversy for a long time: Strictly speaking, Mott's argument leading to Eq. (4.16) does not hold in 1D. It was shown that due to the presence of "breaks", the prefactor α is actually also a function of the temperature and system length [143, 158]. Nevertheless, the T- and L-dependency of α turns out to be so weak that at low temperatures α is almost constant and Mott law is recovered. Taking the proper $\alpha(L,T)$ into account allows an analytical description of the crossover from Mott law to the activated behavior, $\ln G(T) \sim T^{-1}$, above T_a (see Sec. 4.1.1) but the refinement thus introduced is too small to be clearly evidenced by numerical simulations and even less by experimental measurements.

[3] By doing this we lose a feature of Anderson model, namely that states which are close in energy are distant in space, and as a consequence our model may overestimate the hopping between certain pairs of states. However this should not play an important role if L is sufficiently large, $L \gg \xi(\mu)$. In this case states which are accidentally taken close both in space and in energy should be not only rare but, more importantly, can merely be seen – regarding percolation – as one small localized cluster, i.e. as a *s*ingle new effective localized state. The reason is that the optimal percolation path is eventually determined by the most resistive links. Thus, we can always reformulate the problem in order to end up in a situation in which neighbouring states are far away in energy.

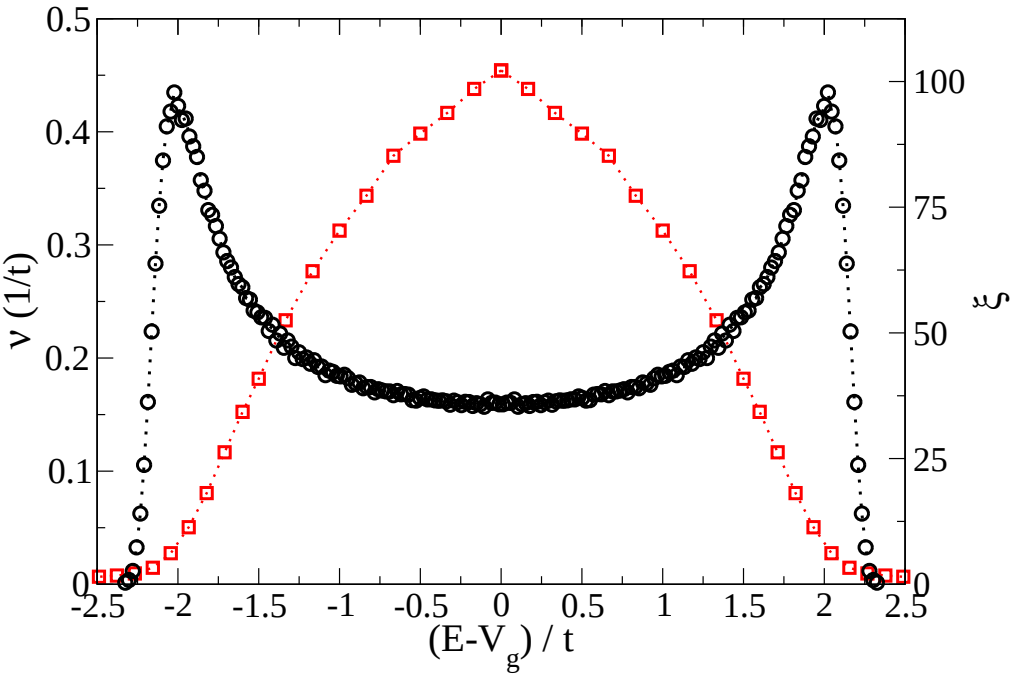


Figure 4.4: Density of states per site ν (○) and localization length ξ (□), as a function of energy E for the 1D Anderson model (4.15) with disorder amplitude $W/t = 1$. The points correspond to numerical data (obtained in the large length limit with $L = 1600$). Analytical expressions describing $\nu((E - V_g)/t)$ and $\xi((E - V_g)/t)$ are given in Ref. [19].

Another limitation of Mott's standard argument and of the subsequent, more elaborate percolation-based ones is the initial assumption of constant DOS and localization length around μ. As long as $\nu(E)$ is slowly varying in the energy window $|E - \mu| < \Delta$ (still keeping ξ constant), Eq. (4.16) is expected to hold, but it lacks justification in the case of strongly varying DOS. In particular, Eq. (4.16) has to be revised when transport through the system occurs at energies around the impurity band edges. This question was tackled by Zvyagin in Refs. [200, 201], by approximating the DOS by a step-like function. If one considers the lower band edge, the approximated DOS reads

$$\nu(E) \simeq \nu_0\, \theta(E - \epsilon_c), \tag{4.17}$$

where ϵ_c plays the role of an effective band edge. Though *three-dimensional* systems were considered in Refs. [200, 201], a similar approach can be extended to our 1D model setting $\epsilon_c = V_g - \bar{\epsilon}$, where $\bar{\epsilon}$ is the 1D effective edge introduced in Sec. 4.1.1 for $V_g = 0$. The idea is that when μ lies outside the impurity band, electrons need an activation energy $\epsilon_c - \mu$ in order to "jump" inside it to find available states. This entails an extra term in Eq. (4.16), which in 1D becomes

$$\ln G(T) \sim -\frac{E_A}{k_B T} - \bar{\alpha}\sqrt{\frac{T_M}{T}}, \tag{4.18}$$

with $E_A \sim \epsilon_c - \mu$ and $\bar{\alpha}$ differing from α by some numerical factors [62, 201].

4.2.2 Numerical results

We have investigated numerically how the typical conductance of a disordered nanowire depends on the temperature when the applied gate voltage is varied. For the model described in Sec. 4.1.3, we have solved the random resistor network problem and calculated the conductance G via Eq.(4.14a). This procedure has been iterated over many random configurations of the energy levels E_i in order to extrapolate the *typical* logarithm of the conductance $[\ln G]_0$, defined as the median of the resulting distribution $P(\ln G)$[4].

In Fig. 4.5, $[\ln G]_0(T)$ is plotted for two values of V_g, corresponding to the bulk and the lower edge of the band. In both cases we show that low temperature data exhibits Mott law $T^{-1/2}$ behavior (red dashed curve), while at higher temperatures they are well fitted by an activated T^{-1} law (green dashed curve). Eq. (4.18) with adjusted values for E_A and $\bar{\alpha}$ describes the crossover between the two regimes (full blue line). More precisely, when μ lies inside the band (Fig. 4.5(a)), the validity range of Mott law ($k_BT/t \lesssim 0.05$) is consistent with the required hypothesis of weakly varying DOS. Indeed, below such temperatures, the energy window $\Delta = k_B\sqrt{T_M T}$ of accessible states around μ is so small ($\Delta \lesssim 0.2$ using for T_M the value given in Fig. 4.3) that the DOS can be considered as weakly energy dependent ($\Delta\, \partial_E \ln \nu(E)|_\mu \approx 0.3 < 1$). This justifies the validity of Eq. (4.16) in such a regime. Note that the onset of activated behavior at $k_BT \approx 0.05\,t$ is also in rough agreement with the predicted value of $k_BT_a \approx 0.1\,t$ in Fig. 4.3. On the other hand, when μ lies in a region where the DOS is exponentially small (Fig. 4.5(b)), there is no more reason to use Mott law to describe our data, even if it appears to be well fitted by Eq. (4.16) at low temperatures. The point is that other power law formula, $[\ln G]_0 \sim T^\beta$, could be used to fit our data in this narrow temperature range. Thus, one cannot use the apparent suitability of Eq. (4.16) to support the validity of Mott law in this regime. Outside the band the correct framework for analysis is provided by Eq. (4.18). The activated contribution to the conductance is always present, which explains why in Fig. 4.5(b) the T^{-1} fit starts to be accurate much below the temperature $k_BT_a/t \approx 0.95$. Finally, at very high temperatures (typically larger than t), the typical conductance is found in both cases to decrease with temperature. This is due to the fact that in the limit $T \to \infty$, the factors $f_i(1-f_j)$ and $f_j(1-f_i)$ on one hand, and $f_i(1-f_\alpha)$, $f_\alpha(1-f_i)$ on the other, converge to the same value. Hence, the opposite rates Γ_{ij}, Γ_{ji} and Γ_{iL}, Γ_{Li} tend to level out, which results in a vanishing net current and a divergent resistance. An expansion of the Fermi functions to the next order in inverse temperature yields I_{ij}, $I_{i\alpha} \sim T^{-1}$, which explains the linear decay at high T of $[\ln G]_0$ versus $\ln T$ in Fig. 4.5 (not marked).

[4]More details concerning the distributions of the logarithm of the conductance for 1D systems in VRH regime can be found in Refs. [147, 158]

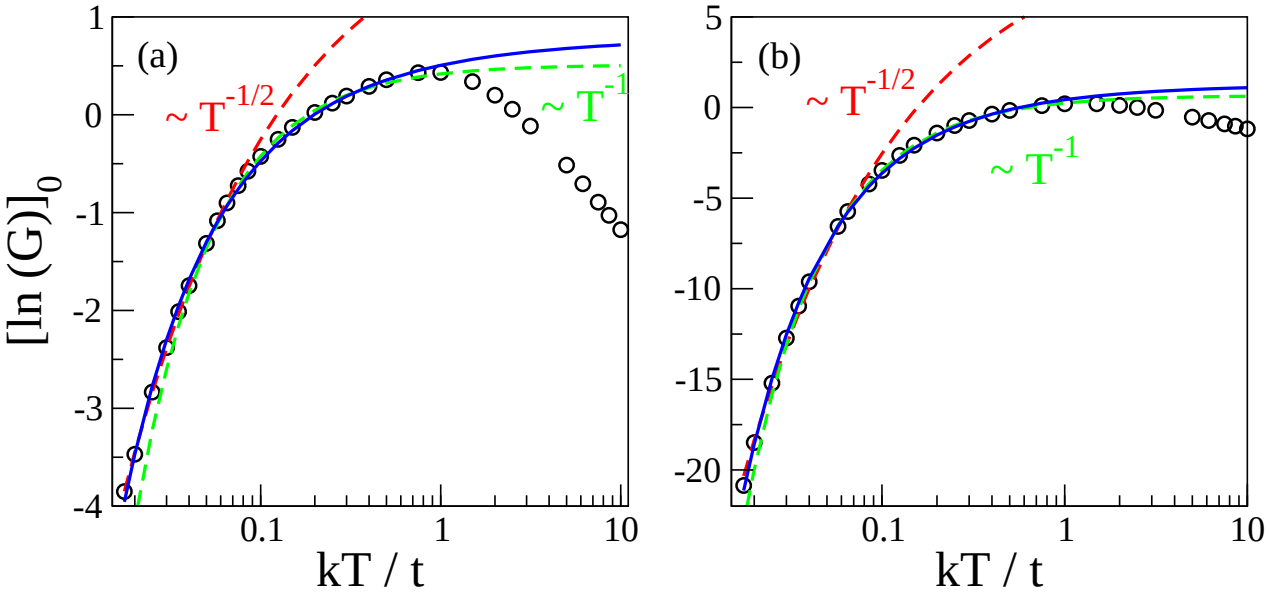


Figure 4.5: Typical value of the logarithm of the conductance $[\ln G]_0$ as a function of T for $\mu = 0$ and two values of the gate voltage: (a) $V_g = 1.9\,t$ inside the band and (b) $V_g = 2.3\,t$ at the edge of the band. In both cases, at low temperatures, numerical data (points) are well fitted by a $T^{-1/2}$ fit (red dashed lines), evolving to a T^{-1} behavior as T increases (green dashed lines). Full blue lines correspond to Eq.(4.18), which describes the crossover between the two regimes. Parameters: $L = 200$, $W = t$ and $\gamma_e = \gamma_{ep} = t$.

4.3 Thermopower

4.3.1 Background

The thermopower is a measure of the average energy $\langle E - \mu \rangle$ transferred by charge carriers from the left lead to the right one. In the low temperature coherent regime [19], transport takes place near the Fermi energy. Hence, in linear response with respect to the bias voltage between the two leads, the thermopower depends on the electron-hole asymmetry at μ. On the contrary, in the VRH regime, all states in the energy window $|E - \mu| < \Delta$ contribute. Since $\Delta \gg k_B T$ when $T \ll T_M$, the thermopower benefits from the contribution of states far below and above μ, despite being in linear response. When the gate voltage is adjusted in order to probe the impurity band edges, the electron contribution dominates over the hole one (or vice-versa), yielding an enhanced thermopower.

To study the thermopower in the VRH regime [5], we use the approach introduced by Zvyagin in [200, 201]. The starting point is the percolation theory of hopping transport,

[5] We stress that the usual Mott formula for the thermopower, $S = (\pi^2 k_B^2 T/(3e))\, \partial_E \ln \sigma|_\mu$ (σ being the electrical conductivity), does not apply in the VRH regime, as pointed out by Mott himself in [121]. Indeed, this formula has been derived by averaging $\langle E - \mu \rangle$ within the standard Boltzmann formalism, not suitable in the VRH regime where $\Delta \gg k_B T$.

according to which transport through the system is achieved via percolation in energy-position space. The average $\langle E-\mu\rangle$ is calculated by averaging the energy over the sites composing the percolation cluster, and the thermopower is given by

$$S = \frac{\langle E-\mu\rangle}{e\,T} = \frac{1}{e\,T}\,\frac{\int dE\,(E-\mu)\,\nu(E)\,p(E)}{\int dE\,\nu(E)\,p(E)}, \tag{4.19}$$

where $p(E)$ is the probability that a state of energy E belongs to the percolation cluster. The latter quantity is supposed to be proportional to the average number of bonds $N_b(E)$, given by

$$N_b(E) = \int dx \int dE'\,\nu(E')\,\theta\left(\sqrt{\frac{T_M}{T}} - \frac{2x}{\xi} - \frac{|E-\mu|+|E'-\mu|+|E-E'|}{2k_BT}\right), \tag{4.20}$$

under the assumptions leading to Eq. ((4.9)) (μ inside the band, low temperature and energy independent localization length $\xi(E) = \xi(\mu)$) [3, 201]. The Heaviside function θ accounts for the existence of a percolating path, and restricts the energy range of integration to the window $[\mu-\Delta, \mu+\Delta]$. After integrating over the single spatial variable x (in 1D), one gets

$$p(E) \propto \theta\left(\Delta - |E-\mu|\right) \times \int_{\mu-\Delta}^{\mu+\Delta} dE'\,\nu(E')\left(1 - \frac{|E-\mu|+|E'-\mu|+|E-E'|}{2\Delta}\right)\theta\left(\Delta-|E-E'|\right). \tag{4.21}$$

Note that if μ lies outside the impurity band, electrons need to jump inside the latter by thermal activation before accessing the percolation cluster. In that case, Eqs. (4.20) and (4.21) have to be modified accordingly, by replacing μ by the energy ϵ_c of the closest band edge and by changing the energy range of integration to $[\epsilon_c, \epsilon_c+\Delta]$ (lower band edge) or $[\epsilon_c-\Delta, \epsilon_c]$ (upper band edge).

Eqs. (4.19) and (4.21) enable us to calculate the thermopower once the DOS $\nu(E)$ is known. Following Zvyagin's works [200, 201], we discuss below a few extreme cases where the DOS takes a simple form. Contrary to those works focused on three-dimensional bulk materials, we derive expressions for the thermopower of nanowires in the 1D case. Despite the simplicity of our approach, we will see in the next subsection that it enables us to qualitatively capture the typical behavior of the thermopower and the role of the gate (see Sec. 4.1).

Let us first consider the case where *(i)* the DOS can be approximated by its first order expansion $\nu(E) \approx \nu(\mu) + (E-\mu)\,\partial_E \ln\nu(E)|_\mu$ in the interval $[\mu-\Delta, \mu+\Delta]$, and *(ii)* ν is expected to vary slowly at the scale of Δ, *i.e.* $\Delta\,\partial_E \ln\nu(E)|_\mu \ll 1$. Using Eqs. (4.19) and (4.21), one finds

$$S \approx \frac{k_B}{e}\left(\frac{k_BT_M}{4}\right)\partial_E \ln\nu(E)|_\mu\ . \tag{4.22}$$

This shows that the thermopower should be temperature independent when the assumptions above are fulfilled, which is always the case at very low temperatures (bottom part of region (2a) in Fig. 4.3). Note that the same hypothesis for the DOS lead to the standard Mott

formula (4.16) for the conductance: Eq. (4.22) describes the thermopower when Eq. (4.16) holds for the conductance.

Let us now consider the case where the impurity band edges are explored, say the lower one. In analogy to the previous section, using a rough step-like model for $\nu(E)$ provides useful insight. Using Eq. (4.17) for the DOS and Eq. (4.19), one gets for the thermopower

$$S = \frac{k_B}{e}\left(\frac{\epsilon_c - \mu}{2k_BT} + \frac{\Delta(T)}{2k_BT}\right) \quad \text{if} \quad \epsilon_c < \mu \quad \text{and} \quad \mu - \epsilon_c < \Delta, \tag{4.23a}$$

$$S = \frac{k_B}{e}\left(\frac{\epsilon_c - \mu}{k_BT} + \frac{\Delta(T)}{2k_BT}\right) \quad \text{if} \quad \epsilon_c > \mu\,, \tag{4.23b}$$

assuming[6] $p(E) = 1$ in the energy window $|E-\mu| < \Delta$ $[0 < E-\epsilon_c < \Delta]$ and 0 elsewhere. Similar formulas can be deduced by symmetry if the upper band edge is explored. The resulting thermopower behavior as a function of temperature turns out to be rich. Indeed, depending on the position of μ with respect to the (bottom) edge ϵ_c of the DOS, and depending on the magnitude of Δ, the thermopower can be an increasing or decreasing function of T. If μ lies outside the impurity band, the thermopower (in unit of k_B/e if not otherwise specified) is found to be a monotonically decreasing function of the temperature (see Eq. (4.23b)). On the other hand, if μ lies inside the band, close to the edge ϵ_c of the DOS, the thermopower increases with the temperature, reaches a maximum (at $k_BT = (\epsilon_c-\mu)^2/(16k_BT_M)$) and then starts to decrease (see Eq. (4.23a)).

Let us finally address the large temperature limit ($k_BT \gtrsim 2E_B$), corresponding to region (4b) and the upper part of region (4a) in Fig. 4.3. In that case, all impurity band states are involved in thermoelectric transport, with $p(E) \approx 1$. As a consequence, the thermopower temperature behavior is merely $S \sim T^{-1}$. Assuming a constant DOS, one gets

$$S = \frac{k_B}{e}\left(\frac{V_g - \mu}{k_BT}\right). \tag{4.25}$$

4.3.2 Numerical results

For the model introduced in Sec. 4.1.3, we now study the thermopower by solving numerically the random resistor network (see 4.4.2).

[6] We have also calculated the thermopower beyond this approximation, by plugging Eq. (4.17) for $\nu(E)$ into Eq. (4.21) for $p(E)$. Instead of Eqs. (4.23a) and (4.23b), we find respectively

$$S = \frac{k_B}{e}\left[\frac{5(\epsilon_c - \mu)}{8k_BT} + \frac{3\Delta(T)}{8k_BT} + O\left(\frac{\epsilon_c - \mu}{k_BT}\right)\right], \tag{4.24a}$$

$$S = \frac{k_B}{e}\left[\frac{\epsilon_c - \mu}{k_BT} + \frac{3\Delta(T)}{8k_BT}\right]. \tag{4.24b}$$

The two sets of equations are obviously very similar. At a qualitative level of analysis, it is meaningless to favour one over the other.

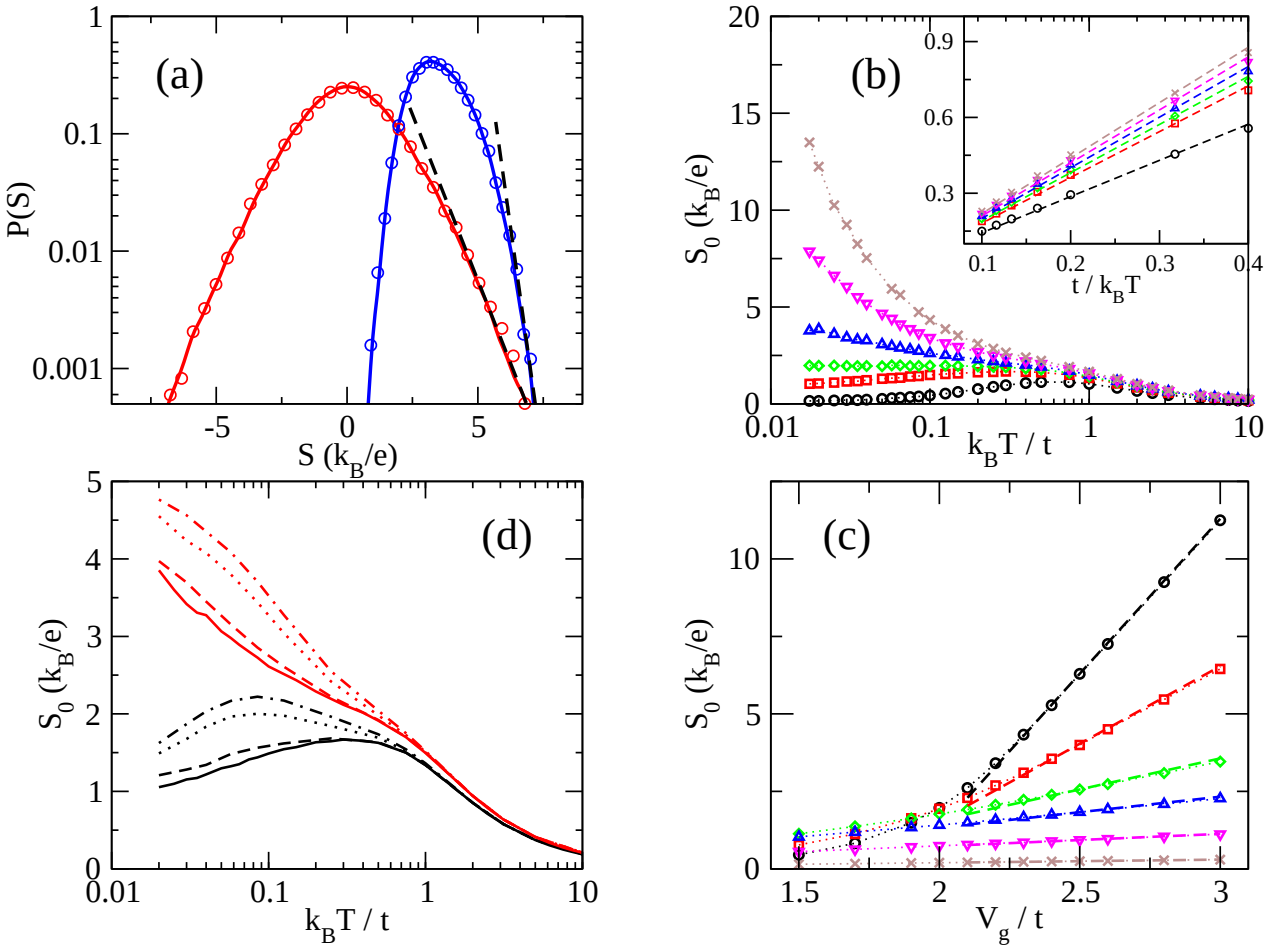


Figure 4.6: In all panels, unless specified, $L = 200$, $\mu = 0$, $W = t$ and $\gamma_e = \gamma_{ep} = t$. (a) Thermopower distributions in the VRH regime, when μ lies in the bulk (left red curve, $V_g = 0$, $W = 4t$) or close to the edge (right blue curve, $V_g = 2.2t$, $W = t$) of the impurity band. Data are given for $L = 200$ (full lines) and $L = 400$ (circles). The straight dashed lines underline the exponential behavior of the tails $\sim \exp\{-cS\}$ predicted in Ref. [85]. In both cases, $k_BT = t$. (b) Main panel: Typical thermopower as a function of T around the (lower) band edge. From the bottom to the top, the various curves correspond to $V_g/t = 1.5\,(\circ), 1.9\,(\square), 2.0\,(\diamond), 2.1\,(\triangle), 2.2\,(\triangledown)$ and $2.3\,(\times)$. Dotted lines are guides to the eye. Inset: zoom at very large temperatures $k_BT \gtrsim E_B$. The fits $f(V_g)/T$ (dashed lines) confirm the expected behavior $S_0 \sim T^{-1}$ (Eq. (4.25)). (c) Typical thermopower as a function of V_g, for $k_BT/t = 0.1\,(\circ), 0.2\,(\square), 0.5\,(\diamond), 1.0\,(\triangle), 2.5\,(\triangledown)$ and $10.0\,(\times)$. At large V_g (when μ lies outside the band), dashed lines are linear fits with slope t/k_BT (Eq. (4.23b)). Dotted lines are guides to the eye. (d) Typical thermopower as a function of T, for electron-phonon coupling strength $\gamma_{ep}/t = 1$ (full line), 0.5 (dashed line), 0.1 (dotted line) and 0.05 (mixed line), at $V_g = 1.9t$ (black curves, bottom set) and $V_g = 2.1t$ (red curves, top set).

Fig. 4.6(a) gives the distribution $P(S)$ of the thermopower S in the VRH regime, when the impurity band center (red curve) and lower edge (blue curve) are probed at μ. While the thermopower distribution is symmetric around a vanishing average value at the band center, it is shifted away from 0 and gets skewed close to the band edges. Such features can be easily understood: The level distribution becomes highly asymmetric with respect to μ when one probes the lower band edge with a positive gate voltage V_g. Consequently, an electron entering the nanowire from the left lead around μ finds more states *above* its energy than below. It has therefore a tendency to absorb energy in order to move to regions of higher DOS, before releasing it at the right side of the nanowire, as illustrated in Fig. 4.2. Recalling that $S = \langle E - \mu \rangle / (eT)$, one can thus explain why $P(S)$ is shifted and skewed at finite V_g. Let us notice that such a skewness cannot be seen in the low-temperature coherent regime [19], where transport only involves electrons at energies very close to μ; In that case, distributions are found to be shifted with V_g but always symmetric. Another important message of Fig. 4.6(a) is that for both values of V_g the thermopower distribution turns to be independent of the nanowire length L. This is consistent with the observation that the thermopower is governed by the edges of the nanowire in the hopping regime, as recently pointed out in Ref. [85].

We then investigate the typical thermopower behavior as a function of temperature and gate voltage, by extracting the median S_0 of the distribution $P(S)$ for different sets of parameters. The temperature dependence of S_0 is shown in Fig. 4.6(b) for different values of the gate voltage, which have been chosen for scanning the vicinity of the lower band edge. The main observation is that our model predicts a huge enhancement of the thermopower around the band edges. Values larger that $10\, k_B/e$ are obtained by properly tuning the strength of the gate voltage in the VRH regime. Other features of those curves are worth emphasizing:

1. S_0 is always positive in unit of k_B/e, hence negative in $\mathrm{V\,K^{-1}}$ (since $e < 0$). This is expected since transport is due to electrons near the lower band edge, the sign of the thermopower reflecting the sign of the charge carriers.[7]

2. At low temperatures the typical thermopower can either increase or decrease with the temperature depending on the gate voltage. Roughly speaking, it increases inside the band and decreases outside, in agreement with the theoretical predictions (4.23a) and (4.23b), obtained assuming a step-like model for the DOS close to the band edge ϵ_c. Moreover, the position of the crossover between the two behaviors is found around $V_g - \mu \approx 2t$, a value consistent with our previous estimation of an effective $\epsilon_c \approx V_g - 2.2t$ for the DOS of the Anderson model (see Sec. 4.1.1).

3. At high temperature (typically larger than the bandwidth), the curves converge to a T^{-1} behavior, as shown in the inset of Fig. 4.6(b). The crude estimation (4.25) turns

[7] The occurrence of negative S_0 is nevertheless possible not far from the lower band edge, as soon as Δ is sufficiently small and the DOS slope at μ becomes strongly negative. In our model, such a negative slope occurs close to the band edges, as shown in Fig. 4.4.

out to be satisfactory in this regime.

4. In the low temperature limit and in the case where μ lies inside the band, the typical thermopower S_0 is expected to saturate, according to Eq. (4.22). Such a saturation is not observed in Fig. 4.6(b). Two reasons can be invoked. The first one is that Eq. (4.22) was actually derived under the assumption of a constant localization length $\xi_i \approx \xi(\mu)$ while the numerical results reported here were obtained going beyond this approximation, by taking into account the energy dependency of the different localization lengths ξ_i of sites i. In 4.4.3, we show that under the assumption $\xi_i \approx \xi(\mu)$, S_0 indeed saturates at low temperature. The other possibility is simply that the saturation appears at lower temperatures, which are not reachable numerically because of round-off errors.

5. For high values of V_g, the typical thermopower seems to diverge as the temperature is lowered. It is obvious that the thermopower eventually decreases below a certain temperature, since all curves in Fig. 4.6(b) are known to drop down to zero in the zero-temperature limit (linearly with T and with a positive slope) [19].

In Fig. 4.6(c), we show how the typical thermopower depends on the gate voltage, for different values of the temperature. Approaching the edge of the impurity band, we see that S_0 increases, the effect being more pronounced at low temperatures. Outside the band, the behavior of S_0 with V_g is perfectly well fitted by the formula $S_0 = (k_B/e)[\frac{V_g}{k_B T} + f(T)]$, as illustrated by the straight lines in Fig. 4.6(c). This linear enhancement of S_0 with V_g, as well as its range of validity, is consistent with the prediction (4.23b) and our initial estimation $\epsilon_c \approx V_g - 2.2t$ for the position of the lower band edge. Note however that Eq. (4.23b) does not capture the y-intercept $f(T) \approx 0.89 - 1.94/(k_B T)$ of the linear fits. On the other hand the fact that S_0 keeps increasing even outside the impurity band, when the conductance drops exponentially, may seem in contrast with recent experimental observations [28]. We think the explanation lies in the fact that, when the nanowire is almost completely depleted by V_g, the probability for an electron at μ to tunnel inside the band becomes extremely small, and so do the electrical and heat currents; consequently, they may be too hard to measure. Nonetheless their ratio, which gives the thermopower, remains formally well defined and finite.

We conclude our analysis by discussing the order of magnitude of our numerical results. In panels (a), (b) and (c) of Fig. 4.6, data was obtained taking $\gamma_e = \gamma_{ep} = t$ as input parameters of the model. In panel (d) we investigate how the typical thermopower depends on the choice of these parameters, finding that S_0 does not vary by more than 50% when the ratio γ_e/γ_{ep} is increased or decreased by an order of magnitude. Remarkably, at the lowest studied temperatures (in the VRH regime) and around the band edges, the typical thermopower is found to reach very large values of the order of $10\,(k_B/e) \sim 1\,\mathrm{mV\,K^{-1}}$. It is worthwhile to note that, despite the simplicity of the model, the order of magnitude of these results is comparable to recent measurements of thermopower in semiconducting nanowires [28, 39,

116, 146], showing strong thermoelectric conversion at the band edges.

Extending our results to quasi-1D systems

In the model considered so far, each site of the chain corresponds to an electronic state localized at a position x_i by disorder or bound to an impurity site. Though such a model is strictly 1D, it should allow us to describe also quasi-1D wires [44, 148, 173] as long as their transverse size L_y remain negligible compared to the Mott typical hopping length L_M. Indeed, since the outcome of our percolative approach is that the *typical* electrons' hop is of the order L_M, we expect that the condition $L_y > L_M$ should be needed to add new spatial degrees of freedom which would alter significantly our predictions (by changing, for instance, the exponents associated to the Mott law for the conductance [201]). Furthermore, the density of states of a quasi 1D system may be different with respect to that corresponding to the 1D Anderson model considered in our calculations; again, this should not alter qualitatively our results, which rely solely on a very general feature of the density of states, that is, it should vanish at some energy. Details concerning *how* it vanishes are of secondary importance.

In conclusion, we draw attention on the universal character of our results, meaning that studying slightly different (and, in particular, quasi 1D) systems may lead to *quantitative* differences, whereas the *qualitative* behaviors of the conductance and of the thermopower shall not change.

4.3.3 Limitations of the present approach

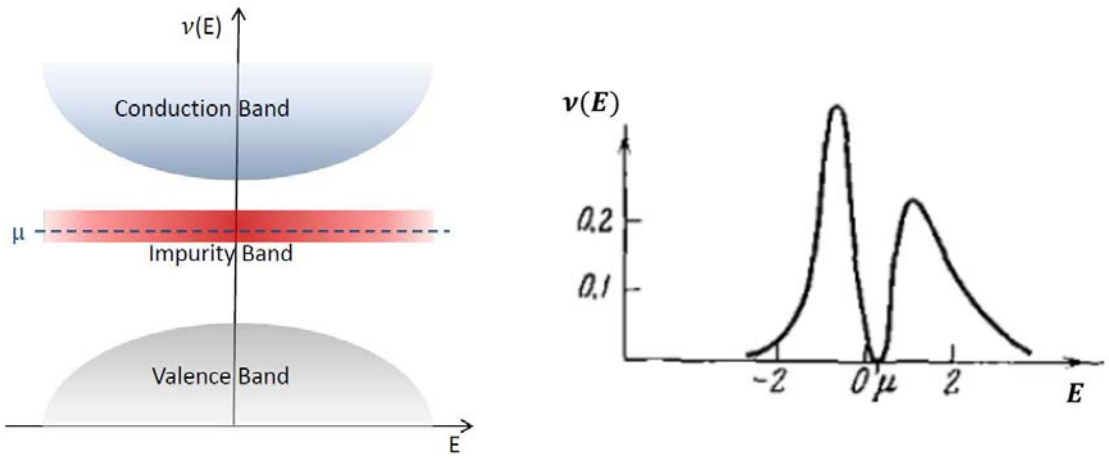
Let us now comment on certain limitations of our treatment. First, the used Anderson model is a single band model and neglects the possibility of temperature activated transport via other bands. This amounts to assuming that $k_B T < E_{act}$, where E_{act} is the interband spacing. E_{act} depends on the considered material, ranging from tens of Kelvin degrees for weakly doped crystalline materials, to hundreds of Kelvin degrees in amorphous materials [160] (see Fig. 4.7(a)).

Secondly, interactions have been neglected, except for the requirement of single-occupation of any given localized state [3]. Whereas this is appropriate in some cases, it is by no means a universally valid assumption. Indeed, numerous delicate issues related to the role of interactions in activated transport are discussed in the book by Efros and Shklovskii [160] and references therein. In particular, when these effects are relevant, the conductance is expected to be described by the Efros-Shklovskii (ES) law, which predicts a behavior of the form

$$\ln G(T) \sim T^{-1/2} \tag{4.26}$$

regardless of the dimensionality, rather than the $T^{-1/(d+1)}$-dependence of the Mott law. However, we believe that as long as the Coulomb energy gap [160] (see Fig. 4.7(b)) is small compared to other relevant energy scales (Mott hopping energy Δ and disorder strength W), including electronic interations should not change qualitatively our results. Moreover, as a partial support to our assumption, we report that according to experimental works, the ES law for the conductance has been validated mostly at low temperatures, where interaction

effects are known to be much important, while at higher temperatures the Mott law seemed to be more correct [90, 99, 164].
Finally, we have ignored phonon-drag effects, which is however a much safer bet. It is well known that the latter can play a prominent role in standard band transport – i.e. when electronic states are delocalized – especially at temperature large enough to prevent any Umklapp processes (for a detailed discussion, see [6]); however, these become irrelevant when transport is due to hopping between localized states [200, 201].



(a) (b)

Figure 4.7: (Left) Sketch of a typical band structure of a doped semiconductor. For the purposes of this thesis, we assume that there is no overlap between the impurity band and the closest band (the conduction one, in the figure). (Right) Example of a doped semiconductor density of states in the presence of a Coulomb energy gap at the Fermi level μ, due to electronic interactions (after [160]).

4.4 Appendix

4.4.1 Thermodynamics of the three-terminal setup

In linear response, we can express the (linearized) currents within the Onsager formalism [32, 128]. In general there are three heat currents flowing between each terminals and the system (J_L^Q, J_R^Q and J_P^Q) and two particle currents (J_L^N and J_R^N) between the two electronic reservoirs and the system. Due to charge and energy conservation, only three of these currents are independent (one particle current and two heat currents). In principle we could describe the transport problem using any three linear combinations of these independent currents. However, the choice of the reference values for the (equilibrium) electrochemical potential μ and temperature T leads us to associate naturally a particular set of currents to the gradients $\delta\mu$, δT and δT_P.

This is a direct consequence of writing explicitly the entropy production rate. For example, if we choose the right terminal as reference, by setting

$$\mu_R \equiv \mu \qquad T_R \equiv T \qquad \mu_L = \mu + \delta\mu \qquad T_L = T + \delta T \qquad T_P = T + \delta T_P,$$

then the entropy production rate is given by:

$$\begin{aligned}
-\dot{S} &= \frac{J_L^Q}{T_L} + \frac{J_R^Q}{T_R} + \frac{J_P^Q}{T_P} = \\
&= \frac{J_L^E - \mu_L J_L^N}{T_L} + \frac{J_R^E - \mu_R J_R^N}{T_R} + \frac{\dot{E}_P}{T_P} = \\
&= \frac{J_L^E - (\mu+\delta\mu) J_L^N}{(T+\delta T)} + \frac{J_R^E - \mu J_R^N}{T} + \frac{J_P^E}{(T+\delta T_P)} \simeq \\
&\simeq \frac{1}{T}\left[J_L^E\left(1-\frac{\delta T}{T}\right) - (\mu+\delta\mu)J_L^N\left(1-\frac{\delta T}{T}\right) + J_R^E - \mu J_R^N + J_P^E\left(1-\frac{\delta T_P}{T}\right)\right] = \\
&= -\frac{1}{T}\left[J_L^N\delta\mu + \left(J_L^E - \mu_L J_L^N\right)\frac{\delta T}{T} + J_P^E\frac{\delta T_P}{T}\right] = \\
&\equiv -\left[J_L^N\,\frac{\delta\mu}{T} + J_L^Q\,\frac{\delta T}{T^2} + J_P^Q\,\frac{\delta T_P}{T^2}\right]
\end{aligned} \tag{4.27}$$

where we used charge and energy conservation and the relation $J^Q_{L(R)} = J^E_{L(R)} - \mu_{L(R)} J^N_{L(R)}$. We thus see that having chosen the right terminal as reference has naturally led to express the currents J_L^N, J_L^Q and J_P^Q. In the Onsager formalism, this can be rewritten as:

$$\begin{pmatrix} J_L^N \\ J_L^Q \\ J_P^Q \end{pmatrix} = \begin{pmatrix} L_{11} & L_{12} & L_{13} \\ L_{12} & L_{22} & L_{23} \\ L_{13} & L_{23} & L_{33} \end{pmatrix} \begin{pmatrix} \delta\mu/T \\ \delta T/T^2 \\ \delta T_P/T^2 \end{pmatrix}. \tag{4.28}$$

Any other different choice of reference would have led to a different set of currents: see, for instance, Jiang *et al.* [85] in which the choice $\mu_{L(R)} = \mu \pm \delta\mu/2$, $T_{L(R)} = T \pm \delta T/2$, and $T_P = T + \delta T_P$ leads to:

$$\begin{pmatrix} (J_L^N - J_R^N)/2 \\ (J_L^Q - J_R^Q)/2 \\ J_P^Q \end{pmatrix} = \begin{pmatrix} L'_{11} & L'_{12} & L'_{13} \\ L'_{12} & L'_{22} & L'_{23} \\ L'_{13} & L'_{23} & L'_{33} \end{pmatrix} \begin{pmatrix} \delta\mu/T \\ \delta T/T^2 \\ \delta T_P/T^2 \end{pmatrix}. \tag{4.29}$$

A crucial point is that transport coefficient such as electrical conductance and thermopower are *not affected* by the specific choice of the reference values of μ and T. Indeed, comparing Eq.(4.28) to (4.29), if the system and the gradients are the same, the particle current J_L^N must also be unchanged, and hence $L_{11} = L'_{11}$, $L_{12} = L'_{12}$ and $L_{13} = L'_{13}$. This entails that there is no ambiguity in the definition of the conductance $G = L_{11}/T$ and the thermopower $S = L_{12}/TL_{11}$, even if in general $|J_L^Q| \neq |J_R^Q|$, due to local exchange with phonons (J_P^Q).

4.4.2 Solution of the random resistor network

In linear response we assume that on each localized state the electron occupation is characterized by a *local distribution* [85, 160]:

$$f_i = f_i^0 + \delta f_i, \tag{4.30}$$

where f_i^0 is the Fermi distribution at equilibrium (i.e., evaluated at the reference values μ and T), and δf_i is the correction induced by the (small) applied bias $\delta\mu$. Linearizing Eqs.(4.13), and making use of Eqs. (4.7), (4.8), and (4.11), the hopping currents between each pair of localized states, and the tunnelling currents from/to the electrodes can be written in terms of "local potentials" U_i's:

$$\begin{aligned} I_{ij} &= G_{ij}(U_i - U_j), \\ I_{iL(R)} &= G_{iL(R)}(U_i - U_{L(R)}), \end{aligned} \tag{4.31}$$

where

$$\begin{aligned} G_{ij} &= \frac{e^2}{k_B T}\,\gamma_{ij} f_i^0(1 - f_j^0)(N_{ij} + 1/2 \mp 1/2), \\ G_{iL(R)} &= \frac{e^2}{k_B T}\,\gamma_{iL(R)} f_i^0(1 - f_i^0), \\ U_i &= \frac{k_B T}{e}\,\delta f_i/[f_i^0(1 - f_i^0)], \\ U_{L(R)}(\epsilon_i) &= \frac{k_B T}{e}\,\delta f_{L(R)}/[f_i^0(1 - f_i^0)]. \end{aligned} \tag{4.32}$$

In the above expressions, in case of double signs, the upper (lower) sign refers to $E_j > E_i$ ($E_j < E_i$).

At steady state, according to Kirchoff's conservation law, the net electric current throughout every node i must vanish:

$$\left(\sum_{j \neq i} I_{ij}\right) + I_{iL} + I_{iR} = 0. \tag{4.33}$$

By plugging Eqs. (4.31), we end up with a set of L equations (one for every node i) to calculate the L local potentials U_i's, which can be written conveniently in the matrix form:

$$\sum_j A_{ij} U_j = z_i, \tag{4.34}$$

where

$$\begin{aligned} A_{ij} &= -G_{ij} \qquad (\text{for } i \neq j), \\ A_{ii} &= \sum_{k \neq i} G_{ik} + G_{iL} + G_{iR}, \\ z_i &= G_{iL}\ (\delta\mu_L/e) \end{aligned} \tag{4.35}$$

In writing the expression for z_i, we exploited the fact that $\delta\mu_R = \delta T_R = 0$, having chosen to set the right terminal as reference (see Sec. 4.1).
Once the system is solved and the U_i are known, all the I_{ij}'s and $I_{iL(R)}$ can be calculated via Eqs. (4.31). The electric and heat currents can be computed by summing the outgoing contributions from the left (right) lead toward every states in the system:

$$\begin{aligned} J^e_L &= -\sum_i I_{iL} = \sum_i I_{iR}, \\ J^Q_{L(R)} &= \sum_i \left(\frac{E_i - \mu_{L(R)}}{e} \right) I_{L(R)i}. \end{aligned} \tag{4.36}$$

4.4.3 Calculation of the hopping probability

Miller and Abrahams[113, 160] described how to calculate the hopping probability γ_{ij} between two donors i and j in a 3D semiconductor, mediated by the absorption or emission of a phonon. When the distance between the donors is large, they obtain for γ_{ij} an expression which depends on the (weak) overlap between the donor wavefunctions and on the mutual electrostatic effect between them:

$$\gamma_{ij} \propto \left| \langle \psi_i | \frac{e^2}{\kappa |\boldsymbol{r} - \boldsymbol{r}_i|} | \psi_j \rangle - \langle \psi_i | \psi_j \rangle \langle \psi_i | \frac{e^2}{\kappa |\boldsymbol{r} - \boldsymbol{r}_j|} | \psi_i \rangle \right|^2 . \tag{4.37}$$

If the donor wavefunctions ψ_i and ψ_j are characterized by the *same* decay length ξ, Eq. (4.37) can be simplified [113, 160]

$$\gamma_{ij} \propto \exp(-2|\boldsymbol{r}_i - \boldsymbol{r}_j|/\xi). \tag{4.38}$$

If the decay lengths of ψ_i and ψ_j are different ($\xi_i \neq \xi_j$), a rigourous evaluation of γ_{ij} from Eq. (4.37) may be complicated, but the key point is that it will always be proportional to the overlap $\langle \psi_i | \psi_j \rangle$. Hence, we can write it in the form

$$\gamma_{ij} \propto |\langle \psi_i | \psi_j \rangle|^2 \sim \left| \mathcal{C}_i \exp(-r_{ij}/\xi_i) + \mathcal{C}_j \exp(-r_{ij}/\xi_j) \right|^2 , \tag{4.39}$$

where $r_{ij} = |\boldsymbol{r}_i - \boldsymbol{r}_j|$ is the distance between i and j, and the coefficients $\mathcal{C}_i$ and $\mathcal{C}_j$ depend on ξ_i, ξ_j and r_{ij}. The explicit form of these coefficients will take into account all details concerning the wavefunction overlap $\langle \psi_i | \psi_j \rangle$. In 1D the calculation becomes simpler and leads to Eq. (4.10). Extending a theory originally developed for lightly doped cristalline semiconductors (where the decay length is the donor Bohr radius) to Anderson insulators (where the decay length becomes the localization length), Ambegaokar *et al.*[3] have used Eq. (4.38) for describing the hopping probability. For similar reasons, we use Eq. (4.10) in our numerical calculations, for both G and S, taking for ξ_i and ξ_j the localization length of two Anderson localized states.

Finally, in order to estimate the difference between taking $\xi(\mu)$ or $\xi(E)$ when computing the transition rates (Eqs.(4.7) and (4.11)), we have calculated the typical logarithm of the

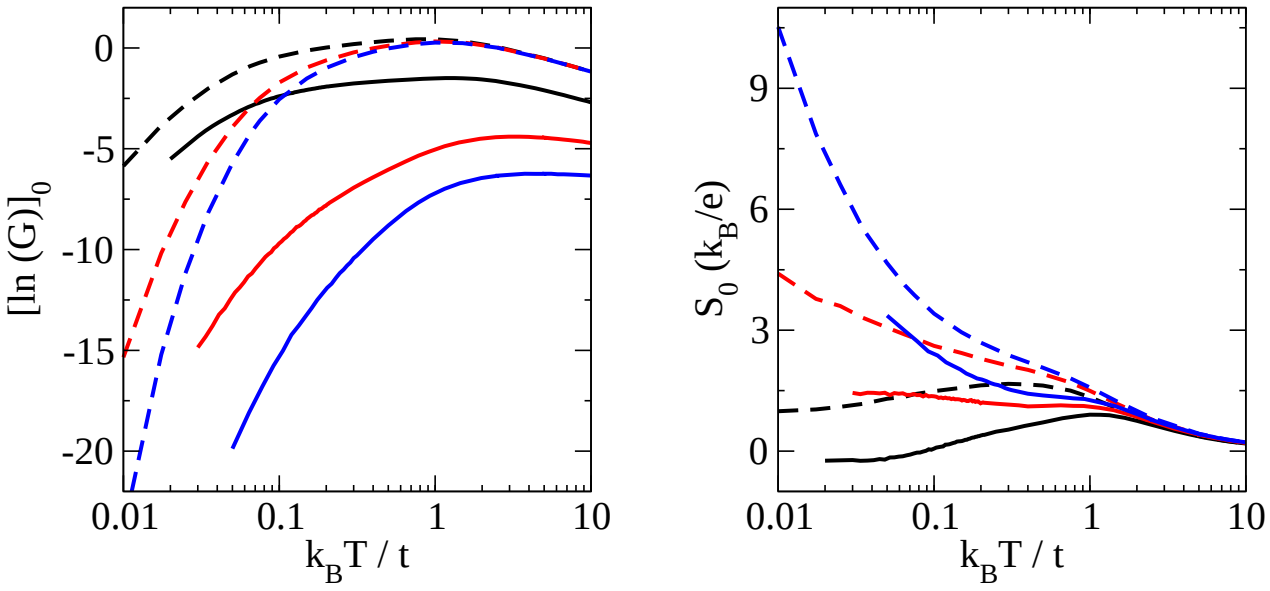


Figure 4.8: Typical logarithm of electrical conductance (left) and typical thermopower (right) of a disordered nanowire as a function of temperature, and for different values of the applied gate voltage. Full lines refer to the approximation in which all $\xi_i = \xi(\mu)$, while dashed lines refer to the improved theory in which the energy dependence of $\xi_i = \xi(E_i)$ is taken into account for evaluating the transition rates. In each set, from the top to the bottom (left panel) or reversely (right panel), the curves correspond to $V_g = 1.9t$ (black), $V_g = 2.1t$ (red) and $V_g = 2.2t$ (blue). Other parameters: $L = 200$, $W = t$, $\mu = 0$, $\gamma_e = \gamma_{ep} = t$.

conductance and the typical thermopower as functions of the temperature in the two cases: Fig. 4.8 shows that there is no *qualitative* difference between the curves computed using $\xi(\mu)$ (full lines) and $\xi(E)$ (dashed lines). The main effect of taking into account the localization length energy dependence is that, according to Eq.(4.10), all transitions toward the more delocalized states around the band center are favoured. This leads to a much better conductance especially at low temperatures, where the difference could be of several orders of magnitude; on the other hand, the effect on the thermopower is weaker.

Chapter 5

Arrays of Parallel Nanowires

Contents

Summary of chapter 5 . . . . . **100**

5.1 Model and method **101**

5.2 Fluctuations **103**

5.3 Power factor and figure of merit **103**

5.3.1 On the dependency on the couplings γ_e and γ_{ep} 107

5.3.2 Size effects 108

5.4 Hot spots cooling **109**

Summary of chapter 5

In this chapter we show how the fundamentals of thermoelectric transport in the activated regime studied in the previous chapter can be exploited to realize a performant thermoelectric device.

In section 5.1 we discuss the model, which is an extension of the one studied in the previous chapter when not just one, but rather an array of disordered semiconductor nanowires is considered. In this case, the transport coefficients depends on the total charge and heat currents, which are found by summing over all the nanowires under the hypothesis that they can be considered as independent.

In section 5.2 we show that when a sufficiently large number M of nanowires is stacked in parallel, the total conductance scales as M times the typical conductance of a *single* wire, while the total thermopower self-averages to the typical value of a single nanowire thermopower. This makes hence possible to design a device allowing for a good thermoelectric conversion, still keeping a finite electrical conductance.

In section 5.3 we summarize the first main result of this chapter, namely the characterization of the power factor $\mathcal{Q}$ and the figure of merit ZT of our device. We show that in a certain regimes of temperatures and applied gate voltage, a compromise between the thermopower and the conductance favors a large (scalable) power factor, while keeping a finite ZT. The difference between considering deposited or suspended nanowires and its impact on the figure of merit is discussed. In addition, we check the robustness of our results upon varying some microscopic parameters of the system (the couplings to the electrodes and to the phonon bath) and the system size.

Finally, in section 5.4 we report an intriguing feature of our setup, namely the possibility of generating and controlling hot and cold spots near the boundaries of the substrate, an effect which could be very interesting for cooling issues in electronic circuits.

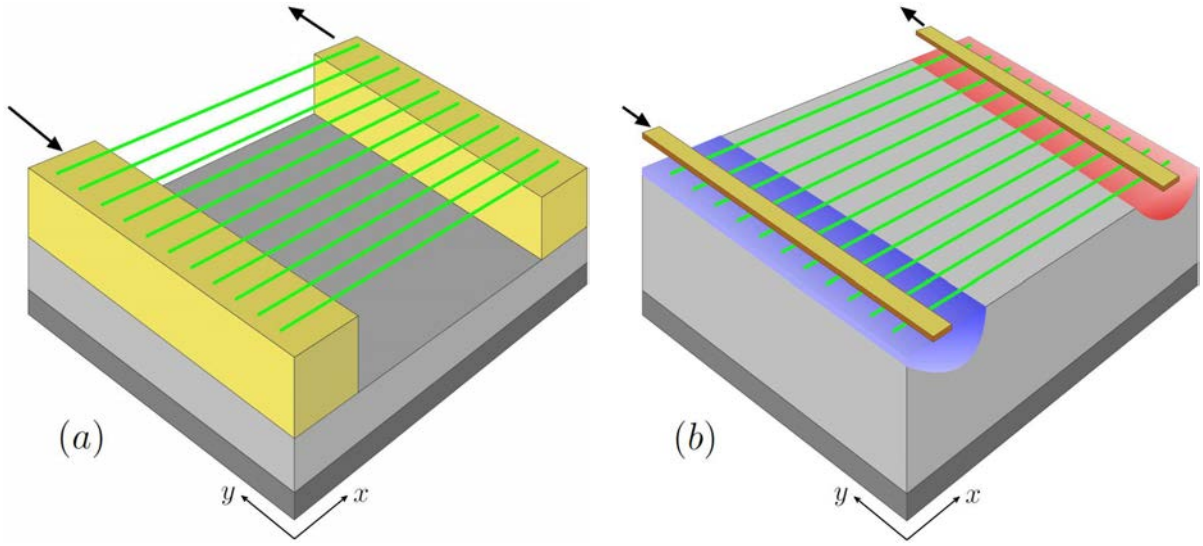


Figure 5.1: Array of suspended (a) and deposited (b) parallel NWs in the FET configuration. The NWs are drawn in green, the two metallic electrodes in yellow, the substrate in grey and the back gate in dark grey. The blue [red] spot in (b) indicates the region of the substrate that is cooled down [heated up] in the phonon-assisted activated regime, when a charge current is enforced to flow from the left electrode to the right one and the gate voltage is tuned so as to probe the bottom edge of the NWs impurity band. In both cases, black arrows denote the sense of current flow.

5.1 Model and method

A typical realization of the system is a set of doped semiconductor NWs, arranged in parallel and attached to two metallic electrodes. The NWs can be either suspended [22, 89, 166] or deposited onto an electrically and thermally insulating substrate [20, 85]. A metallic gate beneath the sample is used to vary the carrier density inside the NWs. This setup is referred to as field effect transistor (FET) configuration and is sketched in Fig. 5.1. If the thermopower or the thermal conductances are to be investigated, an heater (not shown in Fig. 5.1) is added on one side of the sample to induce a small temperature gradient between the electrodes.

We focus on the phonon-assisted activated regime introduced in the previous chapter and assume *(i)* that transport takes place in the NWs impurity band only and *(ii)* that the substrate, or the NWs themselves if they are suspended, act as a phonon bath to which NWs charge carriers are well coupled. This means that we consider an intermediate temperature regime, where thermal energy $k_B T$ is high enough to allow inelastic hoppings between localized states of different energies in the NWs, but also low enough to neglect the presence of other bands. As detailed in the previous chapter and in Refs. [20, 84, 85], we solve numerically the Miller-Abrahams random resistor network problem [113] to deduce S, G, and K^e. The method also allows us to identify the regions where heat exchanges dominantly take place.

We note before going further that parallel NW arrays can nowadays be realized in very different manners, with numerous materials [7, 56, 141, 183, 192, 196]. Architecture and/or material specific predictions, though very important for practical engineering purposes, are however *not* our concern at present. On the contrary, our goal is to avoid specialization and reach conclusions which are as general as possible. We shall therefore rely on a bare-bone but widely applicable model devised to capture the essentials of the physics we are interested in.

Physically, we model each nanowire *exactly* as did in the previous chapter (Eq. (4.15)); in particular, we properly take into account the energy dependence of the localization lengths ξ_i of each electronic state i with eigenenergy E_i. Furthermore, we neglect *inter*-wire hopping by assuming independent nanowires.

The NWs are attached to two electrodes (electronic reservoirs) L and R, and to a phonon bath, so that globally the system is in a three-terminal configuration. Particles and heat(energy) can be exchanged with the electrodes, but only heat(energy) with the phonon bath. At equilibrium the whole system is thermalized at a temperature T and both electronic reservoirs are at electrochemical potential μ (taken as zero energy reference, $\mu \equiv 0$). By applying a voltage and/or temperature bias between the two electrodes, one generates an electron flow through the NWs. Hereafter we consider the linear response regime, i.e. we assume $\delta\mu$, $k_B\delta T \ll k_B T$, with $\delta\mu \equiv \mu_L - \mu_R$ and $\delta T \equiv T_L - T_R$.

We treat the (inelastic) activated regime where transport through the NWs takes place via phonon-assisted hopping between localized states in the impurity band [20, 85]. Charge carriers are assumed to tunnel elastically from reservoir $\alpha = L, R$ into some localized states i whose energies E_i are located in a window of order $k_B T_\alpha$ around μ_α. They then proceed via phonon-assisted hops until they reach the opposite end, finally tunnelling out into the other contact. The carriers' typical hop along the NWs is of the order of the Mott length $L_M = (\xi(\mu)/2\nu(\mu)T)^{1/2}$ in space and of the Mott hopping energy $\Delta = k_B\sqrt{TT_M}$ in energy, $\nu(\mu)$ being the NW density of states per unit length evaluated at μ and $T_M = 2/\xi(\mu)\nu(\mu)$ the Mott temperature. At the lowest temperatures considered our numerical simulations, $\xi(\mu) \ll L_M \ll L$ and transport is of Variable-Range Hopping (VRH) type. An increasing temperature shortens L_M, leading eventually to the Nearest Neighbors Hopping (NNH) regime where $L_M \approx \xi(\mu)$. The crossover temperature between the two regimes is approximately given by T_M.

In both cases, electrical and heat currents are calculated by solving the corresponding random-resistor network problem [3, 85, 113]. The method is summarized in chapter 4 following the lines of Ref. [85]. We point out that the important input parameters the rate γ_e quantifying the coupling between the localized states in the NWs and the extended states in the reservoirs, and the rate γ_{ep} measuring the coupling to the phonons present in the NWs and/or in the substrate. Also, we recall that we go beyond the usual approximation [3, 85, 113]

which consists in neglecting ξ_i's variations from state to state ($\xi_i \approx \xi(\mu)$) because this approximation does not hold in the vicinity of the impurity band edges, where the localization lengths vary strongly with the energy. Following Ref. [20], we account for the different localization lengths $\xi_i \neq \xi_j$ when solving the random resistor network problem. We compute eventually the particle and heat currents flowing toward the system. In linear response, they are related to the small imposed bias $\delta\mu$ and δT through the Onsager matrix [32]. The latter allow us to deduce G, K^e and S.

5.2 Fluctuations

The typical conductance G_0 and thermopower S_0 of a *single* disordered NW was studied in the previous chapter (see also [20]). They are defined as the *median* of the distribution of $\ln G$ and S, obtained when considering a large statistical ensemble of disorder configurations. Indeed, it is known that both G and S exhibit large mesoscopic fluctuations, expecially at lower temperatures [20, 85, 143, 158], the magnitude of the fluctuations being proportional to $\sqrt{T_M/T}$[85, 158], where T_M is the Mott temperature.

In Fig. 5.2 we show that if the system is made of a sufficiently large number $M > M^*$ of parallel nanowires, the *overall* electrical conductance scales as the number of wires times the typical value ($G \approx M\, G_0$), while the thermopower averages out to the typical behavior of that of a single wire ($S \approx S_0$)[1]. For completeness the mean values are also shown and seen to be a less accurate estimate. As expected, convergence is faster at higher temperatures.

5.3 Power factor and figure of merit

In this section we investigate the power factor $\mathcal{Q} = S^2 G$ and the electronic figure of merit $Z_e T = S^2 G T / K^e$. We recall that the former is a measure of the maximal output power $\dot{W}_{max} = \mathcal{Q}(\delta T)^2/4$ that can be extracted from the setup when it works as a thermal engine [13]. The latter is an upper bound on the total figure of merit, obtained when the phononic contribution K^{ph} to the thermal conductance is neglected.

An immediate consequence of the previous finding is that

$$\mathcal{Q} \approx M\, S_0^2 G_0 \quad \text{and}$$
$$Z_e T \approx S_0^2 G_0 T / K_0^e,$$

providing M is large enough (at least a few dozens of NWs). Therefore, $\mathcal{Q}$ can be enhanced by stacking a large number M of NWs in parallel *without* affecting $Z_e T$. In Fig. 5.3, we

[1] Identical results have been obtained for $K^e \approx M\, K_0^e$ (not shown in Fig. 5.2).

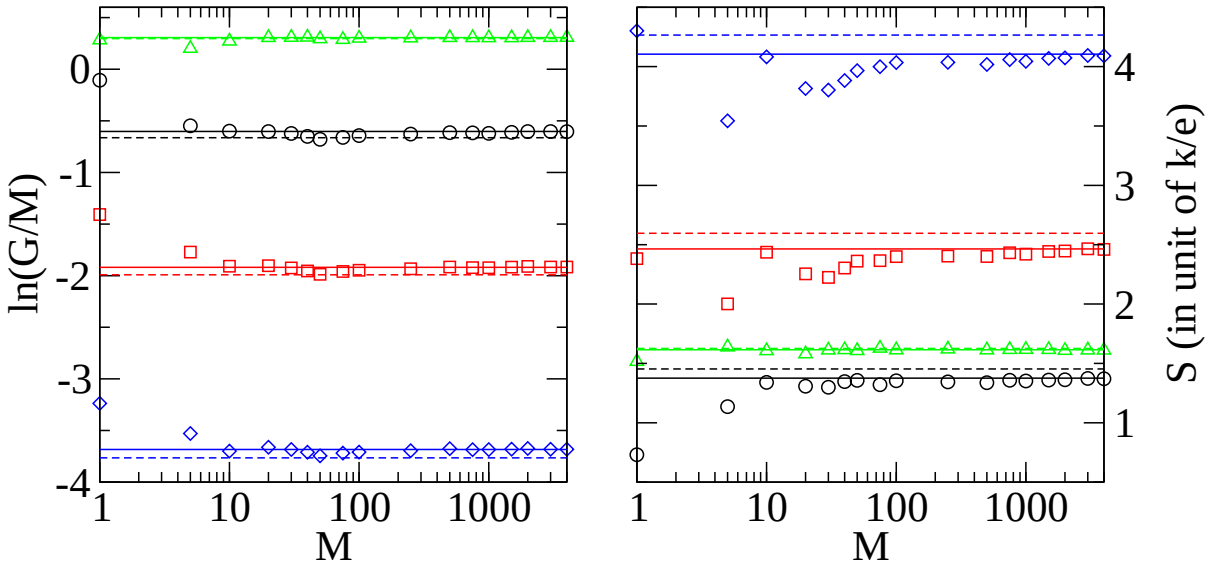


Figure 5.2: Convergence of G/M (left) and S (right) with the number M of parallel NWs. Symbols correspond to $V_g = 1.9t(\circ)$, $2.1t(\square)$ and $2.3t(\diamond)$ at $k_BT = 0.1t$, and $Vg = 1.9t$ at $k_BT = 0.5t(\triangle)$. The horizontal lines indicate the corresponding mean values (dashed lines) and typical values (full lines) of $\ln G$ and S of a single wire ($M = 1$). Parameters: $W = t$, $\gamma_e = \gamma_{ep} = t$ and $L = 450$.

show how the asymptotical values of $\mathcal{Q}/M$ and Z_eT depend on the gate voltage V_g and on the temperature T.

Data are plotted for a given set of parameters $L = 450, W = t$ and $\gamma_e = \gamma_{ep} = t$ (in unit of $\hbar$). However, it turns out that $Q/(\gamma_e/t)$ and Z_eT do not vary by more than 30%, in the range of temperatures $k_BT > 0.2t$ and gate voltage explored in Fig. 5.3, when γ_e and γ_{ep} are varied between $0.1t$ and $10t$ with the constraint $\gamma_{ep} \geq \gamma_e$. In sections 5.3.1 and 5.3.2 we discuss further details concerning how the results depend upon the couplings γ_e and γ_{ep}, and on the length L of the NWs. We will show that they are robust in a certain regime of parameters of interest, and we thus argue that the numerical results shown in Fig. 5.3 can be discussed at a semi-quantitative level.

We observe in the left panel of Fig. 5.3 that the power factor is maximum for μ around the impurity band edge (full black line) and for temperatures close to the onset of the NNH regime ($T \sim 0.5$K). This range of parameters gives the best compromise between two opposite requirements: maximizing the thermopower on one hand (hence favoring low temperatures and large values of V_g) and keeping a reasonable electrical conductance on the other (favoring instead higher temperatures and $V_g \approx 0$).

Recalling Eqs. (4.18) and (4.23b) from the previous chapter for $(\ln G)_0$ and S_0:

$$(\ln G)_0(T) \sim -\frac{E_A}{k_B T} - \bar{\alpha}\frac{\Delta(T)}{T}, \tag{5.1}$$

$$S_0 = \frac{k_B}{e}\left(\frac{E_A}{k_B T} + \frac{\Delta(T)}{2k_B T}\right), \tag{5.2}$$

we may observe that outside the band the only dependency on the gate voltage in these expressions is through the first terms, since $\Delta(T)$ does not depend on V_g in this regime. E_A is a measure of the distance between the chemical potential of the electrodes and the band edge, and thus it depends linearly on V_g. This fact, together with the observation that $\ln G_0 \sim -S_0$, makes it a rather simple task to maximize the power factor $\mathcal{Q}_0 = G_0 S_0^2$ with respect to the gate voltage, at fixed temperature.

We have:

$$\mathcal{Q}_0' = S_0^2 G_0' \left(\frac{G_0'}{G_0} + 2\frac{S_0'}{S_0}\right) \sim S_0^2 G_0' S_0' \left(-1 + \frac{2}{S_0}\right), \tag{5.3}$$

allowing us to predict that $\mathcal{Q}$ is maximal when $S_0 = 2\,k_B/e \approx 0.2\,mV\,K^{-1}$. The iso-curve corresponding to this value is plotted in the $(V_g, k_B T)$-plane in Fig. 5.3(left) [black dashed line], and does indeed lie with a good approximation inside the region of maximal $\mathcal{Q}$.

A comparison between the left and right panels of Fig. 5.3 reveals that, in the range of parameters corresponding to the best power factor (say, $V_g \sim 2.5t$ and $k_B T \sim 0.6t$), $Z_e T \simeq 3$, a remarkably large value. Obviously, much larger values of $Z_e T$ could be obtained at lower temperatures or deep outside the band, but they are not of interest for practical purposes since in those regions $\mathcal{Q}$ is vanishing.

Hereafter, we discuss the order of magnitude of the outcome that can be expected from the device. We assume that the substrate (or the NWs themselves if they are suspended) supply enough phonons to the NWs charge carriers in order to ensure that $\gamma_{ep} \gtrsim \gamma_e$. Besides, we keep explicit the γ_e-linear dependency of $\mathcal{Q}$ (and of K_0^e that will be soon needed). In practice, γ_e depends on the quality of the metal/NW contact. We estimate it to be approximately within the range $0.01 - 1$ in unit of $t/\hbar$ (which gives $\gamma_e \approx 0.02 - 2 \times 10^{13}\,\mathrm{s}^{-1}$ for $t/k_B \approx 150\,\mathrm{K}$). For the sake of brevity, we now introduce the dimensionless number $\tilde{\gamma}_e = \gamma_e \hbar/t$. We focus on the region of Fig. 5.3(left) where the power factor is maximal and evaluate the typical output power and figure of merit than can be hopped in this region. We first notice that the maximum values of power factor $\mathcal{Q}/M \approx 4k_B^2/h$ in Fig. 5.3(left), obtained with $\tilde{\gamma}_e = 1$, would yield in general $\mathcal{Q} \approx 7\tilde{\gamma}_e \times 10^{-7}\,\mathrm{W.K}^{-2}$ for a 1-cm wide chip with typically $M \approx 10^5$ wires in parallel, hence $P_{max} \approx 20\tilde{\gamma}_e\,\mu\mathrm{W}$ for a small temperature bias $\delta T \approx 10\,\mathrm{K}$. In this region, large value $Z_e T \approx 3$ is obtained but to estimate the total figure of merit $ZT = Z_e T/(1 + K^{ph}/K^e)$, the impact of the phononic thermal conductance K^{ph} must also be taken into account.

To limit the reduction of ZT by phonons, the setup configuration with suspended nanowires is preferable (Fig. 5.1(a)). In that case, $K^{ph} \approx MK_0^{nw}$ only, with K_0^{nw} being the typical phononic thermal conductance of a single NW. It has to be compared with $K^e \approx MK_0^e$. Introducing rather the corresponding conductivities κ's, we have to estimate the ratio $K^{ph}/K^e \approx$

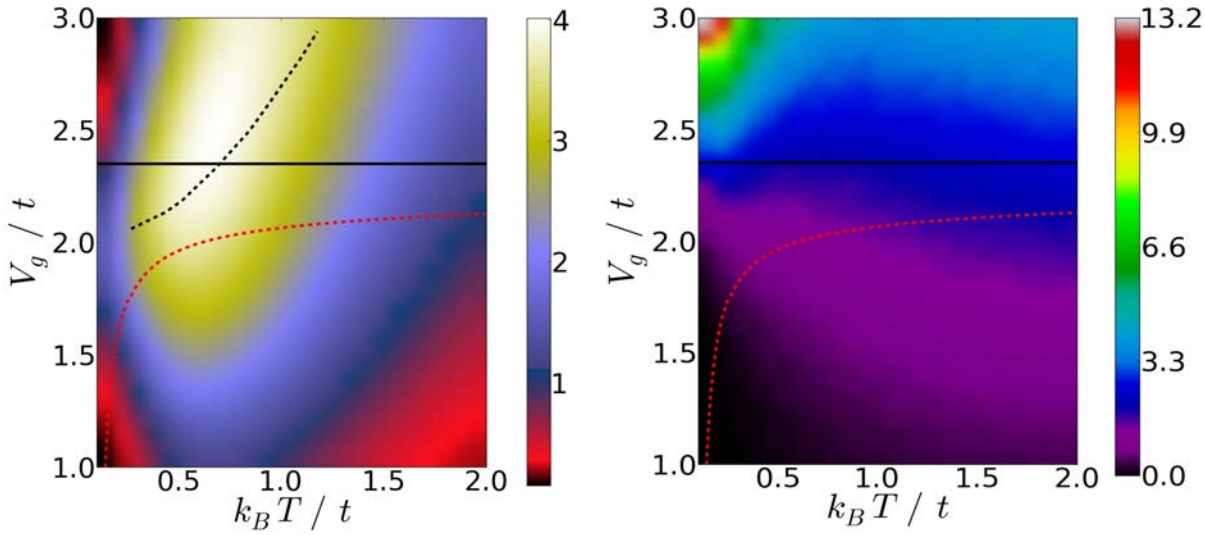


Figure 5.3: Rescaled power factor $\mathcal{Q}/M$ in unit of $k_B^2/\hbar \approx 1.8 \times 10^{-12} W.K^{-2}$ (left panel) and electrical figure of merit $Z_e T$ (right panel) as a function of $k_B T$ and V_g (both in unit of t). Data are shown in the large M limit ($M = 150$) where both quantities have converged. Increasing V_g allows to scan the impurity band from the inside (below the horizontal full lines) to the outside (above). The black dashed line in the left panel indicates the contour along which $S_0 = 2k_B/e$, and lies within the region of maximal power factor (see text). The red dashed line in both panels is the Mott temperature (see Eq. (4.3) and Fig. 4.3), separating the Nearest Neighbor Hopping from the Variable Range Hopping regimes. Parameters: $W = t, \gamma_e = \gamma_{ep} = t$ and $L = 450$.

κ_0^{nw}/κ_0^e. Our numerical results show $K_0^e \approx 1.5\tilde{\gamma}_e k_B t/\hbar$ in the range of interest where $\mathcal{Q}$ is maximal and $Z_eT \approx 3$ (at $V_g = 2.5t$ and $k_BT = 0.6t$, keeping other parameters in Fig. 5.3 unchanged). Taking $t/k_B \approx 150\,\mathrm{K}$, this yields $\kappa_0^e \approx 1\tilde{\gamma}_e\,\mathrm{W/(K.m)}$ for NW length and diameter of $1\,\mu$m and 20 nm respectively, while the thermal conductivity of silicon NWs of similar geometry was measured around $\kappa_0^{nw} \approx 2\,\mathrm{W/(K.m)}$ at $T \approx 100\,\mathrm{K}$ [102]. We thus evaluate for suspended nanowires $ZT \approx Z_eT/(1+2/\tilde{\gamma}_e)$ *i.e* $ZT \approx 0.01-1$ for $Z_eT \approx 3$ and $\tilde{\gamma}_e = 0.01-1$. Obviously, maximizing γ_e turns out to be an important condition for achieving high $\mathcal{Q}$ and ZT. However, keeping a large $\gamma_{ep} \gtrsim \gamma_e$ is also preferable to avoid deterioration of $\mathcal{Q}$ and Z_eT. If the NWs themselves do not ensure a large γ_{ep}, the use of a substrate providing phonons is to be envisaged. It will nevertheless add a detrimental contribution K^{sub} to K^{ph}. Writing

$$\frac{Z}{Z_e} = \left[1 + \frac{\kappa^{sub}\Sigma^{sub} + M\kappa_0^{nw}\Sigma^{nw}}{M\kappa_0^e\Sigma^{nw}}\right]^{-1}, \tag{5.4}$$

with κ^{sub} the substrate thermal conductivity, and $\Sigma^{sub[nw]}$ the cross-section of the substrate [NW], and considering for instance a NW array of 20 nm wire diameter and 40% packing density, deposited on a 200 nm thick silicon dioxide substrate with $\kappa^{sub} \approx 0.7\,\mathrm{W/(K.m)}$ at $T \approx 100\,\mathrm{K}$ [80], we get

$$ZT \approx \frac{Z_eT}{1 + 20/\tilde{\gamma}_e}. \tag{5.5}$$

Note that smaller values of the corrective factor to Z_eT could be obtained for other substrates with lower K^{sub} (Silica aerogels, porous silica [75, 153], very thin substrate layer) but they will not necessary guarantee the same value of γ_{ep}. This illustrates that particular attention has to be paid to phonon engineering of the NWs and the substrate in order to find adequate balance between large γ_{ep} and low K^{ph}.

5.3.1 On the dependency on the couplings γ_e and γ_{ep}

In this section, we investigate how the transport coefficients G, K^e and S, the power factor $\mathcal{Q} = S^2G$ and the electronic figure of merit $Z_eT = S^2GT/K^e$ depend upon varying the couplings γ_e and γ_{ep} of the localized states with the electrodes and the phonon bath, respectively.

We introduce the notation $\alpha \equiv \gamma_{ep}/\gamma_e$. We first notice that if α is kept fixed, the electrical conductance G and the electronic thermal conductance K^e are strictly proportional to γ_e, while the thermopower S is independent of it. This behavior is a direct consequence of the formulation of the random resistor network problem and can be seen at the stage of writing the equations (see Ref. [20]), before solving them numerically. Therefore, for any fixed α, $\mathcal{Q}/\gamma_e$ and Z_eT are necessarily independent of the choice of γ_e. We thus find that G/γ_e, K^e/γ_e, S, $\mathcal{Q}/\gamma_e$ and Z_eT are functions of the single parameter α, and not of the couple of parameters γ_e and γ_{ep} separately. Those functions are plotted in Fig. 5.4(a)-(c) for two different temperatures. The conductances, the power factor and the figure of merit increase with α (as long as lack of phonons is a limiting factor to transport through the NWs), while

the thermopower decreases. All of them tend to saturate for $\alpha \gtrsim 1$. This shows us, *inter alia*, that $\mathcal{Q}/\gamma_e$ and Z_eT are essentially independent of γ_e and γ_{ep} if $\gamma_{ep} \gtrsim \gamma_e$ and only deviate slowly from this limit if $\gamma_{ep} < \gamma_e$. Such a robustness of $\mathcal{Q}/\gamma_e$ and Z_eT to variations of γ_e and γ_{ep} reinforces the impact of the results discussed in this chapter.

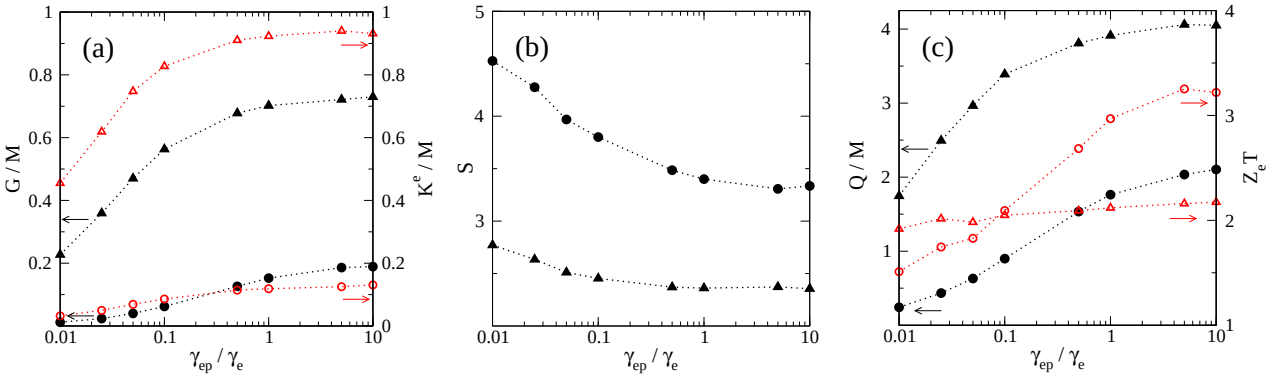


Figure 5.4: (Color online) Dependency of G, K^e, S, $\mathcal{Q}$ and Z_eT on the ratio γ_{ep}/γ_e. (a) Electrical (G/M, black full symbols) and thermal (K^e/M, red empty symbols) conductances, in unit of $e^2/\hbar$ and $k_Bt/\hbar$ respectively. (b) Thermopower in unit of k_B/e. (c) $\mathcal{Q}/M$ in unit of $k_B^2/\hbar$ (black full symbols) and Z_eT (red empty symbols). In all panels, different symbols correspond to $k_BT = 0.2t$ (circles) and $k_BT = 0.5t$ (triangles), while lines are guides to the eye. Data have been plotted for a given set of $M = 150$ parallel NWs of length $L = 450a$, with $\gamma_e = t/\hbar$, $W = t$ and $V_g = 2.4t$. Note that when $\gamma_{ep} \gtrsim \gamma_e$ all these coefficients are nearly constant.

5.3.2 Size effects

We have investigated the effects on the various transport coefficients G, K^e and S, the power factor $\mathcal{Q}$, and the electronic figure of merit Z_eT, of varying the size of the nanowires. The results are shown in Figs. 5.5(a)-(d), for three values of the temperatures $k_BT = 0.1t, 0.5t$ and $1.0t$, and for two configurations corresponding to bulk ($V_g = t$) and edge transport ($V_g = 2.5t$).

We observe that they are essentially always size-independent, for μ inside the impurity band and also around its edge. The only exception the electrical conductance at low temperatures and in the case of edge transport: this causes the electronic figure of merit Z_eT to decrease in this regime ($\circ$ in Fig. 5.5(d)) roughly as $1/L$. The reason is that a low T implies a small Mott hopping energy Δ, and this prevents electrons to make large hops in energy at the impurity band edge, thus limiting their mobility [20]. However, being interested in the regime of temperatures where the power factor is largest ($k_BT \simeq 0.5t$), this does not rise any problem. Also, we note that the small fluctuations observed especially at smaller sizes are a consequence of having taken a finite number of parallel nanowires (M=150): they would vanish in the limit M$\rightarrow \infty$ due to self-averaging.

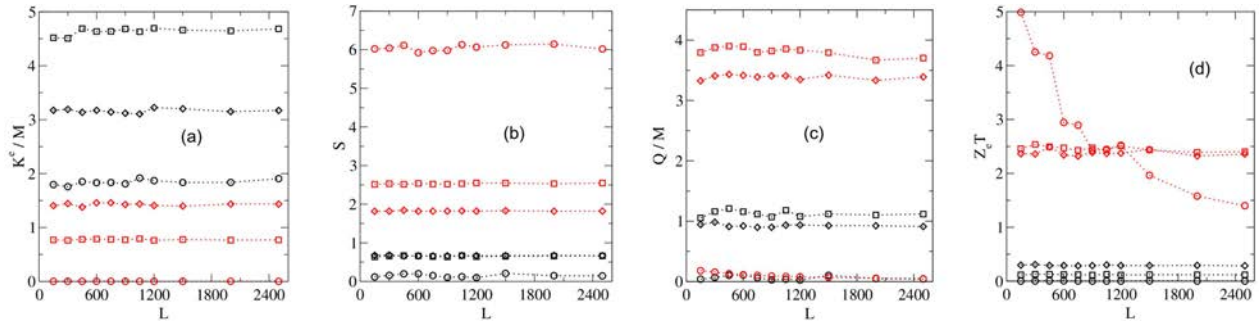


Figure 5.5: Behavior of the transport coefficients as function of the NWs size L (in units of the spacing a). Panels from left to right show (a) the rescaled electronic contribution to the thermal conductance K^e, (b) the thermopower S (in units of k_B/e)), (a) the rescaled power factor $\mathcal{Q}$ (in unit of $k_B^2/\hbar$) and (d) the (electronic) figure of merit Z_eT. In all the four panels, different symbols correspond to $k_BT = 0.1t$ (circles), $k_BT = 0.5t$ (squares) and $k_BT = t$ (rhombus), while different colors refer to the case of bulk transport ($V_g = t$, black) and edge transport ($V_g = 2.5t$, red). Dotted lines are guides to the eye.

5.4 Hot spots cooling

In conclusion to this chapter, we consider the deposited setup sketched in Fig. 5.1(b) and assume a constant temperature T everywhere. We emphasize an intriguing feature of this setup, that is the possibility to generate and control hot and cold spots close to the boundaries of the substrate by applying a voltage bias $\delta\mu/e$. This effect turns out to be a direct consequence of the mechanism of heat exchange between electrons in the NWs and phonons in the substrate. Indeed, given a pair of localized states labelled i and j inside a NW, with energies E_i and E_j respectively, the heat current absorbed from(released to) the phonon bath by an electron in the transition $i \to j$ is [20]

$$I_{ij}^Q = (E_j - E_i)\, I_{ij}^N, \tag{5.6}$$

I_{ij}^N being the hopping particle current between i and j. The overall hopping heat current through each localized state i is then found by summing over all but the i-th states:

$$I_i^Q = \sum_j I_{ij}^Q = \sum_j (E_j - E_i) I_{ij}^N. \tag{5.7}$$

Here, with our convention, the heat current I_i^Q is positive when it enters the NWs at site i, and negative otherwise. Since the energy levels E_i are randomly distributed, the I_i^Q's (and in particular their sign) fluctuate from one site to another. Therefore, for data analysis, we choose to sum up in a single term $\mathcal{I}_{x,y}^Q$ all the contributions I_i^Q coming from states i located in an area of size $\Lambda_{ph} \times \Lambda_{ph}$ around the point of coordinates (x, y). Practically, this means that we map the 2D array of parallel NWs on a square grid and for each square of size Λ_{ph}^2 centered around (x, y), we calculate the net heat current $\mathcal{I}_{x,y}^Q$ entering the NWs. Physically, the scale

Λ_{ph} is the (inelastic) phonon mean free path, i.e. the length on which thermalization takes place in the reservoir of phonons (here the substrate). More details about how to estimate this length scale are gathered in a small digression below. Local fluctuations of the temperature due to the exchange of heat currents described above are observable near the interface between the substrate and the NWs only *within* Λ_{ph}: if $\mathcal{I}^Q_{x,y} > 0$ [< 0], the region of the substrate beneath (x, y) is cooled [heated]. Beyond Λ_{ph}, the substrate definitely thermalizes at its equilibrium temperature T.

In Figs. 5.6 (a) and (b), we show how $\mathcal{I}^Q_{x,y}$ vary spatially with the positions x, y in the 2D array of parallel NWs. Note that data are plotted for an array of $M = 150$ NWs of length $L = 1500a$, assuming a distance $15a$ between the NWs and $\Lambda_{ph} = 150a$ (see the short digression below). This choice corresponds to an estimation of $a \approx 3.2\,\mathrm{nm}$ in highly doped silicon nanowires, $t \approx 150\,\mathrm{K}$, and $\Lambda_{ph} = 480\,\mathrm{nm}$ for silicon dioxide substrate at the temperature $T = 0.25t \approx 37.5\,\mathrm{K}$. Moreover, the interspacing $15a$ comes from the assumption of NWs of $10nm$ diamaters with packing density 20%. Two cases are compared in the figure: on the left (a), the situation in the absence of a gate voltage, when charge carriers tunnel in/out the electrodes at μ in the *center* of the NWs impurity band; and on the right (b), the opposite situation when a large gate voltage is applied in order to probe at μ the *bottom* of the NWs impurity band. All other parameters are fixed.

In the former case, the heat map show some puddles of positive and negative $\mathcal{I}^Q_{x,y}$, corresponding respectively to cooled and heated regions in the substrate below. They are the signature of random absorption and emission of substrate phonons by the NWs charge carriers, all along their propagation through the NWs around the energy μ stuck here to the band center. In the latter case, the regions of positive and negative $\mathcal{I}^Q_{x,y}$ are respectively confined to the entrance and exit of the NWs. This is due to the fact that charge carriers entering the NWs at μ around the bottom edge of the impurity band only find available states to jump to (at a distance L_M in space and Δ in energy, $L_M \approx 10a$ and $\Delta \approx 1.1t$ here) *above* μ. Therefore, they need to absorb phonons to reach states located at higher energies (blue region). After a few hops, they get to the band center and can continue to propagate, sometimes by absorbing phonons, sometimes by emitting phonons (white region). When they reach the other end, they have to release heat to the substrate (red region) in order to come back down to the energy μ at which they tunnel out to the right electrode. As a consequence, the regions of the substrate located below the NWs extremities are cooled on the source side and heated on the drain side (see Fig. 5.1(b)).

In Figs. 5.6 (c) and (d) we show the same data as in panels (a) and (b), the difference being the temperature, which here is doubled to $T = 0.5t \approx 75\,\mathrm{K}$. According to the prescription briefly discussed in the digression below, we estimate Λ_{ph} to be reduced to $75a$ in this case. The fact that the surface inside which the heat currents are summed up is now smaller is

compensated by a smoothing of the I_i^Q's fluctuations at larger temperature. This makes the hot and cold spots still clearly visible and well-defined.

Estimation of the phonon mean free path

The thermalization length is given by the inelastic phonon mean free path Λ_{ph}, because this is the length defining the interaction of a phonon with the phonon reservoir. This mean free path may be different for different wavelengths, and while it does not change much around room temperatures, it can vary significantly at lower (still not vanishing) temperatures. It is possible to relate Λ_{ph} to the *dominant* phonon wave length [137] as $\Lambda_{ph} = 300\lambda_{ph}^{dom}$, where the coefficient 300 is for SiO_2 and may be different for other materials. This allows the calculation of the mean free path, once λ_{ph}^{dom} is known. According to Refs. [91, 199], the latter can be estimated as

$$\lambda_{ph}^{dom} \simeq \frac{hv_s}{4.25k_BT}, \tag{5.8}$$

where h is the Planck constant. Assuming $v_s = 5300\,m/s$ the sound velocity in SiO_2 [199], we can easily deduce $\lambda_{ph}^{dom} \simeq 0.2\,nm$ from which $\Lambda_{ph} \simeq 60\,nm$ at room temperature T=300K. Then, according to the temperature dependence in Eq. (5.8), we infer that $\lambda_{ph} \approx 240nm$ at T=75K, a temperature which roughly correspond to $0.5t$ in unit of the energy scale t appearing in the Hamiltonian, having assumed $t/k_B \approx 150K$. We shall stress that this is nothing but a rough extimation: the real value of Λ_{ph} may differ from our prediction by a small numerical factor, which however is not important within our qualitative approach.

We point out that the maximum values of the heat currents $\mathcal{I}_{x,y}^Q$ exchanged locally between the NWs and the substrate are roughly of the same order of magnitude with or without the gate (see scale bars in Fig. 5.6). The advantage of using a gate, and of probing the band edges, is the ability to split the regions of positive and negative $\mathcal{I}_{x,y}^Q$ into two well separated spots at the NWs extremities. One can then imagine to exploit the cold spot in the substrate to cool down a small hot chip of an electronic circuit put in close proximity (say for instance a cylinder stuck to the side face of the substrate in Figs. 5.1(b) and (d)). On the other hand, we stress to avoid confusion that the assumption of elastic tunneling processes between the electrodes and the NWs is not necessary to observe the gate-induced hot/cold spots in the right panel of Fig. 5.6. Indeed, they just result from the fact that charge carriers must pass from an energy μ far away in the electrodes to energy levels around the center of the impurity band inside the NWs, hopping transport being favored there. In our model, heat exchanges take place at the NWs extremities but if phonon emission/absorption was also taken into account in (the ends of) the electrodes, hot/cold spots would only be shifted or spread towards them.

For completeness, we illustrate in Fig. 5.7 an example of the map of the heat currents $\mathcal{I}_{x,y}^Q$ exchanged with the substrate *before* summing the currents within areas of size $\Lambda_{ph} \times \Lambda_{ph}$ at a relatively low temperature $T = 0.05t$, where large fluctuations are expected. In this case, despite being around the band edge, the hot and cold spots are not clearly visible, as the heat currents exhibit rather large fluctuations, assuming possibly positive and negative values everywhere. It becomes hence evident that the formation of the hot and cold spots is a process which takes place only upon summing.

We conclude the discussion by giving an order of magnitude of the cooling power obtained in Fig. 5.6. Assuming again $t \approx 150\,\mathrm{K}$, $\Lambda_{ph} = 480\,\mathrm{nm}$ and $\delta\mu = 10^{-3}t$, we find that a value of $\mathcal{I}^{Q}_{x,y} = 10^{-3}(t^2/\hbar)$ in Fig. 5.6 corresponds to a cooling power density of the order of $2.10^{-10}\,\mathrm{W}.\mu\mathrm{m}^{-2}$. We underline that this order of magnitude is obtained for the set of parameters considered in Fig. 5.6 and right above. It should not be taken *stricto sensu* but only as a benchmark value to fix ideas.

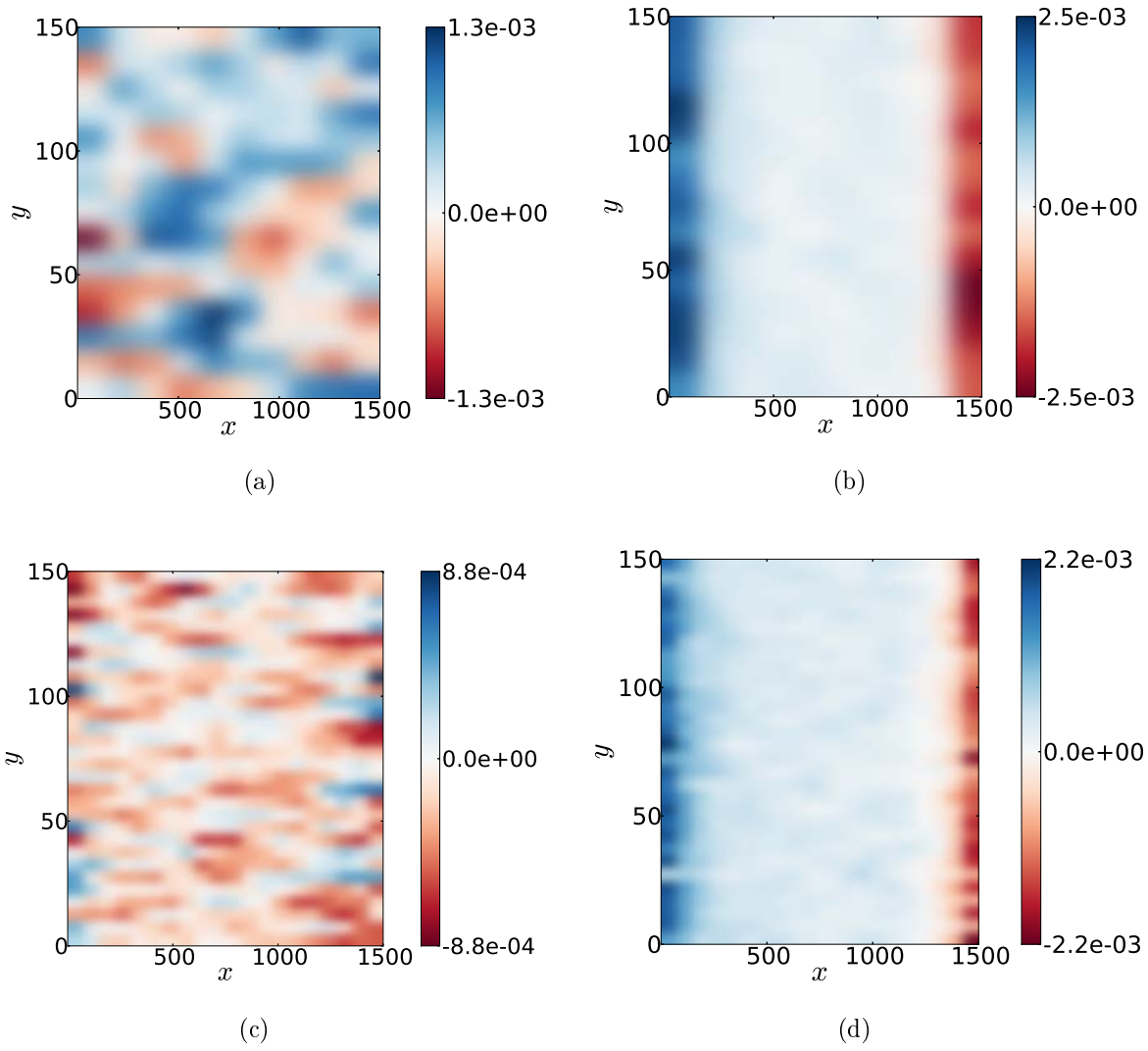


Figure 5.6: Map of the local heat exchanges $\mathcal{I}^Q_{x,y}$ between the nanowires and the phonon bath (substrate), in unit of $t^2/\hbar$. Various panels correspond to different gate voltages and temperatures: $V_g = 0.0$ in (a) and (c), $V_g = 2.25t$ in (b) and (d), $k_BT = 0.25t$ in (a) and (b), $k_BT = 0.5t$ in (c) and (d). The heat currents have been summed inside areas of size $\Lambda_{ph} = 75a$ for $k_BT = 0.5t$ and $\Lambda_{ph} = 150a$ for $k_BT = 0.25t$, as explained in the text. Note that the formation of hot and cold spots at the boundaries of the nanowires is clearly visible when V_g is tuned in order to probe their band edges [(b) and (d)], while no net effect is evident in absence of any gate voltage [(a) and (c)].

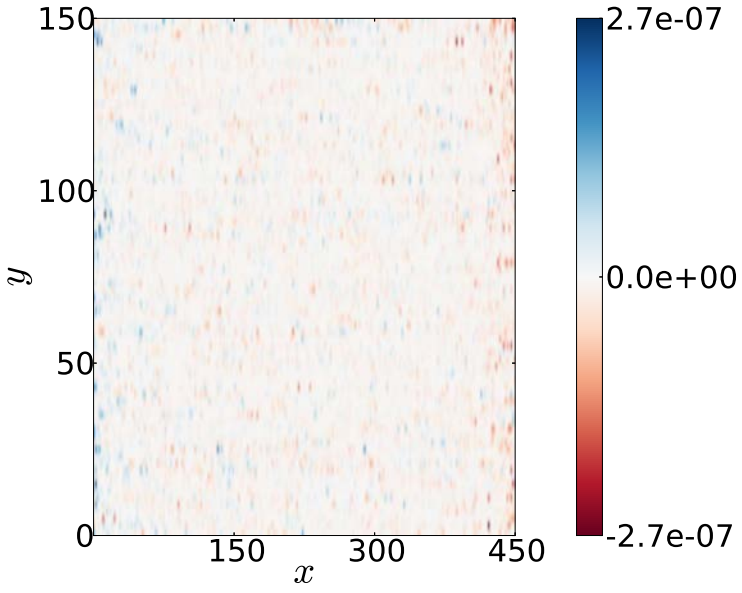


Figure 5.7: Heat current exchanged *locally* between the nanowires and the substrate, as function of the position along the horizontal and the vertical directions, for $k_BT = 0.05t$ and $V_g = 2.25t$. Note that before summing the currents within areas of size equal to the phonon thermalization lengthΛ_{ph}, the presence of hot and cold spots is hidden by the fluctuations.

Chapter 6

Three-terminal Quantum Machines

Contents

Summary of chapter 6 . . . . . **116**

6.1 Linear response for 3-terminal systems **117**

6.1.1 Transport coefficients 117

6.2 Efficiency for 3-terminal systems **120**

6.2.1 Carnot efficiency 121

6.2.2 Efficiency at Maximum Power 122

6.3 Examples **125**

6.3.1 Single dot 126

6.3.2 Double Dot 131

6.4 Appendix **134**

6.4.1 Calculation of the transport coefficients and thermopowers 134

6.4.2 Cholesky Decomposition of the three-terminal Onsager matrix 136

6.4.3 Scattering approach in linear response: the Onsager coefficients . . . 137

6.4.4 Transmission function of a single-level dot 138

Summary of chapter 6

In this chapter we provide a general treatment of the linear response thermoelectric transport for a system in a three-terminal configuration. In most of the investigations found in literature the third terminal is usually treated as a mere probe (i.e. no net flow of energy and charge through it is allowed) [8, 14, 150, 152] or as a bosonic bath, only exchanging energy (and not charge) current with the system [20, 53, 52, 84, 85]. Here we consider the case of three *fermionic* reservoirs, all treated on equal footing. We discuss local and non-local transport coefficients, the latters being naturally requested in a multi-terminal setup, since they connect temperature or voltage biases introduced between two terminals to heat and charge transport among the remaining terminals. Then, we show that the third terminal could be exploited to improve thermoelectric performances with respect to the two-terminal case, by focusing our investigations on the efficiency at maximum power, i.e. when a heat engine operates under conditions where the output power is maximized.

In Section 6.1 we briefly review the linear response (Onsager) formalism for a generic three-terminals setup. We discuss the maximum output power and we trace a derivation of all the local and non-local transport coefficients. In section 6.2 we extend the concept of Carnot bound to the maximum efficiency to the three-terminals setup, and we derive analytical formulas of the efficiency at maximum power in various cases, depending on the flow of the heat currents. These expressions are written in terms of generalized dimensionless figures of merit. This framework will be then applied in Section 6.3 to specific examples in order to illustrate the salient physical picture. In our numerical simulations, we consider a single quantum dot and two dots in series coupled to the three terminals.

6.1 Linear response for 3-terminal systems

We consider a prototypical three-terminal system as depicted in Fig. 6.1: it is characterized by three energy and three particle currents ($J^U_{i=1,2,3}$ and $J^N_{i=1,2,3}$, respectively) flowing from the corresponding reservoirs, which have to fulfill the constraints:

$$\begin{aligned} &\sum_{i=1}^{3} J_i^U = 0 \quad \text{(Energy conservation)} \,, \\ &\sum_{i=1}^{3} J_i^N = 0 \quad \text{(Particle conservation)} \,, \end{aligned} \tag{6.1}$$

(positive values being associated with flows *from* the reservoir *to* the system). In what follows we will assume the reservoir 3 as a reference and the system to be operating in the linear response regime, i.e. set $(T_3, \mu_3) \equiv (T, \mu)$ and write $(T_j, \mu_j) = (T + \Delta T_j, \mu + \Delta\mu_j)$ with $|\Delta\mu_j|/k_B T \ll 1$ and $|\Delta T_j|/T \ll 1$ for $j = 1, 2$, and k_B is the Boltzmann constant. Under these assumptions the relation between currents and biases can then be expressed through the Onsager matrix $\mathbf{L}$ of elements L_{ij} via the identity:

$$\begin{pmatrix} J_1^N \\ J_1^Q \\ J_2^N \\ J_2^Q \end{pmatrix} = \begin{pmatrix} L_{11} & L_{12} & L_{13} & L_{14} \\ L_{21} & L_{22} & L_{23} & L_{24} \\ L_{31} & L_{32} & L_{33} & L_{34} \\ L_{41} & L_{42} & L_{43} & L_{44} \end{pmatrix} \begin{pmatrix} X_1^\mu \\ X_1^T \\ X_2^\mu \\ X_2^T \end{pmatrix} , \tag{6.2}$$

where $X^\mu_{1,2} = \Delta\mu_{1,2}/T$ and $X^T_{1,2} = \Delta T_{1,2}/T^2$ are the generalized forces, and where $J^Q_{1,2} = J^U_{1,2} - \mu_{1,2} J^N_{1,2}$ are the heat currents of the system– the corresponding currents to reservoir 3 being determined from $J^N_{1,2}$ and $J^Q_{1,2}$ via the conservation laws of Eq. (6.1). In our analysis we take $\mathbf{L}$ to be symmetric (i.e. $L_{ij} = L_{ji}\ \forall j \neq i$) by enforcing time reversal symmetry in the problem. We also remind that, due to the positivity of the entropy production rate, such matrix has to be semi-positive definite and that it can be used to describe a two-terminal model connecting (say) reservoir 1 to reservoir 3 by setting $L_{j3} = L_{j4} = L_{3j} = L_{4j} = 0$ for all j.

6.1.1 Transport coefficients

For a two-terminal model the elements of the Onsager matrix $\mathbf{L}$ can be related to four quantities which gauge the transport properties of the system under certain constraints. Specifically these are the electrical conductance G and the Peltier coefficient Π (evaluated under the assumption that both reservoirs have the same temperature), and the thermal conductance K and the thermopower (or Seebeck coefficient) S (evaluated when no net charge current is flowing through the terminal). As we shall see in the following, when generalized to the multi-terminal model, these quantities naturally yield to the introduction of non-local coefficients describing how a bias set between two given reservoirs influences the transport among the remaining ones [111].

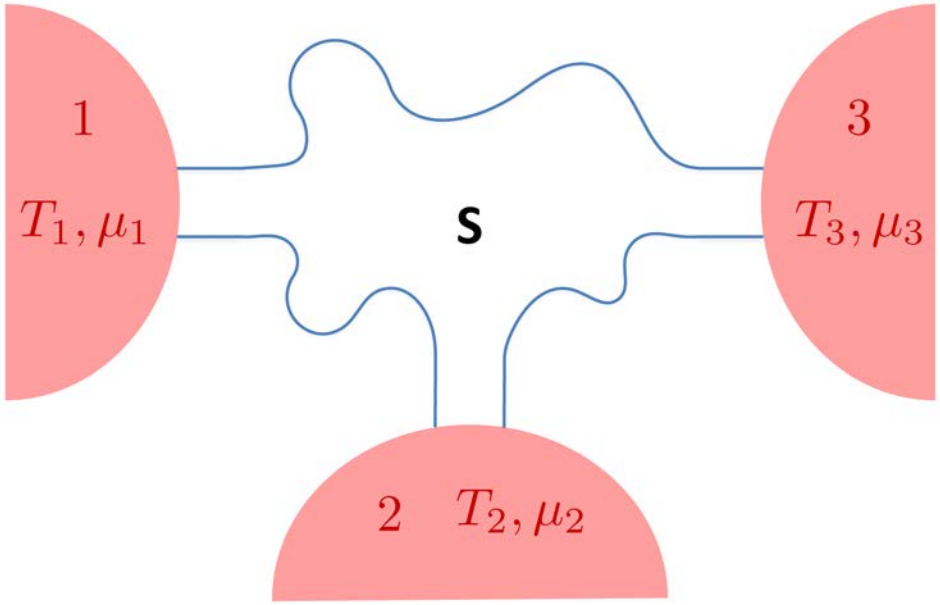


Figure 6.1: Three-terminal thermal machine. A scattering region is connected to 3 different fermionic reservoirs, each of these is able to exchange heat and particles with the system. Reservoir 3 is taken as the reference for measuring temperature and energy: $T_3 \equiv T$; $\mu_3 = \mu$. The reservoirs 1 and 2 have small variations in temperature and chemical potential: $(T_i, \mu_i) = (T + \Delta T_i, \mu + \Delta\mu_i)$, $i \in (1, 2)$. With **S** we denote a generic coherent scattering region.

Thermopower

For a two-terminal configuration the thermopower relates the voltage ΔV that develops between the reservoirs to their temperature difference ΔT under the assumption that no net charge current is flowing in the system, i.e. $S = -\left(\frac{\Delta V}{\Delta T}\right)_{J^N=0}$. A generalization of this quantity to the multi-terminal scenario can be obtained by introducing the matrix of elements

$$S_{ij} = -\left(\frac{\Delta\mu_i}{e\Delta T_j}\right)_{\substack{J_k^N = 0\ \forall k, \\ \Delta T_k = 0\ \forall k \neq j}}, \tag{6.3}$$

with local ($i = j$) and non-local ($i \neq j$) coefficients, e being the electron charge. In this definition, which does not require the control of the heat currents, we have imposed that the particle currents in all the leads are zero (the voltages are measured at open circuits) *and* that all but one temperature differences are zero (of course this last condition is not required in a two-terminal model). It is worth observing that Eq. (6.3) differs from other definitions proposed in the literature. For example in Ref. [106] a generalization of the two-terminal thermopower to a three-terminal system, was proposed by setting to zero one voltage instead of the corresponding particle current. While operationally well defined, this choice does not allow one to easily recover the thermopower of the two-terminal case (in our approach instead this is rather natural, see below). Finally, in the probe approach presented in Refs. [8, 23, 24, 77, 83, 150] it was possible to study a multi-terminal device by using an effective two-terminal

system only, because the heat and particle currents of the probe terminals are set to vanish by definition. Therefore, within this approach, there are no chances of having non-local transport coefficients.

In the three-terminal scenario we can use Eq. (6.2) to rewrite the elements of the matrix (6.3). In particular, introducing the quantities

$$L^{(2)}_{ij;kl} = L_{ik}L_{lj} - L_{il}L_{kj}, \tag{6.4}$$

we get (see 6.4.1 for details)

$$S_{11} = \frac{1}{eT}\frac{L^{(2)}_{13;32}}{L^{(2)}_{13;31}}, \qquad S_{22} = \frac{1}{eT}\frac{L^{(2)}_{14;31}}{L^{(2)}_{13;31}}, \tag{6.5}$$

$$S_{12} = \frac{1}{eT}\frac{L^{(2)}_{13;34}}{L^{(2)}_{13;31}}, \qquad S_{21} = \frac{1}{eT}\frac{L^{(2)}_{13;21}}{L^{(2)}_{13;31}}, \tag{6.6}$$

which yields, correctly, $S_{11} = \frac{1}{eT}\frac{L_{12}}{L_{11}}$ as the only non-zero element, by taking the two-terminal limits detailed at the end of the previous section.

Electrical conductance

In a two-terminal configuration the electric conductance describes how the electric current depends upon the bias voltage between the two terminals under isothermal conditions, i.e. $G = \left(\frac{eJ^N}{\Delta V}\right)_{\Delta T=0}$. The generalization to many-terminal systems is provided by the following matrix:

$$G_{ij} = \left(\frac{e^2 J^N_i}{\Delta\mu_j}\right)_{\substack{\Delta T_k = 0\ \forall k,\\ \Delta\mu_k = 0\ \forall k\neq j}}. \tag{6.7}$$

Using the three-terminal Onsager matrix ((6.2)) we find

$$\begin{pmatrix} G_{11} & G_{12} \\ G_{21} & G_{22} \end{pmatrix} = \frac{e^2}{T}\begin{pmatrix} L_{11} & L_{13} \\ L_{13} & L_{33} \end{pmatrix}, \tag{6.8}$$

which, in the two-terminal limit where reservoir 2 is disconnected from the rest, gives $G_{11} = \frac{e^2}{T}L_{11}$ as the only non-zero element.

Thermal conductance

The thermal conductance for a two-terminal is the coefficient which describes how the heat current depends upon the temperature imbalance ΔT under the assumption that no net charge current is flying through the system, i.e. $K = \left(\frac{J^Q}{\Delta T}\right)_{J^N=0}$. In the multi-terminal scenario this generalizes to

$$K_{ij} = \left(\frac{J^Q_i}{\Delta T_j}\right)_{\substack{J^N_k = 0\ \forall k,\\ \Delta T_k = 0\ \forall k\neq j}}, \tag{6.9}$$

where one imposes the same constraints as those used for the thermopower matrix ((6.3)), i.e. no currents and $\Delta T_k = 0$ for all terminals but the j-th. For a three-terminal case, using Eq. (6.4), this gives

$$K_{11} = \frac{1}{T^2}\frac{L_{13}L^{(2)}_{12;32} - L_{12}L^{(2)}_{13;32} - L_{11}L^{(2)}_{23;23}}{L^{(2)}_{13;31}}, \tag{6.10}$$

$$K_{22} = \frac{1}{T^2}\frac{L_{14}L^{(2)}_{13;43} - L_{13}L^{(2)}_{14;43} - L_{11}L^{(2)}_{34;34}}{L^{(2)}_{13;31}}, \tag{6.11}$$

and

$$K_{12} = K_{21} = \frac{1}{T^2}\frac{L_{24}L^{(2)}_{13;31} + L_{14}L^{(2)}_{13;23} + L_{34}L^{(2)}_{13;12}}{L^{(2)}_{13;31}}. \tag{6.12}$$

Once more, in the two-terminal limit where the reservoir 2 is disconnected from the rest, the only non-zero element is $K_{11} = \frac{1}{T^2}\frac{L^{(2)}_{12;12}}{L_{11}}$.

Peltier coefficient

In a two-terminal configuration, the Peltier coefficient relates the heat current to the charge current under isothermal condition, i.e. $\Pi = \left(\frac{J^Q}{eJ^N}\right)_{\Delta T=0}$. For multi-terminal systems this generalizes to the matrix

$$\Pi_{ij} = \left(\frac{J^Q_i}{eJ^N_j}\right)_{\substack{\Delta T_k = 0\ \forall k,\\ \Delta\mu_k = 0\ \forall k \neq j}}, \tag{6.13}$$

which can be shown to be related to the thermopower matrix (6.3) through the Onsager reciprocity equations, i.e. $\Pi_{ij}(\mathbf{B}) = TS_{ji}(-\mathbf{B})$ ($\mathbf{B}$ being the magnetic field on the system),[32, 45] from which, using Eqs. (6.5) and (6.6), one can easily derive for the three-terminal case the dependence upon the Onsager matrix $\mathbf{L}$.

6.2 Efficiency for 3-terminal systems

In order to characterize the properties of a multi-terminal system as a heat engine we shall now analyze its efficiency. The steady state heat to work conversion efficiency η is defined as the power $\dot{W}$ generated by the machine (which equals to the sum of all the heat currents exchanged between the system and the reservoirs), divided by the sum of the heat currents *absorbed* by the system, i.e.

$$\eta = \frac{\dot{W}}{\sum_{i_+} J^Q_i} = \frac{\sum_{i=1}^{3} J^Q_i}{\sum_{i_+} J^Q_i} = \frac{-\sum_{i=1}^{2} \Delta\mu_i J^N_i}{\sum_{i_+} J^Q_i}\ , \tag{6.14}$$

where the symbol $\sum_{i_+}$ in the denominator indicates that the sum is restricted to positive heat currents only, and where in the last expression we used Eq. (6.1) to express J^Q_3 in terms

of the other two independent currents[1].

The definition (6.14) applies only to the case in which $\dot{W}$ is positive. Since the signs of the heat currents J_i^Q are not known *a priori* (they actually depend on the details of the system), the expression of the efficiency depends on which heat currents are positive. For the three-terminal system depicted in Fig. 6.1 we set for simplicity $T_3 < T_2 < T_1$ and focus on those situations where J_3^Q is negative (positive values of J_3^Q being associated with regimes where the machine effectively works as a refrigerator which extract heat from the coldest reservoir of the system). Under these conditions the efficiency is equal to

$$\eta_{12} = \frac{\dot{W}}{J_1^Q + J_2^Q} \,, \tag{6.15}$$

when both J_1^Q and J_2^Q are positive, or

$$\eta_i = \frac{\dot{W}}{J_i^Q} \,, \tag{6.16}$$

when for $i = 1$ or 2 only J_i^Q is positive.

6.2.1 Carnot efficiency

The Carnot efficiency represents an upper bound for the efficiency and is obtained for an infinite-time (Carnot) cycle. For a two-terminal thermal machine the Carnot efficiency is obtained by simply imposing the condition of zero entropy production, namely $\dot{\mathcal{S}} = \sum_i J_i^Q/T_i = 0$. If the two reservoirs are kept at temperatures T_1 and T_3 (with $T_3 < T_1$), from the definition of the efficiency, Eq. (6.14), one gets the two-terminal Carnot efficiency $\eta_C^{II} = 1 - T_3/T_1$. The Carnot efficiency for a three-terminal thermal machine [111] is obtained analogously by imposing the condition of zero entropy production, when a reservoir at an intermediate temperature T_2 is added. If J_1^Q only is positive as in Eq. (6.16), one obtains

$$\eta_{C,1} = 1 - \frac{T_3}{T_1} + \frac{J_2^Q}{J_1^Q}(1 - \zeta_{32}) = \eta_C^{II} + \frac{J_2^Q}{J_1^Q}(1 - \zeta_{32}), \tag{6.17}$$

where $\zeta_{ij} \equiv T_i/T_j$. Note that Eq. (6.17) is the sum of the two-terminal Carnot efficiency η_C^{II} and a term whose sign is determined by $(1-\zeta_{32})$. Since $J_1^Q > 0$, $J_2^Q < 0$ and $\zeta_{32} < 1$, it follows that $\eta_{C,1}$ is always *reduced* with respect to its two-terminals counterpart η_C^{II}. Analogously if only J_2^Q is positive, one obtains

$$\eta_{C,2} = \eta_C^{II} - \frac{T_3}{T_1}\left[\frac{J_1^Q}{J_2^Q}(1 - \zeta_{13}) - (1 - \zeta_{12})\right], \tag{6.18}$$

[1]Note that Eq. (6.14) can be easily generalized to M terminals, after appropriate change of the numerator. By setting for instance $(T_M, \mu_M) = (T, \mu)$, $\Delta T_i = T_i - T$, and $\Delta\mu_i = \mu_i - \mu$ $(i = 1, ..., M-1)$, the output power reads $\dot{W} = \sum_{i=1}^{M} J_i^Q = -\sum_{i=1}^{M-1} \Delta\mu_i J_i^N$.

which again can be shown to be reduced with respect to η_C^{II}, since $J_1^Q < 0$, $J_2^Q > 0$, $\zeta_{12} > 1$, and $\zeta_{13} > 1$. We notice that this is a hybrid configuration (not a heat engine, neither a refrigerator): the hottest reservoir absorbs heat, while the intermediate-temperature reservoir releases heat. However, the heat to work conversion efficiency is legitimately defined since generation of power ($\dot{W} > 0$) can occur in this situation. Finally, if both J_1^Q and J_2^Q are positive as in Eq. (6.15) one obtains

$$\eta_{C,12} = 1 - \frac{T_3}{T_1}\left(1 + \frac{\zeta_{12} - 1}{1 + \frac{J_1^Q}{J_2^Q}}\right) = \eta_C^{II} - \frac{T_3}{T_1}\frac{\zeta_{12} - 1}{1 + \frac{J_1^Q}{J_2^Q}}. \tag{6.19}$$

Since $T_3 < T_2 < T_1$, the term that multiplies T_3/T_1 is positive so that $\eta_{C,12}$ is reduced with respect to the two-terminal case.

It is worth noticing that, in contrast to the two-terminal case, the Carnot efficiency cannot be written in terms of the temperatures only, but it depends on the details of the system. Moreover, note that the Carnot efficiency is unchanged with respect of the two-terminals case if $T_2 = T_3$ in Eq. (6.17) or if $T_2 = T_1$ in Eq. 6.19. Indeed, in this situation the quantities ζ_{ij} are equal to one, making the extra terms in Eqs. (6.17) or (6.19) vanish.

Notice that within linear response and via Eq. (6.2)) we can express the Carnot efficiencies (6.17)-(6.19) in terms of the generalized forces $X_{1,2}^{\mu}$.

Finally, we observe that the above results for the Carnot efficiency could be generalized to many-terminal systems. In particular, we conjecture that, given a system that works between T_1 and T_3 (with $T_3 < T_1$) and adding an arbitrary number of terminals at intermediate temperatures will in general lead to Carnot bounds smaller than η_C^{II}. On the other hand, adding terminals at higher (or colder) temperatures than T_1 and T_3 will make η_C increase.

6.2.2 Efficiency at Maximum Power

The efficiency at maximum power is the value of the efficiency evaluated at the values of chemical potentials that maximize the output power $\dot{W}$ of the engine. In the two-terminal case the efficiency at maximum power can be expressed as [175]

$$\eta^{II}(\dot{W}_{\max}) = \frac{\eta_C^{II}}{2}\frac{ZT}{ZT + 2}\,, \tag{6.20}$$

where $ZT = \frac{GS^2}{K}T$ is a dimensionless figure of merit which depends upon the transfer coefficients of the system. The positivity of the entropy production imposes that such quantity should be non-negative (i.e. $ZT \geq 0$), therefore $\eta^{II}(\dot{W}_{\max})$ is bounded to reach its maximum value $\eta_C^{II}/2$ only in the asymptotic limit of $ZT \to \infty$ (Curzon-Ahlborn limit [34, 41, 126, 193] within linear response [175]).

For the three-terminal configuration the output power is a function of the four generalized forces $(X_1^\mu, X_1^T, X_2^\mu, X_2^T)$ introduced in Eq. (6.2), i.e.

$$\dot{W} = -T(J_1^N X_1^\mu + J_2^N X_2^\mu) \; . \tag{6.21}$$

In the linear regime this is a quadratic function which can be maximized with respect to X_1^μ and X_2^μ while keeping X_1^T and X_2^T constant (the existence of a maximum being guaranteed by the the positivity of the entropy production). The resulting expression is

$$\dot{W}_{\max} = \frac{T^4}{4}(X_1^T, X_2^T)\, \mathbf{M} \begin{pmatrix} X_1^T \\ X_2^T \end{pmatrix} \; , \tag{6.22}$$

where $\mathbf{M} = \begin{bmatrix} c & a \\ a & b \end{bmatrix}$ is a positive semi-definite matrix, see section 6.4.2, whose elements depends on the Onsager coefficients via the identities

$$\begin{aligned} a &= G_{12}S_{12}S_{21} + G_{12}S_{11}S_{22} + G_{22}S_{21}S_{22} \\ &\quad + G_{11}S_{11}S_{12} \; , \\ b &= G_{11}S_{12}^2 + 2G_{12}S_{12}S_{22} + G_{22}S_{22}^2 \; , \\ c &= G_{11}S_{11}^2 + 2G_{12}S_{21}S_{11} + G_{22}S_{21}^2 \; . \end{aligned} \tag{6.23}$$

Indicating with $\alpha > \beta \geq 0$ the eigenvalues of $\mathbf{M}$ we can then further simplify Eq. (6.22) by writing it as

$$\dot{W}_{\max} = (\alpha \cos^2\theta + \beta \sin^2\theta) X^2 T^4/4 \; , \tag{6.24}$$

where $X = \sqrt{(X_1^T)^2 + (X_2^T)^2}$ is the geometric average of system temperatures, while the angle θ identify the rotation in the X_1^T, X_2^T plane which defines the eigenvectors of $\mathbf{M}$. We call the parameter

$$\mathcal{Q} = \alpha \cos^2\theta + \beta \sin^2\theta \tag{6.25}$$

three-terminal power factor. It relates the maximum power to the temperature difference: by construction it fulfills the inequality $\beta \leq \mathcal{Q} \leq \alpha$, the maximum being achieved for $\theta = 0$ (i.e. by ensuring that (X_1^T, X_2^T) coincides with the eigenvector of $\mathbf{M}$ associated with its largest eigenvalue α). Note that in the two-terminal limit we have $\beta \to 0$, $\alpha \to G_{11}S_{11}^2$, $\cos^2\theta \to 1$, so that the usual two-terminal power factor $G_{11}S_{11}^2$ is recovered.

Exploiting Eq. (6.24) we can now write the efficiency at maximum power for the three cases detailed in Eqs. (6.15) and (6.16). Specifically we have

$$\eta_1(\dot{W}_{\max}) = \frac{1}{2T} \frac{\Delta T_1 Z_{11}^c T + \Delta T_2(\delta^{-1} Z_{11}^b T + 2 Z_{11}^a T)}{\delta^{-1}(2\tilde{y} + Z_{11}^a T) + Z_{11}^c T + 2}, \tag{6.26}$$

$$\eta_2(\dot{W}_{\max}) = \frac{1}{2T}\frac{\Delta T_2 Z_{22}^b T + \Delta T_1(\delta Z_{22}^c T + 2Z_{22}^a T)}{\delta(2y + Z_{22}^a T) + Z_{22}^b T + 2}, \tag{6.27}$$

and

$$\eta_{12}(\dot{W}_{\max}) = \frac{1}{2T}\frac{\Delta T_1 Z_{12}^c T + \Delta T_2(2Z_{12}^a T + \delta^{-1} Z_{12}^b T)}{\delta^{-1}(2(1+y^{-1}) + Z_{12}^a T + Z_{12}^b T) + 2(1+\tilde{y}^{-1}) + Z_{12}^a T + Z_{12}^c T}, \tag{6.28}$$

where we have defined the parameters $\delta = X_1^T/X_2^T = \Delta T_1/\Delta T_2$, $y = K_{12}/K_{22}$ and $\tilde{y} = K_{12}/K_{11}$. Also, we have introduced the following generalized ZT coefficients:

$$Z_{ij}^a T = \frac{aT}{K_{ij}}, \quad Z_{ij}^b T = \frac{bT}{K_{ij}}, \quad Z_{ij}^c T = \frac{cT}{K_{ij}}\,. \tag{6.29}$$

The efficiencies (6.26), (6.27) and (6.28) can also be expressed in terms of the corresponding Carnot efficiencies given in Eqs. (6.17), (6.18) and (6.19), obtaining the following equations [111] which mimic Eq. 6.20 of the two-terminal case:

$$\eta_1(\dot{W}_{\max}) = \frac{\eta_{C,1}}{2}\frac{Z_{11}^b T + 2\delta Z_{11}^a T + \delta^2 Z_{11}^c T}{2\tilde{y}/y + 4\delta\tilde{y} + 2\delta^2 + Z_{11}^b T + 2\delta Z_{11}^a T + \delta^2 Z_{11}^c T} = \frac{\eta_{C,1}}{2}\frac{\mathcal{Z}_{11}T}{C_1 + \mathcal{Z}_{11}T}, \tag{6.30}$$

$$\eta_2(\dot{W}_{\max}) = \frac{\eta_{C,2}}{2}\frac{Z_{22}^b T + 2\delta Z_{22}^a T + \delta^2 Z_{22}^c T}{2\delta^2 y/\tilde{y} + 4\delta y + 2 + Z_{22}^b T + 2\delta Z_{22}^a T + \delta^2 Z_{22}^c T} = \frac{\eta_{C,2}}{2}\frac{\mathcal{Z}_{22}T}{C_2 + \mathcal{Z}_{22}T}, \tag{6.31}$$

$$\begin{aligned}\eta_{12}(\dot{W}_{\max}) &= \frac{\eta_{C,12}}{2}\frac{Z_{12}^b T + 2\delta Z_{12}^a T + \delta^2 Z_{12}^c T + o(\Delta T_i)}{2y^{-1} + 4\delta + 2\delta^2\tilde{y}^{-1} + Z_{12}^b T + 2\delta Z_{12}^a T + \delta^2 Z_{12}^c T + o(\Delta T_i)} \\ &\simeq \frac{\eta_{C,12}}{2}\frac{\mathcal{Z}_{12}T}{C_{12} + \mathcal{Z}_{12}T},\end{aligned} \tag{6.32}$$

where we have introduced the constants

$$C_1 = 2\tilde{y}/y + 4\delta\tilde{y} + 2\delta^2, \tag{6.33}$$

$$C_2 = 2\delta^2 y/\tilde{y} + 4\delta y + 2, \tag{6.34}$$

$$C_{12} = \tilde{y}^{-1} + \delta^2 y^{-1} + 2\delta, \tag{6.35}$$

and the combinations of figures of merit

$$\mathcal{Z}_{ij}T = (Z_{ij}^b + 2\delta Z_{ij}^a + \delta^2 Z_{ij}^c)T\,. \tag{6.36}$$

Notice also that in writing Eq. (6.32) we retained only the leading order neglecting contributions of order ΔT_i or higher.

The above expressions can be used to provide a generalization of the Curzon-Ahlborn limit efficiency for a multi-terminal quantum thermal device. Indeed using the Cholesky decompositions on the Onsager matrix, we can prove that the constants C_1, C_2 defined in Eqs. (6.33), (6.34) are positive, see section 6.4.2 for details. This fact, together with the

positivity of the quantities $\mathcal{Z}_{ii}T$ that we have checked numerically, implies that the efficiencies $\eta_i(\dot{W}_{\max})$ are always upper bounded by half of the associated Carnot efficiencies, i.e.

$$\eta_i(\dot{W}_{\max}) \leq \eta_{C,i}/2 \,, \tag{6.37}$$

the inequality being saturated when the generalized ZT coefficients (6.29) diverge. An analogous conclusion can be reached also for (6.32), yielding

$$\eta_{12}(\dot{W}_{\max}) \leq \eta_{C,12}/2 \,. \tag{6.38}$$

In this case C_{12} is no longer guaranteed to be positive due to the presence of K_{12}. Still, the inequality (6.38) can be derived by observing that the quantities C_{12} and $\mathcal{Z}_{12}T$ entering in the rhs of Eq. (6.32) have always the same sign.

6.3 Examples

In this Section we shall apply the theoretical framework developed so far to two specific non-interacting systems connected to three terminals [111]. Namely, we will discuss the case of a single dot and the case of two coupled dots. Our aim is to show that one can easily find situations where the efficiency and output power are enhanced with respect to the two-terminal case. Furthermore, through the example of the single dot, we find the conditions that guarantee the non-local thermopowers to vanish.

Preliminary comment about the notation: in the previous chapter we explicitly distinguished the electronic contribution to the figure of merit Z_eT from the full ZT, which includes in principles also phononic contributions. Despite the examples considered in this section deal with purely electronic transport, as the formulas for the efficiencies at maximum power derived in this chapter look rather cumbersome, we decided to omit the subscript "e" referring to the various electronic figures of merit ZT, in order to keep the notation as simple as possible. This choice is adopted in section 6.3 only, and hence it will not generate any ambiguity.

The coherent flow of particles and heat through a non-interacting conductor can be described by means of the Landauer-Büttiker formalism. Under the assumption that all dissipative and phase-breaking processes take place in the reservoirs, the electric and thermal currents are expressed in terms of the scattering properties of the system [31, 43, 81]. For instance, in a generic multi-terminal configuration the currents flowing into the system from the i-th reservoir are:

$$J_i^N = \frac{1}{h}\sum_{j\neq i}\int_{-\infty}^{\infty} dE\, \mathcal{T}_{ij}(E)\,[f_i(E) - f_j(E)], \tag{6.39}$$

$$J_i^Q = \frac{1}{h}\sum_{j\neq i}\int_{-\infty}^{\infty} dE\, (E-\mu_i)\,\mathcal{T}_{ij}(E)\,[f_i(E) - f_j(E)], \tag{6.40}$$

where the sum over j is intended over all but the i-th reservoir, h is the Planck's constant, $\mathcal{T}_{ij}(E)$ is the transmission probability for a particle with energy E to transit from the reservoir i to reservoir j, and where finally $f_i(E) = \{\exp[(E-\mu_i)/k_BT_i]+1\}^{-1}$ is the Fermi distribution of the particles injected from reservoir i (notice also that we are considering currents of spinless particles). In what follows we will use the above expressions in the linear response regime where $|\Delta\mu|/k_BT \ll 1$ and $|\Delta T|/T \ll 1$, and compute the associated Onsager coefficients (6.2), see section 6.4.3.

6.3.1 Single dot

In this section we study numerically a simple model consisting of a quantum dot with a single energy level E_d, coupled to three fermionic reservoirs, labeled 1, 2, and 3, see Fig. 6.2. For simplicity, the coupling strength to electrodes 1 and 3 are taken equal to γ, while the coupling strength to electrode 2 is denoted by γ_2. In particular we want to investigate how the efficiencies, output powers and transport coefficients evolve when the system is driven from a two-terminal to a three-terminal configuration, that is by varying the ratio γ_2/γ. The two-terminal configuration corresponds to $\gamma_2 = 0$ and the third terminal is gradually switched on by increasing γ_2/γ. As detailed in section 6.4.3, the transmission amplitudes between each pair of terminals can be used to evaluate the Onsager coefficients L_{ij} – the resulting expression being provided by Eqs. (6.67). Once the matrix L_{ij} is known, all the currents flowing through the system, efficiencies, output powers and transport coefficients can be calculated following the framework developed in the previous sections.

Efficiencies and maximum power

In Fig. 6.3 we show how the Carnot efficiency η_C depends on the temperature differences ΔT_1 and ΔT_2, when the chemical potentials are chosen to guarantee maximum output power, i.e., fixing the generalized forces $X^{\mu}_{1,2}$ in order to maximize $\dot{W}$. As we can see, η_C increases linearly along any "radial" direction defined by a relation $\Delta T_2 = k\,\Delta T_1$, where k is a constant. In particular, the dashed lines corresponding to $k = 0.5$, $k = 2$, and $k = -1$ separate the different regimes discussed in section 6.2.1: for $-1 < k < 0.5$ the system absorbs heat only from reservoir 1 (if $\Delta T_1 > 0$) or from 2 and 3 (if $\Delta T_1 < 0$); for $0.5 < k < 2.0$ the system absorbs heat from reservoirs from 1 and 2 (if $\Delta T_1 > 0$) or from 3 only (if $\Delta T_1 < 0$); finally, for $k > 2$ and $k < -1$ the system absorbs heat only from reservoir 2 (if $\Delta T_2 > 0$) or from 1 and 3 (if $\Delta T_2 < 0$). In the case when only one heat flux is absorbed the Carnot efficiency is given by Eq. (6.17) or Eq. (6.18), while it is given by Eq. (6.19) if two heat fluxes are absorbed.

In Figs. 6.4 and 6.5, we show how the efficiency Eq. (6.14), the output power Eq. (6.21), the efficiency at maximum output power Eqs. (6.26)-(6.28) and the maximum output power Eq. (6.22), vary when the system is driven from a two-terminal to a three-terminal config-

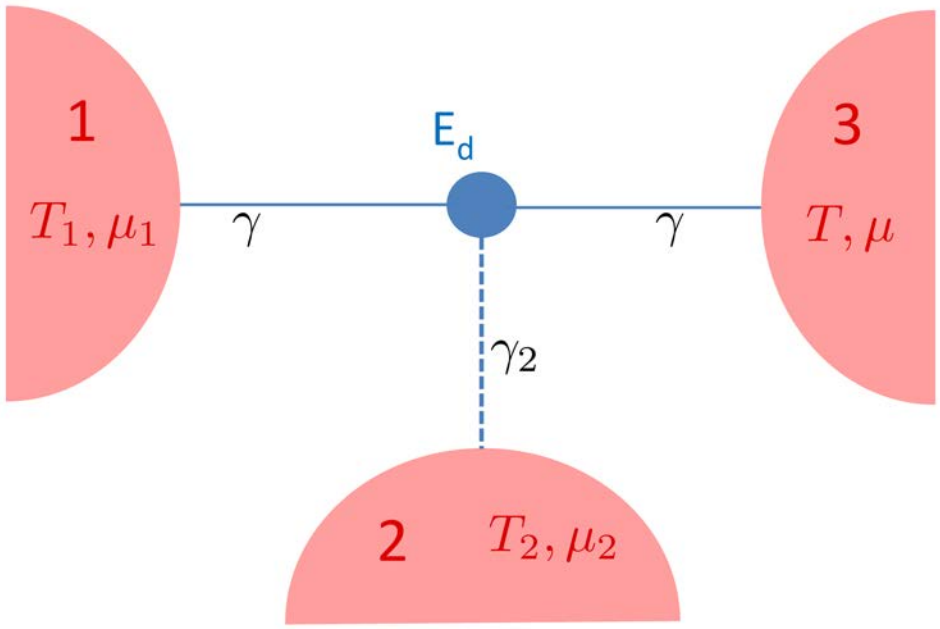


Figure 6.2: Sketch of the single dot model used in the numerical simulations: a quantum dot with a single energy level E_d is connected to three fermionic reservoirs 1, 2, and 3. The chemical potential and temperature of the reservoir 3 are assumed as the reference values μ and T. The constants γ and γ_2 represent the coupling between the system and the various reservoirs (see section 6.4.4 for details). A zero value of γ_2 corresponds to disconnecting the reservoir 2 from the system: in this regime the model describes a two-terminal device where reservoirs 1 and 3 are connected through the single dot.

uration, *i.e.* by varying the ratio γ_2/γ. We set opposite signs for $\Delta\mu_1$ and $\Delta\mu_2$, so that the system absorbs heat only from the hottest reservoir 1, and $\Delta T_2 = 0$, in such a way that the Carnot efficiency η_C coincides with that of a two-terminal configuration, namely $\eta_C = 1 - T/T_1$. Interestingly, we proved that increasing the coupling γ_2 to the reservoir 2 may lead to an improvement of the performances of the system. In particular, as shown in Fig. 6.6, the efficiency and the output power can be enhanced *at the same time* at small couplings γ_2, exhibiting a maximum around $\gamma_2 \sim 0.3\gamma$ and $\gamma_2 \sim 0.6\gamma$, respectively.

In Fig. 6.5 we show results for the same quantities but at the maximum output power, $\eta(\dot{W}_{\max})$ and $\dot{W}_{max}$. In this case, while $\dot{W}_{max}$ still increases with γ_2, the corresponding efficiency decreases approximately linearly.

In Figs. 6.6 and 6.7 we show the same quantities as in Figs. 6.4 and 6.5, but as a function of the coupling γ for two values of γ_2 ($\gamma_2 = 0$ and $\gamma_2 = 0.5\gamma$). From Fig. 6.6 we can see that at small γ the coupling to a third terminal can enhance both the efficiency (for $\gamma \lesssim 0.8 k_B T$) and the power (for $\gamma \lesssim k_B T$). In Fig. 6.7 we note that, both for the two- and the three-terminal system, the efficiency at maximum power tends to $\eta/\eta_C = 0.5$ in the limit $\gamma \to 0$, while the output power vanishes. For two terminals the result is well known, since a delta-shaped transmission function leads to the divergence of the figure of merit

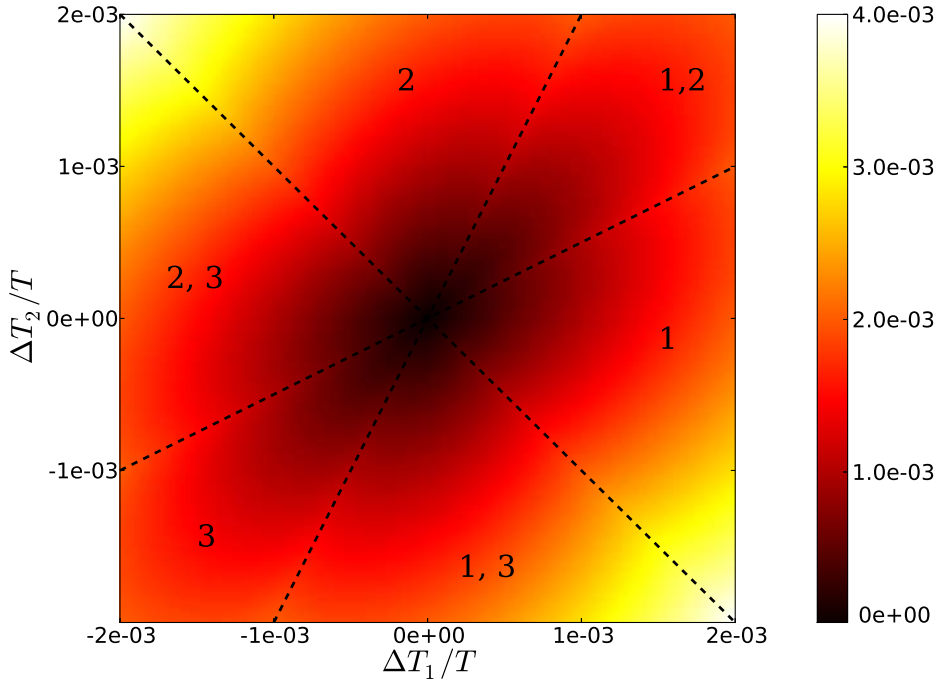


Figure 6.3: Carnot efficiency η_C (density plot) of the three-terminals system depicted in Fig. 6.2, as a function of the gradients of temperature in reservoirs 1 and 2 (the chemical potentials μ_1 and μ_2 being chosen to guarantee maximum output power $\dot{W}$). The coupling with the reservoirs have been set to have a symmetric configuration with respect to 1 and 2 (i.e. $\gamma_2 = \gamma$). Note that η_C increases linearly along any radial direction defined by a relation $\Delta T_2 = k\Delta T_1$, where k is a constant. In particular, the dashed lines corresponding to $k = 0.5$, $k = 2$ and $k = -1$ separate different regimes discussed in section 6.2.1. The numbers in each region identify the reservoirs from which the heat is absorbed. Parameter values: $\gamma = 0.2\, k_B T$, $E_d - \mu = 2.0\, k_B T$.

ZT [79, 108, 123]. Correspondingly, the efficiency at maximum power saturates the Curzon-Ahlborn bound $\eta/\eta_C = 0.5$. The same two-terminal energy-filtering argument explains the three-terminal result. Indeed, we found numerically that for $\gamma \to 0$ the chemical potentials optimizing the output power are such that $\mu_2 = \mu_3$. Since also the temperatures are chosen so that $T_2 = T_3$, we can conclude that terminals 2 and 3 can be seen as a single terminal.

Thermopowers

In this section we show analytically that the non-local thermopowers are always zero in this model, while the local ones are equal. We consider a general situation, with three different coupling parameters: $\gamma_1 = \gamma$, $\gamma_2 = c\,\gamma$ and $\gamma_3 = d\,\gamma$, with $c \neq d$. Under these assumptions, the transmissions are given at the end of section 6.4.3. Substituting these expressions in

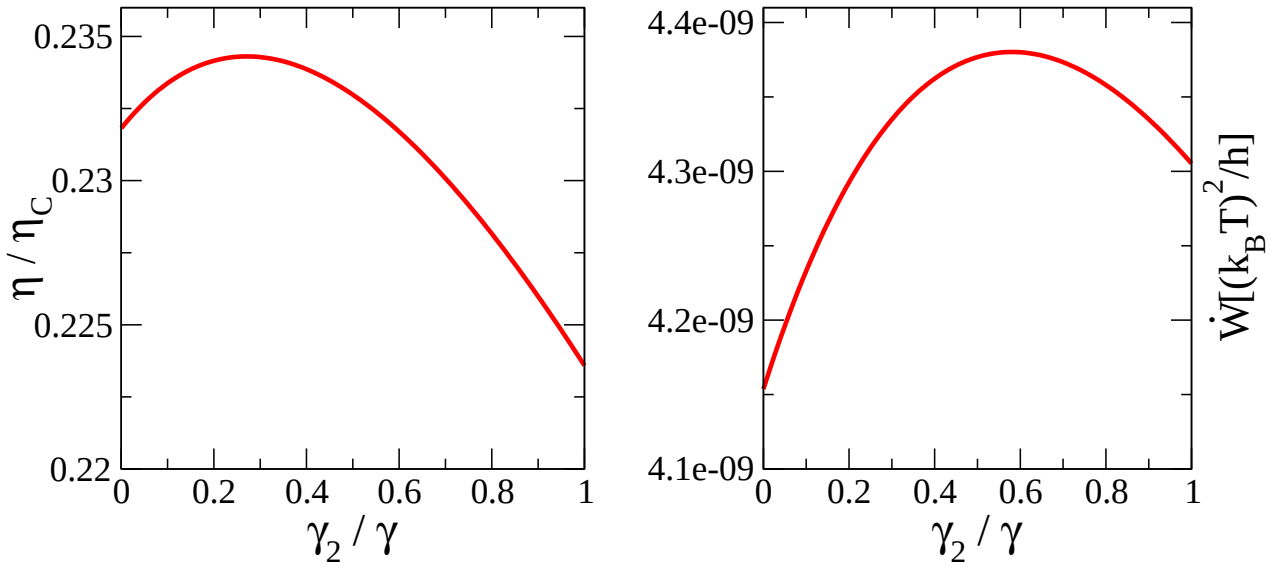


Figure 6.4: Left panel: Efficiency η, normalized over the associated Carnot limit computed as in Sec. 6.2.1, as a function of the coupling to the reservoir 2. Note that as γ_2/γ is switched on, the efficiency increases until it reaches a maximum around $\gamma_2 \sim 0.3\gamma$, and then it decreases. Right panel: Output power $\dot{W}$ extracted from the system, as a function of the coupling to the reservoir 2. Parameters: $\gamma = 0.1\, k_B T$, $E_d - \mu = 2.0\, k_B T$, $\Delta\mu_1 = -\Delta\mu_2 = -5 \times 10^{-4}\, k_B T$, $\Delta T_1 = 10^{-3}\, T$, and $\Delta T_2 = 0$.

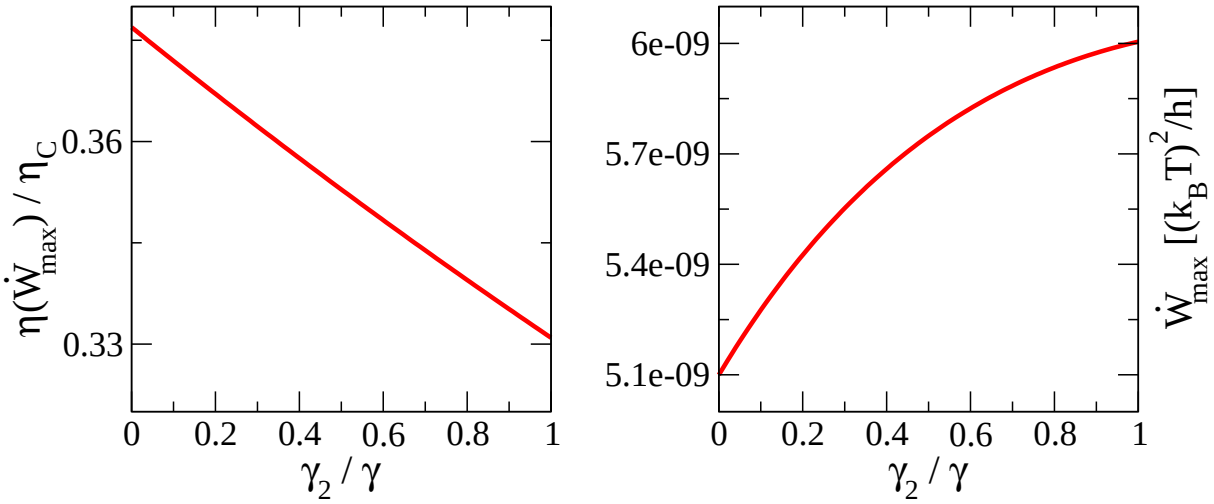


Figure 6.5: Left panel: Efficiency at maximum power $\eta(\dot{W}_{\max})$, normalized over the Carnot limit, as a function of the coupling to the reservoir 2. Right panel: Maximum output power $\dot{W}_{max}$ extracted from the system, as a function of the coupling to the reservoir 2. Parameters: $\gamma = 0.1\, k_B T$, $E_d - \mu = 2.0\, k_B T$, $\Delta T_1 = 10^{-3}\, T$, and $\Delta T_2 = 0$.

Eqs. (6.5) and (6.6), we find:

$$\begin{aligned} S_{11} &= S_{22} = \frac{1}{eT}\frac{L_1}{L_0}, \\ S_{21} &= S_{12} = 0\,. \end{aligned} \tag{6.41}$$

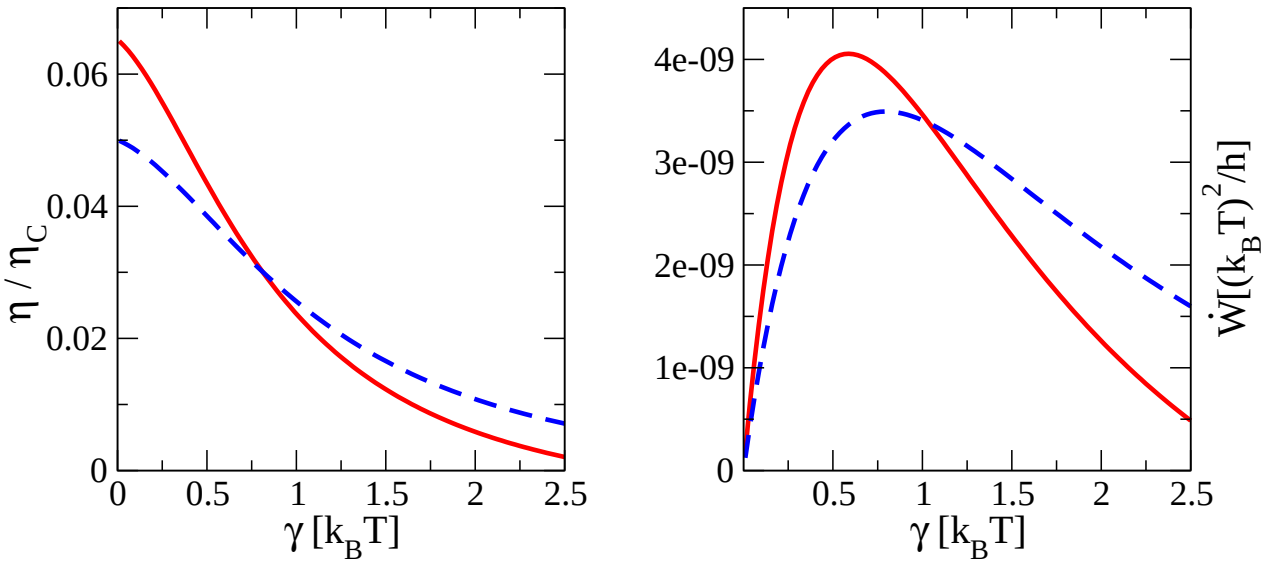


Figure 6.6: Left panel: Efficiency η, normalized over the Carnot limit, as a function of the coupling energy γ. Right panel: Output power $\dot{W}$ extracted from the system, as a function of the coupling energy γ. In both cases, the full red curves correspond to a three-terminals configuration with $\gamma_2 = 0.5\gamma$, while the dashed blue curve refer to the two-terminals case ($\gamma_2 = 0$). Parameters: $E_d - \mu = 2.0\, k_B T$, $\Delta\mu_1 = -\Delta\mu_2 = -10^{-4}\, k_B T$, $\Delta T_1 = 10^{-3}\, T$, and $\Delta T_2 = 0$.

This result is a direct consequence of the factorization of the energy dependence of the transmission probabilities, which are all proportional to the same function $\mathcal{T}$, as shown in Eq. (6.66). Such factorization allows us to rewrite the Onsager's coefficients as in Eq. (6.67) and derive Eq. (6.41). The fact that the non-local thermopowers, for example S_{12}, are zero can be understood as follows. Consider first the case in which $T_1 = T_2 = T_3$ and terminal 2 behaves as a voltage probe. If so, from the condition $J_2^N = L_{31}X_1^\mu + L_{33}X_2^\mu = 0$ we derive $\Delta\mu_2 = -(L_{31}/L_{33})\,\Delta\mu_1$. Due to the factorization of the energy dependence in the transmissions, we obtain $\Delta\mu_2 = (\gamma_1/(\gamma_1+\gamma_3))\Delta\mu_1$. Hence, $\Delta\mu_1$ does not depend on the coupling γ_2. If in particular we consider $\gamma_2 = \gamma$, because of the symmetry of the system under exchange of the terminals 1 and 3 we have $\mu_1 = \mu_3$. We can therefore conclude that, independently of the coupling γ_2, the probe voltage condition for terminal 2 implies $\Delta\mu_1 = 0$. It can be shown that such result remains valid even though $\Delta T_1 = 0$ but $\Delta T_2 \neq 0$, as requested in the calculation of the thermopower S_{12}. As a result, $S_{12} = 0$. The same argument can be repeated for the current J_1^N with the terminal 1 acting as a voltage probe, leading to $S_{21} = 0$.

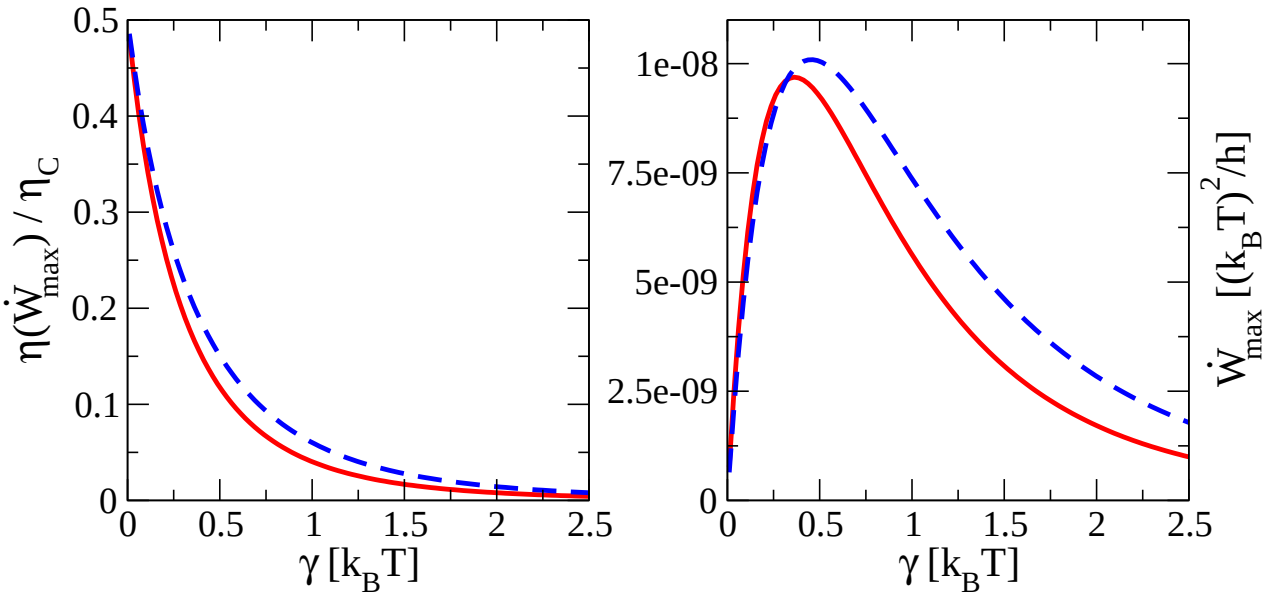


Figure 6.7: Left panel: Efficiency at maximum power $\eta(\dot{W}_{\max})$, normalized over the Carnot limit, as a function of the coupling energy γ. Right panel: Maximum output power $\dot{W}_{max}$ extracted from the system, as a function of the coupling energy γ. In both cases, the full red curves correspond to a three-terminals configuration with $\gamma_2 = 0.5\gamma$, while the dashed blue curves refer to the two-terminals case ($\gamma_2 = 0$). Parameters: $E_d - \mu = 2.0\, k_B T$, $\Delta T_1 = 10^{-3}\, T$, and $\Delta T_2 = 0$.

6.3.2 Double Dot

Let us now consider a system made of two quantum dots in series, each with a single energy level, coupled to three fermionic reservoirs. This system is described by the Hamiltonian:

$$\mathcal{H} = \begin{bmatrix} E_L & -t \\ -t & E_R \end{bmatrix}. \tag{6.42}$$

We call t the hopping energy between the dots, and we assume that dot L is coupled to the left lead (1), dot R is coupled to the right lead (3) and that both are coupled to a third lead (2) (see Fig. 6.8). The self-energies describing these couplings are:

$$\Sigma_1 = \begin{bmatrix} \sigma_1 & 0 \\ 0 & 0 \end{bmatrix}, \quad \Sigma_2 = \begin{bmatrix} \sigma_2 & 0 \\ 0 & \sigma_2 \end{bmatrix}, \quad \Sigma_3 = \begin{bmatrix} 0 & 0 \\ 0 & \sigma_3 \end{bmatrix}. \tag{6.43}$$

In the wide-band approximation, we assume that these quantities are energy-independent and they can be written as purely imaginary numbers $\sigma_i = -i\,\gamma_i/2$. The self-energies thus become:

$$\Sigma_1 = \begin{bmatrix} -i\frac{\gamma_1}{2} & 0 \\ 0 & 0 \end{bmatrix}, \quad \Sigma_2 = \begin{bmatrix} -i\frac{\gamma_2}{2} & 0 \\ 0 & -i\frac{\gamma_2}{2} \end{bmatrix}, \quad \Sigma_3 = \begin{bmatrix} 0 & 0 \\ 0 & -i\frac{\gamma_3}{2} \end{bmatrix}. \tag{6.44}$$

The retarded Green function of the system is then:

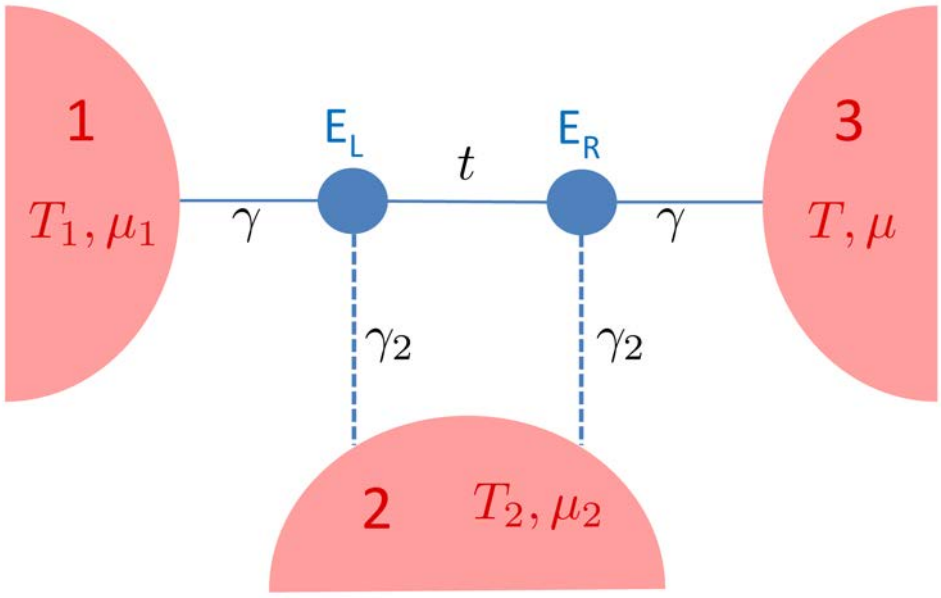


Figure 6.8: Sketch of the double dot model used in the numerical simulations: two quantum dots with a single energy level are connected in series to three fermionic reservoirs 1, 2 and 3. The chemical potential and temperature of reservoir 3 are assumed as the reference values μ and T. A two-terminal configuration is obtained in the case in which the coupling to reservoir 2 (equal for both the dots) vanishes ($\gamma_2 = 0$).

$$\mathcal{G} = [E\mathbb{I} - \mathcal{H} - \Sigma]^{-1} = \begin{bmatrix} E - E_L - \sigma_1 - \sigma_2 & t \\ t & E - E_R - \sigma_3 - \sigma_2 \end{bmatrix}^{-1} = \\ = \frac{1}{\det[\mathcal{G}]} \begin{bmatrix} E - E_R + i\frac{\gamma_3+\gamma_2}{2} & -t \\ -t & E - E_L + i\frac{\gamma_1+\gamma_2}{2} \end{bmatrix}, \tag{6.45}$$

with

$$\det[\mathcal{G}] = \left(E - E_L + i\frac{\gamma_1 + \gamma_2}{2}\right)\left(E - E_R + i\frac{\gamma_3 + \gamma_2}{2}\right) - t^2. \tag{6.46}$$

The matrix of transmission probability $\mathcal{T}_{ij}$ between each pair of reservoirs is given by the Fisher-Lee formula

$$\mathcal{T}_{ij} = \mathrm{Tr}\,\left[\Gamma_i\,\mathcal{G}\,\Gamma_j\,\mathcal{G}^\dagger\right], \tag{6.47}$$

where we have introduced the broadening matrices $\Gamma_i = i(\Sigma_i - \Sigma_i^\dagger)$:

$$\Gamma_1 = \begin{bmatrix} \gamma_1 & 0 \\ 0 & 0 \end{bmatrix}, \qquad \Gamma_2 = \begin{bmatrix} \gamma_2 & 0 \\ 0 & \gamma_2 \end{bmatrix}, \quad \Gamma_3 = \begin{bmatrix} 0 & 0 \\ 0 & \gamma_3 \end{bmatrix}. \tag{6.48}$$

For the system under consideration, we obtain

$$\mathcal{T}_{13} = \frac{\gamma_1\gamma_3}{|\det[\mathcal{G}]|^2}\,t^2, \tag{6.49}$$

$$\mathcal{T}_{12} = \frac{\gamma_1\gamma_2}{|\det[\mathcal{G}]|^2}\left[(E-E_R)^2 + \left(\frac{\gamma_3+\gamma_2}{2}\right)^2 + t^2\right], \tag{6.50}$$

$$\mathcal{T}_{32} = \frac{\gamma_3\gamma_2}{|\det[\mathcal{G}]|^2}\left[(E-E_L)^2 + \left(\frac{\gamma_1+\gamma_2}{2}\right)^2 + t^2\right]. \tag{6.51}$$

At this point, it is clear that the energy dependence of the transmission matrix cannot be factorized as for the single dot case. This model is hence the simplest in which we can observe finite non-local thermopowers and an increase of both the power and the efficiency of the corresponding thermal machine. We find that the behavior of such quantities as functions of the various parameters is qualitatively very similar to the case of the single dot, thus confirming that a third terminal could improve the performance of a quantum machine.

Since in this system all the transport coefficients are different from zero, it is instructive to study the behavior of the generalized figures of merit defined in Eq. (6.29). In Fig. 6.9 we show, in the configuration with only one positive heat flux ($J_1^Q > 0$), $Z_{11}^a T$ (dotted line), $Z_{11}^b T$ (dashed line) and $Z_{11}^c T$ (full line). We investigate their behavior as a function of the coupling γ_2 and of the total coupling γ. Note that in the two-terminal limit ($\gamma_2 \to 0$) $Z_{11}^c T$ reduces to the standard thermoelectric figure of merit ZT, while $Z_{11}^a T$ and $Z_{11}^b T$ tend to zero. When we turn on the interaction with the reservoir 2 (left panel), we notice that the figure of merit $Z_{11}^c T$ decreases, while the figures of merit $Z_{11}^b T$ and $Z_{11}^a T$ increase their absolute values. From the behavior as a function of the total coupling γ we can see that in the limit of δ-shaped transmission function ($\gamma \to 0$), the figures of merit diverge, leading to the Carnot efficiency, while in the limit of broad transmission window ($\gamma \to \infty$), all the figures of merit go to zero and we recover the case of zero efficiency.

Thermopowers

As mentioned before, the fact that the energy-dependence of the transmission matrix for the double dot cannot be factorized is sufficient to guarantee finite non-local thermopowers, as shown in the left panel of Fig. 6.10. As a function of γ_2, S_{12} starts from zero, while S_{21} starts from a finite value. This different behavior for the two non-local thermopowers is due to the different role played by γ_2 in the two cases. As far as S_{12} is concerned, when we set a temperature difference ΔT_2 in lead 2, a chemical potential difference $\Delta\mu_1$ develops in lead 1 to annihilate the current that flows out of the lead 2. When the coupling γ_2 goes to zero, that current goes to zero and so does the chemical potential difference $\Delta\mu_1$. This argument does not hold for S_{21}, because the temperature difference ΔT_1 is set in lead 1, and γ_2 does not control the current anymore. Therefore when the coupling γ_2 approaches zero the current still have a finite value, and so the chemical potential difference $\Delta\mu_2$ needed to annihilate it. Furthermore, the local thermopowers are no more equal, as shown in the right panel of Fig. 6.10.

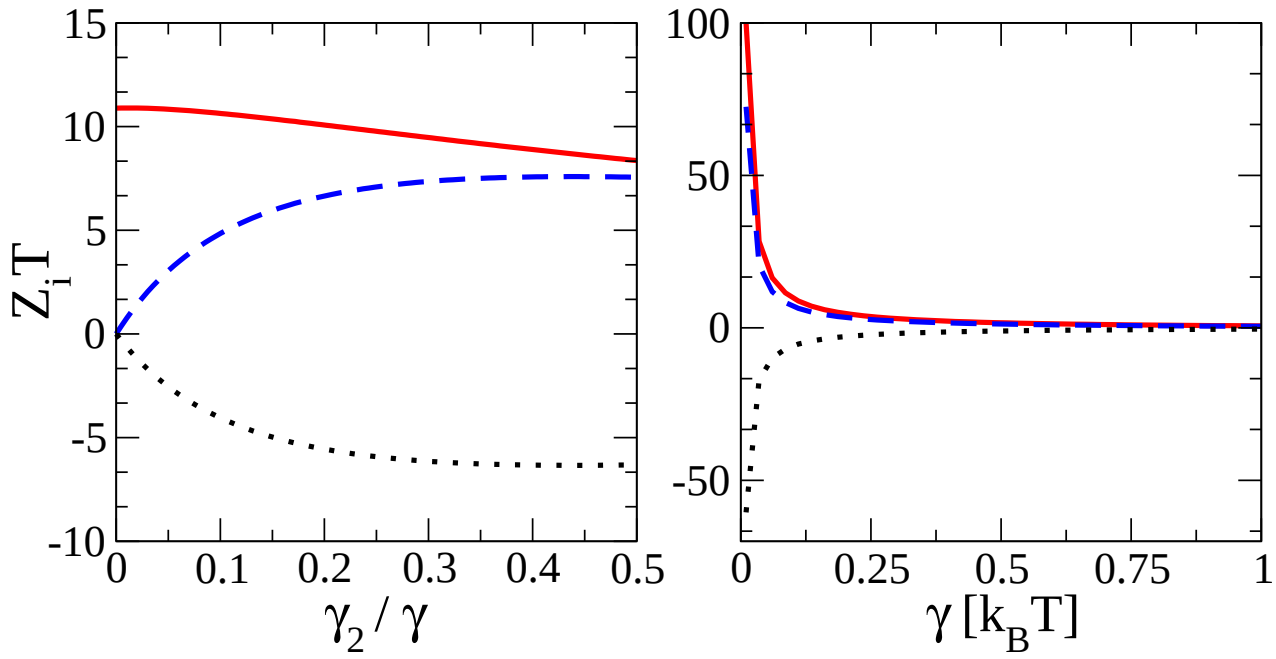


Figure 6.9: Various figures of merit $Z^a_{11}T$ (dotted line), $Z^b_{11}T$ (dashed line) and $Z^c_{11}T$ (full line) as a function of the coupling to the bottom reservoir γ_2 (left panel), and as a function of the total coupling γ (right panel). Parameter values: $E_L - \mu = -2\ k_BT$, $E_R - \mu = -20\ k_BT$, $\gamma = 0.1\ k_BT$ (left panel) and $\gamma_2 = 0.5\ k_BT$ (right panel).

6.4 Appendix

6.4.1 Calculation of the transport coefficients and thermopowers

To compute the multi-terminal thermopowers defined in Eqs. (6.5) and (6.6), we have to express one of the temperatures as a function of a thermal current. For example let us start from the inversion between X_1^T and J_1^Q. In the Onsager's formalism this can be expressed as:

$$0 = -\begin{pmatrix} J_1^N \\ X_1^T \\ J_2^N \\ J_2^Q \end{pmatrix} + \mathcal{L}\begin{pmatrix} X_1^\mu \\ J_1^Q \\ X_2^\mu \\ X_2^T \end{pmatrix} = \begin{pmatrix} \mathbf{L} & -\mathbb{I} \end{pmatrix} \mathbf{A}\,\mathbf{A^{-1}} \begin{pmatrix} \mathbf{X} \\ \mathbf{J} \end{pmatrix}, \tag{6.52}$$

where $\mathbf{A}$ is a permutation matrix that switches X_1^T and J_1^Q, $\mathbf{X}$ and $\mathbf{J}$ are column vectors with components $(X_1^\mu, X_1^T, X_2^\mu, X_2^T)$ and $(J_1^N, J_1^Q, J_2^N, J_2^Q)$, respectively, and $\mathbb{I}$ is the 4×4 identity matrix. Then we obtain:

$$\begin{aligned} 0 = \begin{pmatrix} \mathbf{L} & -\mathbb{I} \end{pmatrix} \mathbf{A}\,\mathbf{A^{-1}} \begin{pmatrix} \mathbf{X} \\ \mathbf{J} \end{pmatrix} = \begin{pmatrix} \mathbf{L} & -\mathbb{I} \end{pmatrix} \mathbf{A} \begin{pmatrix} \mathbf{X^*} \\ \mathbf{J^*} \end{pmatrix} = \\ = \mathbf{B}\mathbf{X^*} + \mathbf{C}\mathbf{J^*}, \end{aligned} \tag{6.53}$$

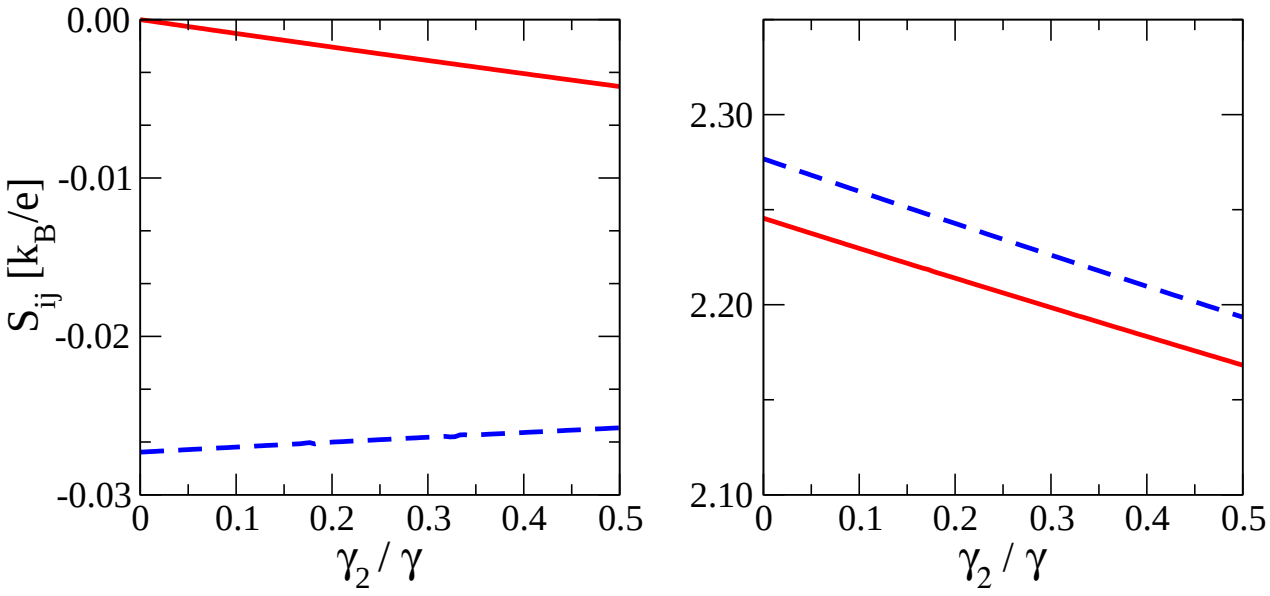


Figure 6.10: (Left panel) Non local thermopowers as a function of the coupling γ_2 to lead 2. The full red line corresponds to $S_{12} = -\Delta\mu_1/\Delta T_2$, while the dashed (blue) line corresponds to $S_{21} = -\Delta\mu_2/\Delta T_1$. (Right panel) Local thermopowers as a function of the coupling γ_2 to lead 2. The full (red) line corresponds to $S_{11} = -\Delta\mu_1/\Delta T_1$, while the dashed (blue) line corresponds to $S_{22} = -\Delta\mu_2/\Delta T_2$. Parameter values as in Fig. 6.9.

where $\mathbf{X}^*$ and $\mathbf{J}^*$ are the vectors $\mathbf{X}$ and $\mathbf{J}$ after the action of A^{-1}, that is, with $X_1^T \leftrightarrow J_1^Q$; $\mathbf{B}$ and $\mathbf{C}$ are the matrices determined by the product $\begin{pmatrix}\mathbf{L} & -\mathbb{I}\end{pmatrix}\mathbf{A}$. We can now define the thermopower from the following equations:

$$\mathbf{X}^* = -\mathbf{B^{-1}}\,\mathbf{C}\mathbf{J}^* \Rightarrow \begin{pmatrix} X_1^\mu \\ J_1^Q \\ X_2^\mu \\ X_2^T \end{pmatrix} = \mathcal{L}^{-1} \begin{pmatrix} J_1^N = 0 \\ X_1^T = 0 \\ J_2^N = 0 \\ J_2^Q \end{pmatrix}. \tag{6.54}$$

For this choice of the parameters we have inverted, two different thermopowers can be defined, the non local S_{12}:

$$S_{12} = -\frac{\Delta\mu_1}{e\Delta T_2} = -\frac{1}{eT}\frac{X_1^\mu}{X_2^T} = \frac{1}{eT}\frac{L^{(2)}_{13;34}}{L^{(2)}_{13;31}}, \tag{6.55}$$

and the local S_{22}:

$$S_{22} = -\frac{\Delta\mu_2}{e\Delta T_2} = -\frac{1}{eT}\frac{X_2^\mu}{X_2^T} = \frac{1}{eT}\frac{L^{(2)}_{14;31}}{L^{(2)}_{13;31}}. \tag{6.56}$$

The two-terminal limit in which reservoirs 2 and 3 only are connected is obtained after setting in the Onsager matrix $L_{ij} = 0$ if $i = 1, 2$ or $j = 1, 2$. In this limit, the previous expressions

reduce to:

$$\begin{aligned} S_{12} &\to 0, \\ S_{22} &\to \frac{1}{eT}\frac{L_{34}}{L_{33}}. \end{aligned} \tag{6.57}$$

The non-local term goes to zero, while the local one goes to the correct value of the 2-terminal system. The two other terms of these generalized thermopowers are obtained with the inversion of X_2^T and J_2^Q. Then we can define S_{21} as the non local quantity, and S_{11} as the local one:

$$\begin{aligned} S_{21} &= -\frac{1}{eT}\frac{X_2^\mu}{X_1^T} = \frac{1}{eT}\frac{L^{(2)}_{13;21}}{L^{(2)}_{13;31}}, \\ S_{11} &= -\frac{1}{eT}\frac{X_1^\mu}{X_1^T} = \frac{1}{eT}\frac{L^{(2)}_{13;32}}{L^{(2)}_{13;31}}. \end{aligned} \tag{6.58}$$

In a similar way all the other transport coefficients can be defined, by inverting a generalized force with a current.

6.4.2 Cholesky Decomposition of the three-terminal Onsager matrix

In linear algebra, the Cholesky decomposition [59] is a tool which allows to write a Hermitian, positive-definite (or semipositive-definite) matrix A as a product of a lower triangular matrix D and its conjugate transpose $D^\dagger$:

$$A = DD^\dagger, \tag{6.59}$$

(in particular, if A is *real*, $D^\dagger$ is simply the transpose of D). It turns out that the sign of some quantities defined throughout this work as combinations of products of Onsager coefficients L_{ij} can be easily studied by using the Cholesky decomposition on the Onsager matrix $\mathbf{L}$. As an example, by writing

$$D = \begin{pmatrix} \rho_{11} & 0 & 0 & 0 \\ \rho_{12} & \rho_{22} & 0 & 0 \\ \rho_{13} & \rho_{23} & \rho_{33} & 0 \\ \rho_{14} & \rho_{24} & \rho_{34} & \rho_{44} \end{pmatrix}, \tag{6.60}$$

it can be shown that the coefficient b and c defined in Eq. (6.23) are equal to

$$\begin{aligned} b &= \frac{\rho_{14}^2(\rho_{23}^2+\rho_{33}^2)+(\rho_{23}\rho_{24}+\rho_{33}\rho_{34})^2}{T^3(\rho_{23}^2+\rho_{33}^2)}, \\ c &= \frac{\rho_{22}^2\rho_{23}^2+\rho_{12}^2(\rho_{23}^2+\rho_{33}^2)}{T^3(\rho_{23}^2+\rho_{33}^2)}, \end{aligned} \tag{6.61}$$

and therefore are non-negative. The coefficient

$$a = \frac{\rho_{12}\rho_{14}(\rho_{23}^2+\rho_{33}^2)+\rho_{22}\rho_{23}(\rho_{23}\rho_{24}+\rho_{33}\rho_{34})}{T^3(\rho_{23}^2+\rho_{33}^2)}$$

instead has undefined sign. Still one can prove that it is such that the determinant of the matrix $\mathbf{M}$ which appears in Eq. (6.22) is non-negative. Indeed we have

$$\det(\mathbf{M}) = \frac{(-\rho_{14}\rho_{22}\rho_{23} + \rho_{12}\rho_{23}\rho_{24} + \rho_{12}\rho_{33}\rho_{34})^2}{T^6(\rho_{23}^2 + \rho_{33}^2)}\,, \tag{6.62}$$

which, together with the positivity of b and c entails that $\mathbf{M}$ is semi-positive definite.

The same procedure can be used to study the sign of the constants C_1, C_2 and C_{12} defined in Eqs. (6.33), (6.34), and (6.35), respectively. As it is shown here below, C_1 and C_2 are always non-negative, while C_{12} has undefined sign:

$$\begin{aligned} C_1 &= \frac{2[(\delta\rho_{22}\rho_{33} + \rho_{24}\rho_{33} - \rho_{23}\rho_{34})^2 + (\rho_{23}^2 + \rho_{33}^2)\rho_{44}^2]}{\rho_{22}^2\rho_{33}^2}\,, \\ C_2 &= \frac{2[(\delta\rho_{22}\rho_{33} + \rho_{24}\rho_{33} - \rho_{23}\rho_{34})^2 + (\rho_{23}^2 + \rho_{33}^2)\rho_{44}^2]}{(\rho_{24}\rho_{33} - \rho_{23}\rho_{34})^2 + (\rho_{23}^2 + \rho_{33}^2)\rho_{44}^2}\,, \\ C_{12} &= \frac{(\rho_{22}\rho_{33} + \delta\rho_{24}\rho_{33} - \delta\rho_{23}\rho_{34})^2 + \delta^2(\rho_{23}^2 + \rho_{33}^2)\rho_{44}^2}{\rho_{22}\rho_{33}(\rho_{24}\rho_{33} - \rho_{23}\rho_{34})}. \end{aligned} \tag{6.63}$$

6.4.3 Scattering approach in linear response: the Onsager coefficients

For a three-terminals configuration, as in the previous sections, we choose the right reservoir 3 as the reference ($\mu_3 = \mu = 0$, $T_3 = T$), and characterize the problem in terms of the particle/heat currents flowing in linear response between the system and leads 1 (held at $\mu_1 = \mu + \Delta\mu_1$ and $T_1 = T + \Delta T_1$) and 2 (held at $\mu_2 = \mu + \Delta\mu_2$ and $T_2 = T + \Delta T_2$). The Onsager's coefficients are obtained from the linear expansion of the currents J_i^N and J_i^Q ($i = 1, 2$) given by Eqs. (6.39) and (6.40). They can be written in terms of the transmission

probabilities $\mathcal{T}_{ij}$, $i,j \in \{1,2,3\}$ as:

$$
\begin{aligned}
L_{11} &= \frac{T}{h}\int dE\ (-\partial_E f)\,(\mathcal{T}_{12}+\mathcal{T}_{13}),\\
L_{12} &= \frac{T}{h}\int dE\ (-\partial_E f)\,(E-\mu)(\mathcal{T}_{12}+\mathcal{T}_{13}) = L_{21},\\
L_{13} &= \frac{T}{h}\int dE\ (-\partial_E f)\,(-\mathcal{T}_{12}) = L_{31},\\
L_{14} &= \frac{T}{h}\int dE\ (-\partial_E f)\,(-(E-\mu)\mathcal{T}_{12}) = L_{41},\\
L_{22} &= \frac{T}{h}\int dE\ (-\partial_E f)\,(E-\mu)^2(\mathcal{T}_{12}+\mathcal{T}_{13}),\\
L_{23} &= \frac{T}{h}\int dE\ (-\partial_E f)\,(-(E-\mu)\mathcal{T}_{12}) = L_{32},\\
L_{24} &= \frac{T}{h}\int dE\ (-\partial_E f)\,(-(E-\mu)^2\mathcal{T}_{12}) = L_{42},\\
L_{33} &= \frac{T}{h}\int dE\ (-\partial_E f)\,(\mathcal{T}_{12}+\mathcal{T}_{23}),\\
L_{34} &= \frac{T}{h}\int dE\ (-\partial_E f)\,(E-\mu)(\mathcal{T}_{12}+\mathcal{T}_{23}) = L_{43},\\
L_{44} &= \frac{T}{h}\int dE\ (-\partial_E f)\,(E-\mu)^2(\mathcal{T}_{12}+\mathcal{T}_{23}),
\end{aligned}
\tag{6.64}
$$

where T is the temperature, f denotes the Fermi-Dirac distribution at μ, and ∂_E is the partial derivative with respect to the energy.

6.4.4 Transmission function of a single-level dot

For a scattering region consisting of a quantum dot with a single energy level, connected to three terminals, we can express the transmission function as [31]

$$
\mathcal{T}_{ij} = \frac{\gamma_i\gamma_j}{(E-E_d)^2+\left(\frac{\Gamma}{2}\right)^2}, \qquad (i\neq j),
\tag{6.65}
$$

where γ_i is the contribution to the broadening due to the coupling to lead i, which is energy-independent in the wide-band limit approximation. Furthermore, at the denominator, $\Gamma = \gamma_1+\gamma_2+\gamma_3$ is the total broadening due to the coupling to *all* leads. If we denote $\gamma_1 = \gamma$, $\gamma_2 = c\gamma$, and $\gamma_3 = d\gamma$ the couplings to the three leads, we obtain for the transmissions the values

$$
\begin{aligned}
\mathcal{T}_{12} &= \frac{c\gamma^2}{(E-E_d)^2+\frac{(1+c+d)^2}{4}\gamma^2} \equiv c\mathcal{T},\\
\mathcal{T}_{13} &= \frac{d\,\gamma^2}{(E-E_d)^2+\frac{(1+c+d)^2}{4}\gamma^2} \equiv d\,\mathcal{T},\\
\mathcal{T}_{23} &= \frac{cd\,\gamma^2}{(E-E_d)^2+\frac{(1+c+d)^2}{4}\gamma^2} \equiv cd\,\mathcal{T}.
\end{aligned}
\tag{6.66}
$$

The Onsager coefficients then read as follows:

$$\begin{aligned}
L_{11} &= L_0\,(c+d),\\
L_{12} &= L_1\,(c+d),\\
L_{13} &= -c\,L_0,\\
L_{14} &= -c\,L_1,\\
L_{22} &= L_2\,(c+d),\\
L_{23} &= -c\,L_1,\\
L_{24} &= -c\,L_2,\\
L_{33} &= c\,L_0\,(1+d),\\
L_{34} &= c\,L_1\,(1+d),\\
L_{44} &= c\,L_2\,(1+d),
\end{aligned} \tag{6.67}$$

with $L_n = \frac{T}{h}\int dE\ (-\partial_E f)\,(E-\mu)^n \mathcal{T}$.

The numerical data shown in section 6.3.1 are obtained for $d = 1$, *i.e.* for $\gamma_1 = \gamma_3 = \gamma$. The two-terminal configuration corresponds to $c = 0$ ($\gamma_2 = 0$), while the coupling to terminal 2 is switched on progressively by increasing c.

Chapter 7

Epilogue

This thesis was aimed to understand thermoelectric conversion in disordered semiconductor nanowires in the field effect transistor configuration. Our study has been carried out at low temperatures in the regime of elastic coherent transport, and at higher temperature for inelastic thermally activated transport.

In the last years low dimensional thermoelectrics have attracted increasing attention, inspired by the constant quest for reliable and environmentally friendly sources of energy on the one hand, and by the progresses made in micro- and nano-scale fabrication and manipulation on the other. In particular, a number of experiments carried out in the last decade has put forward nanowires-based systems as promising thermoelectric devices, in prospect both of energy harvesting and Peltier cooling with applications in micro-electronics.

Motivated by a substantial lack of theoretical works complementary to this intense experimental activity, we have studied electronic transport in disordered nanowires at a fundamental level, which we believe to be of paramount importance in conceiving performant thermoelectric devices.

The analysis carried out in chapter 3 lies on an analytical approach in describing electronic transport at low temperatures: this allowed us to develop a profound comprehension of the mechanism leading to an enhanced thermopower at the NWs impurity band edges. Essentially, the main feature is the strong energy dependence of the localization length (and hence of the density of states also, since they are interdependent) around the band edge. However, in the regime of elastic transport this has the unwanted consequence of exponentially suppressing the conductance, thus forbidding large output powers. Moreover, the validity of the Wiedemann-Franz sets a bound by itself on the thermoelectric power, hence preventing a large figure of merit.

Both these limitations may be overcome by increasing the temperature. In chapter 4, we showed how in the regime of thermally activated transport the NWs thermopower could be drastically enhanced in the field effect transistor configuration, up to values of the order of $\sim 1mV\,K^{-1}$.

When this happens the electrical conductance is reduced, but not as much as in the elastic regime; stacking many nanowires in parallel, as explained in chapter 5, provides a way to scale the conductance, allowing to deliver a finite output power under condition of improved thermoelectric conversion. As an intriguing related effect, we discussed the possibility of generating and controlling hot and cold spots at the boundaries of an insulating substrate, a topic which could be a major concern in the framework of chip cooling in micro- and nanoelectronics.

It is worthwhile to stress that what really makes the systems considered in chapter 5 very promising is the role of the phonon bath, which at an abstract level is nothing but a third (bosonic) terminal added to the standard two-terminal configuration. This leads naturally to wonder whether a third terminal treated on a more general footing is beneficial for thermoelectric conversion. In chapter 6 we tackled this problem within a rather technical approach, and we concluded that in principle a third fermionic terminal can allow for better efficiencies and output power even in linear response.

As this is a very active field of research, there is a number of open questions that could be addressed, ranging from the fundamental to the more practical kind. Some of them could be, for instance:

- A more rigourous treatment of the electron-phonon interaction would allow to better understand if the electrostatic disorder seen by the electrons affects phonons, and by the same token if the microscopic details of phonons do play a role on electrons. Besides, it would lead to a more reliable estimation of all the transport coefficients, and hence of the figure of merit ZT. This task could be done by detailing electron-phonon Hamiltonian $\mathcal{H}_{e-ph}$ at a microscopic level, or also by treating it as a time-dependent noise, by adding an electrostatic corrective energy $E_i^{ph}(t)$. We stress the fact that so far much work has been done to study purely phonon transport, but really few in the direction of understanding its interplay with electrons.

- In addition to the previous point, we could envisage to combine our theoretical approach with a DFT calculation of the various microscopic parameters appearing in the transport equations (γ_e and γ_{ep} overall), in order to make our results quantitatively more robust. Also, this would cast some light on the difference between the phonon populations inside the nanowires and in the substrate, possibly altering at a quantitative level the mechanism of thermal activation.

- Estimating the role of electronic interactions, neglected in this work, would be important since in 1D they can have dramatic effect (Luttinger liquid). In the low temperature regime, this could be done by using suitable (exact) DMRG-based numerical techniques [18, 155], At higher temperature in the activated regime, we could extend the approach by Shklovskii and Efros [160]: as a first step, we may repeat the same analysis carried out in chapter 4, using a different density of states which accounts for the Coulomb gap. Then, another possibility would be to redo all the calculations within a mean-field Hartree approach [4].

- As stressed in chapters 4 and 5, a remarkable feature of the activated regime is that a *finite* window of energies (Mott hopping energy Δ) around the Fermi level is relevant for electronic transport. An intriguing possibility would be to introduce an asymmetry between the couplings of the nanowires to the left/right electronic reservoirs, modelled as a potential barrier, in order to favor transport in a specific direction. Such a system, put in contact with a "hot" substrate, would exploit the temperature difference as a driving force to pump an electric current. Transport would be possible provided that Δ is larger than the barrier. This might be an efficient way to convert the heat evacuated from a hot spot into electric power.

- Going beyond the linear response approximation. Setting *finite* voltage and temperature differences would matter greatly in the quest for systems capable to deliver large output power [187]. On a practical level, this would require to go beyond the standard Onsager framework [151], and to use at least an Hartree-like approach to determine self-consistently how the electrostatic potential profile within a nanowire is locally modified by the (large) charge injected from the electrodes [136]. This point, in the regime of elastic transport at low temperatures, has been the subject of a recent work done in the group, which however has not yet been finalized. An extension to higher temperatures in the activated transport regime is naturally envisaged: in this last case, we would need to solve a non-linear version of the Random Resistor Network. Despite seeming in principle a computationally tough task, this can be done thanks to a method described by Rodin [147].

- Exploring various possibilities offered by the presence of a third terminal may lead to a better understanding of the bounds on the efficiency of these devices. In line with Refs. [8, 14, 23, 24], it could be instructive to consider the effects of a magnetic field on the performance of the system studied in this work. Furthermore, the possibility of separating and controlling the reversible and irreversible components of the currents may lead to novel and surprising effects.

Bibliography

[1] H. Adhikari, A. F. Marshall, C. E. D. Chidsey, and P. C. McIntyre. Germanium nanowire epitaxy: Shape and orientation control. *Nano Lett.*, 6:318, 2006.

[2] E. Altenkirch. Über den Nutzeffekt der Thermosäulen. *Physikalische Zeitschrift*, 10:560, 1909.

[3] V. Ambegaokar, B. I. Halperin, and J. S. Langer. Hopping conductivity in disordered systems. *Phys. Rev. B*, 4:2612, 1971.

[4] A. Amir, Y. Oreg, and Y. Imry. Variable range hopping in the Coulomb glass. *Phys. Rev. B*, 80:245214, 2009.

[5] L. Anatychuk, J. Stockhom, and G. Pastorino. On the discovery of thermoelectricity by A. Volta. *Proc. of the VIII ECT2010*, 2010.

[6] N. W. Ashcroft and N. D. Mermin. *Solid state physics*. Saunders College Publishing, 1976.

[7] M. Z. Atashbar, D. Banerji, S. Singamaneni, and V. Bliznyuk. Deposition of parallel arrays of palladium nanowires and electrical characterization using microelectrode contacts. *Nanotechnology*, 15:374, 2004.

[8] V. Balachandran, G. Benenti, and G. Casati. Efficiency of three-terminal thermoelectric transport under broken time-reversal symmetry. *Phys. Rev. B*, 87:165419, 2013.

[9] V. Balachandran, R. Bosisio, and G. Benenti. Validity of Wiedemann Franz law in small molecular wires. *Phys. Rev. B*, 86:035433, 2012.

[10] A. Balandin and K. L. Wang. Effect of phonon confinement on the thermoelectric figure of merit of quantum wellsl. *J. Appl. Phys.*, 84:6149, 1998.

[11] A. Balandin and K. L. Wang. Significant decrease of the lattice thermal conductivity due to phonon confinement in a free-standing semiconductor quantum well. *Phys. Rev. B*, 58:1544, 1998.

[12] I. Bejenari and P. Kratzer. Atomistic calculation of the thermoelectric properties of Si nanowires. *arXiv:1406.7167*, 2014.

[13] G. Benenti, G. Casati, T. Prosen, and K. Saito. Colloquium: Fundamental aspects of steady state heat to work conversion. *arXiv:1311.4430*, 2014.

[14] G. Benenti, K. Saito, and G. Casati. Thermodynamic bounds on efficiency for systems with broken time-reversal symmetry. *Phys. Rev. Lett.*, 106:230602, 2011.

[15] M. T. Björk, H. Schmid, C. M. Breslin, L. Gignac, and H. Riel. InAs nanowiregrowthonoxide-masked ⟨111⟩ silicon. *Journal of Crystal Growth*, 344:31, 2012.

[16] C. Blanc, A. Rajapbour, S. Volz, T. Fournier, and O. Bourgeois. Phonon heat conduction in corrugated silicon nanowires below the Casimir limit. *Appl. Phys. Lett.*, 103:043109, 2013.

[17] G. Bohm and G. Zech. *Introduction to statistics and data analysis for physicists*. DESY, 2010.

[18] D. Bohr, P. Schmitteckert, and P. Wölfle. DMRG evaluation of the Kubo formula - Conductance of strongly interacting quantum systems. *Europhys. Lett.*, 73(2):246, 2006.

[19] R. Bosisio, G. Fleury, and J.-L. Pichard. Gate-modulated thermopower of 1-D disordered nanowires: I. Low temperature coherent regime. *New J. Phys.*, 16:035004, 2014.

[20] R. Bosisio, C. Gorini, G. Fleury, and J.-L. Pichard. Gate-modulated thermopower of 1-D disordered nanowires: II. Variable Range Hopping regime. *arXiv:1403.7475*, 2014.

[21] H. Böttner, G. Chen, and R. Venkatasubramanian. Aspects of thin-film superlattice thermoelectric materials, devices and applications. *Mat. Res. Soc. Bulletin*, 31:211, 2006.

[22] A. I. Boukai, Y. Bunimovich, J. Tahir-Kheli, J.-K. Yu, W. A. Goddard, and J. R. Heath. Silicon nanowires as efficient thermoelectric materials. *Nature*, 451:168, 2008.

[23] K. Brandner, K. Saito, and U. Seifert. Strong bounds on Onsager coefficients and efficiency for three-terminal thermoelectric transport in a magnetic field. *Phys. Rev. Lett.*, 110:070603, 2013.

[24] K. Brandner and U. Seifert. Multi-terminal thermoelectric transport in a magnetic field: bounds on Onsager coefficients and efficiency. *New J. Phys.*, 15:105003, 2013.

[25] E. Braun, Y. Eichen, U. Sivan, and G. Ben-Yoseph. DNA-templated assembly and electrode attachment of a conducting silver wire. *Nature*, 391:775, 1998.

[26] P. W. Brouwer, K. M. Frahm, and C. W. J. Beenakker. Distribution of the quantum mechanical time-delay matrix for a chaotic cavity. *Waves Random Media*, 9:91, 1999.

[27] P. W. Brouwer, S. A. van Langen, K. M. Frahm, M. Büttiker, and C. W. J. Beenakker. Distribution of parametric conductance derivatives of a quantum dot. *Phys. Rev. Lett.*, 79:913, 1997.

[28] Y. M. Brovman, J. P. Small, Y. Hu, Y. Fang, C. M. Lieber, and P. Kim. Electric field effect thermoelectric transport in individual Silicon and Germanium/Silicon nanowire. *arXiv:1307.0249*, 2013.

[29] A. Bulusu and D.G. Walker. Review of electronic transport models for thermoelectric materials. *Superlattices and Microstructures*, 44:1, 2008.

[30] P. N. Butcher. Thermal and electrical transport formalism for electronic microstructures with many terminals. *J. Phys.: Condens. Matter*, 2:4869, 1990.

[31] M. Büttiker. Coherent and sequential tunneling in series barriers. *IBM. J. Res. Dev.*, 32:63, 1988.

[32] H.B. Callen. *Thermodynamics and an Introduction to Thermostatics.* John Wiley & Sons, New York, 1985.

[33] H. B. G. Casimir. On Onsager's principle of microscopic reversibility. *Rev. Mod. Phys.*, 17:343, 1945.

[34] P. Chambadal. *Les centrales nucléaires.* Armand Colin, Paris, 1957.

[35] G. V. Chester and A. Thellung. The law of Wiedemann and Franz. *Proc. Phys. Soc.*, 77:1005, 1961.

[36] Y. Cui, X. Duan, J. Hu, and C. M. Lieber. Doping and electrical transport in silicon nanowires. *J. Phys. Chem. B*, 104:5213, 2000.

[37] Y. Cui, Z. Zhong, D. Wang, W. U. Wang, and C. M. Lieber. High performance silicon nanowire field effect transistors. *Nano Lett.*, 3:149, 2003.

[38] B. M. Curtin and J. E. Bowers. Thermoelectric power factor enhancement with gate-all-around silicon nanowires. *J. Appl. Phys.*, 115:143704, 2014.

[39] B. M. Curtin, E. A. Codecido, S. Krämer, and J. E. Bowers. Field-effect modulation of thermoelectric properties in multigated silicon nanowires. *Nano Lett.*, 13:5503, 2013.

[40] B. M. Curtin, E. W. Fang, and J. E. Bowers. Highly ordered vertical silicon nanowire array composite thin films for thermoelectric devices. *J. Electron. Mat.*, 41:887, 2012.

[41] F Curzon. and B. Ahlborn. Efficiency of a Carnot engine at maximum power output. *Am. J. Phys.*, 43:22, 1975.

[42] P. Das Kanungo, H. Schmid, M. T. Björk, L. Gignac, C. Breslin, J. Bruley, C. D. Bessire, and H. Riel. Selective area growth of III-V nanowires and their heterostructures on silicon in a nanotube template: towards monolithic integration of nano-devices. *Nanotechnology*, 24:225304, 2013.

[43] S. Datta. *Electronic Transport in Mesoscopic Systems.* Cambridge University Press, 1995.

[44] J.-F. Dayen, T. L. Wader, G. Rizza, D. S. Golubev, C.-S. Cojocaru, D. Pribat, X. Jehl, M. Sanquer, and J.-E. Wegrowe. Conductance of disordered semiconducting nanowires and carbon nanotubes: a chain of quantum dots. *Eur. Phys. J. Appl. Phys.*, 48:10604, 2009.

[45] S. R. De Groot and P. Mazur. *Nonequilibrium Thermodynamics.* North-Holland, Amsterdam, 1962.

[46] B. Derrida and E. Gardner. Lyapounov exponent of the one dimensional Anderson model: weak disorder expansions. *J. Physique*, 45:1283, 1984.

[47] M. S. Dresselhaus, G. Chen, M. Y. Tang, R. G. Yang, H. Lee, D. Z. Wang, Z. F. Ren, J.-P. Fleurial, and P. Gogna. New directions for low-dimensional thermoelectric materials. *Adv. Mater.*, 19:1043, 2007.

[48] M.S. Dresselhaus. *Nanostructures and energy conversion, in 2003 Rohsenhow Symposium on Future Trends of Heat Transfer.* Cambridge, 2003.

[49] Z. Dughaish. Lead telluride as a thermoelectric material for thermoelectric power generation. *Physica B*, 322:205, 2002.

[50] E. N. Economou. *Green's functions in quantum physics.* Springer, third edition, 2006.

[51] L. Eisenbud. *Ph.D. thesis.* Princeton, 1948.

[52] O. Entin-Wohlman, , and A. Aharony. Three-terminal thermoelectric transport under broken time-reversal symmetry. *Phys. Rev. B*, 85:085401, 2012.

[53] O. Entin-Wohlman, Y. Imry, and A. Aharony. Three-terminal thermoelectric transport through a molecular junction. *Phys. Rev. B*, 82:115314, 2010.

[54] H. J. Fan, P. Werner, and M. Zacharias. Semiconductor nanowires: from self-organization to patterned growth. *Small*, 2:700, 2006.

[55] Z. Fan, J. C. Ho, Z. A. Jacobson, R. Yerushalmi, R. L. Alley, H. Razavi, and A. Javey. Wafer-scale assembly of highly ordered semiconductor nanowire arrays by contact printing. *Nano Lett.*, 8:20, 2008.

[56] R. A. Farrell, N. T. Kinahan, S. Hansel, K. O. Stuen, N. Petkov, M. T. Shaw, L. E. West, V. Djara, R. J. Dunne, O. G. Varona, P. G. Gleeson, Jung S.-J, H.-Y. Kim, M. M. Koleśnik, T. Lutz, C. P. Murray, J. D. Holmes, P. F. Nealey, G. S. Duesberg, V. Krstić, and M. A. Morris. Large-scale parallel arrays of silicon nanowires via block copolymer directed self-assembly. *Nanoscale*, 4:3228, 2012.

[57] D. K. Ferry and S. M. Goodnick. *Transport in nanostructures.* Cambridge University Press, Cambridge, England, 1997.

[58] J.-P. Fleurial, A. Borshchevsky, A. Caillat, D. T. Morelli, and G. P. Meisner. *in Proceedings of the 15th Int. Conf. on Thermoelectrics.* Eds. T. Caillat, J.-P. Fleurial, A. Borshchevsky, IEEE catalog number 96TH8169, Piscataway (NJ), 1996.

[59] J. E. Gentle. *"Cholesky Factorization" in* Numerical Linear Algebra for Applications in Statistics. Springer-Verlag, Berlin, 1998.

[60] H. Goldsmid and R. Douglas. The use of semiconductors in thermoelectric refrigeration. *British Journal of Applied Physics*, 5:386, 1954.

[61] H. J. Goldsmid. *Introduction to thermoelectricity.* Springer, 2009.

[62] A. J. Grant and E. A. Davis. Hopping conduction in amorphous semiconductors. *Sol. State Comm.*, 15:563, 1974.

[63] M. Y. Han, J. C. Brant, and P. Kim. Electron transport in disordered graphene nanoribbons. *Phys. Rev. Lett.*, 104:056801, 2010.

[64] T. C. Harman, P. J. Taylor, M. P. Walsh, and B. E. LaForge. Quantum dot superlattice thermoelectric materials and devices. *Science*, 297:2229, 2002.

[65] H. Hasegawa, H. Fujikura, and H. Okada. Molecular-beam epitaxy and device applications of III-V semiconductor nanowires. *MRS Bulletin*, 24:25, 1999.

[66] D. G. Hasko, J. R. A. Cleaver, H. Ahmed, C. G. Smith, and J. E. Dixon. Hopping conduction in a free-standing GaAs-AlGaAs heterostructure wire. *Appl. Phys. Lett.*, 62:2533, 1993.

[67] J. R. Heath, P. J. Kuekes, G. S. Snider, and R. S. Williams. A defect-tolerant computer architecture: Opportunities for nanotechnology. *Science*, 280:1716, 1998.

[68] J. R. Heath and F. K. Legoues. A liquid solution synthesis of single-crystal germanium quantum wires. *Chem. Phys. Lett.*, 208:263, 1993.

[69] J. P. Heremans. Low-dimensional thermoelectricity. *Acta Phys. Pol.*, 4:609, 2005.

[70] J.-S. Heron, C. Bera, T. Fournier, N. Mingo, and O. Bourgeois. Blocking phonons via nanoscale geometrical design. *Phys. Rev. B*, 82:155458, 2010.

[71] L. D. Hicks and M. S. Dresselhaus. Effect of quantum-well structures on the thermoelectric figure of merit. *Phys. Rev. B*, 47:12727, 1993.

[72] L. D. Hicks and M. S. Dresselhaus. Thermoelectric figure of merit of a one-dimensional conductor. *Phys. Rev. B*, 47:16631, 1993.

[73] L. D. Hicks, T. C. Harman, and M. S. Dresselhaus. Use of quantum-well superlattices to obtain a high figure of merit from nonconventional thermoelectric materials. *Appl. Phys. Lett.*, 63:3230, 1993.

[74] A. I. Hochbaum, R. Chen, R. D. Delgado, W. Liang, E. C. Garnett, M. Najarian, A. Majumdar, and P. Yang. Enhanced thermoelectric performance of rough silicon nanowires. *Nature*, 451:163, 2008.

[75] P. E. Hopkins, B. Kaehr, L. M. Phinney, T. P. Koehler, A. M. Grillet, D. Dunphy, F. Garcia, and C. J. Brinker. Measuring the thermal conductivity of porous, transparent SiO_2 films with time domain thermoreflectance. *J. Heat Transfer*, 133:061601, 2011.

[76] G. Hornyak, M. Kroll, R. Pugin, T. Sawitowski, G. Schmid, J. O. Bovin, G. Karsson, H. Hofmeister, and S. Hopfe. Gold clusters and colloids in alumina nanotubes. *Chem.-Eur. J .*, 3:1951, 1997.

[77] M. Horvat, T. Prosen, G. Benenti, and G. Casati. Railway switch transport model. *Phys. Rev. E*, 86:052102, 2012.

[78] G. Y. Hu and R. F. O'Connell. Analytical inversion of symmetric tridiagonal matrices. *J. Phys. A: Math. Gen.*, 29:1511, 1996.

[79] T. E. Humphrey, R. Newbury, R. P. Taylor, and H. Linke. Reversible quantum brownian heat engines for electrons. *Phys. Rev. Lett.*, 89:116801, 2002.

[80] M.-T. Hung, C.-C. Wang, J.-C. Hsu, J.-Y. Chiou, S.-W. Lee, T. M. Hsu, and P.-W. Li. Large reduction in thermal conductivity for Ge quantum dots embedded in SiO_2 system. *Appl. Phys. Lett.*, 101:251913, 2012.

[81] Y. Imry. *Introduction to Mesoscopic Physics*. Oxford University Press, 1997.

[82] A. F. Ioffe. *Semiconductor thermoelements and thermoelectric cooling*. Infosearch, ltd., London, 1957.

[83] P. A. Jacquet. Thermoelectric transport properties of a chain of quantum dots with self-consistent reservoirs. *J. Stat. Phys.*, 134:709, 2009.

[84] J-H. Jiang, O. Entin-Wohlman, and Y. Imry. Thermoelectric three-terminal hopping transport through one-dimensional nanosystems. *Phys. Rev. B*, 85:075412, 2012.

[85] J-H. Jiang, O. Entin-Wohlman, and Y. Imry. Hopping thermoelectric transport in finite systems: boundary effects. *Phys. Rev. B*, 87:205420, 2013.

[86] J. P. Joule. On the calorific effects of magneto-electricity, and on the mechanical value of heat. *The London, Edinburgh, and Dublin Philosophical Magazine and Journal of Science*, 23:263, 1843.

[87] C. L. Kane and M. P. A. Fisher. Thermal transport in a Luttinger liquid. *Phys. Rev. Lett.*, 76:3192, 1996.

[88] M. Kappus and E. Wegner. Anomaly in the band centre of the one-dimensional Anderson model. *Z. Phys. B*, 45:15, 1981.

[89] S. Karg, P. Mensch, B. Gotsmann, H. Schmid, P. Das Kanungo, H. Ghoneim, V. Schmidt, M. T. Björk, V. Troncale, and H. Riel. Measurement of thermoelectric properties of single semiconductor nanowires. *J. Electron. Mat.*, 42:2409, 2013.

[90] S. I. Khondaker, I. S. Shlimak, J. T. Nicholis, M. Pepper, and D. A. Ritchie. Two-dimensional hopping conductivity in a δ-doped GaAs/$Al_xGa_{1-x}As$ heterostructure. *Phys. Rev. B*, 59:4580, 1999.

[91] T. Klitsner and R. O. Pohl. Phonon scattering at silicon crystal surfaces. *Phys. Rev. B*, 36:6551, 1987.

[92] S. Kodambaka, J. Tersoff, M. C. Reuter, and F. M. Ross. Germanium nanowire growth below the eutectic temperature. *Science*, 316:729, 2007.

[93] T. Koga, S. B. Cronin, M. S. Dresselhaus, J. L. Liu, and K. L. Wang. Experimental proof-of-principle investigation of enhanced $Z_{3D}T$ in (001) oriented Si/Ge superlattices. *Appl. Phys. Lett.*, 77:1, 2000.

[94] B. Kramer and A. MacKinnon. Localization: theory and experiment. *Rep. Prog. Phys.*, 56:1469, 1993.

[95] J. Kurkijärvi. Hopping conductivity in one dimension. *Phys. Rev. B*, 8:922, 1973.

[96] R. F. Kwasnick, M. A. Kastner, J. Melngailis, and P. A. Lee. Nonmonotonic variations of the conductance with electron density in 70-nm-wide inversion layers. *Phys. Rev. Lett.*, 52:224, 1984.

[97] F. Ladieu and J.-P. Bouchaud. Conductance statistics in small GaAs:Si wires at low temperatures. I. Theoretical analysis: truncated quantum fluctuations in insulating wires. *J. Phys. I France*, 3:2311, 1993.

[98] F. Ladieu, D. Mailly, and M. Sanquer. Conductance statistics in small insulating GaAs:Si wires at low temperature. II: experimental study. *J. Phys. I France*, 3:2321, 1993.

[99] F. Ladieu and M. Sanquer. Pertinence et limitations de la loi de Mott dans les isolants désordonnées. *Ann. Phys. Fr.*, 21:267, 1996.

[100] A. Lassl, P. Schlagheck, and K. Richter. Effects of short-range interactions on transport through quantum point contacts: A numerical approach. *Phys. Rev. B*, 75:045346, 2007.

[101] P. A. Lee. Variable-range hopping in finite one-dimensional wires. *Phys. Rev. Lett.*, 53:2042, 1984.

[102] D. Li, Y. Wu, P. Kim, L. Shi, P. Yang, and A. Majumdar. Thermal conductivity of individual silicon nanowires. *Appl. Phys. Lett.*, 83:2934, 2003.

[103] G. Liang, W. Huang, C. S. Koong, J-S. Wang, and J. Lan. Geometry effects on thermoelectric properties of silicon nanowires based on electronic band structures. *J. Appl. Phys.*, 107:014317, 2010.

[104] Y.-M. Lin, X. Sun, and M. S. Dresselhaus. Theoretical investigation of thermoelectric transport properties of cylindrical bi nanowires. *Phys. Rev. B*, 62:4610, 2000.

[105] W. Lu, J. Xiang, B. P. Timko, Y. Wu, and C. M. Lieber. One-dimensional hole gas in germanium/silicon nanowire heterostructures. *Proc. Natl. Acad. Sci. U.S.A.*, 102:10046, 2005.

[106] P. Machon, M. Eschrig, and W. Belzig. Nonlocal thermoelectric effects and nonlocal Onsager relations in a three-terminal proximity-coupled superconductor-ferromagnet device. *Phys. Rev. Lett.*, 110:047002, 2013.

[107] G. D. Mahan, B. Sales, and Sharp. J. Thermoelectric materials: new approaches to an old problem. *Phys. Today*, 50:42, 1997.

[108] G. D. Mahan and J. O. Sofo. The best thermoelectric. *Proc. Natl. Acad. Sci. USA*, 93:7436, 1996.

[109] A. Majumdar. Thermoelectricity in semiconductor nanostructures. *Science*, 303:777, 2004.

[110] C. B. Mao, D. J. Solis, B. D. Reiss, S. T. Kottmann, R. Y. Sweeney, A. Hayhurst, G. Georgiou, B. Iverson, and A. M. Belcher. Virus-based toolkit for the directed synthesis of magnetic and semiconducting nanowires. *Science*, 303:213, 2004.

[111] F. Mazza, R. Bosisio, G. Benenti, V. Giovannetti, R. Fazio, and F. Taddei. Thermoelectric efficiency of three-terminal quantum termal machines. *New J. Phys*, 16:085001, 2014.

[112] J. D. Meindl, Q. Chen, and J. A. Davis. Limits on silicon nanoelectronics for terascale integration. *Science*, 293:2044, 2001.

[113] A. Miller and E. Abrahams. Impurity conduction at low concentrations. *Phys. Rev.*, 120:745, 1960.

[114] N. Mingo. Thermoelectric figure of merit and maximum power factor in III-V semiconductor nanowires. *Appl. Phys. Lett.*, 84:2652, 2004.

[115] M. I. Molina. Nonlinear surface impurity in a semi-infinite two-dimensional square lattice: Green function approach. *Phys. Rev. B*, 74:045412, 2006.

[116] J. Moon, J.-H. Kim, Z. C. Y. Chen, J. Xiang, and R. Chen. Gate-modulated thermoelectric power factor of hole gas in Ge-Si core-shell nanowires. *Nano Lett.*, 13:1196, 2013.

[117] A. M. Morales and C. M. Lieber. A laser ablation method for the synthesis of crystalline semiconductor nanowires. *Science*, 279:208, 1998.

[118] D. T. Morelli, T. Caillat, J.-P. Fleurial, A. Borshchevsky, J. Vandersande, B. Chen, and C. Uher. Low-temperature transport properties of p-type $CoSb_3$. *Phys. Rev. B*, 51:9622, 1995.

[119] T. Morita. Useful procedure for computing the lattice Green functions of square, tetragonal, and bcc lattices. *J. Math. Phys.*, 12:1744, 1971.

[120] N. F. Mott. Conduction in non-crystalline materials III. Localized states in a pseudogap and near extremities of conduction and valence bands. *Phil. Mag.*, 19:835, 1969.

[121] N. F. Mott and E. A. Davis. *Electronic Processes in Non Crystalline Materials*. Clarendon, Oxford, (2nd ed.), 1979.

[122] T. Koga S.B. Cronin O. Rabin M.R. Black G. Dresselhaus M.S. Dresselhaus, Y.M. Lin. *Semiconductors and Semimetals, III, ed. T.M. Tritt*. Academic Press, New York, 2001.

[123] N. Nakpathomkun, H. Q. Xu, and H. Linke. Thermoelectric efficiency at maximum power in low-dimensional systems. *Phys. Rev. B*, 82:235428, 2010.

[124] N. Neophytou and H. Kosina. Effects of confinement and orientation on the thermoelectric power factor of silicon nanowires. *Phys. Rev. B*, 83:245305, 2011.

[125] G. S. Nolas, J. Sharp, and H. J. Goldsmid. *Thermoelectricity.* Springer-Verlag, Berlin, 2000.

[126] I. I. Novikov. The efficiency of atomic power stations. *J. Nuclear Energy*, 7:125, 1958.

[127] G. S. Ohm. *Die galvanische Kette.* Riemann, Berlin, 1827.

[128] L. Onsager. Reciprocal relations in irreversible processes. I. *Phys. Rev.*, 37:405, 1931.

[129] A. Ossipov, T. Kottos, and T. Geisel. Statistical properties of phases and delay times of the one-dimensional Anderson model with one open channel. *Phys. Rev. B*, 61:11411, 1999.

[130] H. Ouerdane, C. Goupil, Y. Apertet, A. Michot, and A. Abbout. *"A linear nonequilibrium thermodynamics approach to optimization of thermoelectric devices" in Thermoelectric Nanomaterials (K. Koumoto et T. Mori eds.), vol. 182 of Springer Series in Materials Science, 323.* Springer Berlin Heidelberg, 2013.

[131] J. Peltier. Nouvelles expériences sur la caloricité des courants électriques. *Annales de chimie*, 56:371, 1834.

[132] J. B. Pendry. Quantum limits to the flow of information and entropy. *J. Phys. A: Math. Gen.*, 16:2161, 1983.

[133] K. Peng, Y. Yan, S. Gao, and J. Zhu. Dendrite-assisted growth of silicon nanowires in electroless metal deposition. *Adv. Funct. Mater.*, 13:127, 2003.

[134] K. Peng, Y. J. Yan, S. P. Gao, and J. Zhu. Synthesis of large-area silicon nanowire arrays via self-assembling nanochemistry. *Adv. Mater.*, 14:1164, 2002.

[135] J.-L. Pichard. in *Quantum Coherence in Mesoscopic Systems,* NATO ASI Series, Series B: Phys. vol. 254, ed. B. Kramer. Plenum Press, 1990.

[136] S. Pleutin, H. Grabert, G-L. Ingold, and A. Nitzan. The electrostatic potential profile along a biased molecular wire : A model quantum mechanical calculation. *J. Chem. Phys.*, 118:3756, 2003.

[137] R. O. Pohl, X. Liu, and E. Thompson. Low-temperature thermal conductivity and acoustic attenuation in amorphous solids. *Rev. Mod. Phys.*, 74:991, 2002.

[138] W. Poirier, D. Mailly, and M. Sanquer. Tunneling and interferences in very small GaAs metal-semiconductor field-effect transistors. *Phys. Rev. B*, 59:10856, 1999.

[139] M. Pollack. Hopping transport in solids. *J. Non-Cryst. Solids*, 11:1, 1972.

[140] E. Pop, S. Sinha, and K. E. Goodson. Heat generation and transport in nanometer scale transistors. *Proceedings of the IEEE*, 94:1587, 2006.

[141] S. Pregl, W. M. Weber, D. Nozaki, J. Kunstmann, L. Baraban, J. Opitz, T. Mikolajick, and G. Cuniberti. Parallel arrays of schottky barrier nanowire field effect transistors: Nanoscopic effects for macroscopic current output. *Nano Research*, 6:381, 2013.

[142] Y. W. Ra, K. S. Choi, J. H. Kim, Y. B. Hahn, and Y. H. Im. Fabrication of ZnO nanowires using nanoscale spacer lithography for gas sensors. *Small*, 4:1105, 2008.

[143] M. È. Raikh and I. M. Ruzin. Fluctuations of the hopping conductance of one-dimensional systems. *Zh. Eksp. Teor. Fiz.*, 95:1113, 1989.

[144] S. A. Ramakrishna and N. Kumar. Distribution of the delay time and the dwell time for wave reflection from a long random potential. *Eur. Phys. J. B*, 23:515, 2001.

[145] L. G. C. Rego and G. Kirczenow. Quantized thermal conductance of dielectric quantum wires. *Phys. Rev. Lett.*, 81:232, 1998.

[146] S. Roddaro, D. Ercolani, M. A. Safeen, S. Suomalainen, F. Rossella, F. Giazotto, L. Sorba, and F. Beltram. Giant thermovoltage in single InAs nanowire Field-Effect Transistors. *Nano Lett.*, 13:3638, 2013.

[147] A. S. Rodin and M. M. Fogler. Numerical studies of variable-range hopping in one-dimensional systems. *Phys. Rev. B*, 80:155435, 2009.

[148] A. S. Rodin and M. M. Fogler. Apparent power-law behavior of conductance in disordered quasi-one-dimensional systems. *Phys. Rev. Lett.*, 105:106801, 2010.

[149] A. S. Rodin and M. M. Fogler. Hopping transport in systems of finite thickness or length. *Phys. Rev. B*, 84:125447, 2011.

[150] K. Saito, G. Benenti, G. Casati., and T. Prosen. Thermopower with broken time-reversal symmetry. *Phys. Rev. B*, 84:201306(R), 2011.

[151] D. Sánchez and R. López. Scattering theory of nonlinear thermoelectric transport. *Phys. Rev. Lett.*, 110:026804, 2013.

[152] D. Sánchez and L. Serra. Thermoelectric transport of mesoscopic conductors coupled to voltage and thermal probes. *Phys. Rev. B*, 84:201307(R), 2011.

[153] P. Scheuerpflug, M. Hauck, and J. Fricke. Thermal properties of silica aerogel between 1.4 and 330 K. *J. Non-Cryst. Solids*, 145:196, 1992.

[154] V. Schmidt, P. F. J. Mensch, S. F. Karg, B. Gotsmann, P. Das Kanungo, H. Schmid, and H. Riel. Using the Seebeck coefficient to determine charge carrier concentration, mobility, and relaxation time in InAs nanowires. *Applied Physics Letters*, 104:012113, 2014.

[155] P. Schmitteckert. Calculating Green functions from finite systems. *J. Phys.: Conf. Ser.*, 220:012022, 2010.

[156] C. Schonenberger, B. M. I. van der Zande, L. G. J. Fokkink, M. Henny, C. Schmid, M. Kruger, A. Bachtold, R. Huber, H. Birk, and U. Staufer. Template synthesis of nanowires in porous polycarbonate membranes: electrochemistry and morphology. *J. Phys. Chem. B*, 101:5497, 1997.

[157] T. J. Seebeck. Ueber den Magnetismus der galvanische Kette. *Abhandlungen der Deutschen Akademie der Wissenschaften zur Berlin*, page 289, 1822.

[158] R. A. Serota, R. K. Kalia, and P. A. Lee. New aspects of variable-range hopping in finite one-dimensional wires. *Phys. Rev. B*, 33:8441, 1986.

[159] G. Shin, C. H. Yoon, M. Y. Bae, Y. C. Kim, S. K. Hong, J. A. Rogers, and J. S. Ha. Stretchable Field-Effect-Transistor array of suspended SnO_2 nanowires. *Small*, 9:1181, 2011.

[160] B. Shklovskii and A. Efros. *Electronic Properties of Doped Semiconductors.* Springer-Verlag, Berlin, 1984.

[161] G. A. Slack. *in* CRC Handbook of Thermoelectrics*, ed. by D. M. Rowe.* CRC Press, FL, 1995.

[162] F. T. Smith. Lifetime matrix in collision theory. *Phys. Rev.*, 118:349, 1960.

[163] G. J. Snyder and E. S. Toberer. Complex thermoelectric materials. *Nature Mater.*, 7:105, 2008.

[164] A. M. Somoza, M. Ortuño, and M. Pollak. Collective variable-range hopping in the Coulomb gap: Computer simulations. *Phys. Rev. B*, 73:045123, 2006.

[165] A. D. Stone, P. A. Mello, K. A. Muttalib, and J.-L. Pichard. in *Mesoscopic Phenomena in Solids,* vol. 30, ed. B. L. Altschuler, P. A. Lee and R. A. Webb. North-Holland, 1991.

[166] A. Stranz, Waag A., and E. Peiner. High-temperature performance of stacked silicon nanowires for thermoelectric power generation. *J. Electron. Mat.*, 42:2233, 2013.

[167] C. Suryanarayana. Mechanical alloying and milling. *Progress in Materials Science*, 46:1, 2001.

[168] C. Texier and A. Comtet. Universality of the wigner time delay distribution for one-dimensional random potentials. *Phys. Rev. Lett.*, 82:4220, 1999.

[169] W. Thomson. On a mechanical theory of thermo-electric currents. *Proceedings of the Royal Society of Edinburgh*, 1851.

[170] W. Thomson. On the dynamical theory of heat. *Transactions of the Royal Society of Edinburgh*, 1852.

[171] W. Thomson. The bakerian lecture. on the electro-dynamic qualities of metals. *Philosophical Transactions of the Royal Society of London*, 146:649, 1856.

[172] Y. Tian, M. R. Sakr, J. M. Kinder, D. Liang, M. J. MacDonald, R. L. J. Qiu, H.-J. Gao, and X. P. A. Gao. One-dimensional quantum confinement effect modulated thermoelectric properties in InAs nanowires. *Nano Lett.*, 12:6492, 2012.

[173] A. Tilke, R. H. Blick, H. Lorenz, J. P. Kotthaus, and D. A. Wharam. Coulomb blockade in quasimetallic silicon-on-insulator nanowires. *Appl. Phys. Lett.*, 75:3704, 1999.

[174] T. J. Trentler, K. M. Hickman, S. C. Goel, A. M. Viano, P. C. Gibbons, and W. E. Buhro. Solution-liquid-solid growth of crystalline III-V semiconductors: an analogy to vapor-liquid-solid growth. *Science*, 270:1791, 1995.

[175] C. Van den Broeck. Thermodynamic efficiency at maximum power. *Phys. Rev. Lett.*, 95:190602, 2005.

[176] S. A. van Langen, P. G. Silvestrov, and C. W. J. Beenakker. Thermopower of single-channel disordered and chaotic conductors. *Supperlattices Microstruct.*, 23:691, 1998.

[177] M. G. Vavilov and A. D. Stone. Failure of the Wiedemann-Franz law in mesoscopic conductors. *Phys Rev. B*, 72:205107, 2005.

[178] R. Venkatasubramanian, E. Siivola, T. Colpitts, and B. O'Quinn. Thin-film thermoelectric devices with high room-temperature figures of merit. *Nature*, 413:597, 2001.

[179] C. J. Vineis, A. Shakouri, A. Majumdar, and M. G. Kanatzidis. Nanostructured thermoelectrics: Big efficiency gains from small features. *Advanced Materials*, 22:3970, 2010.

[180] A. Volta. Nuova memoria sull'elettricità animale. *Lettere al signor Abate Anton Maria Vassalli*, 1794.

[181] R. S. Wagner and W.C. Ellis. Vapor-liquid-solid mechanism of single crystal growth. *Appl. Phys. Lett .*, 4:89, 1964.

[182] N. Wakeham, A. F. Bangura, X. Xu, J.-F. Mercure, M. Greenblatt, and N. E. Hussey. Gross violation of the Wiedemann-Franz law in a quasi-one-dimensional conductor. *Nat. Commun.*, 2:396, 2011.

[183] M. C. P. Wang and B. D. Gates. Directed assembly of nanowires. *Materials Today*, 12:34, 2009.

[184] Z. L. Wang. Oxide nanobelts and nanowires-growth, properties and applications. *J. Nanosci. Nanotechnol.*, 8:27, 2008.

[185] R. A. Webb, A. Hartstein, J. J. Wainer, and A. B. Fowler. Origin of the peaked structure in the conductance of one-dimensional silicon accumulation layers. *Phys. Rev. Lett.*, 54:1577, 1985.

[186] L. W. Whitlow and T. Hirano. Superlattice applications to thermoelectricity. *J. Appl. Phys.*, 78:5460, 1995.

[187] R. S. Whitney. Most efficient quantum thermoelectric at finite power output. *Phys. Rev. Lett.*, 112:130601, 2014.

[188] E. P. Wigner. Lower limit for the energy derivative of the scattering phase shift. *Phys. Rev.*, 98:145, 1955.

[189] Y. Wu, Y. Cui, L. Huynh, C. J. Barrelet, D. C. Bell, and C. M. Lieber. Controlled growth and structures of molecular-scale silicon nanowires. *Nano Lett.*, 4:433, 2004.

[190] Y. T. Wu and P. D. Yang. Germanium nanowire growth via simple vapor transport. *J. Chem. Mater.*, 12:605, 2000.

[191] P. D. Yang. The chemistry and physics of semiconductor nanowires. *MRS Bulletin*, 30:85, 2005.

[192] R. Yerushalmi, Z. A. Jacobson, J. C. Ho, Z. Fan, and A. Javey. Large scale, highly ordered assembly of nanowire parallel arrays by differential roll printing. *Appl. Phys. Lett.*, 91:203104, 2007.

[193] J. Yvon. *in Proceedings of the International Conference on Peaceful Uses of Atomic Energy.* United Nations, Geneva, 1955.

[194] T. Zhai and J. Yao. *One-Dimensional Nanostructures, Principles and Applications.* John Wiley & Sons, 2012.

[195] F. L. Zhang, T. Nyberg, and O. Inganas. Conducting polymer nanowires and nanodots made with soft lithography. *Nano Lett.*, 2:1373, 2002.

[196] G. Zhang, K. Tateno, H. Gotoh, and H. Nakano. Parallel-aligned GaAs nanowires with <110> orientation laterally grown on [311]B substrates via the gold-catalyzed vapor-liquid-solid mode. *Nanotechnology*, 21:095607, 2010.

[197] Y. J. Zhang, J. Zhu, Q. Zhang, Y. J. Yan, N. L. Wang, and X. Z. Zhang. Synthesis of GeO_2 nanorods by carbon nanotubes template. *Chem. Phys. Lett.*, 317:504, 2000.

[198] G. Zheng, W. Lu, S. Jin, and C. M. Lieber. Synthesis and fabrication of high-performance n-type silicon nanowire transistors. *Adv. Mater.*, 16:1890, 2004.

[199] J. M. Ziman. *Electrons and Phonons: The Theory of Transport Phenomena in Solids.* Clarendon Press, 1996.

[200] I. P. Zvyagin. On the theory of hopping transport in disordered semiconductors. *Phys. Stat. Sol. (b)*, 58:443, 1973.

[201] I. P. Zvyagin. *Hopping Transport in Solids.* ed. by M. Pollak and B. I. Shklovskii (North-Holland, Amsterdam), 1991.